

UNCLASSIFIED

AD NUMBER
AD357617
NEW LIMITATION CHANGE
TO Approved for public release, distribution unlimited
FROM Distribution Controlled. All requests to Air Force Flight Dynamics Lab, Research and Technology Div, Air Force Systems Cmd, WPAFB, OH 45433
AUTHORITY
DoDD 5200.20; September 15, 1971.

THIS PAGE IS UNCLASSIFIED

UNCLASSIFIED



AD NUMBER

AD-357 617

CLASSIFICATION CHANGES

TO UNCLASSIFIED

FROM CONFIDENTIAL

AUTHORITY

ASTIA Tab No. 71-18, dtd September 15, 1971.

1999102/200

THIS PAGE IS UNCLASSIFIED

UNCLASSIFIED

AD 357 617-4

DEFENSE DOCUMENTATION CENTER

FOR

SCIENTIFIC AND TECHNICAL INFORMATION

CAMERON STATION ALEXANDRIA, VIRGINIA

CLASSIFICATION CHANGED
TO UNCLASSIFIED
FROM CONFIDENTIAL
PER AUTHORITY LISTED IN

TAB. 71-18

15 SEPTEMBER 1971



UNCLASSIFIED

AD 357 617-L

THIS REPORT HAS BEEN DELIMITED
AND CLEARED FOR PUBLIC RELEASE
UNDER DOD DIRECTIVE 5200.20 AND
NO RESTRICTIONS ARE IMPOSED UPON
ITS USE AND DISCLOSURE.

DISTRIBUTION STATEMENT A

APPROVED FOR PUBLIC RELEASE;
DISTRIBUTION UNLIMITED.

UNCLASSIFIED

FIL TDR 64-147

CATALOGED BY DDC
AS AD No. 357617

(Unclassified Title)

APPROXIMATELY 100,000
OF UNCLASSIFIED LITERATURE

J.E. Martuscelli
G. Zarterian
R.B. McCallum

Massachusetts Institute of Technology

TECHNICAL DOCUMENTARY REPORT NO. FIL TDR 64-147

February 1965

DOWNLOADED AT 3 YEAR INTERVALS;
DECLASSIFIED AFTER 12 YEARS.
DOD DIR 5800.10

This document contains information affecting the National Defense of the United States within the meaning of the Espionage Laws, Title 18, U.S.C., Sections 793 and 794. Its transmission or the revelation of its contents in any manner to any unauthorized person is prohibited by law.

Air Force Flight Sciences Laboratory
Research and Technology Division
Air Force Systems Command
Wright-Patterson Air Force Base,

DDC

MAR 15 1965

DOC-IRA

AFD-2203

AF-WF-0-MAR 65 70

UNCLASSIFIED

Reproduced From
Best Available Copy

357617

NOTICE: When government or other drawings, specifications or other data are used for any purpose other than in connection with a definitely related government procurement operation, the U. S. Government thereby incurs no responsibility, nor any obligation whatsoever; and the fact that the Government may have formulated, furnished, or in any way supplied the said drawings, specifications, or other data is not to be regarded by implication or otherwise as in any manner licensing the holder or any other person or corporation, or conveying any rights or permission to manufacture, use or sell any patented invention that may in any way be related thereto.

When Government drawings, specifications, or other data are used for any purpose other than in connection with a definitely related Government procurement operation, the United States Government thereby incurs no responsibility nor any obligation whatsoever; and the fact that the Government may have formulated, furnished, or in any way supplied the said drawings, specifications, or other data, is not to be regarded by implication or otherwise as in any manner licensing the holder or any other person or corporation, or conveying any rights or permission to manufacture, use, or sell any patented invention that may in any way be related thereto.

Qualified users may obtain copies of this report from the Defense Documentation Center.

Copies of this report should not be returned to the Research and Technology Division, Wright-Patterson Air Force Base, Ohio, unless return is required by security considerations, contractual obligations, or notice on a specific document.

FOREWORD

This report, which presents the experimental and theoretical results of an investigation of aerothermoelastic instabilities of inflatable vehicles, was prepared by the Aeroelastic and Structures Research Laboratory, Massachusetts Institute of Technology, Cambridge, Massachusetts for the AF Flight Dynamics Laboratory, Research and Technology Division, Wright-Patterson Air Force Base, Ohio. The major portion of the work was performed at MIT under the supervision of Professor H. Ashley, with Mr. J. R. Martuccelli and Mr. G. Zartarian as co-project leaders. The flutter tests were carried out in Tunnel A, Gas Dynamics Facility, ARO Inc., AEDC, Tullahoma, Tenn., the transonic tunnel at the Cornell Aeronautical Laboratories, Inc., Buffalo, New York, and the Wright Brothers Wind Tunnel, Massachusetts Institute of Technology, Cambridge, Massachusetts.

The research was accomplished under Air Force Contract No. AF33(657)-8468, Project No. 1370, "Dynamic Problems in Flight Vehicles", and Task No. 137003, "Prediction and Prevention of Aerothermoelastic Instabilities", with Mr. S. J. Pollock of the Flight Dynamics Laboratory as task engineer. This research was started in June 1962 and was completed in August 1964.

Authors of the main report are J. R. Martuccelli, G. Zartarian, and R. B. McCallum. Appendices II and III are mainly the work of Professors M. Landahl and J. W. Mar, respectively. The authors wish to express their appreciation to Professor J. Dugundji for his guidance in the development of the vibration theory for inflatable vehicles, and to the personnel of the wind tunnel facilities used in the course of this program for their help in conducting the flutter tests.

Portions of this document are classified CONFIDENTIAL since the data revealed can be employed to establish design criteria for the prevention of aeroelastic instabilities of future inflatable vehicles. This report has been given the Aeroelastic and Structures Research Laboratory number ASRL TR 114-1.

This technical documentary report has been reviewed and is approved.

Walter J. Minton
WALTER J. MINTON
Asst. for Research & Technology
Vehicle Dynamics Division
AF Flight Dynamics Laboratory

ABSTRACT

This report covers a program of research on analytical studies and experimental verification of the vibration and flutter characteristics of inflatable structures, as a first step toward establishing design criteria which will insure that lifting surfaces for future inflatable vehicles will be free from dynamic instabilities. The research effort was mainly confined to the AIRMAT-type structure, where the spacing of the surfaces is achieved by chords held in tension by internal pressure.

A method is presented for constructing AIRMAT models which are suitable for use as wind tunnel flutter models. In addition to the standard vibration data, the vibration mode shapes of a delta wing, as determined by use of mirrors mounted on the model, are presented. Shear- and bending-type deformations are shown to be equally important for the models used in the programs by comparing the results of static and dynamic tests with theoretical calculations. Some experimental results on the properties of the model surface material are also included.

Sixty-five flutter points were obtained for cantilevered, half-span, delta-wing models over the Mach number range from 0.116 to 6.0. In addition to determining an experimental boundary for a basic delta model, the effects of leading-edge sweep, angle of attack, and the pressure differential between the model and ambient air pressures were investigated at several supersonic Mach numbers.

A series of theoretical calculations were carried out, employing various combinations of mode shapes (based on measured vibration node lines). The predicted flutter

64FD-2203

UNCLASSIFIED

FDL TDR 64-147

~~CONFIDENTIAL~~

boundaries are in fair agreement with experimental results. The lack of better agreement can be attributed to the simplifying assumptions made in the analysis, particularly those dealing with the assumed mode shapes.

A theoretical investigation on membrane-type flutter of an inflatable panel and the development of the equations governing the structural behavior of an inflated AIRMAT section are presented in separate appendices.

~~CONFIDENTIAL~~

UNCLASSIFIED

TABLE OF CONTENTS

SECTION	PAGE
1 INTRODUCTION	1
2 MODEL INFORMATION	9
A. Model Construction and Instrumentation	9
B. Static Tests	12
C. Vibration Tests	13
1. Test Procedures	13
2. Test Results and Discussion	14
D. Vibration Mode Shapes Using the Mirror Technique	20
1. Test Procedures	20
2. Results and Discussion	21
E. Influence Coefficients	24
1. General	24
2. Results and Discussion	26
F. Material Properties	27
1. General	27
2. Description of Models	27
3. Static Tests	29
4. Dynamic Tests	34
5. Results and Discussion	36
3. WIND-TUNNEL TESTS	79
A. Wind Tunnels	79
B. Testing Procedures	79
1. Supersonic Tests	79
2. Transonic Tests	81
3. Low-Speed Tests	81

TABLE OF CONTENTS (Cont'd)

SECTION	PAGE
C. Flutter Results and Discussion	82
1. General	82
2. Results and Discussion	83
4 CONCLUSIONS AND RECOMMENDATIONS	119
REFERENCES	123
APPENDIX	
I ANALYTICAL PROCEDURES	125
A. An Approximate Method of Deflection and Vibration Analysis	125
B. Flutter Analyses	136
1. Equations of Motion	136
2. Mode Shapes Used in the Calculations	138
3. Aerodynamic Forces	142
4. Summary of Calculations	148
C. Flutter of Blunt Wings at Large Initial Angles of Attack	151
1. General	151
2. Aerodynamic Forces on a Blunt Deformable Surface at Large Angles of Attack, According to Newtonian Theory	152
3. Applications to Two-Dimensional Sections	161
REFERENCES	164
II MEMBRANE-TYPE FLUTTER OF AN INFLATABLE PANEL	191
A. Simplified Mathematical Model	191
B. Aerodynamic Considerations	192

TABLE OF CONTENTS (Cont'd)

APPENDIX		PAGE
	C. Structural Considerations	194
	D. Structural Damping	198
	E. Eigenvalue Problem	199
	F. Stability of Subsonic Waves	200
	G. Stability of Supersonic Waves	201
	H. Effect of Boundary Layer	203
	I. Conclusions	206
	REFERENCES	208
	LIST OF SYMBOLS FOR APPENDIX II	209
III	STRUCTURAL ANALYSIS OF AN INFLATED, AIRMAT-TYPE STRUCTURE	211
	A. Introduction	211
	B. The Geometry of the Deformed Middle Surface	211
	C. The Geometry of the Deformed Shell: The Strain Tensor	215
	D. Definition of Force and Moment Resultants	220
	E. Equations of Equilibrium	233
	F. Stress-Strain Relations for Small Strain	237
	G. Incremental Theory Leading to Large Displacements	239
	H. Finite Deflection of an Initially Flat, Inflated, Uniform Sandwich Plate	250
	LIST OF SYMBOLS FOR APPENDIX III	258

ILLUSTRATIONS

FIGURE		PAGE
1.1	Sketches of Typical Blunted Delta Inflatable Vehicles, Showing Type of Construction	5
1.2	Basic Structural Components of Inflatable Re-Entry Vehicles	6
1.3	Typical Re-Entry Trajectory for an Inflatable Vehicle $\gamma_i = -1$ deg (Entry Angle), $L/D = 0.577$, $h_0 = 400$ K ft	7
2.1	Samples of Inflatable Models	41
2.2	Schematic of Mode Pressure Regulating System and Strain Gages	42
2.3	Wing Deflection vs Uniform Load for Model 1	43
2.4	Excitation System Used for Vibration Tests	44
2.5	Typical Free Vibration Node Lines for 65-deg Sweep Models	45
2.6	Typical Free Vibration Node Lines for 75-deg Sweep Models	46
2.7	Typical Free Vibration Node Lines for Models 1 and 2	47
2.8	Typical Free Vibration Node Lines for Model 10	48
2.9	Free Vibration Node Lines for Model 18	49
2.10	Effect of Ambient Pressure on Frequencies of First Three Modes of Model 2	50
2.11	Mirror Stations Used for Determining Vibration Mode Shapes	51
2.12	Schematic of Mirror Test Setup	52

ILLUSTRATIONS (Cont'd)

FIGURE		PAGE
2.13	Typical Photograph for Mirror Mode Shape Data. For Data Reduction, a 15 x 24 in. Print is Used	53
2.14	Experimental Mirror Mode Shape for First Vibration Mode of Model 8 at $p_d = 2$ psig	54
2.15	Experimental Mirror Mode Shape for Second Vibration Mode of Model 8 at $p_d = 2$ psig	55
2.16	Experimental Mirror Mode Shape for Third Vibration Mode of Model 8 at $p_d = 2$ psig	56
2.17	Influence Coefficient Stations and Mass Data for Model 5	57
2.18	Comparison of Experimental Node Lines and Node Lines Calculated from Measured Influence Coefficients, for Model 5 at a Pressure of 2 psig	58
3.1	Views of Models Mounted in Wind Tunnels	97
3.2	Typical Strain-Gage Responses	98
3.3	High-Speed Movie Samples	99
3.4	Photographs of Typical Flutter Models after Destruction During Flutter	100
3.5	Experimental Flutter Index ($V_f/b_o \omega_2 \sqrt{\mu}$) vs M, and Comparison with Theory, for 65-deg Delta-Wing Models at a Model Pressure Differential of $p_d = 2$ psig and $\alpha = 0$ deg	101
3.6	Experimental Flutter Frequency Parameter (ω_f/ω_2) vs M, and Comparison with Theory, for 65-deg Delta-Wing Models at a Model Pressure Differential of $p_d = 2$ psig and $\alpha = 0$ deg	102

ILLUSTRATIONS (Cont'd)

FIGURE		PAGE
3.7	Experimental Flutter Parameter ($V_f/b_0\omega_2$) vs μM , and Comparison with Theory, for 65-deg Delta-Wing Models at a Model Pressure Differential of $p_d = 2$ psig and $\alpha = 0$ deg	103
3.8	Experimental Flutter Frequency Parameter (ω_f/ω_2) vs μM , and Comparison with Theory, for 65-deg Delta-Wing Models at a Model Pressure Differential of $p_d = 2$ psig and $\alpha = 0$ deg	104
3.9	Experimental Flutter Index ($V_f/b_0\omega_2\sqrt{\mu}$) vs M , and Comparison with Theory, for 65-deg Delta-Wing Models at Model Pressure Differentials of $p_d \geq 3$ psig and $\alpha = 0$ deg	105
3.10	Experimental Flutter Frequency Parameter (ω_f/ω_2) vs M , and Comparison with Theory, for 65-deg Delta-Wing Models at Model Pressure Differentials of $p_d \geq 3$ psig and $\alpha = 0$ deg	106
3.11	Experimental Flutter Parameter ($V_f/b_0\omega_2$) vs μM , and Comparison with Theory, for 65-deg Delta-Wing Models at Model Pressure Differentials of $p_d \geq 3$ psig and $\alpha = 0$ deg	107
3.12	Experimental Flutter Frequency Parameter (ω_f/ω_2) vs μM , and Comparison with Theory, for 65-deg Delta-Wing Models at Model Pressure Differentials of $p_d \geq 3$ psig and $\alpha = 0$ deg	108
3.13	Experimental Flutter Index ($V_f/b_0\omega_2\sqrt{\mu}$) and Flutter Frequency Parameter (ω_f/ω_2) vs Model Pressure Differential (p_d) at $\alpha = 0$ deg. (All Data for Model 7)	109

ILLUSTRATIONS (Cont'd)

FIGURE		PAGE
3.14	Experimental Flutter Index ($V_f/b_0\omega_2\sqrt{\mu}$) and Flutter Frequency Parameter (ω_f/ω_2) vs Angle of Attack (α). (All Data for Model 7)	110
3.15	Photographs Showing Steady-State Deflections of Model 8 at Several Angles of Attack for $M = 5$. Portions of Root and Trailing Edges are indicated by Dotted Lines	111
3.16	Experimental Flutter Index ($V_f/b_0\omega_2\sqrt{\mu}$) vs M for 75-deg Delta-Wing Models, at $\alpha = 0$ deg Low-Frequency Flutter	112
3.17	Experimental Flutter Index ($V_f/b_0\omega_2\sqrt{\mu}$) vs M for 65- and 75-deg Delta-Wing Models at $\alpha = 0$ deg. High-Frequency Flutter	113
3.18	Experimental Boundaries ($V_f/b_0\omega_2\sqrt{\mu}$) vs M , and Comparison with Theory for all Low-Frequency Flutter. All Theory Based on 65-deg Model Data at $p_d = 2$ psig	114
I.1	Coordinate Systems and Deflection Notations for Simplified Analysis	125
I.2	Coordinate System and Notation for the Delta Models	165
I.3	Equal Deflection Lines for First Mode Shapes of Sets A and B	166
I.4	Equal Deflection Lines for Second Mode Shape of Set A	167
I.5	Equal Deflection Lines for Second Mode Shape of Set B	168

ILLUSTRATIONS (Cont'd)

FIGURE		PAGE
I.6	Equal Deflection Lines for Third Mode Shape of Set B	169
I.7	Theoretical Flutter Parameter ($V_f/b_o\omega_2$) and Static Divergence Parameter ($V_D/b_o\omega_2$) vs μM for Stated Conditions	170
I.8	Theoretical Flutter Frequency Parameter (ω_f/ω_2) vs μM for Stated Conditions	171
I.9	Theoretical Flutter Parameter ($V_f/b_o\omega_2$) and Static Divergence Parameter ($V_D/b_o\omega_2$) vs μM for Stated Conditions	172
I.10	Theoretical Flutter Frequency Parameter (ω_f/ω_2) vs μM for Stated Conditions	173
I.11	Theoretical Flutter Parameter ($V_f/b_o\omega_2$) and Static Divergence Parameter ($V_D/b_o\omega_2$) vs μM for Stated Conditions	174
I.12	Theoretical Flutter Frequency Parameter (ω_f/ω_2) vs μM for Stated Conditions	175
I.13	Theoretical Flutter Parameter ($V_f/b_o\omega_2$) vs μM for Stated Conditions	176
I.14	Theoretical Flutter Frequency Parameter (ω_f/ω_2) vs μM for Stated Conditions	177
I.15	Theoretical Flutter Parameter ($V_f/b_o\omega_2$) and Flutter Frequency Parameter (ω_f/ω_2) vs μM for Stated Conditions	178
I.16	Theoretical Flutter Parameter ($V_f/b_o\omega_2$) and Flutter Frequency Parameter (ω_f/ω_2) vs μM for Stated Conditions	179

ILLUSTRATIONS (Cont'd)

FIGURE		PAGE
I.17	Theoretical Flutter Parameter ($V_f/b_o\omega_2$) and Flutter Frequency Parameter (ω_f/ω_2) vs μM for Stated Conditions	180
I.18	Theoretical Flutter Parameter ($V_f/b_o\omega_2$) and Flutter Frequency Parameter (ω_f/ω_2) vs μM for Stated Conditions	181
I.19	Theoretical Flutter Parameter ($V_f/b_o\omega_2$) and Flutter Frequency Parameter (ω_2/ω_2) vs μM for Stated Conditions	182
I.20	Theoretical Flutter Parameter ($V_f/b_o\omega_2$) and Flutter Frequency Parameter (ω_f/ω_2) vs μM for Stated Conditions	183
I.21	Theoretical Flutter Parameter ($V_f/b_o\omega_2$) and Flutter Frequency Parameter (ω_f/ω_2) vs μM for Stated Conditions	184
I.22	Theoretical Flutter Parameter ($V_f/b_o\omega_2$) and Flutter Frequency Parameter (ω_f/ω_2) vs μM for Stated Conditions	185
I.23	Theoretical Flutter Parameter ($V_f/b_o\omega_2$) and Flutter Frequency Parameter (ω_f/ω_2) vs μM for Stated Conditions	186
I.24	Theoretical Flutter Parameter ($V_f/b_o\omega_2$) and Flutter Frequency Parameter (ω_f/ω_2) vs μM for Stated Conditions	187
I.25	Variations of Center-of-Pressure Location and Force L with Bluntness and Initial Angle of Attack, for Various Two-Dimensional Sections	188

TABLES

TABLE		PAGE
2.1	Model Data for Inflatable Delta Wings	59
2.2	Comparison of Theoretical and Experimental Deflections of Model 1 under a Uniform, Static Load. Model Pressure is 2 psig	60
2.3	Model Vibration Data	61
2.4	Effect of Temperature on the Free Vibration Frequencies of Model 6 at $p_d = 2$ psig	72
2.5	Comparison of Experimental Frequencies and Analytical Frequencies Based on Pure-Shear-Type Deformations, for three Models at $p_d = 2$ psig	72
2.6	Effect of Pad Size on Influence Coefficient Measurements	72
2.7	Experimentally-Determined Force-Deflection Influence Coefficient Matrix for Model 5. (Corrected for Maxwell's Reciprocity Relation; Units in in./lb)	73
2.8	Normalized Mode Shapes for Model 5 from Calculations Based on Measured Influence Coefficients	74
2.9	Comparison of Experimental Frequencies and Frequencies Calculated from Measured Influence Coefficients, for Model 5 at a Pressure of 2 psig	74
2.10	Extensional Stiffnesses E_{wt} , E_{ft} , and E_{45t} Along Directions of Warp, Fill and 45 Degrees to Warp, Respectively	75

TABLES (Cont'd)

TABLE		PAGE
2.11	Influence of Temperature and Humidity on the Extensional Stiffness E_{ft} , at Cylinder Pressure of 0.688 psig	75
2.12	Shear Stiffnesses G_{wt} , G_{ft} and G_{45t} from Cylinders with Axis in Direction of Warp, Fill, and 45 degrees to Warp, Respectively	76
2.13	Poisson's Ratios μ_{fw} , μ_{wf} , μ_{45}	77
2.14	The Ratio $\mu_{wf}E_f/\mu_{fw}E_w$ from the Experimental Measurements	77
3.1	Experimental Flutter Data	115
I.1	Summary and Index of Flutter and Divergence Analyses	189

SYMBOLS

a	Speed of sound; also acceleration
a_{nj}, b_{nj}	Out-of-phase and in-phase aerodynamic coefficients defined by Eq. (1.26)
b_o	Root semichord
c	Chord at any spanwise station
c_o	Root chord
f	Frequency in cps
f_n	Frequency in cps associated with free vibration mode n
f_p	Fundamental frequency at any ambient pressure, in cps
f_v	Fundamental frequency in vacuum, in cps
g	Acceleration of gravity; also structural damping coefficient
g_n	Structural damping coefficient associated with free vibration mode n
h	Depth of wing, i.e., spacing of AIRMAT covers
h	Translational displacement; also altitude in Fig. 1.3
h_o	Altitude where entry is initiated; see Fig. 1.3
h_s, h_u	Steady and unsteady parts of h ; see Section C, Appendix I
i	The imaginary index, $i = \sqrt{-1}$
i, j	Indices

SYMBOLS (Cont'd)

$\hat{i}, \hat{j}, \hat{k}$	Unit vectors in the x, y, z directions, respectively
$\hat{i}_1, \hat{i}_2, \hat{i}_3$	Unit vectors in the x_1, x_2, x_3 directions, respectively
$\hat{i}'_1, \hat{i}'_2, \hat{i}'_3$	Unit vectors in the x'_1, x'_2, x'_3 directions, respectively
k	Reduced frequency based on root semichord, $k = \frac{\omega b_r}{V}$
k_{ij}	Generalized stiffness associated with modes i and j
m	Model total mass (half-span); also mass of sliding weights in the cylinder dynamic torsional tests (see Section 2)
\bar{m}	Average mass per unit area of model
\hat{n}	Unit vector normal to the body, directed in
p	Pressure at any point on body
p_c	Pressure differential in the cylinder models
p_d	Pressure differential between model internal pressure and ambient pressure
p_0	Stagnation point pressure
p_∞	Free-stream pressure
Δp_j	Difference in pressure between bottom and top surfaces of the wing oscillating in mode j
q	Dynamic pressure

SYMBOLS (Cont'd)

$q^{(j)}$	Eigenvector associated with the j-th eigenvalue
\vec{Q}_b	Velocity vector of a body point
q_n	Generalized coordinates, defined by Eq. (I.17)
s	Local dimensionless semispan, see Fig. I.2
t	"Thickness" of latex-coated material; also denotes time
u, v	Displacements in the x, y directions, respectively; see Section A, Appendix I
w	Lateral deflection (in z-direction) of model mid-plane; see Fig. I.1
\bar{w}	Time-dependent lateral deflection; see Eq. (I.17)
w_n	Trial modal functions; see discussion following Eq. (I.16)
x_a	Distance of rotation axis from the leading edge
\bar{x}, \bar{y}	Modified Cartesian coordinates made dimensionless with respect to root chord; see Eq. (I.16)
x, y, z	Cartesian coordinates, see Fig. I.1
$\{x_1, x_2, x_3\}$ $\{x'_1, x'_2, x'_3\}$	Coordinate systems defined in Section C, Appendix I
$A, B, C-1, C-2$	Denote mode shape sets, see Section B.2, Appendix I
C_{ij}	Flexibility influence coefficients associated with modes i and j

SYMBOLS (Cont'd)

 C_p

Pressure coefficient, defined as

$$C_p = \frac{p - p_\infty}{\frac{1}{2} \rho_\infty V^2}$$

 C_{p_s}

Stagnation point pressure coefficient

 D

Cylinder model diameter

 E_A, E_H Axial and hoop extensional moduli,
respectively E

Extensional modulus

 Et

Cover "extensional stiffness"

 G

Shear modulus

 Gt

Cover "shear stiffness"

 M

Mach number

 M_a Mass of air contained in the semichord
formed by rotating the delta model about
its root chord M_{ij} Generalized masses associated with modes i
and j M_n Generalized mass for the n -th orthogonal
mode, i.e., $M_n = M_{nn}$ Q_i
 $\overline{Q_{ij}}^{(n)}$ i -th generalized external forceGeneralized aerodynamic forces associated
modes i and j , according to slender-body
theory $Q_{ij}^{(n)}$ Modified generalized aerodynamic forces;
see Section B, Appendix I R Radius of circular leading and trailing
edges

SYMBOLS (Cont'd)

T	Temperature in degrees Fahrenheit, unless specified otherwise; also torque applied to cylinder models (see Section 2); also kinetic energy, Eq. (I.19)
U_s	Strain energy, Eq. (I.18)
V	Free-stream velocity
W	Weight added to cylinder model to equalize hoop and axial stress levels
Z_j	Elementary modal functions used in the transonic flutter analyses; see Section B, Appendix I
α, β	Shear angles defined in Fig. I.1
α	Angle of attack; angle of attack at root section in Section 3
α_0	Initial steady constant angle of attack
α_s, α_u	Steady and unsteady parts of α ; see Section C, Appendix I
γ	Adiabatic exponent (= 1.4 for air); also angle related to twist of cylinder models (see Section 2).
δ_i	Entry angle; see Fig. 1.3
ϵ_A, ϵ_H	Axial and hoop strains in the cylinder models, respectively
$\epsilon_{ij}, \sigma_{ij}$	Components of strain and stress, respectively; defined in Section A, Appendix I
λ	Eigenvalue (Eq.(I.21)) related to free vibration frequencies

SYMBOLS (Cont'd)

μ	Mass ratio parameter, defined as $\mu = \frac{3m}{2\pi \rho b^2 \sigma}$ Also Poisson's ratio, when latter is discussed generally, or for isotropic materials; accompanied by subscript when referred to specifically for nonisentropic materials
μ_{AH}	Poisson's ratio relating hoop strain to axial stress
μ_{HA}	Poisson's ratio relating axial strain to hoop stress
μ_{fw}	Poisson's ratio relating warp strain to fill stress
μ_{wf}	Poisson's ratio relating fill strain to warp stress
μ_{45}	Poisson's ratio relating strain along a direction at 45 degrees to the warp (or fill) to a stress along a perpendicular to this direction
ξ_n	n-th generalized coordinate
ρ	Free-stream density
ρ_∞	Free-stream density
σ	Tangent of the semiapex angle; also the cotangent of the leading-edge sweep; also semispan made dimensionless with respect to root chord, see Fig. 1.2
σ_A, σ_H	Axial and hoop stresses in the cylinder models, respectively
σ_s	Stress level in the model cover, see Section 2

SYMBOLS (Cont'd)

$\bar{\phi}_j^{(1)}$	Complex amplitude of the velocity potential associated with elementary modal function Z ; superscript (1) denotes slender-body solution. When with subscript \bar{x} , it denotes differentiation of $\bar{\phi}_j^{(1)}$ with respect to \bar{x}
ϕ_n	n-th orthogonal mode shape
ω	Frequency of oscillation in rad/sec
ω_n	Frequency in rad/sec associated with free vibration mode n
Λ	Leading edge sweep angle

Superscripts, Subscripts, etc.

$(A), (B), (C)$	Denote the particular set of mode shapes to be considered
(\cdot)	Dot indicates differentiation with respect to time
f	Refers to fill direction; also flutter condition
w	Refers to warp direction
x, y (or \bar{x}, \bar{y})	On α, β, w , they indicate differentiation with respect to x, y (or \bar{x}, \bar{y}) in Section A, Appendix I
D	Refers to static divergence
45	Refers to a direction at 45 degrees to the warp (or fill)

SECTION 1

INTRODUCTION

Among the many configurations proposed for re-entry vehicles, the concept of an inflatable structure (Refs. 1, 2, 3) offers some important advantages which bear directly on the problems encountered during re-entry. The configurations representative of the type likely to be used for recoverable inflatable vehicles are shown in Fig. 1.1. The basic features of these configurations are a hemispherical nose, a swept-back leading edge (usually a large diameter tube), and a sail, AIRMAT,* or several tubes connecting the right and left leading edges (see Fig. 1.2).

Two trajectories, which are typical for the types of re-entry vehicles shown in Fig. 1.1, are presented in Fig. 1.3, in terms of dynamic pressure vs Mach number. The additional parameters T (temperature), h (altitude), a (acceleration) and t (time from initiation of entry) are also given since they influence the final design of an actual vehicle. The trajectories were obtained from Ref. 1 and some additional calculations based on the 1959 USAF model atmosphere. The angle of attack, α , and the lift drag ratio, $L/D = 0.577$, are assumed constant during entry. The entry height is 400,000 feet, the initial flight path angle is -1 degree, and the leading edge radius is taken as one foot.

From the foregoing and other published studies of inflatable re-entry vehicles (Refs. 2, 4) one can draw the following general observations which are applicable to most situations:

*Trademark of Goodyear Aerospace Corporation

Manuscript released by the authors August 1964 for publication as an FDL Technical Documentary Report.

64-2202

- (1) With the light wing loadings required (W/S of the order of unity), the maximum dynamic pressures will occur at relatively high Mach numbers, say $2 < M < 10$, at altitudes in the neighborhood of 200-250,000 feet.
- (2) The variation in dynamic pressure, for the range of Mach number in Fig. 1.3, is less than 20 per cent.
- (3) While the descent will be at very shallow angles, the lifting surfaces will be oriented at relatively large angle of attack (between 20 and 60 degrees), because of the low dynamic pressures which will be encountered at these higher altitudes. The minimum C_L will be dependent on the maximum tolerable leading-edge temperature.
- (4) Maximum allowable heating conditions dictate blunt leading edges for such surfaces.
- (5) The lower wing loadings give lower values of the radiation equilibrium stagnation-point temperature because lower speeds are encountered at any given altitude.
- (6) The very compact packaging of the vehicle for launching into orbit and assembly in space removes the necessity of having to place a large lifting surface vehicle on top of a large rocket vehicle, and thereby puts the task of placing such a vehicle in orbit within the capabilities of present day boosters. A packaged volume to inflated volume ratio of 0.03 to 0.05 is possible for an AIRMAT wing, while for a complete re-entry vehicle, ratios of 0.15 are possible (Ref. 2).

The high degree of flexibility exhibited by these inflatable structures indicates that the prevention of instabilities such as flutter may be a significant problem. This report covers

a program of research on analytical studies and experimental verification of the vibration and flutter characteristics of inflatable structures, as a first step toward establishing design criteria which will insure that lifting surfaces for future inflatable vehicles will be free from dynamic instabilities.

The research effort was mainly confined to the AIRMAT-type structure, where the spacing of the surfaces is achieved by chords held in tension by internal pressure. With regard to the type of models that should be employed, the first question which naturally arises is the amount of effort which should be expended in attempting to achieve dynamic similarity between the wind tunnel model and a full-scale vehicle. A strict adherence to the requirements for dynamic similitude, as found from dimensionless analysis, is most often precluded by lack of suitable construction materials and the properties of the wind tunnels used in the test program. It was decided that the goals of the program could best be served by adopting the viewpoint that the models should provide a means for checking theoretical calculations based on model parameters, as opposed to the use of models to check or simulate a full-scale vehicle. At the least, the models should have the same planform and the same type of internal construction as the full-scale vehicle.

Section 2 contains the model information, which includes a description of the model construction and a complete summary of all the preliminary static and vibration tests carried out on the models prior to the wind tunnel tests. The relative importance of shear- and bending-type deformations are determined by comparing experimental results with some simplified theoretical calculations. The initial attempts at measuring the structural properties of the surface material are also fully described, along with a discussion of the problems encountered and a presentation of results obtained using some new testing techniques. A preliminary account of some of the material presented in

Section 2 can also be found in Ref. 5.

Section 3 contains a description of the wind-tunnel-test procedures and the results and discussion of all the wind-tunnel-flutter tests. During the program, a total of 65 flutter points was obtained from the 21 flutter models which were constructed.

The conclusions and recommendations drawn from the investigation comprise Section 4.

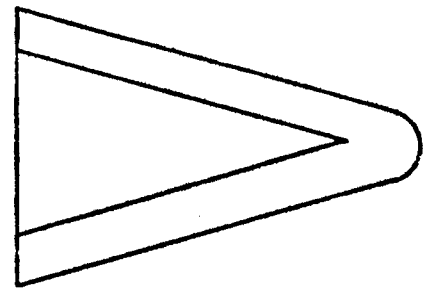
The analytical procedures and summaries of the theoretical calculations are presented in Appendix I. Also included, is a discussion on the effects of leading- and trailing-edge bluntness and large angles of attack on the unsteady aerodynamic forces.

Appendix II presents some theoretical work on membrane-type flutter of an inflatable panel, which is principally the effort of Professor M. T. Landahl of the Department of Aeronautics and Astronautics, MIT.

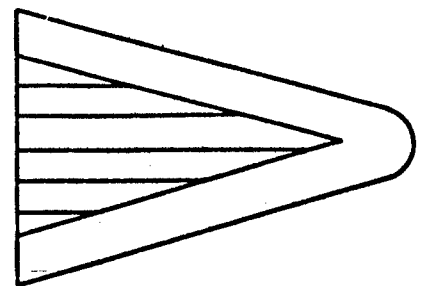
Appendix III contains the development of the equations governing the structural behavior of an inflated AIRMAT section. This is the work of Professor J. W. Mar of the Department of Aeronautics and Astronautics, MIT.

Appendices II and III are presented as separate entities, and each contains its own list of symbols and references.

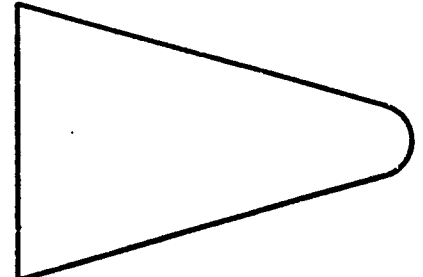
An extension of this work up to Mach numbers 8 and 10 is being sponsored by the Flight Dynamics Laboratory, Research and Technology Division, Wright-Patterson Air Force Base, Ohio, under U.S. Air Force Contract No. AF 33(615)-1155.



Cylinder - Sail - Hemisphere Construction

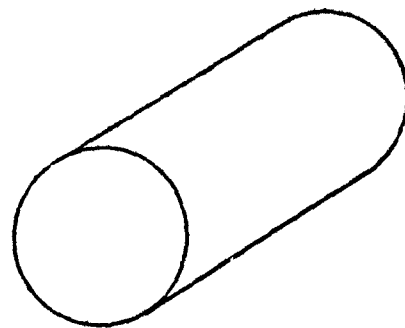


Tubular - Cylinder - Hemisphere Construction

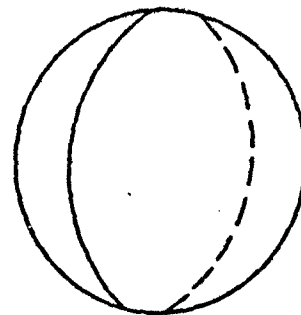


AIRMAT - Hemisphere Construction

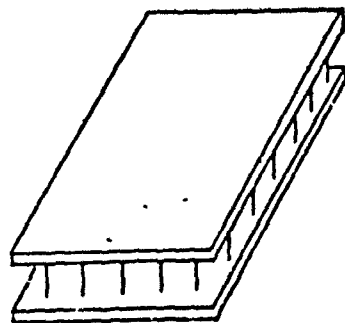
Figure 1.1 Sketches of Typical Blunted Delta Inflatable Vehicles, Showing Type of Construction.



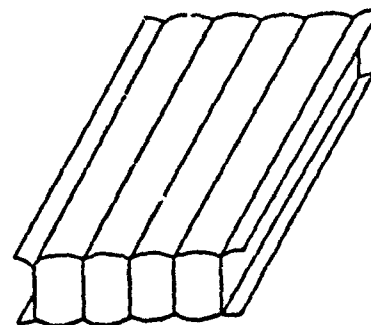
Cylinder



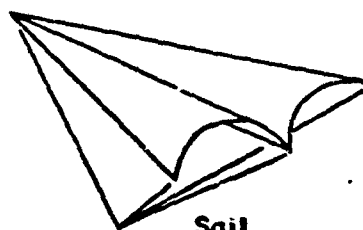
Spherical



AIRMAT



Tubular



Sail

Figure 1.2 Basic Structural Components of Inflatable Re-Entry Vehicles.

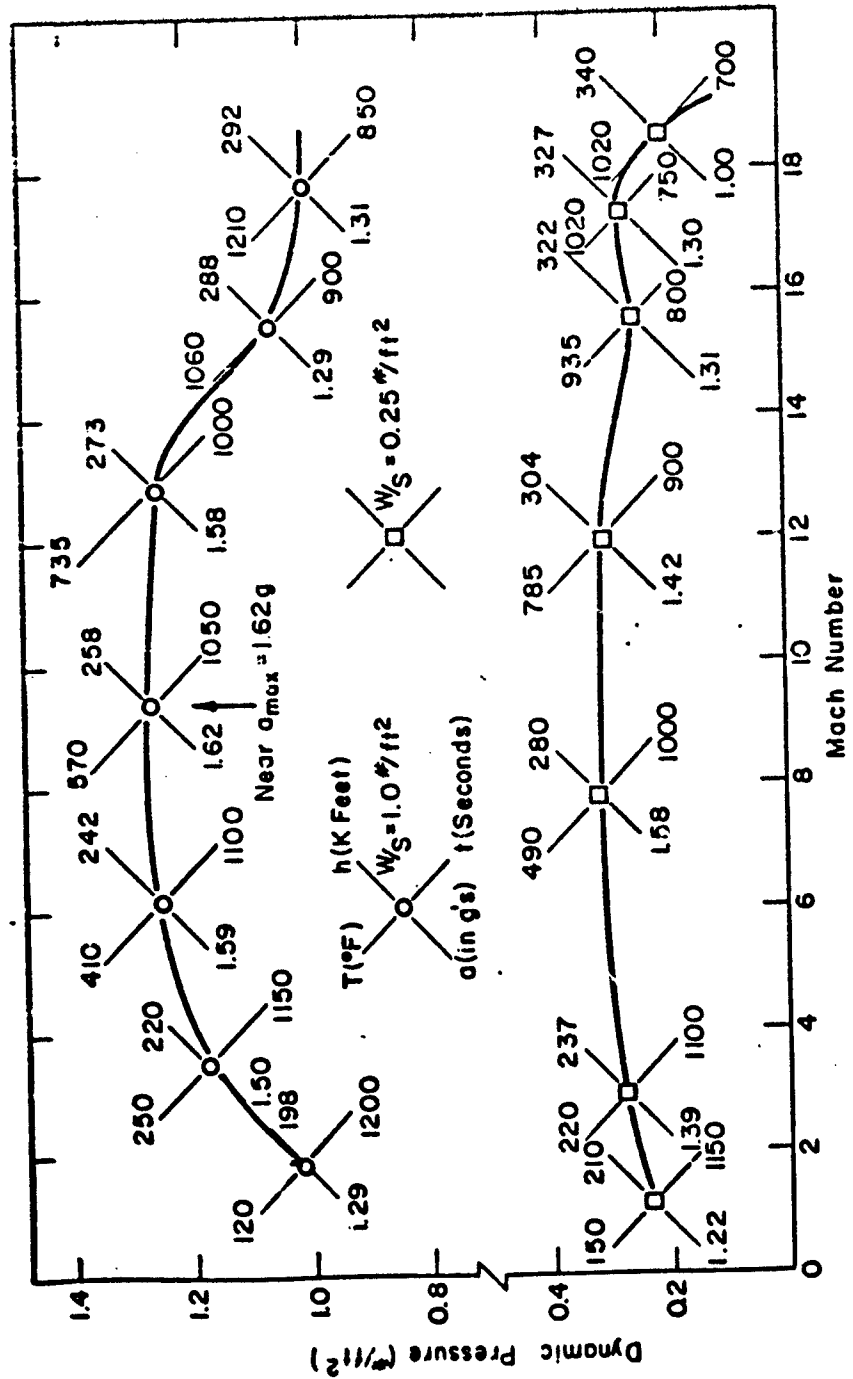


Figure 1.3 Typical Re-Entry Trajectory for an Inflatable Vehicle $\gamma_i = -1 \text{ deg}$ (Entry Angle), $L/D = 0.577$, $h_0 = 400 \text{ K ft.}$

SECTION 2

MODEL INFORMATION

A. MODEL CONSTRUCTION AND INSTRUMENTATION

The AIRMAT type of lifting surface construction, where the spacing of the surfaces is achieved by chords held in tension by internal pressure, was conceived and is under development by Goodyear Aerospace Corporation, Akron, Ohio. Special looms have been developed which weave the two surfaces and the drop chords in one integral operation. The elastomer, which makes the material surface impermeable to air, is applied after the weaving operation. Variable depth mats can also be formed on these looms.*

Because of the relatively small number of models required for the program, highly productive methods of model construction, with their correspondingly long setup times and scheduling difficulties, were not desirable. Even more importantly, previous experience indicates that eventually some recourse will have to be made to the use of models which will simulate the static and dynamic response characteristics of the full-size vehicle, to assist in the development of theoretical techniques and to evaluate the accuracy and reliability of these methods.** The full-size vehicles are expected to be constructed of a stainless steel or René 41 mesh sealed with an elastomer capable of withstanding the 1500 °F temperatures which will be experienced

* Development work on these looms was sponsored by the Manufacturing Technology Laboratory, Wright-Patterson Air Force Base, Dayton, Ohio under Contract No. AF 33(600)-43036.

** In this program no effort was made to fully simulate the static or dynamic characteristics of full-size vehicles. The planform shape and the relative outside dimensions were chosen as representative of the type currently being proposed for use as re-entry vehicles.

during re-entry. To achieve dynamic similarity, the materials used in the model will necessarily have to be different from those used for the full-scale vehicle. In such cases, it is considered likely that simple rubber or impermeable cloth material will suffice. On the basis of these considerations, it was decided to explore alternate methods of model construction which would require very little equipment and permit a large degree of flexibility insofar as model properties were concerned. The following method of model construction was finally adopted.

A styrofoam mandril, shaped to the dimensions of the desired model, is attached to a wooden root fitting. A nylon (or dacron) cloth, which has been pre-impregnated with latex rubber (General Latex Code No. IV-10) and cut to the correct size, is wrapped around the styrofoam core and wooden root fitting. All seams are sealed with neoprene cement. Next, the drop chords are put in by sewing back and forth through the top and bottom surfaces with a needle and thread. To insure that the drop chords are reasonably perpendicular to the model surface, it has been found necessary to pre-drill the styrofoam core using an array of heated needles, since the sewing needle has a tendency to become misaligned when piercing the styrofoam. For the models used in this program, a drop chord spacing of one-quarter inch has been found to be satisfactory. Also, it is not necessary to sew the leading- and trailing-edge regions since they are rounded and will automatically assume the desired cylindrical shape upon inflation. After all the drop chords are sewn, a coat of latex is applied to seal the holes made by the drop chords. The final step is to remove the styrofoam core by dissolving it with a common solvent such as toluene.

It is evident that the foregoing is a relatively quick and inexpensive way to produce inflatable models. One of its greatest advantages, which has not yet been utilized to any great extent, is that the size or shape of the model depends on the styrofoam

core and can therefore be very easily changed. In addition, the model characteristics can be varied by (1) selecting a different cloth material for the model surface, (2) selecting a different latex, (3) varying the number of layers of cloth imbedded in the latex, (4) varying the number of coats of latex, and (5) varying the orientation of the cloth threads.

Twenty-one delta-wing models were constructed for use in the program. A summary of the model configurations and pertinent model properties is given in Table 2.1.

For the first two models, the nylon cloth was simply wrapped around the leading edge of the styrofoam mandril; thus, the warp orientation (with respect to the model root) was zero degrees for the top surface and 50 degrees for the bottom surface. In all the other models, the surface material was cut and a seam made along the leading edge, so that the warp orientation was the same for both top and bottom surfaces.

In addition to these models, other models, including square, rectangular, and even a model with a large initial curvature, have been constructed by students at MIT while working on thesis or laboratory projects. Photographs of some of the models are shown in Fig. 2.1, which also includes a picture of a model constructed and donated by the Goodyear Aerospace Corporation, Akron, Ohio.

A system for maintaining any desired pressure differential p_d , between model internal pressure and any reference pressure (atmospheric pressure during static and vibration testing, tunnel static pressure during wind-tunnel tests) is connected to the model through the wooden root fitting (Fig. 2.2).

The basic model instrumentation consisted of four strain gages (Baldwin PA-3 post-yield type) for use in static and dynamic measurements. The gages were fastened to the outer model surface (Fig. 2.2) using neoprene cement and then covered by a

protective coating of latex. Each of the strain gages was used as a single active arm in a four-arm strain-gage system, giving four independent strain-gage circuits.* Because of the large deflections encountered in these models, care was taken to allow enough slack in the strain-gage leads (such as zigzagging the leads as shown in Fig. 2.2) to prevent lead-wire breakage during model tests.

B. STATIC TESTS

The response of Model 1 to a static uniform load was determined by placing sheets of lead on the model surface and measuring the deflection at three points along the leading and trailing edges. The lead sheet was cut into small pieces (2 x 2 in.) which were joined by tape, so that the lead's contribution to the overall stiffness of the complete system (model and weight) was negligible. The results of the tests are given in Fig. 2.3. In Table 2.2, the experimental values are compared with theoretical predictions based on the assumption of pure shear deformations (see Appendix I, Section A), for the case when the model pressure is 2 psig.

From the results, several important observations can be made.

- (1) The model deflection does not vary inversely with model pressure, as it would if the deformations were due entirely to shear.
- (2) The range of linearity of model deflection versus load depends on the model pressure.

*The original models were instrumented with only the two aft strain gages which were wired to give two independent strain-gage circuits. It was later found necessary to add two more strain gages to overcome the problem of frequent tunnel shut-downs for replacement of gages ruptured during tunnel starts and model flutter.

- (3) The theoretical deflections, wherein bending-type deformations are not accounted for, are considerably lower than the experimental deflections.

From the foregoing, it is evident that the deflection is composed of bending and shear type deformations, and that both are equally important. This fact is also verified by the vibration results which are presented in the following section.

C. VIBRATION TESTS

1. Test Procedures

The excitation system used for the vibration tests is a low frequency speaker. The speaker cone is covered with a tapered aluminum cover, about 0.020-in. thick, which has a 1.25-in. orifice to concentrate the air column at the model surface. The vibration frequencies and damping coefficients were obtained from vibration decay records. Node lines* were determined by sprinkling No. 40 grit carborundum dust on the model surface, while the model was vibrating in a natural mode. This system was found to be suitable for light vibrating models. The only problems encountered were in connection with: (a) overexcitation, especially of the higher modes, and (b) difficulty in properly locating the fourth mode.

For large excitation forces, local deflections were found to be superimposed on the natural mode responses. This effect was minimized by positioning the speaker, for each mode, such that the largest amplitude was obtained for a fixed speaker power input. Changing the speaker position had little effect on the node lines of most modes. However, in a few isolated instances when weak and not clearly-defined modes were encountered, the node line positions were strongly dependent on the speaker

* More specifically, l-g lines. In the node line presentations of Figs. 2.5 through 2.9, the shaded areas are the regions where the accelerations are less than 1g.

position. In these cases, the speaker was positioned so that a sizable amplitude and clearly-defined node lines were obtained at the same time.

Another difficulty, in varying degree, was experienced when exciting the fourth mode. The speaker position was critical for two reasons: (a) it influenced the model frequency for maximum peak, and (b) if somewhat removed from its optimum, this mode could be easily overlooked in the frequency tests. (The latter actually occurred in some of the earlier tests.) Despite the care exercised in testing of some models, it was not possible to excite the fourth mode to a satisfactory amplitude level; and the vibration traces showed a beat frequency which was approximately equal to that of the first mode. The damping coefficient was difficult to measure in any of these cases, as the lower mode decay overshadowed that of the higher mode following speaker shut-off.

2. Test Results and Discussion

Table 2.3 presents in chronological order, the measured frequencies and damping coefficients of all 21 models. The list includes the following free-air vibration tests.

- (a) Those conducted a few days before the wind-tunnel test periods (at MIT).
- (b) Those conducted just prior to the flutter tests (at wind-tunnel location).
- (c) All repeat tests made between flutter runs.

Node lines, which are typically representative of most of the models tested, are presented in Figs. 2.5 and 2.6, for 65- and 75-degree-sweep models, respectively. These figures apply for the range of internal pressures considered, since in the majority of cases the node line locations were not altered appreciably with changes in p_d . Separate node line patterns are also presented in

Figs. 2.7 to 2.9 for those models which behaved otherwise. These cases are also noted in Table 2.3. Whenever accurate mode shapes were needed for analysis of a given model, the actual node-line data obtained during the pertinent vibration tests were used (see Appendix I, Section B).

As previously mentioned, difficulty was experienced in exciting the fourth mode. The fourth mode was not detected at all in Models 1 and 2. This mode was first observed in an early test made on Model 3, which has the warp direction parallel to the root. At that time, it was felt to be the third mode strongly distorted by speaker position. Because the mode could not be found in Model 4 at the low pressures (equal or less than 4 psi, pressures used in the initial tests), it was no longer looked for. Later, when the last of the dacron models were introduced and tested, the fourth mode, which was vague or nonexistent in the early nylon models, was rediscovered and found to be much stronger. It was traced and recorded for all succeeding tests. In the data presented, the mode numbers were assigned on the basis of the observed node lines; the fact that no data are given for Mode 4 should be interpreted, in most instances, to mean that the fourth mode was present and simply overlooked during the vibration tests. For some special cases, as noted in the table, repeated attempts to excite this fourth mode were unsuccessful, and thus it must be assumed that no such mode exists.

The damping coefficients g_1, \dots, g_5 are missing from certain sections of Table 2.3, because either the procedure used was later found to be unsatisfactory or the trace amplitudes were so small that the signal-to-noise ratio of the recorded strain-gage output was too low to give an accurate reading. In the early vibration tests on Models 1 through 10, the decay records were obtained following cutoff of speaker power at the oscillator. Thus, the slow decay of the oscillator was incorporated into the model decay, which resulted in an apparent reduction in g 's. In all the

remaining tests, the power was cut off at the speaker. The speaker cone had sufficiently high damping characteristic and did not influence the model decay.

The mode lines depicted in Figs. 2.5 and 2.6 for the first four typical mode shapes of the inflatable model resemble those of a cantilevered delta wing with approximately the same sweep and made of a uniform thickness aluminum plate (Ref. 6). However, the frequency ratios between various modes are quite different for the two types of models. There is also some similarity between the fifth mode of the inflatable model and the sixth mode of the aluminum wing.

For the single-layer nylon models, the effect of changing the surface material warp direction from zero and 50 degrees relative to the root chord on top and bottom surfaces (as in Models 1 and 2) to zero degrees (as in all models of this group) shows up mainly as differences between the fifth mode shapes (see Figs. 2.5 and 2.6). The first three modes and frequencies were essentially the same for both orientations, with the minor variations present attributed to the slight differences in the masses (due to different thicknesses of rubber coatings). On the other hand, the warp orientation had a marked effect on the mode frequencies of the double-layer dacron model. With the warp orientations at zero and 45 degrees for the two plies (as in Models 9 and 13), the frequencies were substantially higher than those with both warp directions at zero degrees (as in Models 13-1 and 19). Model 20, which was designed to duplicate Model 13, did not exhibit this type of behavior. In fact the vibration frequencies of Model 20 are very close to those of Models 13-1 and 19. This discrepancy cannot be explained on the basis of mass differences alone; Model 20 is about 21 per cent heavier than Model 13, but the frequency variations are of the order of 30 per cent.

For the double-layer dacron models, the mode shapes are similar to those of the typical single-layer models. However, one should note the closeness of the second and third frequencies, especially at low internal pressures. Specifically, Model 9 at $p_d = 1$ psig has $f_2 = 44.0$ and $f_3 = 45.1$ cps; Models 13, 13-1, 19, and even 10 (with 75-degree sweep) exhibited similar behavior, but to a lesser degree. The closeness of modes is not limited to the second and third. For Models 19 and 20, the frequency ratios between modes four and five are closer to unity than that between any other two observed frequencies. This trend towards the higher frequencies is noted also for the 75-degree sweep, single-layer models; and in particular between the third and fourth modes of Models 15, 16, and 17, and the fourth and fifth of Model 18. For the latter cases, this persists even for the higher pressures. Such a proximity of two modes presents potential flutter problems, a point that will be further discussed in connection with the flutter results.

Variations of frequency, between different tests of the same model inflated to equal internal pressures, are sometimes greater than what could be attributed to experimental error alone. Some reasons can be given to explain such variations. The most important are the changes in material properties with temperature and humidity, and to a lesser degree with age. This point is further discussed in the section on material properties (see Section 2, Subsection F). In order to obtain an estimate of the temperature effect on the free-vibration frequencies of the nylon models, Model 6 was vibrated in a temperature environment which could be varied from room temperature (70°F) to about 150°F . The results of the test, for the range of temperatures $70^\circ\text{F} \leq T \leq 130^\circ\text{F}$, are presented in Table 2.4 for modes 1, 2, 3, and 5 and a model internal pressure of 2 psig. It may be seen that around room temperatures, the first frequency decreases by about 4 to 5 per cent for every 20-degree rise in temperature. The same

trend may be noted for the higher modes, but to a lesser degree. A second reason for variations in frequencies between repeated tests is the possibility of undetectable damage to the model. A particular case in point is Model 1, where the frequencies of the last set are lower than in the initial set. And yet another reason may be found in possible amplitude effects. No attempt was made to vibrate any model with the same amplitude for each test. The material stiffnesses are somewhat nonlinear with respect to loading. Whether this alters noticeably the frequencies is not known at the present.

In conventional flutter work, the configurations are relatively heavy, and the apparent mass effects are so small that they are usually ignored. Because of the lightness of the present models, however, it is anticipated that there will be a noticeable apparent mass effect on the vibration frequencies measured in air when compared with those measured in vacuum.* The extent of this effect on the fundamental mode of the present models may be estimated simply as follows: Let M_a denote the mass of air contained in the semicone formed by rotating the delta model about its root chord; and let it be distributed uniformly as added mass to the total mass m of the model. If f_v and f_p are the fundamental frequencies in vacuum and at any ambient pressure, respectively, the rough approximation

$$\frac{f_p}{f_v} = \sqrt{\frac{m}{m + M_a}} \approx 1 - \frac{1}{2} \frac{M_a}{m}$$

holds under the stated assumption, recognizing that M_a/m is still a small quantity. Applied to the lightest model (No. 2), for instance, this results in a reduction of 13 per cent in frequency, when f_p is compared to f_v . To confirm this experimentally,

*The frequencies and mode shapes in vacuum are the appropriate ones to use in flutter work.

the model was vibrated in a vacuum chamber at several values of reduced ambient pressures and at two model pressures (2 and 4 psig). The experimental values are given in Fig. 2.10, where a straight line is passed through the points, since f_p/f_v is expected to have linear variation with M_a (or equivalently with ambient pressure) according to the above equation. For Model 2, the predicted reduction in the fundamental frequency due to apparent mass effects is somewhat higher than the corresponding value of 7.1 per cent from the observations. For the higher frequencies, one may anticipate smaller influences; this point is confirmed by the experimental results. The fact that experiment shows about half the predicted effect may be easily explained. The assumption in the analysis would be appropriate if all the points of the wing were vibrating at the same amplitude. For the first cantilever frequency, with parabolic spanwise variation in mode shape, a more realistic distribution of apparent air mass would have included some weighting factors based on the mode shape.

Some of the experimental frequencies are compared in Table 2.5 with those from the simplified calculations based on the assumption that the deformations are only of the pure shear type (see Appendix I, Section A). The comparison indicates that this sort of simplification is not valid. For Models 1 and 8, the experimental frequencies are substantially lower than those predicted, even with due allowance for apparent mass effects, indicating appreciable bending deformations. The comparison becomes worse when one considers that the additional shear stiffnesses from the leading and trailing edges were unaccounted for in the analysis. For Model 9, the results are reversed in that the experimental values are somewhat higher than the predicted ones. This is mainly due to two causes. First, bending effects should be much lower in Model 9 with its double layer of dacron material. Second, Model 9 actually has four layers of cloth material along

the leading and trailing edges, due to overlap at the seams, and the transverse shear rigidity of these edges adds a large amount of stiffness to the model.

The effect of model pressure differential on the vibration frequencies can be determined from Table 2.3. The frequencies do not vary as the square root of the model pressure differential, as would be expected if the model stiffness was totally derived from the internal pressure.

D. VIBRATION MODE SHAPES USING THE MIRROR TECHNIQUE

1. Test Procedures

An accurate knowledge of the vibration mode shapes of inflatable models would be extremely useful for checking the results of theoretical vibration calculations and also for calculating the generalized mass and aerodynamic forces needed in the flutter analyses. In this manner, the mode-shape data can be used in the final steps of one problem area (vibration analysis) and the initial steps of another problem area (flutter analysis), making it possible to proceed on both problems independently of one another.

As an initial effort toward providing this mode-shape data, an attempt was made to measure vibration mode shapes using an optical technique which has been successfully applied to mode-shape measurements on rectangular- and delta-wing models (Refs. 7, 8, 9). For the tests, optically flat mirrors ($3/16 \times 3/16 \times 0.020$ inches) were glued to one side of the wing at each of 37 stations, using bee's wax as an adhesive (Fig. 2.11). As shown in Fig. 2.12, the wing was mounted vertically, with the root parallel to the floor, and with the mirrors facing a 4×8 -foot board located about 10 feet away and covered with grid lines spaced at 0.40-inch intervals. Light, from a point source placed under the 4×8 -foot board, was passed through 37 lenses ($1/4$ -in. \times 1-in. diameter) mounted in a rigid board placed just in front

of the wing. The light rays were made parallel by the lenses and then reflected from the mirrors back through the lenses, forming an image of the point source (called a dot from here on) on the 4 x 8-foot board, for each mirror on the wing.

When the wing was vibrated in one of its natural modes, the dots traced out lines on the 4 x 8-foot board which gave a direct measure of the relative magnitude and direction of the slopes of the wing, during each cycle of vibration, at each mirror station. The slope in the horizontal (x or streamwise) and vertical (y or spanwise) directions was then determined by measuring the appropriate components of the lines traced out by the moving dots. Integration of these slopes along any given direction yielded the modal deflection amplitude at the various stations.

To facilitate data reduction and insure that all the data were recorded at the same vibration amplitude, a photograph was taken of all the lines on the board while the model was vibrating in a natural mode. No particular effort was made to initially place the dots at a particular spot on the board. The dots were simply identified prior to taking the photograph and an identification number was written beside each dot on the board. This procedure required a double exposure; the first exposure was made with room lights on to record the grid lines and identifying numbers, while the second exposure was made in complete darkness to record the dot traces. Figure 2.13 is typical of the photographs obtained; for data-reduction purposes, the photographs were enlarged to 15 x 24 inches.

2. Results and Discussion

Mode-shape data was taken for the first six modes of Models 7 and 8 at model pressure differentials of 1, 2, 3, and 4 psig. Only the data for the first three modes of Model 8 at a

model pressure of 2 psig have been reduced to provide data for the two- and three-degrees-of-freedom flutter calculations discussed in Appendix I. The mode shapes are drawn in Figs. 2.14 through 2.16.

As previously mentioned, the data was reduced by measuring the streamwise and spanwise components of the trace for each mirror. The data was plotted in both directions and along diagonals as well, and the curves were used to find values of the slope at the root and at intermediate stations where there were no mirrors. It should be noted that the algebraic signs of the slope cannot be obtained from the photographs, but must be determined by recourse to node lines obtained from previous vibration tests using the techniques discussed in Section 2C; this presents a difficult problem for the higher modes. The vibration amplitude was then found by numerical integration of the curves obtained in the previous step. To find the vibration amplitude at any point, there are two main paths along which one may proceed. Taking point 22 in Fig. 2.11, for example, it is possible to find its amplitude by (1) integrating along the spanwise direction starting from point 20R, or (2) integrating along another spanwise station, say the rearmost station, from point 1R to point 3 and from there integrating in a streamwise direction to point 22. In practice it has been found necessary to carry out such a dual process for each point, compare the results, and then reiterate on the original data to make the overall agreement better. From the type of agreement obtained for the inflatable models by this method, it is recognized that the results shown in Figs. 2.14 through 2.16 are not nearly as accurate as previous results obtained by applying essentially the same techniques to solid wing models (Refs. 7, 8). The main source of error lies in determining the spanwise slope at the model root. This slope is zero for solid cantilever models, but such is not the case for inflatable cantilever models, as indicated by Figs. 2.14 through

2.16. In fact, the results showed that there are very marked fluctuations in the spanwise slope near the root, and that the mirrors should have been placed much closer to the root than the one-inch spanwise spacing shown in Fig. 2.11.

Another problem encountered during the tests was that the mirrors were found to bend as the model pressure was increased. This was caused by local stretching of the model surface between drop chords and could be alleviated by using slightly stronger (and heavier) mirrors. The bending of a mirror manifested itself by turning the dot on the board into a line. In an extreme case, the dot, which is normally about $3/32$ inches in diameter, was expanded into a $3/16 \times 3/4$ -inch line. When this occurred, it was necessary to remount the mirrors. The effect was found to be minimized by installing the mirrors at the higher model pressures, the bending of the mirrors being less noticeable with a decrease in model pressure.

With regard to the effect of the mirrors on the vibration results, the experimental frequencies and node lines were determined at a model pressure of 2 psig, both with and without mirrors mounted on the model, using the vibration techniques described previously. There was no measurable difference between the results for both cases.

As a check on the orthogorality of the measured modes, the first three mode shapes were used to compute the generalized masses (relative values):

$$\begin{array}{ll} M_{11} = 1197 & M_{12} = 34.4 \\ M_{22} = 582.4 & M_{13} = 39.0 \\ M_{33} = 141.3 & M_{23} = 18.3 \end{array}$$

Since the cross terms are not zero, the modes are not normal to each other and are therefore not the true vibration modes. An estimate of the error can be determined by comparing M_{1j} with the

square root of $M_{ii} \times M_{jj}$. In the worst case (M_{13} compared with $\sqrt{M_{11}M_{33}}$), this amounts to a little less than ten per cent. It should be noted that the generalized masses presented above have been corrected for the effect of a nonuniform mass distribution caused by material lap-over at the leading- and trailing-edge seams. In some cases this correction, which was only approximate in the sense that the exact amount of lap-over was not known, was of the same order of magnitude as the cross terms and could account for an appreciable part of the error.

E. INFLUENCE COEFFICIENTS

1. General

Although the techniques for measuring influence coefficients and calculating the natural vibration modes and frequencies are well known (Ref. 10), several interesting observations pertinent to inflatable-type models are noteworthy.

In the measurement of influence coefficients on solid models, it is customary to use a "point force" in order to accurately locate the point of application. This point load essentially acts as a distributed force, with the centroid of force acting through the point of application. In measurements on actual aircraft it is sometimes necessary to use re-enforcing pads at the loading points to prevent local buckling. For inflatable models, locally applied load results in a large local deformation which is not at all representative of the type of loads and deformations that will normally be experienced by the model. It was therefore decided to apply the loads to the model with lead pads placed on the top surface of the model. The pads had small holes in the centers to enable relatively accurate placement over the desired loading point, and additional weights could be added on top of the pads as required. The effects of the loading-pad diameter were investigated using three lead pads with diameters of 1, 2, and 4 inches. Three representative in-

fluence coefficients were measured using the different pads and the results are given in Table 2.6. It is evident that the local deflection (C_{55}) increases as the load approaches a point application, while pad diameters between 2 inches and 4 inches give essentially the same results. Therefore, all subsequent tests were carried out using the 2-inch pads.

In influence-coefficient measurements it is important that the transducers used in measuring deflections do not introduce any extraneous forces and restraints into the system. Because of the large deformations experienced with inflatable models, under even low loadings, it was possible to use glass vernier scales hung from the bottom surface of the model. The movement of the scales was observed through a surveyor's transit. With this system, which satisfies the criterion of not adding extraneous forces and restraints to the system, it was possible to estimate deflections to within ± 0.001 inch.

In order to keep the deflection resolution error to within 2 per cent, the applied loads were chosen to give a deflection of over 0.100 inch at the measuring station.* Where this was not possible, a large number of repeated measurements were made and an average deflection was determined.

Another problem encountered was that of hysteresis, which was minimized by repeating the load-no-load cycle until a number of repeatable deflection measurements were obtained. In general, this required 5 to 6 cycles.

In the iteration procedures used to determine normal modes and frequencies analytically, it is customary to impose a convergence criterion based on successive eigenvalues. In the present example, a more restrictive criterion had to be adopted in order

* Each measurement involves two readings, load on and load off, each with a possible error of 0.001 inch.

to obtain a satisfactory third mode shape. The convergence criterion used for the first and second mode shapes required that no component of the eigenvector computed during successive iterations differed by more than 1×10^{-7} ; this was with reference to a normalized mode shape with maximum component equal to one. For the third mode, the convergence criterion required that the difference in any eigenvector component be less than 1×10^{-4} ; again with maximum component equal to one. The use of the convergence criterion on the eigenvectors, rather than on the eigenvalues, resulted in marked changes in some of the components of the third mode shape, with differences as high as 30 per cent in some cases; the final eigenvalues were the same, irrespective of the convergence criterion used.

2. Results and Discussion

The first three mode shapes of Model 5 were calculated for a model pressure differential of 2 psig, using measured flexibility influence coefficients; influence coefficient stations and mass data are given in Fig. 2.17. The influence coefficient matrix, which has been made symmetrical by averaging reciprocal elements C_{ij} and C_{ji} , to correspond with Maxwell's reciprocity relation, is given in Table 2.7. The calculated mode shapes for the first three modes are given in Table 2.8. The calculated and experimental frequencies and node lines are compared in Table 2.9 and Fig. 2.18, respectively. In the figure, the experimental node lines at the root are indicated as extending over an area, since it is not possible to locate them exactly within this region by the 1-g acceleration technique.

The comparison between theory and experiment is reasonable, and it appears that carefully measured influence coefficients can be used to determine the natural modes and frequencies of inflatable wings.

F. MATERIAL PROPERTIES

1. General

Comparison between experimental model vibration results and theoretical calculations, based on an assumption of pure shear-type deformations only, suggests that the bending deformations may be of the same order of magnitude as the shear deformations. The bending characteristics are dependent upon the properties of the model surface material. Accordingly, a limited amount of testing was performed to determine the structural properties of the nylon cloth used in the construction of the models.

Three test procedures were used to measure the structural properties: (1) uniaxial, (2) biaxial on cruciform-shaped samples, and (3) biaxial on cylinders. The uniaxial and biaxial cruciform tests suffered from size limitations and severe creep effects. Their results are inconclusive and thus are not reported here. The biaxial tests on the cylinder are described below in detail.

2. Description of Models

Two sets of rubberized nylon* cylinders were constructed and tested. The initial set, used early in the investigation, consisted of two 4-inch diameter, 17-inch length cylinders. The cloth warp was oriented in the axial direction for one of the cylinders, and in the circumferential direction for the other. The other set consisted of three 4-inch diameter, 20-inch length cylinders. These cylinders differed from one another, in that the warp directions were axial, circumferential and at 45 degrees to the cylinder axis, respectively. Each cylinder was sealed at both ends with 4-inch diameter wooden disks, and was inflated to a pressure, p_c , which made the hoop (circumferential) stress

*This was the same material as was used for Models 1 through 8 inclusive, having 98 x 98 thread counts per inch. All cylinders were coated with two layers of latex.

equal to the stress in the cover of the wing model under a pressure differential, p_d . Testing at the same stress levels in the cylinders and in the models is required since material properties are known to be dependent on the stress conditions. The cylinders were inflated to various pressures, with the objective of covering the contemplated p_d -range of the models.

To find the required pressure in a cylinder as a function of the model pressure, consider the typical inflated delta model (Fig. 2.1). Except for parts near the edges, the stress level, σ_s , in the covers is essentially equal in all directions, and is given approximately by

$$\sigma_s = \frac{p_d h}{2t}$$

where h , t are the model depth and the cover thickness, respectively. On the other hand, the hoop stress in the cylinder, σ_H , is given by

$$\sigma_H = \frac{p_c D}{2t}$$

where D is the diameter of the cylinder. The thickness, t , is the same for cylinder and model, as the same coated material was used for both. The requirement that the model and the cylinder have the same stress conditions yields

$$p_c = \frac{h}{D} p_d$$

Since the axial stress in the cylinder is equal to one half of the hoop stress, an additional axial load must be added to increase the axial stress level to that of the hoop stress. This additional load turns out to be

$$(\text{Load}) = \frac{\pi D^2}{4} p_c$$

The tests were run with the longitudinal axis of the cylinder in a vertical direction, so that a weight, W , could be applied by simply hanging it from the bottom face of the cylinder. In this position, the weight of the cylinder end plates contributes to the load. Thus, the added weight, W , was taken to be the required load minus one half the total weight of the cylinder unit.*

The tests on the cylinders may be split into two phases: the static and the dynamic series. The dynamic tests were needed in view of the sizable creep observed during the static tests. In each case, the material stiffnesses, E_t and G_t , were measured for each cylinder and for various levels of internal pressure. Static tests were also performed to measure the Poisson's ratios, μ . No attempt was made to measure μ dynamically, for this presents a more difficult and, as yet, unresolved problem.

3. Static Tests

In the static tests, each cylinder was deformed in a particular way with application of a known stress, and the deformation was measured to find the corresponding strain. For the determination of the effective moduli E_f , E_w , E_{45} , extensional loads were applied. Here the subscripts f , w , and 45 denote the fill, the warp and the 45 degrees to the warp directions, respectively. The last of these is referred to as the 45-degree direction hereafter. For the shear moduli G_f , G_w , and G_{45} , torques were imposed at the base of the cylinders. G_f and G_w denote the values obtained from the cylinders with axes parallel to the fill and the warp, respectively. Since the warp and fill are at 90 degrees, the values of G_f and G_w should be the same, theoretically. G_{45} is that value of G associated with shear imposed on a cylinder with its axis at 45 degrees to the warp.

*The major contribution to the cylinder mass comes from the cylinder end plates.

The test for finding E_t consisted of setting up the equilibrium conditions in the cylinder corresponding to some value of model pressure and of recording the distance, l , between two reference points on the cylinder, one point near each end. The applied load was then varied through a range which bracketed the original load by removing or adding weights. The elongated distance between the reference points, $l + \Delta l$, was recorded after each loading. The cylinder was allowed ample time between loadings to return to its preloaded position. All readings were taken as quickly as possible to minimize creep effects. In terms of the strain, $\Delta l/l$, the extensional stiffness is given by

$$E_t = \frac{\Delta P}{\pi D (\Delta l/l)}$$

where ΔP is the added or subtracted weight.

To measure G_t , equilibrium conditions (median state) were again established as before. The cylinder was subjected to a torque at the bottom disk, and the resultant rotation was measured with a double-ended pointer attached to the bottom disk. Angular deflections were read from a protractor mounted on a shelf below the rotating cylinder. As was done with the extensional tests, readings were taken as quickly as possible after load applications, and after each reading the torque was removed to allow the cylinder to return to its zero position.

The contributions to the effective (or total) shear stiffness, G_t ,* are primarily from two sources: (1) from the coated nylon, and (2) from the internal pressure. It can be shown that the relation between the effective shear stiffness, and the measured deflection angle, θ , is approximately

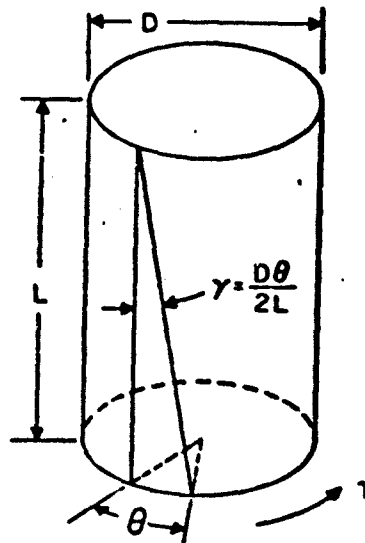
*The parameter (G_t), corresponding to A_{33} of Ref. 11, required for vibration calculations which include bending deformations.

$$Gt = \frac{4\pi L}{\pi D^3 \theta}$$

where T is the applied torque and L is the length of the cylinder (see sketch below). Under ideal conditions of no friction between junctions of fill and warp filaments, etc. . . . , the effect of the internal pressure can be estimated. Consider the case of the cylinder with the warp parallel to the axis. When a torque is applied, the warp filaments, which are assumed to act as the vertical strands of a bifilar pendulum, impose a restoring moment of magnitude

$$T_r = \left\{ \left(W_r + \frac{\pi D^2}{4} p_c \right) \times (\text{factor}) \right\} \left(\frac{D\theta}{2L} \right) \frac{D}{2}$$

where W_r is the total suspended weight, and the (factor) corresponds to that fraction of the total load carried by the vertical strands. Since the rubber matrix supports only a small percentage of the vertical load, the (factor) was taken to be unity. This restoring torque resists a part of the applied torque T . Thus the contribution to Gt from the material alone, in the absence of initial stresses, would be approximately



$$\begin{aligned}
 (Gt)_{mat.} &= \frac{4(T-T_r)L}{\pi D^3 \theta} \\
 &= Gt - \frac{(W_r + \frac{\pi D^2}{4} p_c)}{\pi D} \\
 &= Gt - \frac{D}{2} p_c
 \end{aligned}$$

since W_r has to equal $\frac{\pi D^2}{4} p_c$ for equal hoop and axial stresses. If the effect of internal pressure is similar to that of a bifilar pendulum as described above, then $(Gt)_{mat.}$ should be independent of p_c . As will be seen later from the experimental results, the dependence of $(Gt)_{mat.}$ on p_c is considerably less than that for Gt . Had $(Gt)_{mat.}$ exhibited independence on p_c , it would have been possible to test these types of materials at one pressure, and calculate the effective Gt at any other pressure according to

$$Gt = (Gt)_{mat.} + \frac{D}{2} p_c$$

The magnitude of the term $\frac{D}{2} p_c$, obtained by assuming the bifilar pendulum effect is comparable to $(Gt)_{mat.}$, when the warp or fill are along the axis of the cylinder. For the tests, with the warp filaments at 45 degrees to the cylinder axis, this sort of estimation of the effects of internal pressure is not necessarily valid. However, as will be seen later, $G_{45}t$ is considerably larger than $G_r t$ or $G_w t$, and exhibits smaller percentage dependence on the internal pressure than either $G_r t$ or $G_w t$.

Several static methods were attempted to measure Poisson's ratio μ . These were:

- (1) An optical method, using a transit and a scale
- (2) The usual technique of strain gages mounted lengthwise and circumferentially
- (3) A "null-gage" method, which is described below.

Method (1) was abandoned when the extension in the circumferential direction was found to be too small to be measured with any degree of accuracy. If much larger diameter cylinders ($D = 2$ ft or more) had been used, useful data might have been obtained, provided the cylinders were made correspondingly longer to minimize end-plate effects. Method (2) was also abandoned since no reliable method could be found for calibrating the gages, particularly in the circumferential direction where the extensions were very small. Method (3) afforded some promise for determining μ . Let σ and ϵ , denote the stress and the strain, respectively; and further, let subscripts H and A designate the hoop and axial directions, respectively. Assuming linearity, one of the stress-strain equations is

$$\epsilon_H = \frac{\sigma_H}{E_H} - \mu_{AH} \frac{\sigma_A}{E_A}$$

where μ_{AH} is the Poisson's ratio relating strain in the hoop direction due to stress in the axial direction. If one sets $\epsilon_H = 0$, then

$$\mu_{AH} = \frac{\sigma_H}{\sigma_A} \frac{E_A}{E_H}$$

If σ_A is changed after balancing the strain gage at the reference pressure and loading, σ_H must also be changed to keep

$\epsilon_H = 0$. This was done as follows: the strain gage was first nulled at the reference pressure and loading condition (median position). The axial load was altered by adding or subtracting known weights. This unbalanced the strain gage in the hoop direction. The strain gage was then nulled again by increasing or decreasing the internal pressure as needed. Assuming linearity about the median state, it is easily deduced from the above

* At the median position, $\sigma = \epsilon = 0$, i.e., σ and ϵ represent the incremental stress and strain.

stress-strain relation that

$$\mu_{AH} = \frac{E_A}{E_H} \frac{2}{\left(1 + \frac{4 \Delta W}{\pi D^2 \Delta p_z}\right)}$$

where Δp_z is the change in internal pressure required for nulling, and ΔW is the added weight to alter the axial stress.

The ratio (E_A/E_H) has to be taken from separate tests.

4. Dynamic Tests

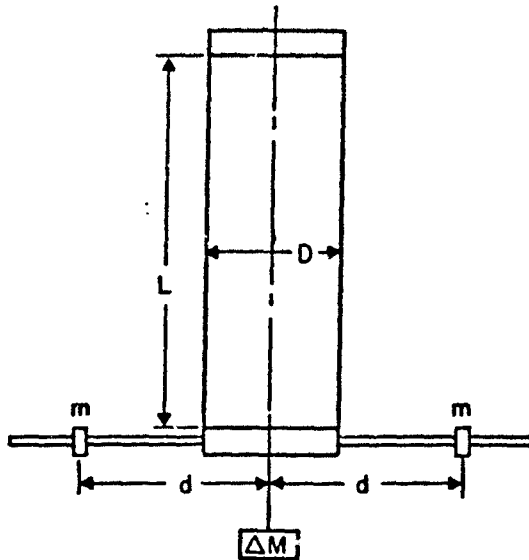
The dynamic method for measuring Et of the inflated cylinders consisted of exciting the fundamental axial vibration mode of the cylinder while it was in its desired biaxial stress condition, and recording the vibration trace using the output of an axially-aligned strain gage. The axial mode was excited by supporting a small weight (about 1 pound) with an electromagnet attached to the original equilibrium vertical load. When the magnet was switched off, the weight fell, exciting the longitudinal mode. Knowing the frequency from analysis of the vibration records, it is a simple matter to obtain the stiffness, Et , from the relation

$$Et = \frac{4\pi f^2 L m}{D}$$

where m is the total suspended mass (including one third the material mass, which corresponds to the well-known approximation for the effective mass of a spring, and the mass of one end plate), and f is the frequency in cps.

Gt was measured dynamically by using each cylinder as the spring of a torsional pendulum. The cylinder had one of its ends clamped to a horizontal strut from which the cylinder hung vertically. A three-foot bar was fixed horizontally to the cylinder's lower free end. Equal known masses were placed near the ends of the bar, equidistant from the center of the cylinder. A sketch of the setup is given below. The added mass, required to

equalize the hoop and axial stresses, was attached to the bottom of the cylinder from the end of a long wire. This allowed the



cylinder to twist independently of the added mass. After the required weights were added to the bottom of the cylinder, the cylinder was inflated to the required pressure. The adjustable (sliding) masses (each of m slugs) were positioned at a known distance, d_1 , from the center of the rod. The natural torsion frequency, f_1 (cps), of the cylinder-weight combination was recorded using the output of a strain gage mounted on the cylinder at an angle of 45 degrees to the axial direction. The masses were moved to new positions on the rod, at a distance d_2 from the center, thus changing the mass moment of inertia by an amount

$$\Delta I = 2m(d_2^2 - d_1^2)$$

The natural frequency, f_2 , corresponding to the new

mass positions was recorded as before, and the effective torsional "stiffness" was computed according to

$$Gt = \frac{32\pi Lm (d_2^2 - d_1^2) f_1^2 f_2^2}{D^3 (f_1^2 - f_2^2)}$$

5. Results and Discussion

The experimental results from the cylinder tests are summarized in Tables 2.10 through 2.14. They include three series of tests which were conducted at different times. In the first series the initial 17-inch long cylinder models were used; in the last two series these models were replaced by the 20-inch cylinder models. Within each series, repeated tests were run in the majority of cases, and the indicated values are the computed averages.

In Table 2.10, the extensional stiffnesses, E_t , along the directions of warp, fill, and 45 degrees, are presented for cylinder internal pressures corresponding to model pressure of $p_i = 1.0 - 6.0 \text{ lbs/in.}^2$ in 1-lb/in.² intervals.

The dynamic and static test results, generally, agree within the experimental accuracy.

There exist substantial differences between dynamic tests 2 and 3; in each series, the repeatability was within a much narrower band than this comparison indicates. Since series 2 was conducted on hot days in the summer and series 3 on cool days in late fall (four months apart), it was originally thought that aging of the rubber was responsible for this change, with possibly some temperature and humidity effects. Additional tests revealed, however, that both temperature and humidity are strong influencing factors. Table 2.11 summarizes some repeat dynamic tests for E_t .

The presented values are for internal pressure $p_2 = 0.688$ psig (corresponding to $p_2 = 2$ psig).^{*} To assess the influence of humidity, the surface was wetted with water at room temperature using a sponge. The effect of temperature change was assessed by heating the model with a 100-watt light bulb and reflector placed about 3 inches from the model. The results indicate substantial reductions in $E_f t$ with higher temperature and humidity. The significant variations of model frequencies with temperature as noted in Table 2.4 further substantiate this point.

The values of the extensional stiffnesses along the warp, $E_w t$, are higher than the corresponding quantities along the fill, $E_f t$. As the mean stress levels are raised (i.e., with larger internal pressures), both $E_w t$ and $E_f t$ increase, but the ratio $E_w t / E_f t$ decreases. This can be explained by postulating that, at low stress levels, the fabric stretches by thread straightening (also called "crimp interchange"), whereas at higher pressures, thread stretching is the dominant mechanism with a resultant increase in stiffness.

$E_{45} t$ is considerably less than either $E_f t$ or $E_w t$; this is as one might expect, for the contribution of the nylon cloth in this direction is considerably smaller than in the filament directions.

Parallel test results for the effective shear stiffnesses $G_w t$, $G_f t$, and $G_{45} t$ are given in Table 2.12, for essentially the same cylinder pressures as before. For the test series 2, the following procedure was used. One torsional frequency was observed for each of the two positions of mass m , d_1 , and d_2 . Let the value of Gt obtained from these two frequencies (f_1 , f_2) be denoted by $(Gt)_{12}$. The test was repeated for a new mass position d_3 , and a third frequency, f_3 , was recorded. In con-

^{*} Although not reported here, a few additional test points showed similar behavior at higher internal pressures.

junction with the data for position d_2 , another value $(Gt)_{23}$ was calculated. Ideally, identical results should be obtained for $(Gt)_{12}$ and $(Gt)_{23}$. This was not the situation however, especially in cases involving small changes in frequencies between f_1 and f_3 . The calculated result for Gt , being inversely proportional to the difference of two observed periods of oscillation, requires good accuracy in the frequency measurements. In cases where the vibration traces were clear and of sufficient length, reasonable agreement was obtained between $(Gt)_{12}$ and $(Gt)_{13}$. The entries given in the table for these series of tests are the averages of $(Gt)_{12}$ and $(Gt)_{23}$. For the test series 3 results, the presented values are for $(Gt)_{13}$, with positions d_1 and d_3 as the extreme locations of mass m . For test series 1, 2, and for $G_u t$ and $G_f t$, two values are entered in each box, with the top value for the effective stiffness, and the lower for $(Gt)_{mat}$. The latter, which is due solely to the material, is computed by subtracting from the effective value an amount due to the bifilar effect, as discussed previously.

The dynamic and static test results agree within experimental accuracy.

Like the extensional stiffnesses, the shear stiffnesses are temperature dependent as evidenced by differences in the dynamic tests 2 and 3, but this dependency appears to a lesser degree.

The experiments confirm the expected results that $G_u t \approx G_f t$, and that both are raised with increasing pressure.

The bifilar effect does not account for the total increase in Gt with increasing pressure. The additional and unaccounted increase may be possibly explained by postulating that the friction at each crossing point of the threads is larger at the higher pressures and the threads cannot move as freely relative to one another.

$G_{45}t$ shows a smaller percentage dependence on internal pressure and is an order of magnitude larger than either $G_w t$ or $G_f t$.

The static test results for the Poisson's ratios μ_{fw} , μ_{wf} and μ_{45} , are presented in Table 2.13. Large differences exist between series 2 and 3 values, with the most marked ones at the lower pressures. Since the latex is a major contributing factor for μ_{fw} and μ_{wf} , it is not surprising to see a large influence of temperature and humidity.

μ_{fw} and μ_{wf} decrease rapidly with increasing pressure. At low pressures, Poisson's ratios are large since crimp interchange dominates. At higher pressures, the effect of thread stretching dominates, and smaller μ 's may be expected.

The limiting value of unity is obtained for the μ_{45} -results. This suggests that the material is deforming as a pin-jointed trellis. At higher pressures, thread stretching and friction between warp and fill threads cause μ_{45} to decrease somewhat.

A comparison of the series 2 results with those of series 1, in which slightly thicker latex coating was used, suggests little change in warp and fill extensional stiffnesses. Although the cruciform tests gave no reliable quantitative results, they indicated a strong influence of latex thickness on $E_{45}t$. A similar influence on $G_f t$ and $G_w t$ may be anticipated.

The effect of the number of coatings on the vibration frequencies of rectangular cantilever models was investigated in Ref. 12. Adding extra coats of latex decreases the model frequencies, but also adds some additional stiffness, as evidenced by the fact that the changes in frequencies were not inversely proportional to the square root of the total masses.

In the absence of internal losses, one would expect the

relation

$$\mu_{wf} E_f = \mu_{fw} E_w \quad \left(\text{or} \quad \frac{\mu_{wf}}{\mu_{fw}} = \frac{E_w t}{E_f t} \right)$$

to be satisfied, if the material is assumed to behave linearly. Table 2.14 presents the ratio $(\mu_{wf} E_f / \mu_{fw} E_w)$. The closer this ratio is to one, the better the experimental results satisfy the above relation. Except for the isolated starred point in the table which is questionable, this ratio stays within 12 per cent of 1. This is well within the expected experimental accuracy considering the fact that the static μ -measurements are not believed to be very accurate.

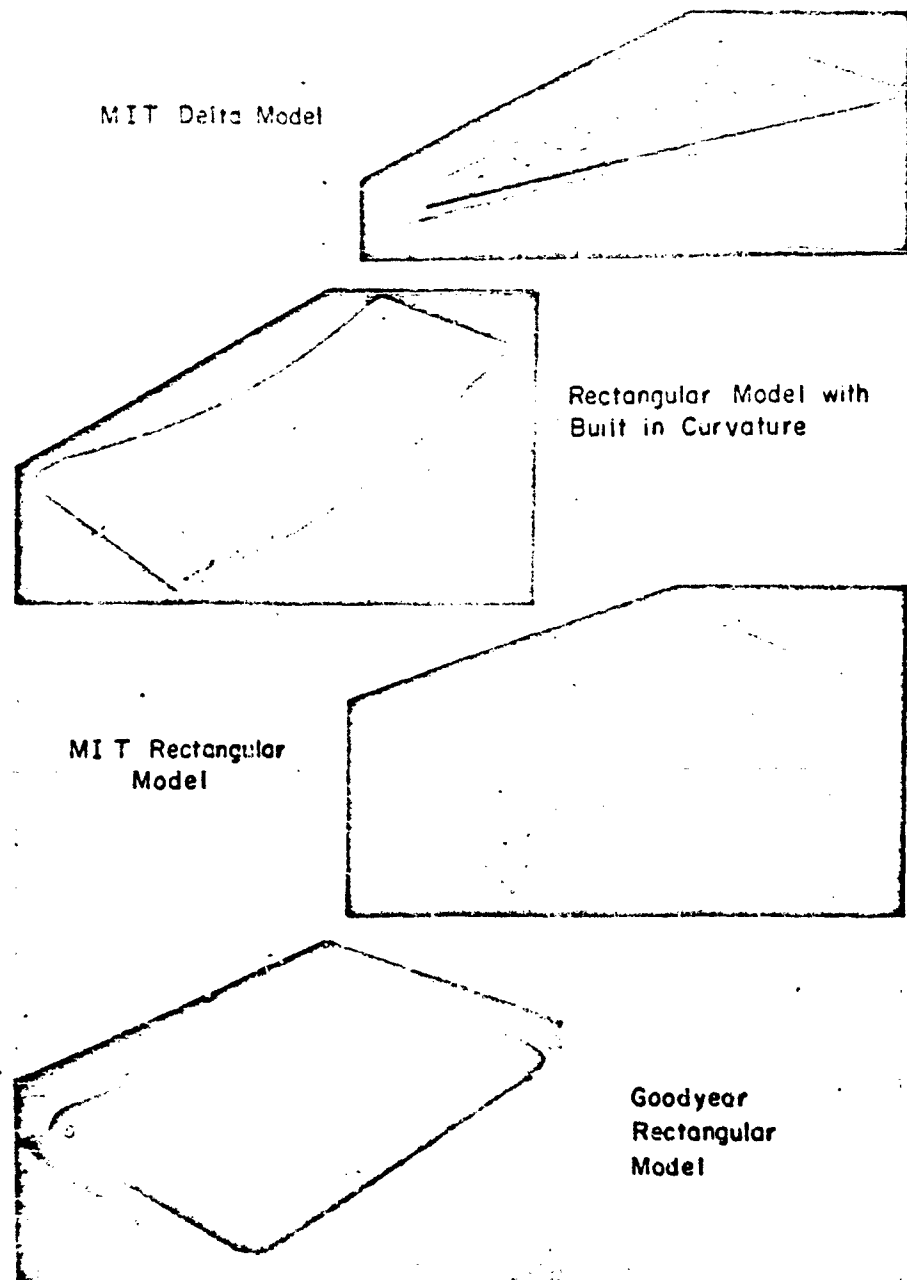


Figure 2.1 Samples of Inflatable Models.

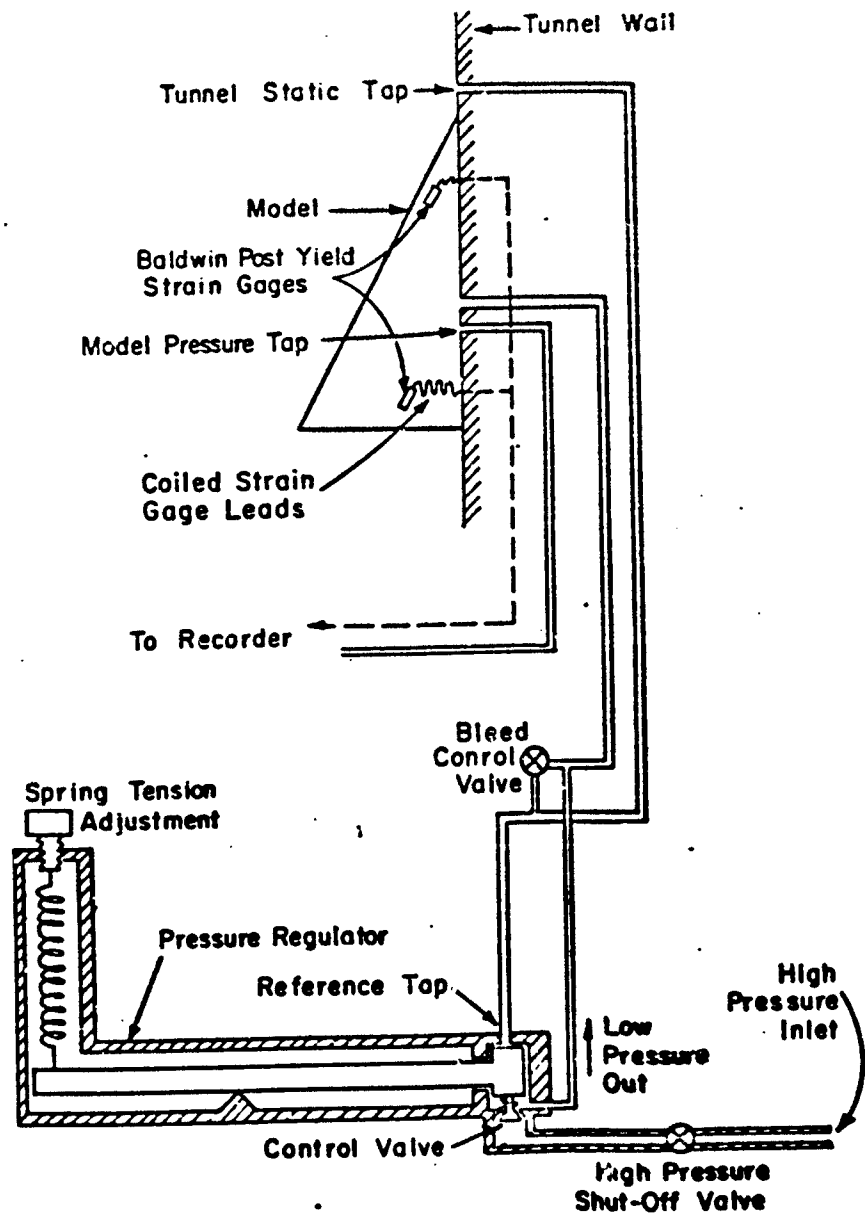


Figure 2.2 Schematic of Model Pressure Regulating System and Strain Gages.

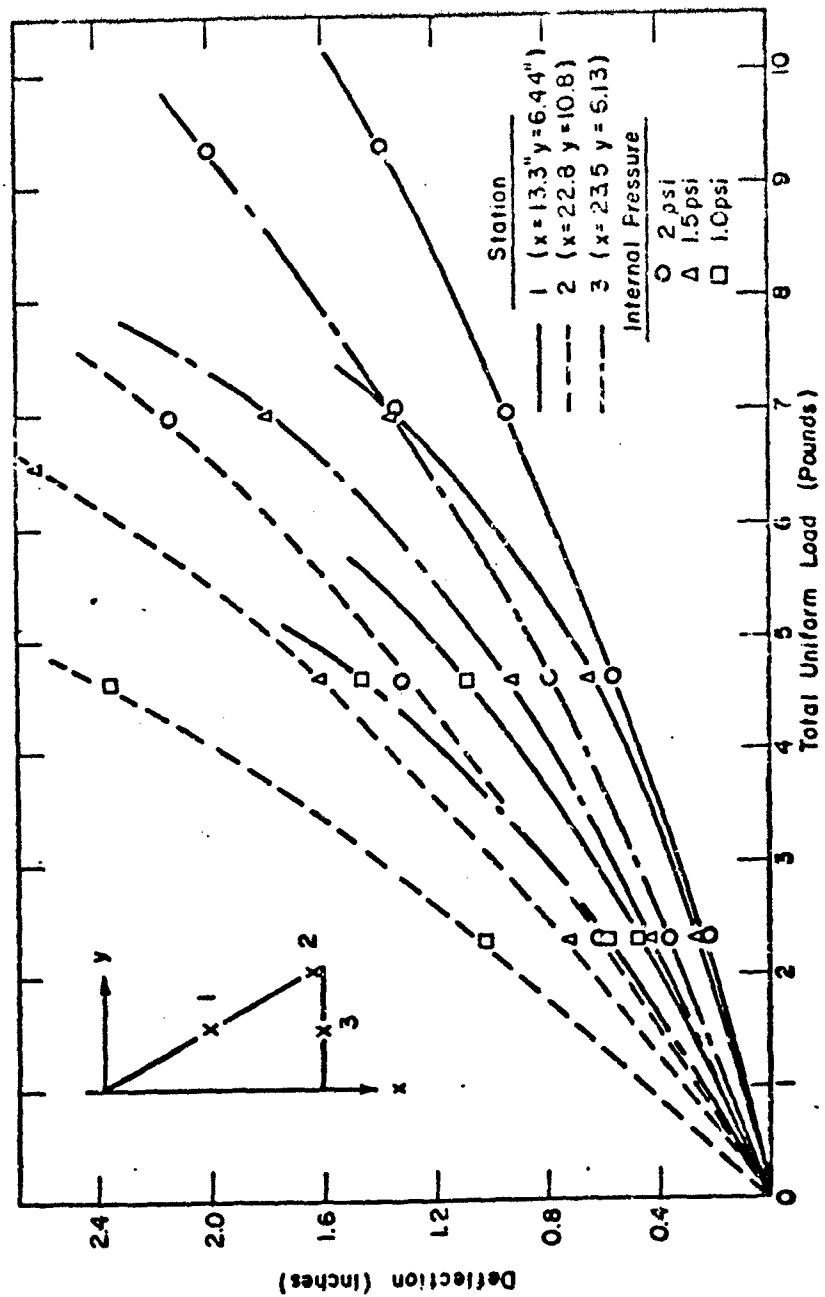
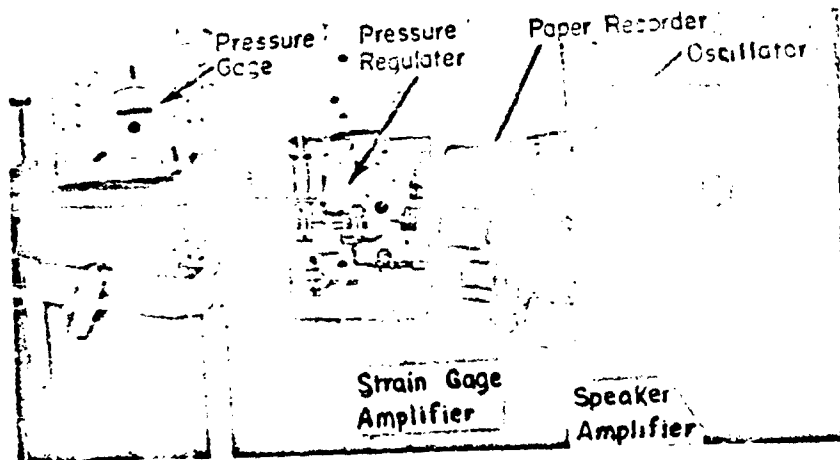
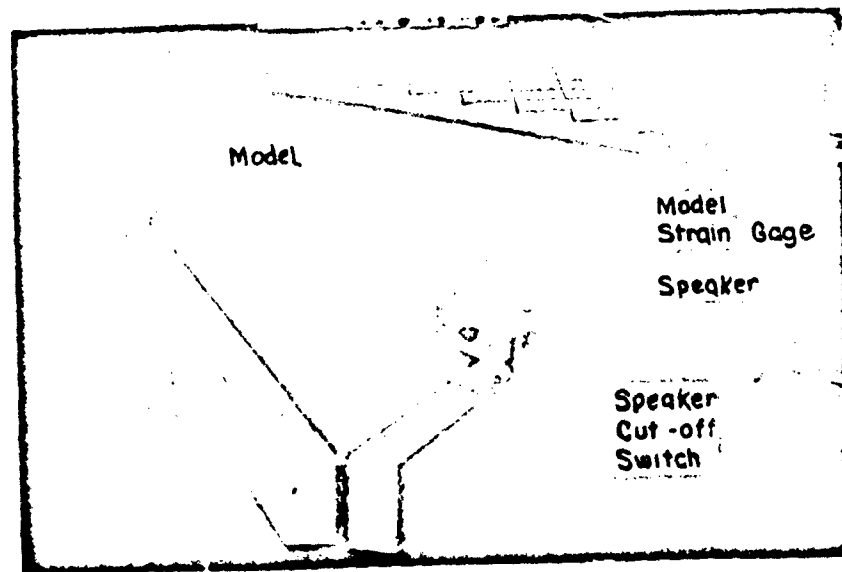


Figure 2.3 Wing Deflection vs Uniform Load for Model 1.



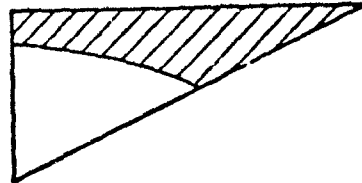
Complete System



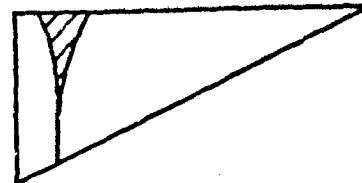
Closeup of Speaker and Model

Figure 2.4 Excitation System Used for Vibration Tests.

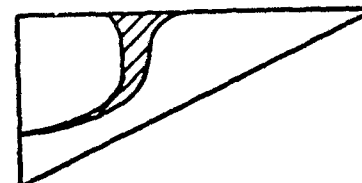
Mode 1



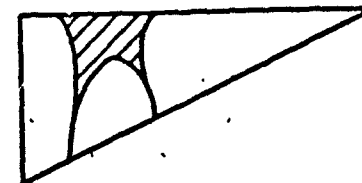
Mode 2



Mode 3



Mode 4



Mode 5

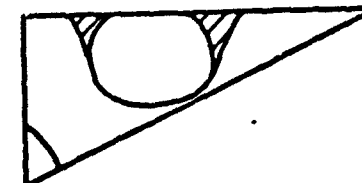
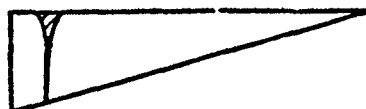


Figure 2.5 Typical Free Vibration Node Lines for 65-deg Sweep Models.

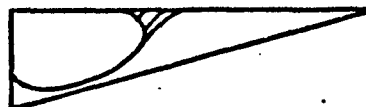
Mode 1



Mode 2



Mode 3



Mode 4



Mode 5



Figure 2.6 Typical Free Vibration Node Lines for 75-deg Sweep Models.

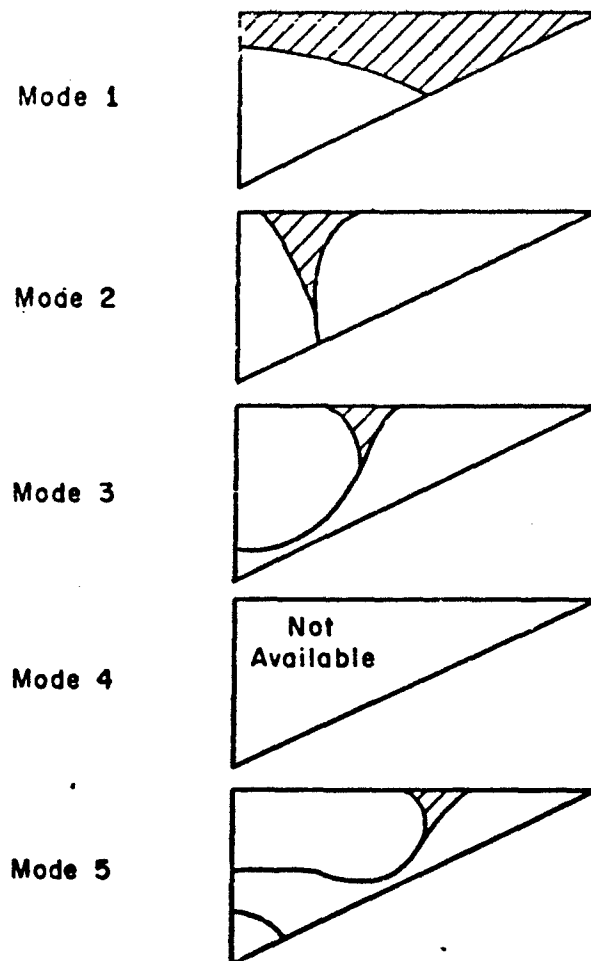
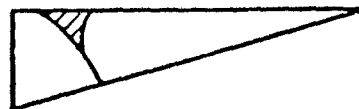


Figure 2.7 Typical Free Vibration Node Lines of Models 1 and 2.

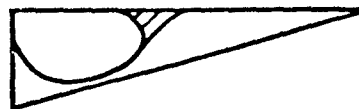
Mode 1



Mode 2



Mode 3



Mode 4



Mode 5

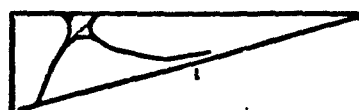


Figure 2.8 Typical Free Vibration Node Lines for Model 10.

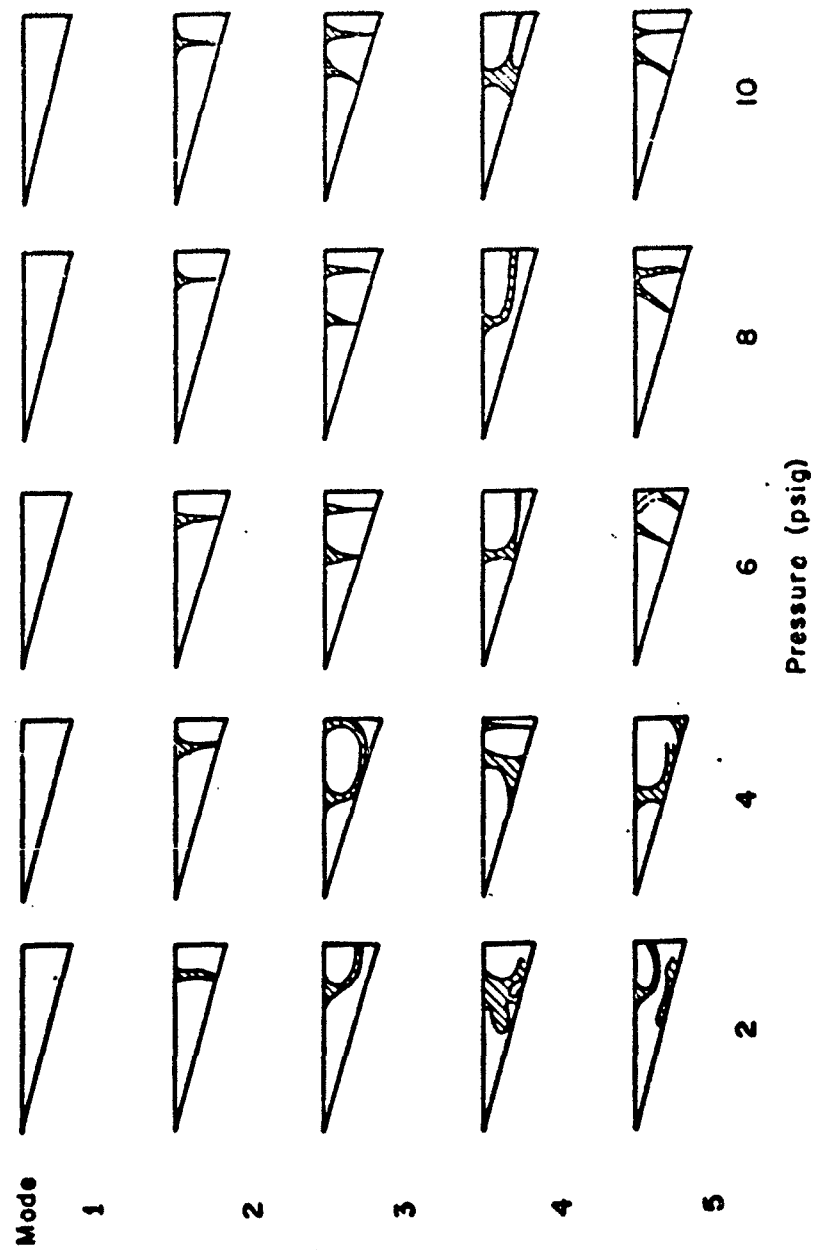


Figure 2.9 Free Vibration Node Lines for Model 18.

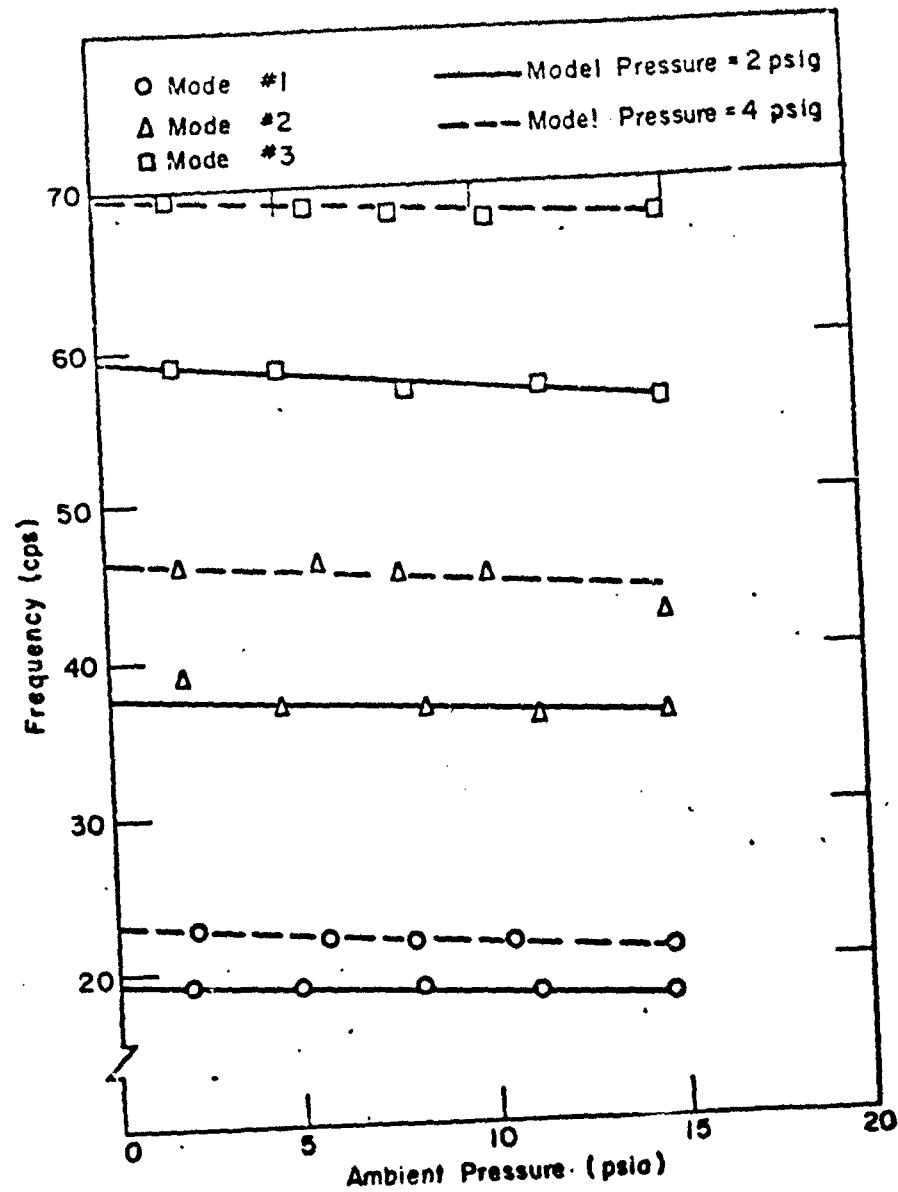


Figure 2.10 Effect of Ambient Pressure on Frequencies of First Three Modes of Model 2.

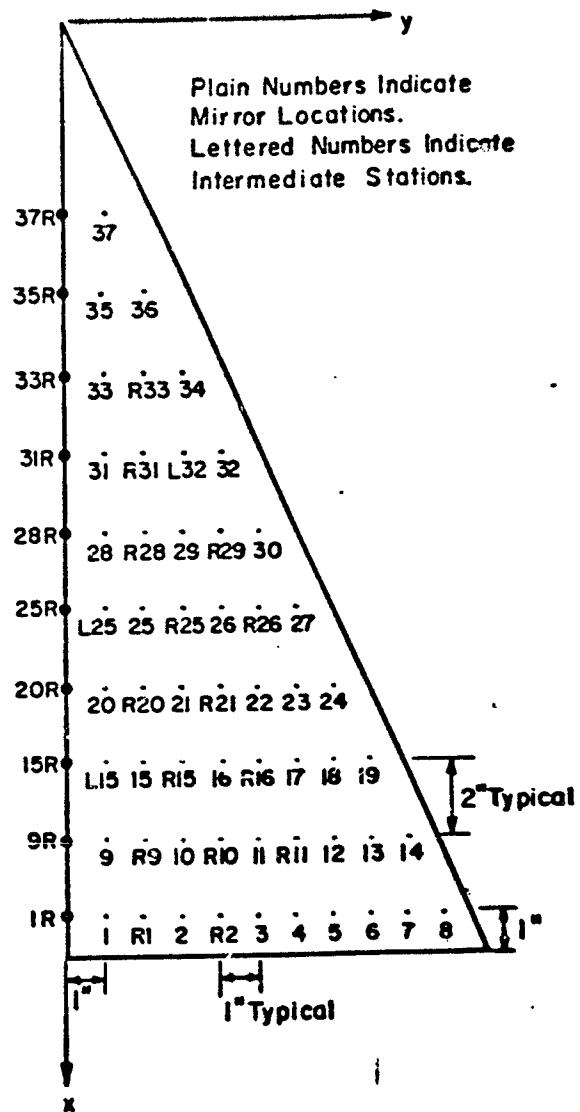


Figure 2.11 Mirror Stations Used for Determining Vibration Mode Shapes.

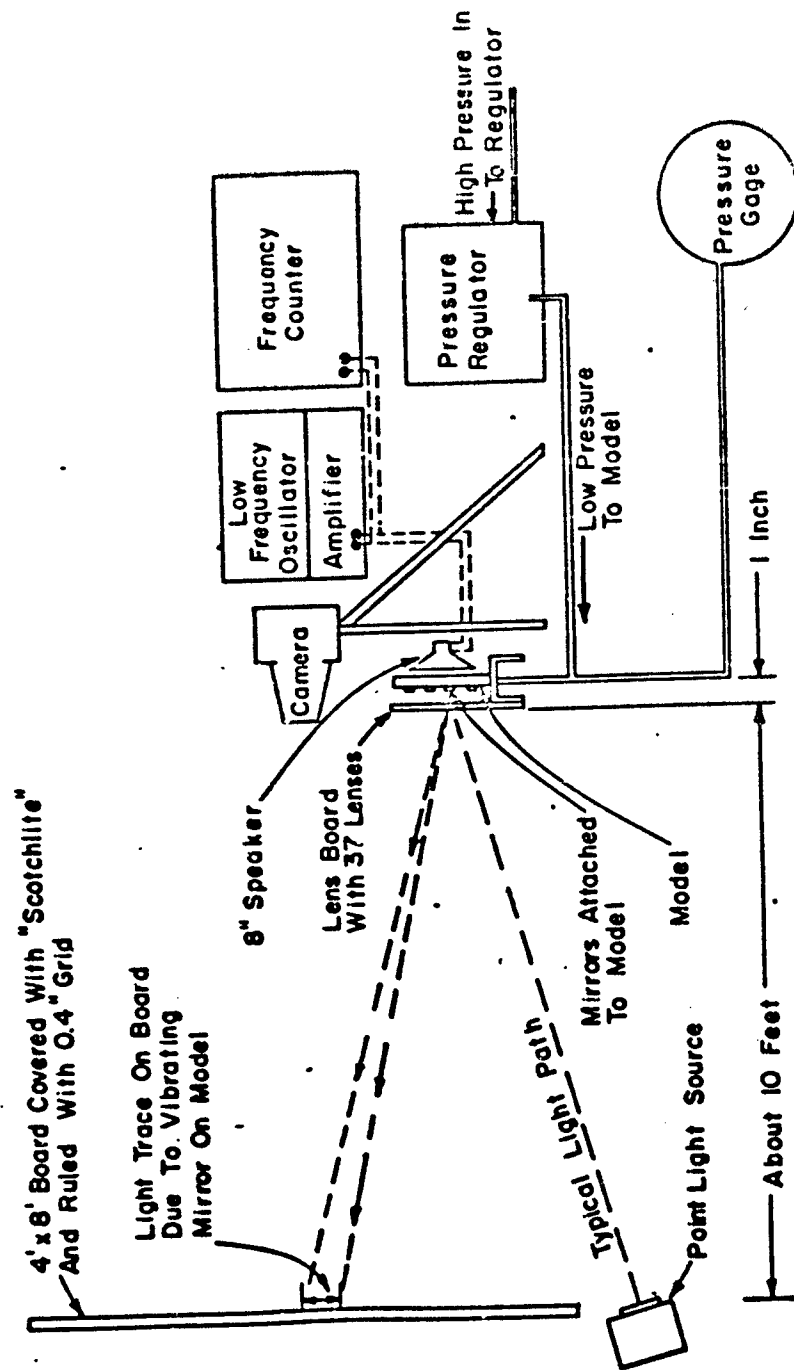


Figure 2.12 Schematic of Mirror Test Setup.

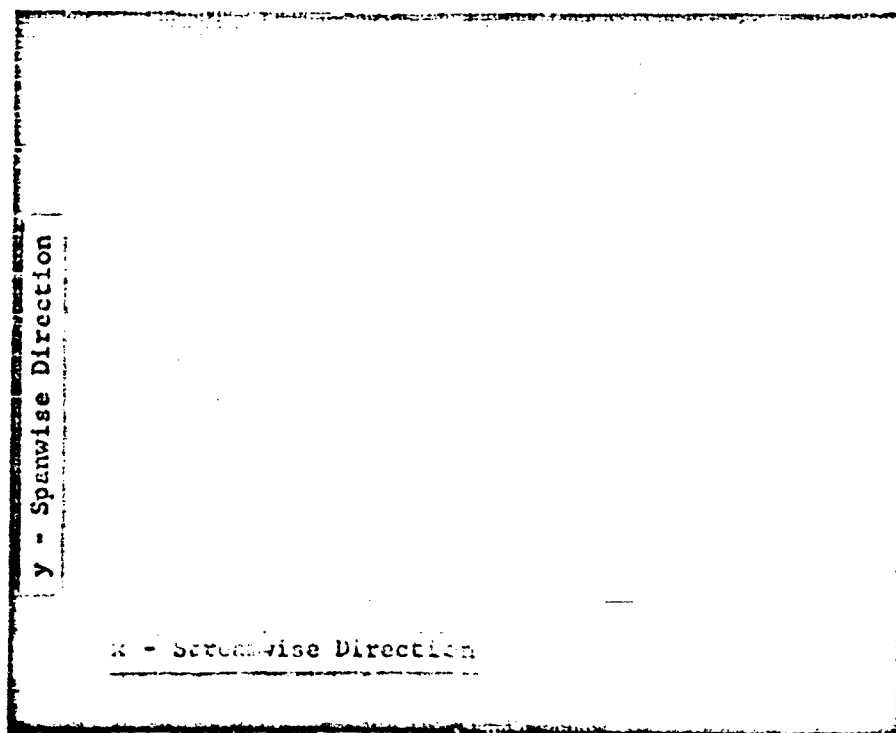


Figure 2.13 Typical Photograph for Mirror Mode Shape Data. For Data Reduction, a 15 x 24 in. Print is Used.

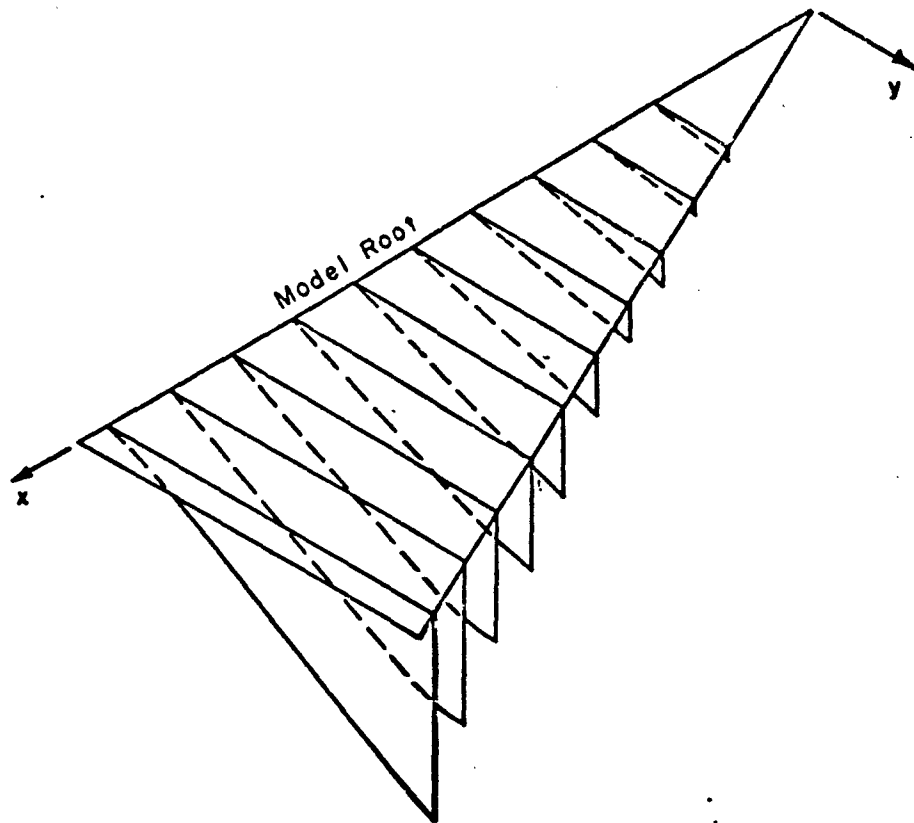


Figure 2.14 Experimental Mirror Mode Shape for First Vibration Mode of Model 8 at $p_d = 2$ psig.

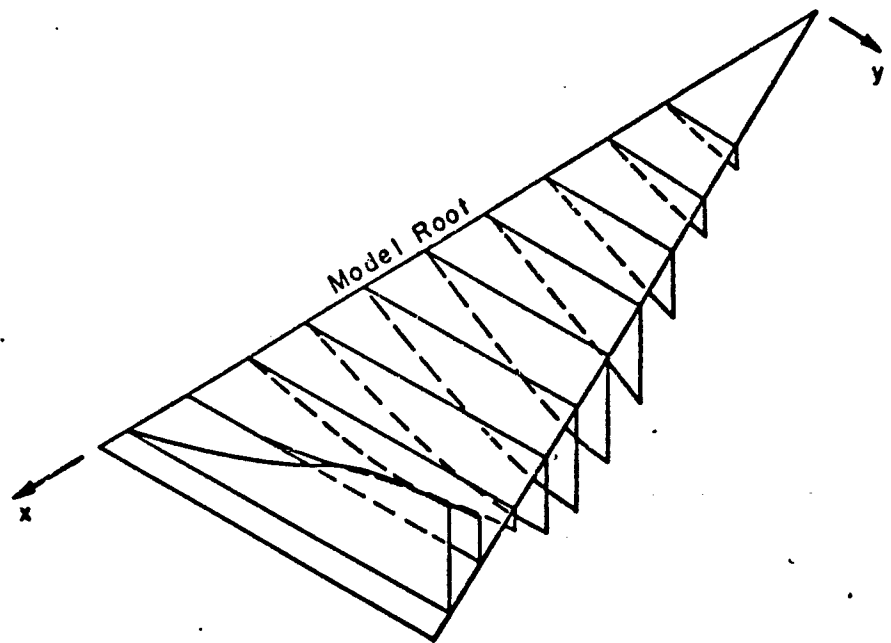


Figure 2.15 Experimental Mirror Mode Shape for Second
Vibration Mode of Model 8 at $p_d = 2$ psig.

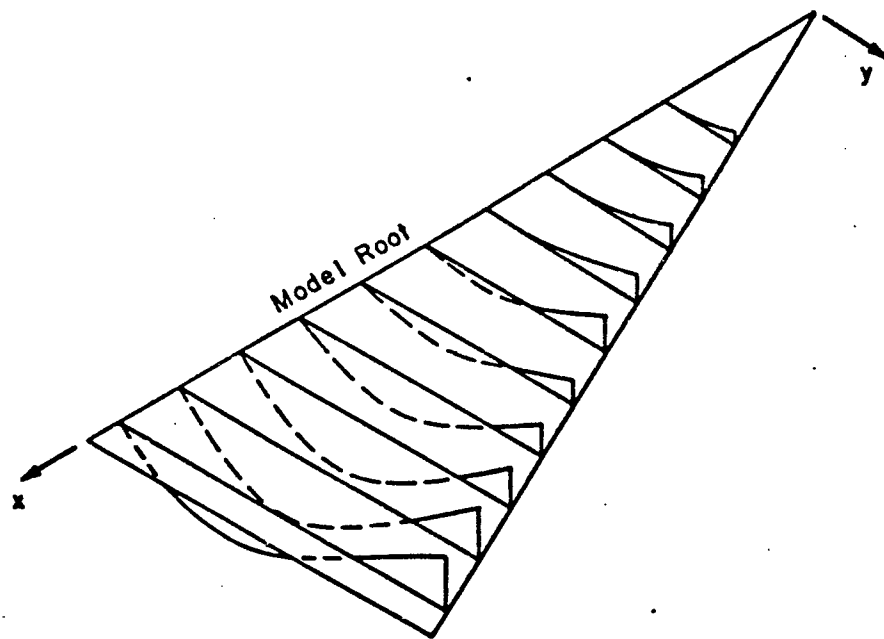
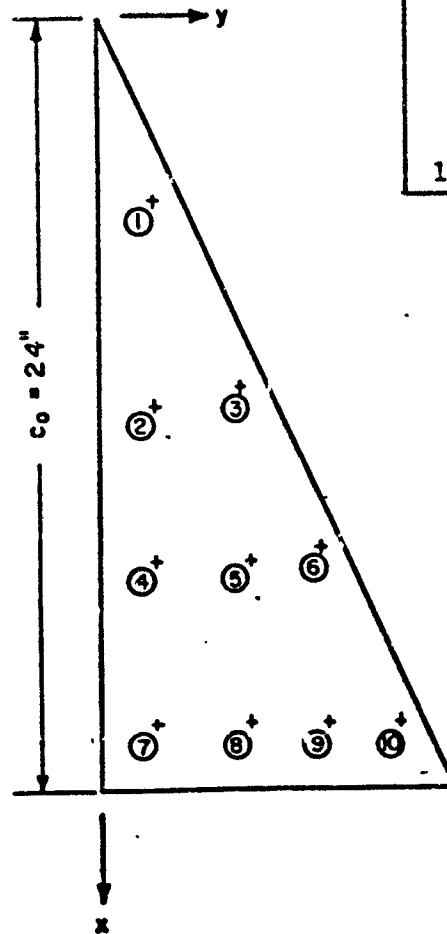


Figure 2.16 Experimental Mirror Mode Shape for Third
Vibration Mode of Model 8 at $p_d = 2$ psig.



Point	Mass (lb)	\bar{x}	\bar{y}
1	.04605	.2366	.0590
2	.02901	.5000	.0700
3	.02870	.4753	.1868
4	.02901	.7000	.0700
5	.02316	.7000	.1959
6	.02190	.6889	.2915
7	.03317	.9125	.0700
8	.02649	.9125	.1959
9	.02251	.9125	.2992
10	.02787	.9125	.3951

Figure 2.17 Influence Coefficient Stations and Mass Data for Model 5.

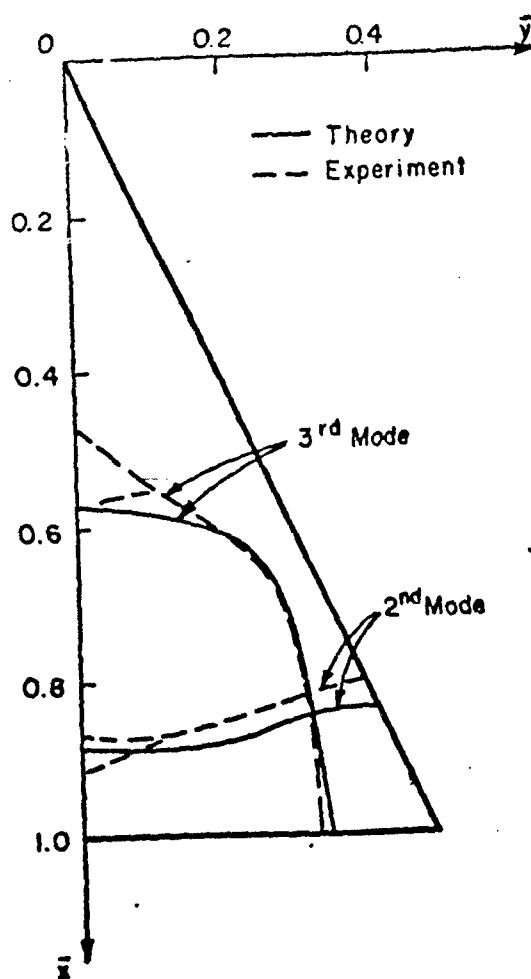


Figure 2.19 Comparison of Experimental Node Lines and Node Lines Calculated from Measured Influence Coefficients, for Model 5 at a Pressure of 2 psig.

TABLE 2.1 MODEL DATA FOR INFLATABLE DELTA WINGS

Model	Symbol*	Nominal Sweep (deg)	Root Chord (in.)	Semi-Span (in.)	Depth (in.)	Total Mass (Slugs) x 10 ²	Construction		
							Material	No. of Plies	Thread** Direction (deg)
1	none	65	23.5	11.0	1 5/16	1.081	Nylon	1	0, 50 †
2	none	65	24	11.2	1 3/8	0.7453	"	1	0, 50 †
3	O	65	"	11.2	"	1.105	"	1	0
4	□	65	"	11.2	"	0.8540	"	1	0
5	none	65	"	11.2	"	0.8942	"	1	0
6	none	65	"	11.2	"	0.8791	"	1	0
7	◇	65	"	11.2	"	0.8305	"	1	0
8	◇	65	"	11.2	"	0.8695	"	1	0
9	O	65	"	11.2	"	1.006	Dacron	2	0 & 45
10	◇	75	"	6.43	"	0.6799	"	2	0 & 45
11	◇	65	"	11.2	"	1.108	"	1	0
12	Λ	65	"	11.2	"	1.006	"	1	0
13	◇	65	"	11.2	"	1.184	"	2	0 & 45
13-1	◇	65	"	11.2	"	1.028	"	2	0 & 0
14	◇	65	"	11.2	"	0.9657	"	1	0
15	Δ	75	"	6.43	"	0.5580	"	1	0
16	Δ	75	"	6.43	"	0.5676	"	1	0
17	Δ	75	"	6.43	"	0.6619	"	1	0
18	◇	75	"	6.43	"	0.6700	"	1	0
19	none	65	"	11.2	"	1.140	"	2	0 & 0
20	X	65	"	11.2	"	1.432	"	2	0 & 45

* Individual symbol assigned to model and used for plotting flutter data

** Warp orientation relative to x-axis, see Fig. 2.3

† Warp orientation was 0° for top surface and 50° for bottom surface

TABLE 2.2 COMPARISON OF THEORETICAL AND EXPERIMENTAL DEFLECTIONS OF MODEL 1 UNDER A UNIFORM, STATIC LOAD. MODEL PRESSURE IS 2 PSIG

Total Load		Station*		
		1	2	3
2.33 lbs	Theory	0.164 in.	0.290 in.	0.242 in.
	Experiment	0.22	0.60	0.36
4.66	Theory	0.328	0.580	0.484
	Experiment	0.56	1.32	0.78
6.99	Theory	0.492	0.870	0.726
	Experiment	0.94	2.14	1.34
*See Fig. 2.3 for location of stations				

TABLE 2.3. MODEL VIBRATION DATA

Model No.	Test No.	Model Pressure (psig)	Mode 1 f ₁ (cps)	2	3	4	5	Remarks
				f ₂ 81	f ₃ 83	f ₄ 84	f ₅ 85	
1	1	1.0	13.0	-	41.9			See Fig. 2.7 for node lines
		1.5	14.3					
		2.0	15.5	33.0	53.2			
		2.0	14.3	30.7	47.9		66.2	
2	1	2.0	17.8	35.9	56.0			See Fig. 2.10 for vibration data at other ambient pressures
		4.0	21.1	44.2	68.0			
		2.0	15.4	30.5	51.1	60.0	81.0	
		2.0	15.0	28.6	48.3			
3	3	2.0	14.9	28.9	48.5			Fourth mode difficult to peak Data used for flutter points 3-8 Data used for flutter points 9-10 Data used for flutter point 2
		4.0	17.3	35.7	60.0			
		2.0	12.9	23.0	38.5		51.0	
		2.0	15.6	28.5	49.0		66.2	
4	1	1.0	13.2	26.9	40.0		52.6	Refer to Figs. 2.5 and 2.6 for typical node lines of 65- and 75-degree sweep models, respectively, except as noted.
		2.0	16.8	32.3	52.5		70.0	

TABLE 2.3 (CONTINUED)

Model No.	Test No.	Model Pressure (psig)	Model f_1 (cps)	2	3	4	5	Remarks
4	2	2.0	15.1	30.2	48.9		69.2	Data used for flutter point 12 Data used for flutter point 11 Unable to excite 4th mode at 2 psig internal pressure
	3	2.0	15.0	30.4	49.5			
	4	2.0	13.9	29.6	48.3		70.2	
	5	2.0	14.6	31.4	50.6		71.4	
			0.055	0.073	0.088		0.073	
	6	2.0	15.6	32.5	52.0		72.6	
5			0.042	0.037	0.027		0.031	
	1	4.0	18.3	40.1	64.9	72.6	94.9	
			0.039	0.038	0.044			
		2.0	16.2	32.6	51.6		72.5	
	2	4.0	19.5	39.9	65.3		92.8	
		2.0	16.7	32.3	54.0		73.2	
			0.038	0.052	0.031		0.022	
		4.0	19.9	40.4	65.6	78.8	93.4	
			0.028	0.040	0.042			
		6.0	22.7	46.1	74.4	87.1	111	
			0.024	0.027				
		8.0	24.2	49.9	82.8	94.4	120	
3			0.026	0.020				
		2.0	16.1	32.1	52.2	61.3	74.8	
			0.049	0.062	0.039		0.018	

Refer to Figs. 2.5 and 2.6 for typical node lines of 65- and 75-degree sweep models, respectively, except as noted.

TABLE 2.3 (CONTINUED)

Model No.	Test No.	Model Pressure (psig)	Mode 1 f ₁ (cps)	2 f ₂	3 f ₃	4 f ₄	5 f ₅	Remarks
5	3 Cont.	4.0	19.8 0.033	40.6 0.046	64.9 0.023	78.3	92.3	Data used for flutter points 13-23
		6.0	21.6 0.029	45.2 0.030	71.5 0.027	86.2	111	
		8.0	24.0 0.031	49.7 0.031	81.1	96.3	118 0.028	
6	1	2.0	17.8	33.5	56.9		77.3	
		4.0	21.4	40.9	71.9		98.3	
		2.0	17.6 0.047	34.1 0.045	59.1 0.031	67.1	78.9 0.023	
	2	4.0	21.3 0.055	41.8 0.042	73.3 0.032	81.9	102	
		6.0	23.7 0.039	46.3 0.032	83.6 0.023	91.7	116	
		8.0	25.6 0.035	50.6 0.025	90.4 0.024	101	128	
7	1	1.0	13.7	27.4	42.4		57.6	
		2.0	16.0	33.3	53.8		76.5	
		4.0	19.6	40.9	65.9		97.4	
	2	1.0	13.3 0.073	27.0 0.040	41.7 0.044			
		2.0	15.7 0.088	32.5 0.044	52.0 0.049			
Refer to Figs. 2.5 and 2.6 for typical node lines of 65- and 75-degree sweep models, respectively, except as noted.								

TABLE 2.3 (CONTINUED)

Model No.	Test No.	Model Pressure (psig)	Model 1 f ₁ (cps) g ₁	2 f ₂ g ₂	3 f ₃ g ₃	4 f ₄ g ₄	5 f ₅ g ₅	Remarks
7	2 Cont.	3.0	17.4 0.049	38.8 0.032	58.6 -			Data used for flut- points 24-37
		4.0	18.6 0.044	40.0 0.036	64.0 0.010			
	3	2.0	15.0 0.073	31.7 0.052	50.0 0.055			
		4.0	17.9 0.044	38.3 0.042	61.7 0.022			
8	1	6.0	20.3 0.042	43.8 0.037	71.5 0.028			Data used for flut- points 38-40
		1.0	14.2	27.5	41.8		59.4	
	2	2.0	16.7	33.6	52.6		76.5	
		4.0	19.8	40.8	64.9		97.0	
9	2	1.0	13.8	27.5	41.2			Data used for flut- points 38-40
		2.0	15.8	32.2	51.0			
	3	3.0	18.6	37.9	58.7			
		4.0	19.7	41.2	64.0			
9	1	1.0	23.8	44.0	45.1		66.8	
		2.0	27.3	54.0	59.6		87.2	

Refer to Figs. 2.5 and 2.6 for typical node lines of 65- and 75-degree sweep models, respectively, except as noted.

TABLE 2.3 (CONTINUED)

Model No.	Test No.	Model Pressure (psig)	Mode 1 f_1 (cps) g_1	2 f_2 g_2	3 f_3 g_3	4 f_4 g_4	5 f_5 g_5	Remarks	
9	1	4.0	31.1 — g_1	65.0 — g_2	77.8 — g_3		116 — g_5	Data used for flutter points 41, 42, 43	
	Conc.								
	2	2.0	26.4 — g_1	52.5 — g_2	59.2 — g_3		85.1 — g_5		
		4.0	30.0 — g_1	62.9 — g_2	77.5 — g_3		113 — g_5		
		6.0	33.0 — g_1	70.0 — g_2	89.0 — g_3		133 — g_5		
		8.0	34.6 — g_1	75.0 — g_2	96.6 — g_3		146 — g_5		
		10.0	36.3 — g_1	80.0 — g_2	117 — g_3		161 — g_5		
	3	2.0	26.3 — g_1	52.6 — g_2	58.3 — g_3		85.5 — g_5		
		4.0	29.6 — g_1	63.7 — g_2	76.4 — g_3		114 — g_5		
10		6.0	32.9 — g_1	70.5 — g_2	89.3 — g_3		132 — g_5		
	1	1.0	33.6 — g_1	62.7 — g_2	69.7 — g_3	85.6 — g_4	110 — g_5	See Fig. 2.8 for node lines	
		2.0	39.0 — g_1	77.2 — g_2	92.5 — g_3	113 — g_4	121 — g_5		
	2	8.0	58.8 — g_1	108 — g_2	156 — g_3	189 — g_4			
	Refer to Figs. 2.5 and 2.6 for typical node lines of 65- and 75-degree sweep models, respectively, except as noted.								

TABLE 2.3 (CONTINUED)

Model No.	Test No.	Model Pressure (psig)	Mode 1 f_1 (cps) g1	2 f_2 g2	3 f_3 g3	4 f_4 g4	5 f_5 g5	Remarks
11	1	2.0	14.4 0.044	33.8 0.055	45.3 0.049		67.4	Data used for flutter points 48,49
	2	2.0	14.0 0.043	32.6 0.055	44.7 0.052		65.9	
	3	2.0	13.5 0.041	32.1 0.052	45.7 0.034		64.3	
		4.0	16.8 0.028	41.3 0.046	58.0 0.049		88.5	
		6.0	19.3 0.026	45.5 0.034	68.2 0.029		105	
		8.0	20.9 0.027	48.3 0.036	75.5 0.024		119	
		10.0	22.5 0.022	51.7 0.025	82.2 0.024		128	
	4	2.0	13.9 0.049	31.8 0.067	45.3 0.048	60.9	66.3	
		4.0	17.0 0.054	39.2 0.038	58.6 0.041	79.0	90.3	
		6.0	18.8 0.037	45.4 0.034	69.2 0.023	90.2	106	
12		8.0	21.3 0.037	49.7 0.028	76.6 0.019	98.9	118	Refer to Figs. 2.5 and 2.6 for typical node lines of 65- and 75-degree sweep models, respectively, except as noted.
		10.0	22.3 0.031	51.7 0.027	80.9 0.020	106	131	
	1	2.0	15.7 0.049	34.5 0.063	47.5 0.063		69.2	
	2	2.0	15.6 0.037	35.0 0.050	47.6 0.052		70.2	

TABLE 2.3 (CONTINUED)

Model No.	Test No.	Model Pressure (psig)	Mode 1 f ₁ (cps) g ₁	2 f ₂ g ₂	3 f ₃ g ₃	4 f ₄ g ₄	5 f ₅ g ₅	Remarks
12	3	2.0	15.9 0.026	34.8 0.050	47.3 0.034		69.6	Data used for flutter point 50
		4.0	18.7 0.032	42.1 0.037	52.0 0.040		92.8	
		6.0	21.7 0.019	48.6 0.025	73.7 -		111	
		8.0	23.5 0.015	51.9 0.018	80.2 0.031		122	
		10.0	25.2 0.023	57.4 0.020	87.6 -		136	
		2.0	14.2 0.054	33.5 0.078	46.0 0.031	63.4	69.0	
13	4	4.0	18.8 0.034	41.1 0.042	60.3 0.027	81.6	91.3	Data used for flutter point 51
		6.0	20.5 0.034	48.7 0.026	71.0 0.024	95.8	109	
		8.0	22.8 0.034	52.2 0.027	78.6 0.017	104	122	
		10.0	25.0 0.030	55.2 0.024	86.5 0.016	112	132	
		2.0	26.2 0.038	49.7 0.032	57.0 0.020		80.8	
		2.0	25.9 0.024	50.0 0.022	57.0 0.015		79.6	
13	1	2.0	25.8 0.021	49.1 0.031	57.0 0.018		79.1	Data used for flutter point 51
	2	2.0	29.6 0.031	60.5 0.020	74.7 0.018		104	
	3	4.0						

Refer to Figs. 2.5 and 2.6 for typical node lines of 65- and 75-degree sweep models, respectively, except as noted.

TABLE 2.3 (CONTINUED)

Model No.	Test No.	Model Pressure (psig)	Mode 1 f ₁ (cps) g ₁	2 f ₂ g ₂	3 f ₃ g ₃	4 f ₄ g ₄	5 f ₅ g ₅	Remarks
13	3	6.0	31.8 0.031	66.5 0.022	86.7 0.014		122	Data used for flutter point 52
	Cont.	8.0	33.5 0.028	72.2 0.016	96.1 0.017		136	
		10.0	35.8 0.031	76.6 0.015	105 0.016		152	
	1	2.0	18.1 0.049	39.2 0.055	52.0 0.043		74.8	
13-1	2	2.0	17.7 0.032	38.9 0.036	51.1 -		75.0*	Data used for flutter point 53
	3	2.0	17.2 0.042	37.7 0.051	51.5 0.044		73.3	
		4.0	21.0 0.031	46.0 0.042	64.9 0.044		98.0	
		6.0	23.5 0.024	53.0 0.031	76.2 0.031		115	
14		8.0	25.8 0.023	57.8 0.027	85.0 0.028		130	Data used for flutter point 53
		10.0	27.2 0.028	61.2 0.0328	91.8 0.037		142	
	1	2.0	16.4 0.058	35.6 0.049	48.7 0.049		69.4	
	2	2.0	15.8 0.051	34.5 0.061	49.0 0.042		69.8	
	3	2.0	16.3 0.035	34.7 0.052	47.9 0.042		69.5	
		4.0	19.4 0.023	43.4 0.022	63.0 0.031	91.2	124	
Refer to Figs. 2.5 and 2.6 for typical mode lines of 65- and 75-degree sweep models, respectively, except as noted.								

TABLE 2.3 (CONTINUED)

Model No.	Test No.	Model Pressure (psig)	Mode 1 f ₁ (cps) g ₁	2 f ₂ g ₂	3 f ₃ g ₃	4 f ₄ g ₄	5 f ₅ g ₅	Remarks
14	3 Cont.	6.0	21.8 0.022	48.7 0.023	72.4 -	-	107 -	Fourth mode difficult to peak
		8.0	23.3 0.013	53.5 0.023	80.0 0.024	-	122 -	
		10.0	25.7 0.020	57.0 0.025	88.1 -	-	134 -	
	4	2.0	16.3 0.038	34.5 0.055	47.7 0.042	65.4 -	68.7 -	
		4.0	19.5 0.031	43.1 0.041	63.6 0.029	85.2 -	92.3 -	
		6.0	21.8 0.028	49.4 0.021	73.0 0.021	96.2 -	109 -	
		8.0	23.6 0.026	54.2 0.024	81.1 0.020	106 -	124 -	
15	1	10.0	25.4	56.3	87.7	114	134	Data used for flutter points 54, 55
		2.0	31.8 0.050	60.8 0.027	88.8 0.019	96.8 0.028	120 0.022	
		4.0	40.4 0.054	77.0 0.040	116 0.013	124 -	159 -	
		6.0	46.7 0.035	85.8 0.026	141 0.024	155 -	194 -	
		8.0	53.2 0.022	92.4 0.016	150 0.015	162 -	217 -	
		10.0	55.5 0.029	101 0.019	162 0.015	172 -	242 -	
		2.0	33.3 0.052	58.6 0.051	89.4 0.021	98.5 0.019	116 -	
16	1	2.0						Data used for flutter point 56
Refer to Figs. 2.5 and 2.6 for typical mode lines of 65- and 75-degree sweep models, respectively, except as noted.								

TABLE 2.3 (CONTINUED)

Model No.	Test No.	Model Pressure (psig)	Mode 1 f_1 (cps) g_1	2 f_2 g_2	3 f_3 g_3	4 f_4 g_4	5 f_5 g_5	Remarks
16	1 Cont.	4.0	40.9 0.044	71.2 0.031	116 0.018	129 0.018	159 -	Data used for flutter point 57
		6.0	47.0 0.035	85.8 0.021	137 0.018	148 -	187 -	
		8.0	52.5 0.027	93.4 0.024	152 0.015	164 -	212 -	
		10.0	55.6 0.027	100 0.021	166 0.015	182 -	232 -	
17	1	2.0	30.3 0.051	54.6 0.037	80.6 0.022	91.0 0.017	106 -	Data used for flutter points 58-61
		4.0	37.9 0.051	67.7 0.031	105 0.015	115 0.013	141 -	
		6.0	44.4 0.015	76.3 0.021	121 0.011	134 0.015	172 -	
		8.0	48.5 0.034	84.8 0.023	136 -	151 0.014	193 -	
18	1	10.0	51.5 0.056	88.9 0.019	146 0.018	162 0.014	202 -	Data used for flutter points 62, 63
		2.0	30.3 0.042	52.5 0.034	89.9 -	130 -	152 -	
		4.0	36.9 0.055	62.6 0.027	101 0.016	137 -	152 -	
		6.0	42.2 0.034	72.2 0.019	116 0.016	134 0.015	166 -	
		8.0	46.7 0.029	80.3 0.019	131 -	152 0.010	177 -	See Fig. 2.9 for node lines
		10.0	50.5 0.025	85.8 0.016	138 -	162 -	192 -	

Refer to Figs. 2.5 and 2.6 for typical node lines of 65- and 75-degree sweep models, respectively, except as noted.

TABLE 2.3 (CONCLUDED)

Model No.	Test No.	Model Pressure (psig)	Mode 1 f_1 (cps)	2 f_2	3 f_3	4 f_4	5 f_5	Remarks
19	1	2.0	17.2	38.8	51.2	65.2	71.5	Data used for flutter points 64-66
			0.055	0.055	0.041	-	-	
		4.0	20.5	44.9	63.6	84.4	91.3	
			0.042	0.035	0.040	-	-	
		6.0	22.6	49.9	71.7	96.3	109	
			0.044	0.030	0.026	-	-	
20	1	8.0	23.6	53.2	79.8	106	123	
			0.044	0.030	0.025	-	-	
		10.0	25.2	56.5	87.0	113	132	
			0.045	0.028	0.020	-	-	
		2.0	17.6	36.0	53.2	65.1	70.5	
			0.065	0.055	0.024	0.024	-	
		4.0	21.0	45.6	71.0	82.1	93.5	
			0.055	0.034	0.016	0.022	-	
		6.0	23.2	51.2	81.1	96.3	112	
			0.041	0.034	0.018	-	-	
		8.0	25.1	56.1	91.3	106	121	Refer to Figs. 2.5 and 2.6 for typical node lines of 65- and 75-degree sweep models, respectively, except as noted.
			0.049	0.028	0.014	0.024	-	
		10.0	26.6	59.8	96.7	112	132	
			0.035	0.025	0.016	0.014	-	

TABLE 2.4 EFFECT OF TEMPERATURE ON THE FREE VIBRATION FREQUENCIES OF MODEL 6 AT $P_2 = 2$ PSIG

Mode 1		Mode 2		Mode 3		Mode 5	
Temperature T(in. °F)	f_1 (in. cps)	T	f_2	T	f_3	T	f_5
71	17.2	70.5	32.3	70.5	56.2	70.5	74.0
89	16.6	87	31.7	86	55.2	85	73.6
115	15.5	109	30.7	112	52.6	111	72.0
134	15.4	129	30.8	134	51.8	130	74.0*
* Questionable value							

TABLE 2.5 COMPARISON OF EXPERIMENTAL FREQUENCIES AND ANALYTICAL FREQUENCIES BASED ON PURE-SHEAR-TYPE DEFORMATIONS, FOR THREE MODELS AT $P_2 = 2$ PSIG

	Experiment			Simplified Analysis		
	Model 1	8	9	Model 1	8	9
f_1 (cps)	14.3	16.7	26.4	18.2	20.8	19.3
f_2	30.7	33.7	52.5	36.6	41.7	38.8
f_3	47.9	52.6	59.2	50.5	57.5	53.4

TABLE 2.6 EFFECT OF PAD SIZE ON INFLUENCE COEFFICIENT MEASUREMENTS

C_{ij}	Lead Pad Diameter		
	1 inch	2 inch	4 inch
C_{54}	0.059	0.055	0.055
C_{55}	0.228	0.210	0.212
C_{56}	0.173	0.174	0.170

TABLE 2.7 EXPERIMENTALLY-DETERMINED FORCE-DEFLECTION INFLUENCE COEFFICIENT MATRIX FOR MODEL 5. (CORRECTED FOR MAXWELL'S RECIPROcity RELATION; UNITS IN IN./LB)

	1	2	3	4	5	6	7	8	9	10
1	.0707	.0118	.0293	.0035	.0085	.0119	-.0003	-.0013	-.0015	-.0005
2	.0118	.0877	.0547	.0172	.0316	.0413	.0045	.0137	.0208	.0282
3	.0293	.0547	.184	.0311	.0792	.118	.0088	.0270	.0428	.0635
4	.0035	.0172	.0311	.0827	.0577	.0538	.0175	.0585	.0500	.0599
5	.0085	.0316	.0792	.0577	.212	.172	.0358	.0970	.0440	.179
6	.0119	.0413	.118	.0538	.172	.325	.0410	.128	.213	.283
7	-.0003	.0045	.0088	.0175	.0358	.0410	.113	.0770	.0816	.0862
8	-.0013	.0137	.0270	.0385	.0970	.128	.0770	.274	.273	.297
9	-.0015	.0208	.0428	.0500	.0440	.213	.0816	.273	.469	.512
10	-.0005	.0282	.0635	.0599	.179	.283	.0862	.297	.512	.766

TABLE 2.8 NORMALIZED MODE SHAPES FOR MODEL 5 FROM CALCULATIONS BASED ON MEASURED INFLUENCE COEFFICIENTS

Station	Mode Amplitude (Normalized with Respect to Station 10)		
	Mode 1	Mode 2	Mode 3
1	0.00777	-0.71470	0.0999
2	0.06226	-1.20041	0.0248
3	0.14429	-2.94835	0.1623
4	0.11510	-0.86345	-0.3390
5	0.28120	-2.64691	-0.3287
6	0.47852	-2.73049	0.1257
7	0.15755	0.11175	-1.2230
8	0.48997	0.59971	-1.4191
9	0.74594	1.61580	-0.1107
10	1.00000	1.00000	1.0000

See Fig. 2.17 for station locations

TABLE 2.9 COMPARISON OF EXPERIMENTAL FREQUENCIES AND FREQUENCIES CALCULATED FROM MEASURED INFLUENCE COEFFICIENTS, FOR MODEL 5 AT A PRESSURE OF 2 PSIG.

	Frequency (cps)		
	Model 1	Mode 2	Mode 3
Experiment	16.7	32.3	54.0
Calculated	15.9	32.5	46.4

TABLE 2.10 EXTENSIONAL STIFFNESSES $E_w t$, $E_f t$, AND $E_{45} t$ ALONG DIRECTIONS OF WARP, FILL AND 45 DEGREES TO WARP, RESPECTIVELY

Test Series	Method of Test	$E_w t$ (lb/in.)					
		$p_d = 1$ (psig)	2	3	4	5	6
1	Static	-	148	163	-	-	-
2	Static	-	153	-	172	-	-
2	Dynamic	139	143*	164	181	-	189
3	Dynamic	-	175	181	193	197	207
		$E_f t$ (lb/in.)					
		1	2	3	4	5	6
1	Static	-	109	119	-	-	-
2	Static	-	96.3	-	135	-	170
2	Dynamic	96	113	124	136	-	163
3	Dynamic	-	133	146	157	163	171
		$E_{45} t$ (lb/in.)					
		1	2	3	4	5	6
2	Dynamic	25.5	30.0	31.6	34.6	36.8	41.7
3	Dynamic	-	34.7	37.5	39.7	42.1	44.1
*Questionable point							

TABLE 2.11 INFLUENCE OF TEMPERATURE AND HUMIDITY ON THE EXTENSIONAL STIFFNESS $E_f t$, AT CYLINDER PRESSURE OF 0.688 PSIG

1	Humidity	$E_f t$	Remarks
73 °F	38%	133	
75	W	124	Surface wetted
-	W	118	Wetted and heated for a short period
-	W	109	Wetted and heated for a longer period

TABLE 2.12 SHEAR STIFFNESSES G_t , G_{gt} AND G_{gst} FROM CYLINDERS WITH AXIS IN DIRECTION OF WARP, FILL, AND 45 DEGREES TO WARP, RESPECTIVELY

Test Series	Method of Test	G_{gt} (G_{gt}) _{mat.} (lb/in.)						Remarks
		$P_d = 1$ (psig)	2	3	4	5	6	
1	Static	-	4.35	5.79	-	-	-	Average of (G_t) ₁₂ and (G_t) ₂₃ .
2	Dynamic	-	2.97	3.73	-	-	-	
		-	4.39	5.77	7.16	8.51	10.00	
		-	3.01	3.71	4.41	5.07	5.87	
		G_{gt} (G_{gt}) _{mat.} (lb/in.)						
		1	2	3	4	5	6	
1	Static	-	4.64	5.51	-	-	-	Average of (G_t) ₁₂ and (G_t) ₂₃ Value of (G_t) ₁₃
2	Dynamic	-	3.26	4.13	-	-	-	
		3.60	4.44	5.53	6.39	7.49	8.28	
		2.91	3.06	3.47	3.64	4.05	4.15	
3	Dynamic	-	4.85	-	-	-	-	Value of (G_t) ₁₃
		-	3.47	-	-	-	-	
		(G_{gst}) (lb/in.)						
		1	2	3	4	5	6	
2	Dynamic	41.0	53.7	66.3	76.9	-	99.0	Value of (G_t) ₁₃
3	Dynamic	-	59.6	-	77.9	-	99.6	

TABLE 2.13 POISSON'S RATIOS μ_{fw} , μ_{wf} , μ_{45}

Test Series	Method of Test	μ_{fw}		
		$p_d = 2$ (psig)	4	6
2	Static	0.343	0.289	0.279
3	Static	0.545	0.488	0.439
		μ_{wf}		
		2	4	6
2	Static	0.578	0.412	0.342
3	Static	0.802	0.641	0.470
		μ_{45}		
		2	4	6
2	Static	1.005	0.947	0.681
3	Static	0.942	0.815	0.740

TABLE 2.14 THE RATIO $\mu_{wf} E_f / \mu_{fw} E_w$ FROM THE EXPERIMENTAL MEASUREMENTS

Test Series	Method of Test	$\mu_{wf} E_f / \mu_{fw} E_w$		
		$p_d = 2$ psi	4	6
2	Static	1.06	1.12	-
2	Static for μ Dynamic for E	1.33*	1.07	1.06
3	Static for μ Dynamic for E	1.12	1.07	0.884

* Questionable point

SECTION 3

WIND-TUNNEL TESTS

A. WIND TUNNELS

The supersonic wind-tunnel tests were conducted in Tunnel A, Gas Dynamics Facility, Arnold Engineering Development Center (AEDC), Tullahoma, Tennessee. This is a 40- by 40-inch continuous, closed-circuit, variable-density wind tunnel with a Mach number range of 1.5 to 6.0 at maximum stagnation pressures from 29 to 200 psia, respectively, and stagnation temperatures up to 300 °F (M = 6).

The transonic wind-tunnel tests were run in the 8-foot transonic wind tunnel at Cornell Aeronautical Laboratory, Inc. (CAL), Buffalo, New York. This is a pressurized wind tunnel capable of operating from 1/6 to 2-1/2 atmospheres and over a Mach number range from zero to approximately 1.4.

A single incompressible flutter point was obtained in the 7-1/2-ft x 10-ft Wright Brothers Wind Tunnel at MIT. This is a low-speed, variable-density wind tunnel with a maximum speed of about 140 mph.

B. TESTING PROCEDURES

1. Supersonic Tests

For the supersonic tests, the models were mounted on a 30-inch circular splitter plate which was designed and built as part of this program (Fig. 3.1).

It was originally anticipated that some difficulty would be experienced from the dynamic loads imposed on the models by the starting and stopping shocks; however, the models were flexible enough so that they were not destroyed by these starting loads and special equipment to protect the models was not re-

quired. Some difficulty was experienced with the breaking of strain gages during wind-tunnel starts, but this problem was alleviated by making the wind-tunnel starts at the minimum stagnation pressures and by increasing the number of strain gages mounted on the model from 2 to 4, so as to increase the probability of having at least one usable gage circuit after the tunnel start.

The normal test procedure was to establish the desired steady-state-test conditions in the tunnel with the model inflated to a known pressure differential above tunnel static pressure. The model was then excited by the plucking mechanism (Fig. 3.1); if flutter occurred, the stagnation pressure was lowered until flutter stopped; if the model did not flutter, the stagnation pressure was increased to obtain a new steady-state-flow condition and the model was again excited with the plucking mechanism. This procedure was repeated until either flutter occurred, or the maximum tunnel stagnation pressure was achieved.

In some tests, flutter was initiated, or checked, by varying the model pressure while maintaining steady-state-tunnel conditions.

A record of the outputs of the strain gages and the pressure differential between the model pressure and tunnel static pressure was obtained on a direct writing oscillograph. During the first tests, some flutter frequencies were not obtained because the oscillograph was not running at a high enough speed at the time flutter occurred. Therefore, for the later tests, this data was also continuously recorded on magnetic tape to provide a more reliable frequency reading capability.

The model pressure, the tunnel static and stagnation pressures, the pressure differential between the model pressure and tunnel static pressure, the stagnation temperature, and the Mach number were all recorded and used in conjunction with the VKF

CONFIDENTIAL

(This report is unclassified)

ERA 1102 computer to tabulate tunnel parameters and the outputs of the pressure transducers. The continuous oscillograph record was tied in with the tabulated data (which was taken, tabulated, and printed out every three seconds) through the use of a manual "flutter-on-off" switch which (1) controlled a two-position trace on the oscillograph record, and (2) caused a "0" (flutter-off), or a "1" (flutter-on) to be printed in one column of the tabulated data. Another two-position trace on the oscillograph recorded whenever data was being taken. In this manner it was possible to determine the onset or termination of flutter from the output of the strain-gage traces on the oscillograph records, and then determine the corresponding tunnel and model conditions from the tabulated data.

Visual records of the flutter motion, which provided information on flutter-mode shapes, were obtained using high-speed motion picture cameras.

2. Transonic Tests

For the transonic tests, the models were attached to an aluminum base plate which was installed on the reflection plane cart of the transonic wind tunnel (Fig. 3.1). A rotating mechanism was used to excite the model in the transonic tests.

The testing procedures were essentially the same as those used for the supersonic tests.

3. Low-Speed Tests

For the low-speed test at MIT the model was mounted on a plywood board which was placed vertically in the center of the tunnel and spanned the entire height of the tunnel. For these tests, the tunnel density was atmospheric, and the flutter point was determined by varying tunnel speed while maintaining constant model pressure. Essentially the same data was recorded as in the supersonic and transonic tests.

CONFIDENTIAL

(This report is unclassified)

CONFIDENTIAL

(This page is UNCLASSIFIED)

ERA 1102 computer to tabulate tunnel parameters and the outputs of the pressure transducers. The continuous oscillograph record was tied in with the tabulated data (which was taken, tabulated, and printed out every three seconds) through the use of a manual "flutter-on-off" switch which (1) controlled a two-position trace on the oscillograph record, and (2) caused a "0" (flutter-off), or a "1" (flutter-on) to be printed in one column of the tabulated data. Another two-position trace on the oscillograph recorded whenever data was being taken. In this manner it was possible to determine the onset or termination of flutter from the output of the strain-gage traces on the oscillograph records, and then determine the corresponding tunnel and model conditions from the tabulated data.

Visual records of the flutter motion, which provided information on flutter-mode shapes, were obtained using high-speed motion picture cameras.

2. Transonic Tests

For the transonic tests, the models were attached to an aluminum base plate which was installed on the reflection plane cart of the transonic wind tunnel (Fig. 3.1). A rotating mechanism was used to excite the model in the transonic tests.

The testing procedures were essentially the same as those used for the supersonic tests.

3. Low-Speed Tests

For the low-speed test at MIT the model was mounted on a plywood board which was placed vertically in the center of the tunnel and spanned the entire height of the tunnel. For these tests, the tunnel density was atmospheric, and the flutter point was determined by varying tunnel speed while maintaining constant model pressure. Essentially the same data was recorded as in the supersonic and transonic tests.

CONFIDENTIAL

(This page is UNCLASSIFIED)

CONFIDENTIAL**C. FLUTTER RESULTS AND DISCUSSION****1. General**

The plucking mechanisms used to excite the flutter models in the transonic and supersonic tests (Fig. 3.1) were a very important part of the test procedure. If the model was not excited, it was possible to penetrate deeply into the unstable region without encountering flutter.

For the supersonic tests, once flutter was initiated by exciting the model with the plucking mechanism, the flutter motion would continue for many cycles (at limited amplitude) as the stagnation pressure was decreased, even in regions where the model had previously been stable. Figure 3.2 presents photographs of typical strain-gage responses showing (1) response to plucking excitation in a stable region, (2) response to plucking excitation in an unstable region, and (3) limited amplitude flutter continuing while the stagnation pressure decreases, until finally the flutter motion suddenly subsides. It is this latter point, where the motion suddenly ceases, which was taken as the flutter boundary. For the supersonic tests the model was excited by an up and down movement of the plucking mechanism. Because of the placement of the model with respect to the plucking mechanism, the downward, or second excitation gave a larger forcing amplitude, as can be seen from the strain-gage responses. In general, flutter was initiated by this second excitation, with a rapid buildup to a steady-state amplitude after a few initial cycles of erratic motion. It should be noted that the shape of the decaying portions of the strain-gage responses are not exponential as is usually the case for linear systems.

The inflatable models used in this program were capable of withstanding many cycles of limited amplitude oscillation without damage. For the supersonic tests, it was almost always possible to enter into the unstable region, initiate flutter by

CONFIDENTIAL

CONFIDENTIAL

exciting the model, and return to the stable region without destroying the model, so that more than one flutter point could be obtained from one model. In fact, Model 7 alone accounted for 25 flutter points before it was finally destroyed. The model's destruction usually occurred after some local rupture in the model surface resulted in a complete loss of internal air pressure, and therefore model stiffness. The model would then buffet against the splitter plate and be destroyed. Figure 3.3, taken from the high-speed motion picture film, shows a model during flutter and after losing pressure.

Unlike the supersonic tests at AEDC, flutter in the CAL transonic tunnel was most often catastrophic. The models usually failed after a few cycles and it was only possible to get eight flutter points from six models. This may be attributed to the fact that the transonic tests were generally made at higher values of model pressure differential and dynamic pressures.

Figure 3.4 shows some typical models after failure occurred and the tunnel had been shut down. Incidentally, it may be noted that all model failures were not necessarily catastrophic, as evidenced by Model 1 which developed a large bubble at the wing tip caused by drop-chord failure during flutter.

2. Results and Discussion

A complete summary of all the experimental flutter data is given in Table 3.1, which also includes calculated flutter parameters based on model properties and tunnel conditions at flutter.

As previously mentioned, the vibration characteristics of the inflatable models were somewhat variable; vibration tests made on the same model at different times gave frequencies which differed by more than the experimental error. The flutter parameters given in Table 3.1 are based on the last frequencies

CONFIDENTIAL

CONFIDENTIAL

measured before the actual flutter test. In some instances the models fluttered at values of model pressure differential for which no vibration data exists. For these cases, the vibration frequencies were estimated by interpolation and extrapolation of the available vibration data. The vibration results used to reduce the flutter data for particular flutter points is indicated in Table 2.3.

No corrections have been made in the tabulated data to account for temperature or apparent mass effects through their influence on the measured vibration frequencies (see Section 2, Subsection C). The apparent mass effects can be accounted for by appropriate modification of the still-air vibration tests, based on the results of the vibration tests carried out on Model 2 under reduced ambient pressures. This effect is small and is considered to be negligible for the present program. A theoretical method of correcting for temperature effects,* accounting for the temperature variations occurring over the model surfaces during the wind-tunnel tests, is beyond the state of the art. This approach is further complicated by the fact that it would require accurate knowledge of material structural and thermal properties as a function of temperature. A more feasible approach would be to determine the actual temperature distributions by appropriate wind-tunnel tests, and then measure the model frequencies through vibration tests performed under thermal conditions simulating those measured in the wind tunnel. The main problem encountered here would be that of simulating the required temperature gradients with the relatively small models used in the present program. While the uniform tempera-

*For models where only shear-type deformations are of importance, the temperature effects will be nonexistent, since all the stiffness is derived from the model pressure differential. The fact that the models exhibit a marked dependence on temperature is further indication that bending-type deformations must be considered in any analysis carried out on the present type models.

CONFIDENTIAL

CONFIDENTIAL

ture tests carried out under this program are not useful for any quantitative evaluation of the effects of temperature on the flutter results, they do serve to indicate that these effects are important. The effect of increased temperature is to lower the natural vibration frequencies. Thus, the experimental flutter parameters $V_f/b_0 \omega_2 \sqrt{\mu}$ and ω_f/ω_2 , which are based on ω_2 's measured at room temperature, would be lower than the actual values for stagnation temperatures considerably above room temperature. This particular point will be brought up again during subsequent discussions of the flutter data.

Eight of the flutter points given in Table 3.1 correspond to repeated tests for identical model configurations. Except for flutter points 17, 22, and 24, each pair of duplicate tests was made during the same tunnel run. The results are repeatable to within approximately 1 to 1-1/2 per cent in the flutter index, $V_f/b_0 \omega_2 \sqrt{\mu}$, and 2 to 2-1/2 per cent in the flutter frequency parameter, ω_f/ω_2 , which is within the accuracy of the measurements. For flutter points 17, 22, and 24 which all correspond to the same test configuration, the maximum variations between the flutter parameters are somewhat larger (3.7 per cent for $V_f/b_0 \omega_2 \sqrt{\mu}$ and 6.2 per cent for ω_f/ω_2). Flutter points 17 and 22 were obtained during the same tunnel run (at the beginning and end of the series of tests made to determine the effects of model pressure differential). Flutter point 24 was obtained at a much later time, Model 7 having been removed from the tunnel while other models were tested. The variation in the flutter parameters can be attributed mainly to the fact that the stagnation temperature for flutter point 24 is 40 degrees higher than that for points 17 and 22.

In order to determine the variation of the flutter index, $V_f/b_0 \omega_2 \sqrt{\mu}$, and the flutter frequency parameter, ω_f/ω_2 , with Mach number, a large number of tests were made on a basic model

CONFIDENTIAL

CONFIDENTIAL

configuration, consisting of a 65-degree-sweep delta, cantilevered model with a model pressure differential of 2 psig and an angle of attack of zero degree. The value of 2 psig for model pressure differential was selected on the basis of preliminary calculations which indicated that this value would provide the largest Mach number range over which model instabilities would be encountered, within the operating range of the wind tunnel used in the supersonic tests. The results for this basic configuration, in terms of the parameters $V_f/b_o \omega_2 \sqrt{\mu}$ and ω_1/ω_2 vs M, are plotted in Figs. 3.5 and 3.6.* With a few exceptions which will be covered later, the flutter mode for the basic configuration was a combination of the first and second vibration modes, and only this type of flutter mode will be considered here. Henceforth this will be referred to as low-frequency flutter.

An alternate choice of dimensionless parameters, which arise in theoretical calculations based on piston theory or slender-body theory, are the flutter parameter $V_f/b_o \omega_2$, the flutter frequency parameter, ω_1/ω_2 , and the mass-ratio-Mach-number product, μM . Figures 3.7 and 3.8 present the results of the experiments on the basic model configuration in terms of these parameters. Again, only the low frequency flutter points are considered.

Theoretical curves, based on the first two vibration modes of a typical model, are also included in Figs. 3.5 through 3.8. The calculations are for zero structural damping in all modes and for frequency ratios $(\omega_1/\omega_2) = 0.470$ (for mode shapes A and B) and $(\omega_1/\omega_2) = 0.478$ (for mode shapes C-1 and C-2). They are taken from the lower boundaries in Figs. I.7 through I.12 and the boundary in Fig. I.16 of Appendix I.

* Refer to Table 2.1 for identification of symbols assigned to models for use in plotting flutter data.

CONFIDENTIAL

CONFIDENTIAL

Theoretically, the variation of the flutter index, $V_f/b_o \omega_2 \sqrt{\mu}$, with Mach number is not independent of μ , so that one cannot strictly draw a single theoretical curve of $V_f/b_o \omega_2 \sqrt{\mu}$ vs M, as is done in Figs. 3.5 and 3.6. Owing to the fact that the ambient density becomes progressively lower as M is raised, the mass ratio, μ , at flutter increased by a factor exceeding 8 at the supersonic and transonic ends of the speed range. Since this behavior seems unavoidable in such experiments, it is fortunate that a large amount of theoretical and experimental evidence exists that shows that the dependency of $V_f/b_o \omega_2 \sqrt{\mu}$ upon μ is very weak, particularly at supersonic speeds and for the range of μ 's considered here. This point is further illustrated by the closeness of the calculations shown in Figs. 3.5 and 3.6 for $\mu = 71.7$ and $\mu = 317$.

The analysis using mode shape sets A and B were conducted early in the program and preceded the initial flutter tests on Models 3, 4, 7, and 8. As pointed out in Appendix I, the first mode is the same for mode shape sets A and B. The second modes are different, but they both satisfy the mode line locations obtained from Model 1 vibration data, and variations between these two second modes are seemingly small (see Figs. I.4 and I.5). However, the theoretical flutter boundaries are quite separated, that of set A differing from that of set B by as much as 15 per cent.

The experimental flutter parameters $V_f/b_o \omega_2 \sqrt{\mu}$ and $V_f/b_o \omega_2$ for Models 3, 4, and 8 are bracketed by the two theoretical boundaries, obtained using mode shape sets A and B, each boundary giving better correlation at a different range on the M or μM scale; set A is better at the higher end ($M \geq 5$, $\mu M \geq 1200$) and set B is better for the middle range ($M \approx 3$, $\mu M \approx 800$). The experimental frequency ratios, ω_f/ω_2 , compare more favorably with calculations based on mode shape set B.

CONFIDENTIAL

CONFIDENTIAL

As the experimental vibration mode shape obtained from the mirror tests on Model 8 became available, two additional sets of calculations were performed (sets C-1 and C-2). In these calculations the nonuniformity of the mass distribution was accounted for approximately (see Appendix I, Section B). Additionally, in the analysis with set C-2, an attempt was made to estimate the influence of the blunt leading and trailing edges on flutter, by simply omitting the aerodynamic contributions from these regions. Although such an empirical correction is a rough approximation, particularly when the leading and trailing edges are not circular in planes parallel to the free stream, one would have expected that the experimental results for Model 8 would lie somewhere between the boundaries of C-1 and C-2. However, this is not the case.

The results for Model 7 are not consistent with those for the other models. This lack of consistency, especially between Models 7 and 8, is somewhat surprising. Models 7 and 8 were built to be identical; they differed slightly in mass and in frequencies, but displayed identical node-line patterns. The fact that the Model 7 tests were run at slightly lower stagnation temperatures cannot account for the difference in the level of the boundaries for Models 7 and 8. Because of the strong dependence of the flutter results on mode shapes as indicated by the theoretical calculations, the only plausible explanation that can be offered here is that Models 7 and 8 did have slightly different mode shapes and that this critically affected the flutter results.

A comparison can also be made as to how well theory predicts the trends of the various flutter parameters with respect to M and μM . Recalling that (1) the experimental flutter parameters $V_f/b\omega_2\sqrt{\mu}$, $V_f/b\omega_2$, and ω_f/ω_2 , which are based on ω_2 's measured at room temperature, would be lower than the true values for stagnation temperatures considerably above room temperature

CONFIDENTIAL

CONFIDENTIAL

and would be higher than the true values for stagnation temperatures at or below room temperature, (2) the high Mach number tests were conducted at stagnation temperatures well above room temperature, and (3) the lower Mach number tests were conducted at stagnation temperatures at or below room temperatures, the experimental results, corrected for this temperature effect, would be slightly lower at the lower Mach numbers and slightly higher at the higher Mach numbers. This would tend to increase the slope of the experimental data presented in Figs. 3.5 through 3.8. Therefore, the ability of the theory to correctly indicate the trends in $V_f/b_0\omega_2\sqrt{\mu}$ and $V_f/b_0\omega_2$ with M and μM is expected to be somewhat better than that indicated by Figs. 3.5 and 3.7.

As shown in Figs. 3.6 and 3.8, ω_f/ω_2 , based on the experimental results uncorrected for temperature effects, is essentially independent of M and μM , as predicted by theory. Correcting for temperature effects would lessen the agreement between theory and experiment. Since it is a matter of common experience that flutter frequency is predicted less accurately than the flutter speed, the correlation with regard to the trends in the flutter frequency ratio is considered adequate.

The only low Mach number point obtained at a model pressure differential of 2 psig was for Model 4 at a Mach number of 0.116. No calculations were carried out for this case.

At the lower Mach numbers and in the transonic tests at CAL, the 65-deg models could not be flown in a stable region at model pressure differentials of 2 psig, and higher pressure differentials (up to 10 psig) were required. The results for model pressure differentials equal or greater than 3 psig are plotted in Figs. 3.9 through 3.12. The results are for low frequency flutter only, and the supersonic values are predominantly from Model 7. The high pressure, high Mach number

CONFIDENTIAL

CONFIDENTIAL

tests were made to determine the effects of model pressure, which will be discussed later, and are included here as also being appropriate.

In general, the discussions presented in the preceding paragraphs apply to the results of Figs. 3.9 through 3.12, the correlation between theory and experiment being about the same as for the basic model configuration with model pressure differentials of 2 psig. It should be noted that the theoretical boundaries used in Figs. 3.9 through 3.12 are based on mode shape data obtained at a pressure differential of 2 psig. Again, because of the marked dependence of the theoretical results on mode shapes, no particular significance can be attached to the fact that the experimental results agree with calculations based on mode sets B and C-1, for the supersonic region, and with mode shape set A for the transonic region.

A sharp rise in the boundary of $V_f/b_0\omega_2\sqrt{\mu}$ vs M , at Mach numbers slightly above transonic, is evident from both theory and experiment. From the experimental data, the flutter index, $V_f/b_0\omega_2\sqrt{\mu}$ is essentially constant for subsonic speeds, with no dip in the transonic region.

The effect of model pressure differential on flutter of Model 7 is shown in Fig. 3.13. Increasing model pressure differential from 2 to 4 psig causes a slight decrease in the flutter index $V_f/b_0\omega_2\sqrt{\mu}$. Further increase in pressure to 6 psig results in a leveling off of the $V_f/b_0\omega_2\sqrt{\mu}$ curve for $M = 2.98$, and a sudden increase in the curve for $M = 4.99$. The same type of behavior is exhibited by the frequency ratio ω_f/ω_2 .

The $M = 2.50$ and 2.98 tests were all made at constant stagnation temperature (85 to 87 °F), so that correction for temperature effects, if any, would be uniform over the range of pressures. The $M = 4.99$ tests were conducted at higher stagnation temperatures (121 to 176 °F), with the higher temperatures

CONFIDENTIAL

CONFIDENTIAL

associated with the higher pressures. In this case, any correction for temperature effects would raise the $M = 4.99$ results (relative to the lower Mach number results) and accentuate the sudden increase for the pressure differentials of 5 and 6 psig.

As seen from Table 3.1, the vibration measurements made prior to the $M = 2.98$ tests showed that the frequencies increased, but the frequency ratio ω_1/ω_2 decreased, with increasing model pressure differential. Vibration measurements made prior to the $M = 4.99$ tests also showed increases in frequencies, but at a constant frequency ratio, as the pressure differential was varied from 2 to 6 psig. Theoretically, a slightly lower value for ω_1/ω_2 results in a small increase in $V_f/b_o \omega_2 \sqrt{\mu}$ and ω_f/ω_2 (see Fig. 1.15). For the present case, these effects are negligible.

Finally, mode-shape effects are known to be important, and probably account for the major portion of the variation of the flutter parameters with pressure differential. Since it is expected that mode-shape effects would be similar for supersonic Mach numbers, the different behavior at $M = 2.98$ and 4.99 cannot be explained on this basis.

The variations of $V_f/b_o \omega_2 \sqrt{\mu}$ and ω_f/ω_2 with the root angle of attack are presented in Fig. 3.14. Theoretical calculations for comparison purposes were not carried out, since many complicating factors must be considered in the analysis. The most important are (1) changes in vibration mode shapes and frequencies which are certain to occur when the model deforms under the steady aerodynamic loads at angle of attack, and (2) the variations in the local angles of attack due to the steady-state deformations and their effect on the unsteady aerodynamic loads. The typically large deformations experienced by the present models are shown in Fig. 3.15 for root angles of attack

CONFIDENTIAL

CONFIDENTIAL

up to 15 degrees, at $M = 5$.* Although models were flown at steady-state root angles of 15 degrees, no flutter data was sought beyond 12 degrees, because of the excessive deformations encountered at 12 degrees and dynamic pressures required for flutter.

For a typical section, Ref. 13 demonstrates that the effect of angle of attack on flutter is destabilizing according to third order piston theory. For a flat plate, the influence of angle of attack may be estimated by interpreting the $\sqrt{V_\infty}/h \omega_2$ vs μM results (for $\alpha = 0$) through the use of an effective μM according to

$$(\mu M)_{\text{eff.}}^{\alpha=0} = \frac{(\mu M)_{\text{actual}, \alpha \neq 0}}{1 + \frac{\gamma+1}{4} M^2 \alpha_o^2}$$

where α_o is the angle of attack of the flat plate and is assumed constant over the planform. A similar correction could be applied to the present models, if the model possessed a constant angle of attack in its steady deformed state. This is not the case, as is evident from Fig. 3.15. To include the effects of angle of attack, when the local angle varies over the planform, one must start from the basic pressure equation (Eq.(16), Ref. 13). This approach would require a priori knowledge of the deformed state which would have to be obtained by a static aeroelastic analysis or appropriate experiments. On the basis of the preceding discussion, it is not evident whether the effect of angle of attack would be stabilizing or destabilizing in the present case.

* The dynamic pressures, under which the photographs shown in Fig. 3.15 were taken, were about two orders of magnitude larger than those which would be experienced during an actual re-entry flight (Fig. 1.3). It is interesting to note the extremely large deflections which these models are capable of sustaining without collapse or subsequent change in structural characteristics.

CONFIDENTIAL

CONFIDENTIAL

The experimental results indicate that $V_f/b_2\omega_2\sqrt{\mu}$ remains constant for $M = 2.99$ and $p_2 = 4$ psig, and that it increases substantially with angle of attack for $M = 4.99$ and $p_2 = 2$ psig. It appears that the effect of increasing α is slightly stabilizing.

In addition to the 65-degree-sweep-delta models, a number of tests were conducted on five 75-degree models. Of these, Models 15, 16, and 17 were observed to flutter in the low-frequency mode. The corresponding experimental results are presented in Fig. 3.16. The tests were limited to Mach number 3, or below. No parallel calculations were made for these cases; throughout the low supersonic range to $M = 3$, the leading edges are subsonic and piston theory cannot be expected to yield accurate flutter predictions.

When compared with the corresponding curve for the 65-degree models, one notes that the rapid rise of the flutter boundary occurs at higher values of M for the 75-degree models. Also, for this low supersonic range, the level of $V/b_2\omega_2\sqrt{\mu}$ is slightly below that for the 65-degree models. This may be partially due to the higher frequency ratios obtained with the lower-aspect-ratio models ($\omega_1/\omega_2 = 0.546$ to 0.582); the effect of higher frequency ratios is destabilizing in the supersonic range (see Fig. I.15). In the transonic region, the results agree well with the data for the higher-aspect-ratio models.

A second type of flutter, involving modes higher than the first and second, which will be referred to as high-frequency flutter, was obtained with two of the 65- and 75-degree models; specifically, Models 9, 10, 18, and 20. For the high-frequency flutter, it was very difficult to determine the flutter boundary. Some motion persisted throughout all of the tests, as could be seen from the response of the strain gages mounted on the models. Since the strain gages could not be used to determine the boundary,

CONFIDENTIAL

CONFIDENTIAL

recourse was made to visually observing the model and determining the tunnel conditions for which some motion was just discernible. All of the high-frequency flutter data given in Table 3.1 and presented in Fig. 3.17 was determined in this way. The results for Model 9 are typical of the behavior of the models which fluttered in the high-frequency mode, and the following discussion will be mainly restricted to this particular model.

Referring to the Model 9 flutter data given in Table 3.1 for $p_d = 2$ psig, $M = 4.98$, and $\omega_3/\omega_2 = 1.11$, the experimental value of the flutter parameter $V_f/b_0\omega_2$ is 7.21. This compares well with the theoretical prediction of 7.50, based on the results presented in Fig. 1.17 for $(\omega_3/\omega_2)^2 = 1.27$ (or $\omega_3/\omega_2 = 1.13$) and at the experimental value for μM of 1115. This value of $V_f/b_0\omega_2$ is considerably lower than that for low-frequency flutter. It is a well-recognized fact, that the closeness in frequency of two natural modes greatly influences the location of the flutter boundary, and the most critical flutter boundary is most often the one based on those modes which are the closest. Such is the case here for modes 2 and 3, when $p_d = 2$ psig. As the pressure differential is increased to 4 psig, the flutter frequency is very near that for the fifth mode, indicating strong coupling of the fifth mode with either a close fourth or a close sixth mode.

Referring to Fig. 3.17, it is seen that raising the pressure from 2 to 4 psig at $M = 4.98$ results in a large increase in the critical value of $V_f/b_0\omega_2\sqrt{\mu}$, mainly as a consequence of the spreading apart of the frequencies of modes 2 and 3 (see Table 3.2, Model 9; Test No. 3). For $M = 3$ and $p_d = 5$ psig, the value of the critical $V_f/b_0\omega_2\sqrt{\mu}$ is somewhat below the flutter results based on low-frequency flutter. A rise in p_d to 8.10 psig is accompanied by a significant rise in $V_f/b_0\omega_2\sqrt{\mu}$; in fact, the value of $V_f/b_0\omega_2\sqrt{\mu}$ is in excellent agreement with

CONFIDENTIAL

CONFIDENTIAL

the low-frequency flutter results for the other 65-degree models. For these two tests (and also the Model 9 test at $M = 2.48$), the recorder monitoring the strain-gage outputs was run at too low a paper speed, and the frequencies could not be counted from the record. What is certain, however, is that the flutter frequencies are above 200 cps, and that the flutter frequency for $p_2 = 8.10$ psig is higher than that for $p_2 = 5.13$ psig. This indicates that modes substantially higher than the fifth mode are involved. For the $M = 2.48$, $p_2 = 8.42$ psig case, the strain-gage records were not at all clear. Bursts of low-frequency oscillations are evident, but are not clean enough for the frequency to be counted. Apparently, at this pressure the model may be close to flutter in the low-frequency mode, and further increases in p_2 may have resulted in a low-frequency-type flutter.

The amplitude of the high-frequency flutter was too low for the mode shape to be determined from the high-speed movies. From visual observations, the flutter mode had two node points on the leading edge. The first was approximately midway on the leading edge, and the second was about 1 1/2 to 2 inches up from the trailing edge. The high-frequency flutter invariably commenced with a pure tip motion, the node line extending back from the second node point on the leading edge at an angle of 45 degrees with respect to the streamwise direction. It was the motion of these few square inches of model tip which was observed while visually determining the onset or termination of flutter.

The results for Models 17 and 18 are interesting in that the models were built to be identical, yet Model 17 fluttered in the low frequency mode while Model 18 fluttered in the high frequency mode. Table 2.3 reveals significant differences in the vibration results for the higher modes. It would have been quite informative if Model 18 could have been tested at the high pressures that Model 17 was tested at, to determine if the flutter mode would indeed have changed from a high-frequency to a low-

CONFIDENTIAL

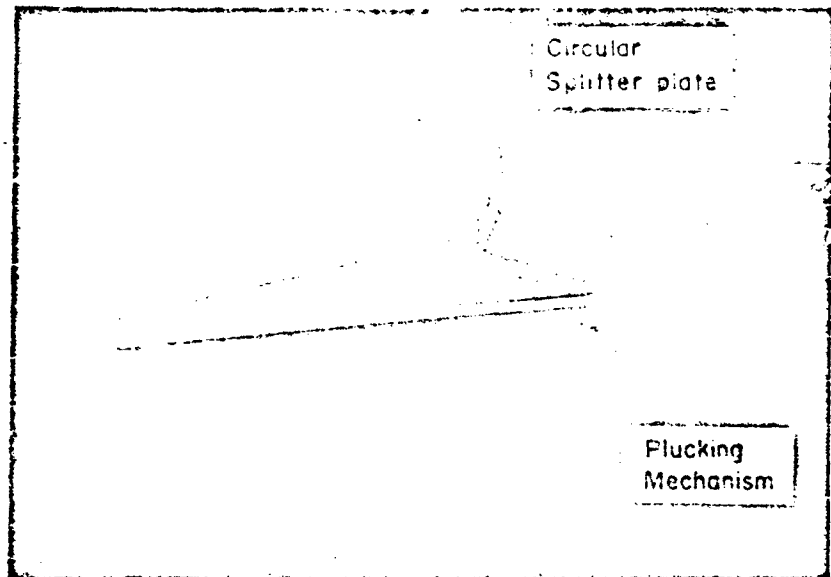
CONFIDENTIAL

frequency one, as postulated earlier. Unfortunately, Model 18 was destroyed while testing at the lower \dot{p}_d 's.

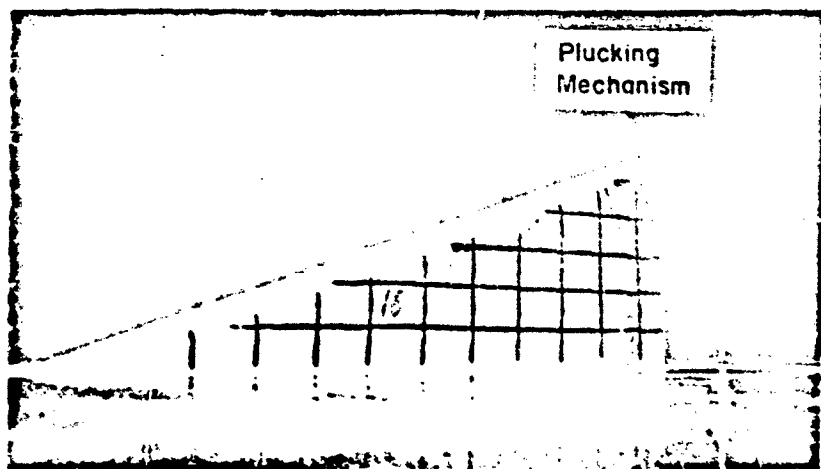
As a final presentation, all of the low-frequency flutter data have been combined and the results for various classifications are presented, in terms of $V_f/b_2\omega_2\sqrt{\mu}$ vs M, in Fig. 3.18. In lieu of plotting the individual points, the data are presented as bands encompassing the experimental points pertinent to one of the particular classifications shown in the figure. It is noted here once again that no corrections have been introduced in Fig. 3.18 to account for apparent-mass and thermal effects.

From the figure, it is evident that the experimental results are quite consistent, considering the variations encountered between some of the models. All of the supersonic results (for $M \geq 2.5$) lie in a band of ± 8 per cent about a median experimental line. The region from $M = 1.2$ to 2.5 is not too well covered, but the trend for the 65-degree models is reasonably well defined. It is also clear that the 75-degree boundary lies below that for the 65-degree models over the Mach number range from, say, 1.2 to 3.0.

CONFIDENTIAL

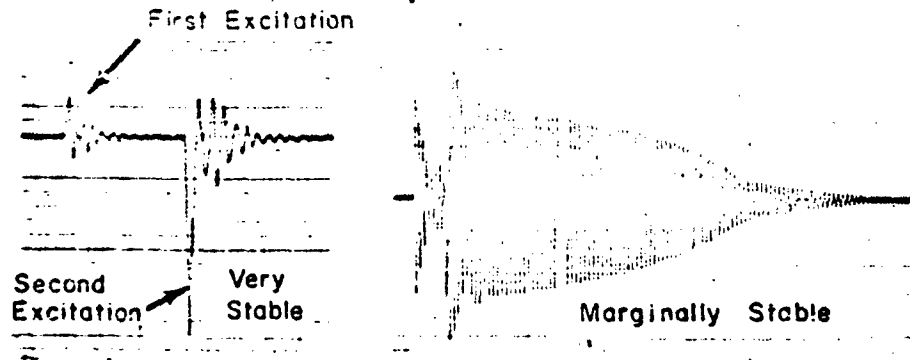


Supersonic Installation

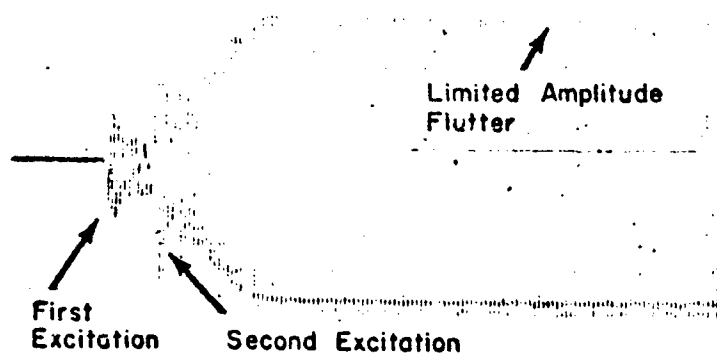


Transonic Installation

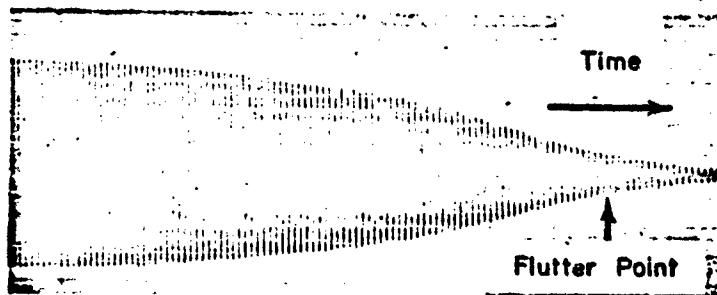
Figure 3.1 Views of Models Mounted in Wind Tunnels.



(a) Plucked Response in Stable Region

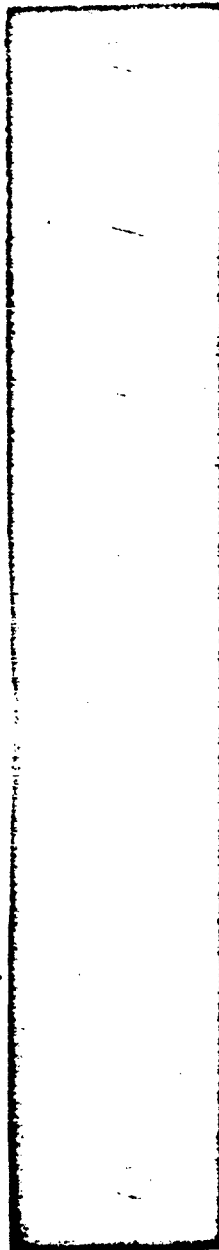


(b) Plucked Response in Unstable Region

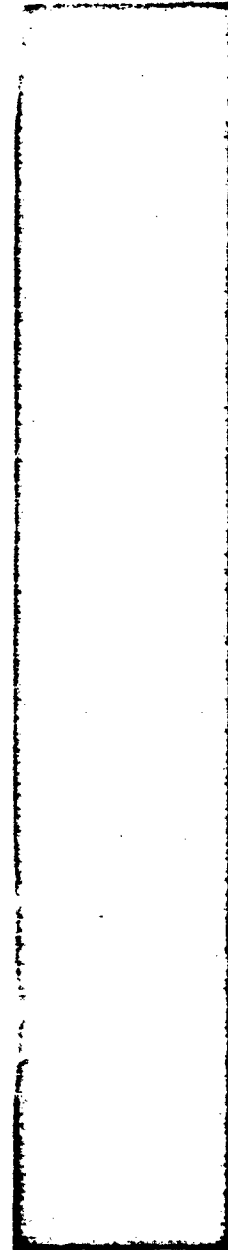


(c) Limited Amplitude Flutter and Flutter Stop

Figure 3.2 Typical Strain-Gage Responses.



(a) During Flutter



(b) After Losing Pressure

Figure 3.3 High-Speed Movie Samples.

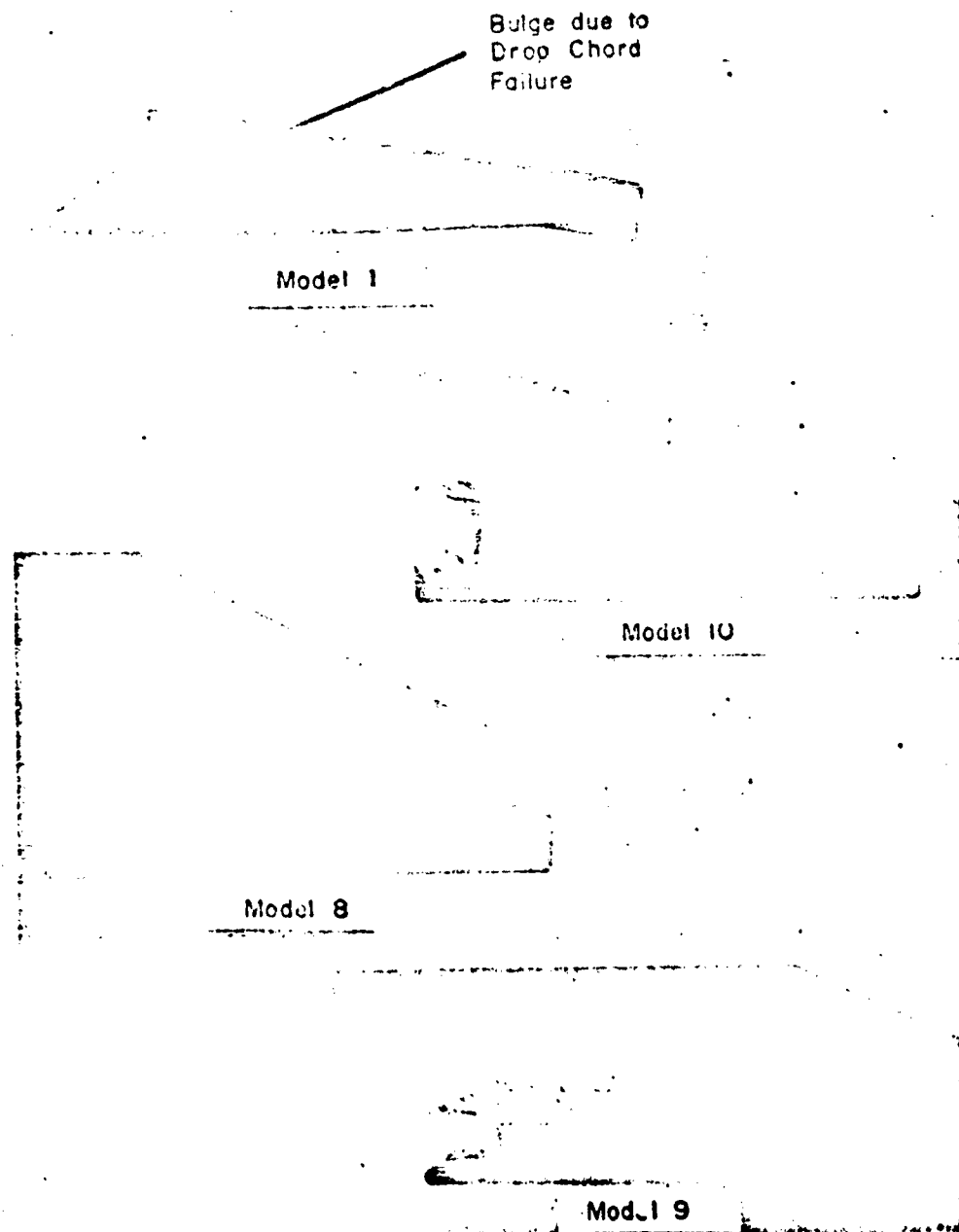


Figure 3.4 Photographs of Typical Flutter Models after Destruction During Flutter.

CONFIDENTIAL

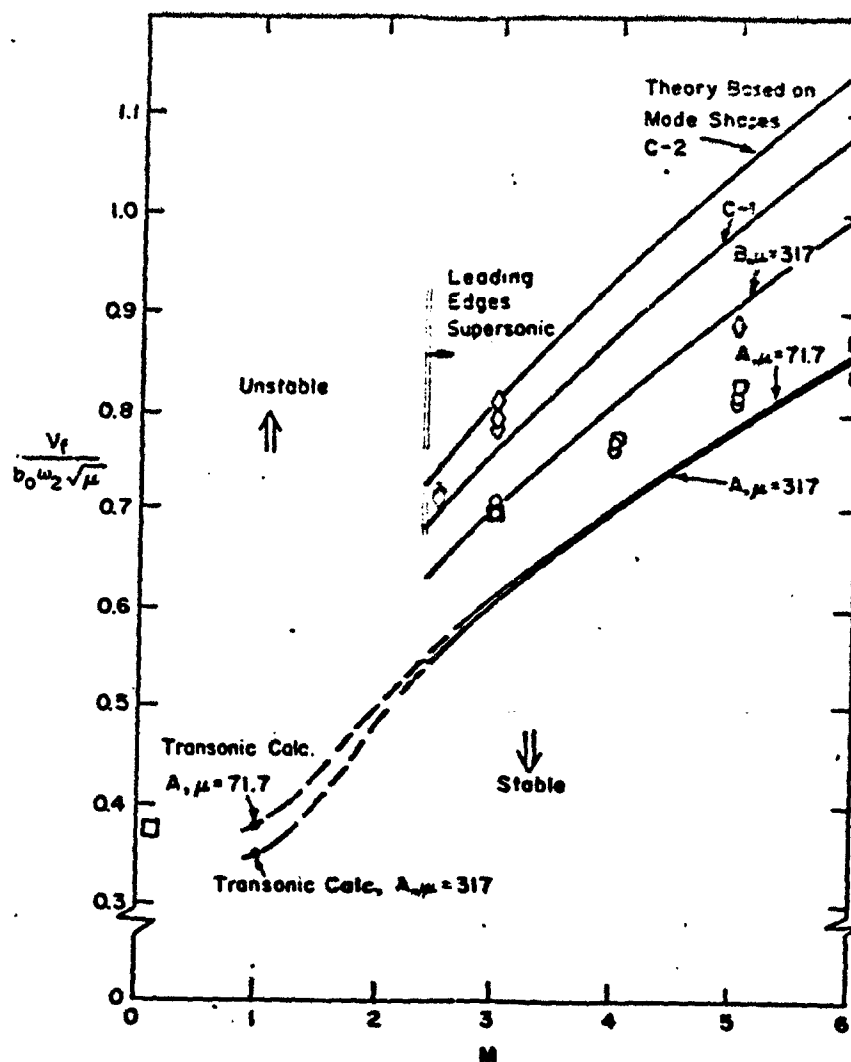


Figure 3.5 Experimental Flutter Index ($V_F/b_0 \omega_2 \sqrt{\mu}$) vs M , and Comparison with Theory, for 65-deg Delta-Wing Models at a Model Pressure Differential of $p_d = 2$ psig and $\alpha = 0$ deg.

CONFIDENTIAL

CONFIDENTIAL

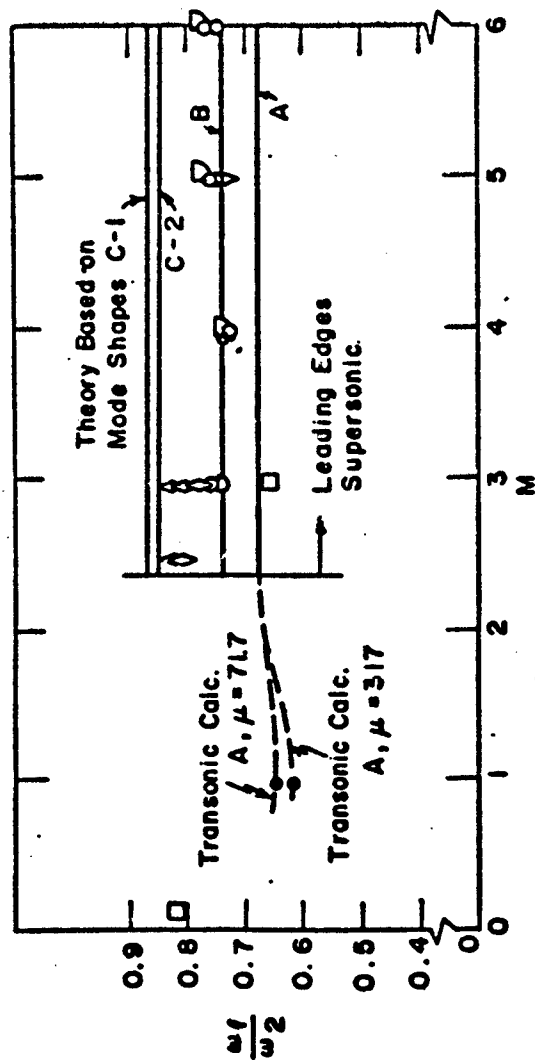


Figure 3.6 Experimental Flutter Frequency Parameter (w_1/w_2) vs M , and Comparison with Theory, for 65-deg Delta-Wing Models at a Model Pressure Differential of $P_d = 2$ psig and $\alpha = 0$ deg.

CONFIDENTIAL

CONFIDENTIAL

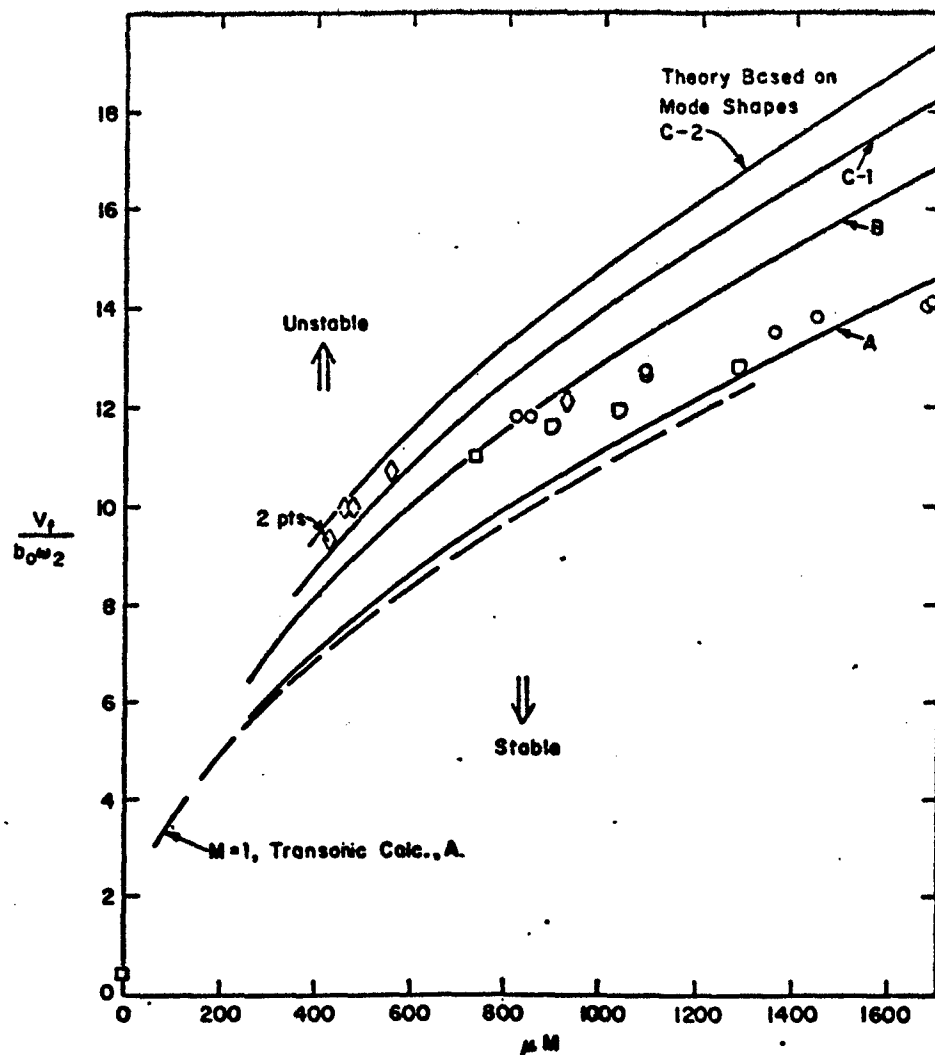


Figure 3.7 Experimental Flutter Parameter ($V_f/b_0 \omega_2$) vs μM , and Comparison with Theory, for 65-deg Delta-Wing Models at a Model Pressure Differential of $p_d = 2$ psig and $\alpha = 0$ deg.

CONFIDENTIAL

CONFIDENTIAL

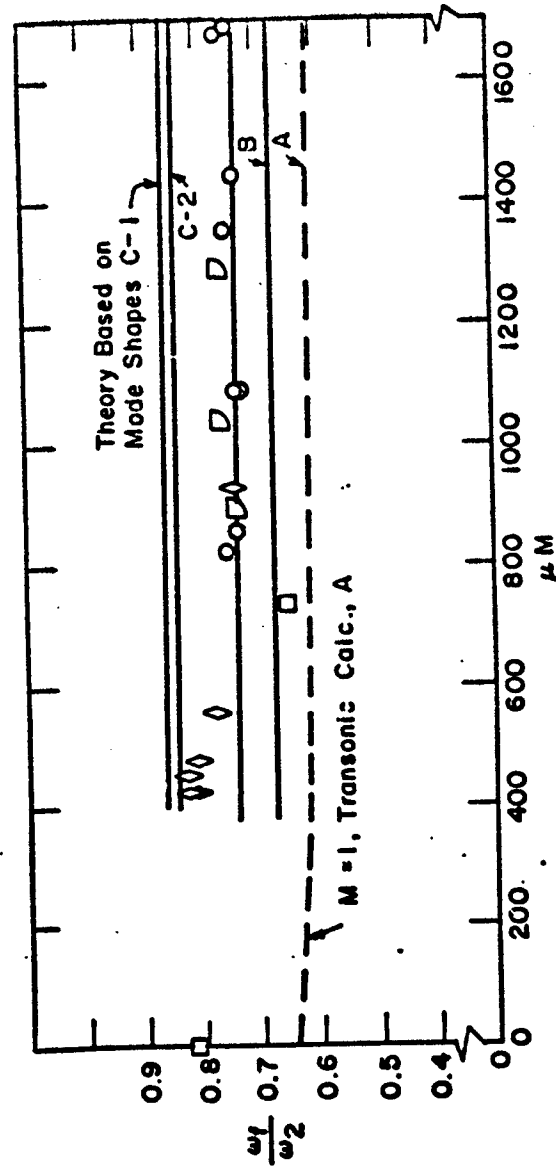


Figure 3.8 Experimental Flutter Frequency Parameter (ω_f/ω_2) vs μM , and Comparison with Theory, for 65-deg Delta-Wing Models at a Model Pressure Differential of $P_d = 2$ psig and $\alpha = 0$ deg.

CONFIDENTIAL

CONFIDENTIAL

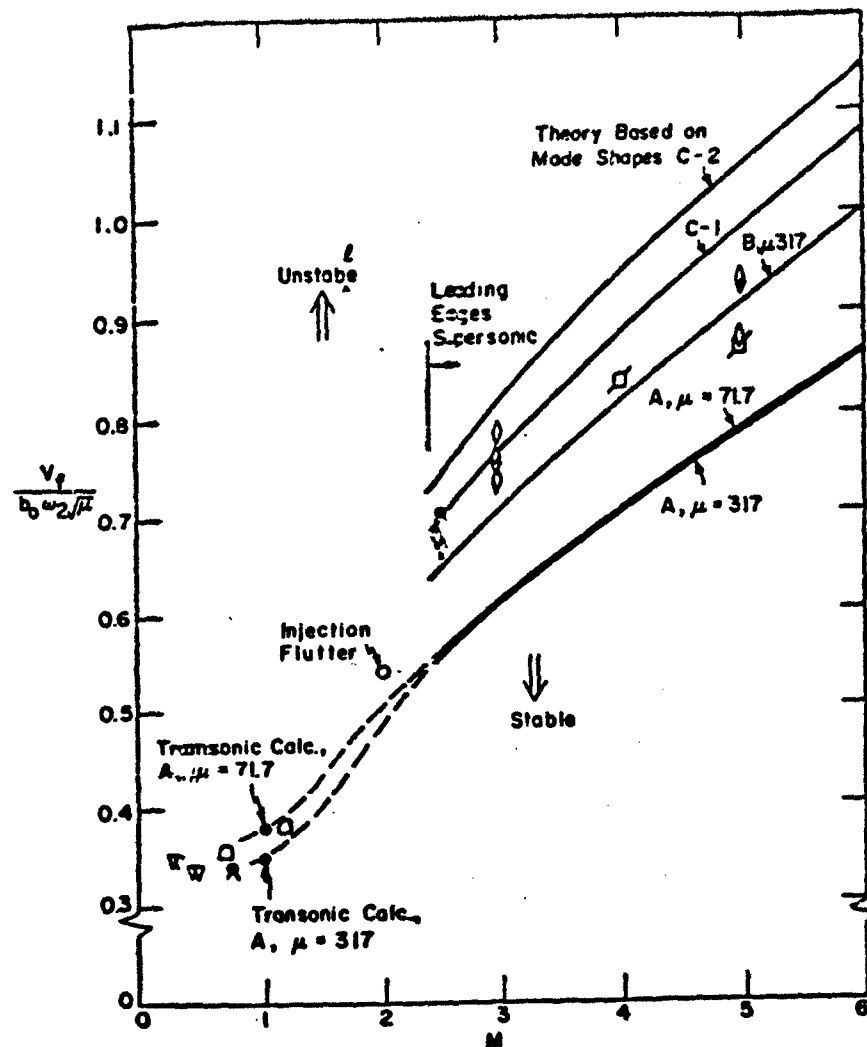


Figure 3.9 Experimental Flutter Index ($V_f/b_0 \omega_2 \sqrt{\mu}$) vs M , and Comparison with Theory, for 65-deg Delta-Wing Models at Model Pressure Differentials of $p_d \geq 3$ psig and $\alpha = 0$ deg.

CONFIDENTIAL

CONFIDENTIAL

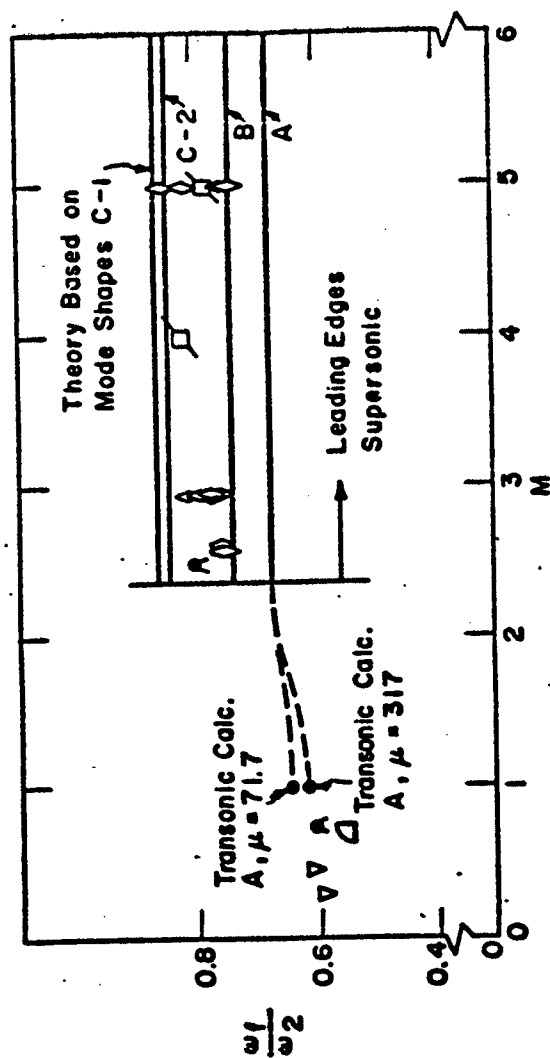


Figure 3.10 Experimental Flutter Frequency Parameter (ω_1/ω_2) vs M , and Comparison with Theory, for 65-deg Delta-Wing Models at Model Pressure Differentials of $P_d \geq 3$ psig and $\alpha = 0$ deg.

CONFIDENTIAL

CONFIDENTIAL

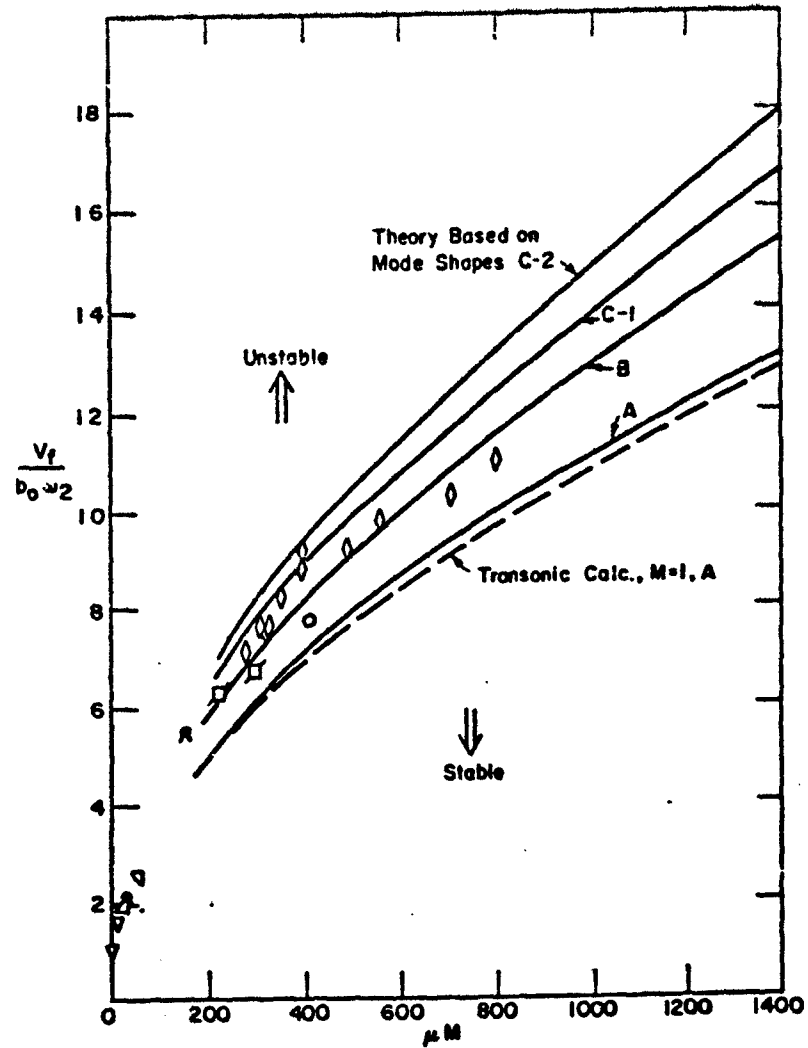


Figure 3.11 Experimental Flutter Parameter ($V_f/b_0 \omega_2$) vs μM , and Comparison with Theory, for 65-deg Delta-Wing Models at Model Pressure Differentials of $p_d \geq 3$ psig and $\alpha = 0$ deg.

CONFIDENTIAL

CONFIDENTIAL

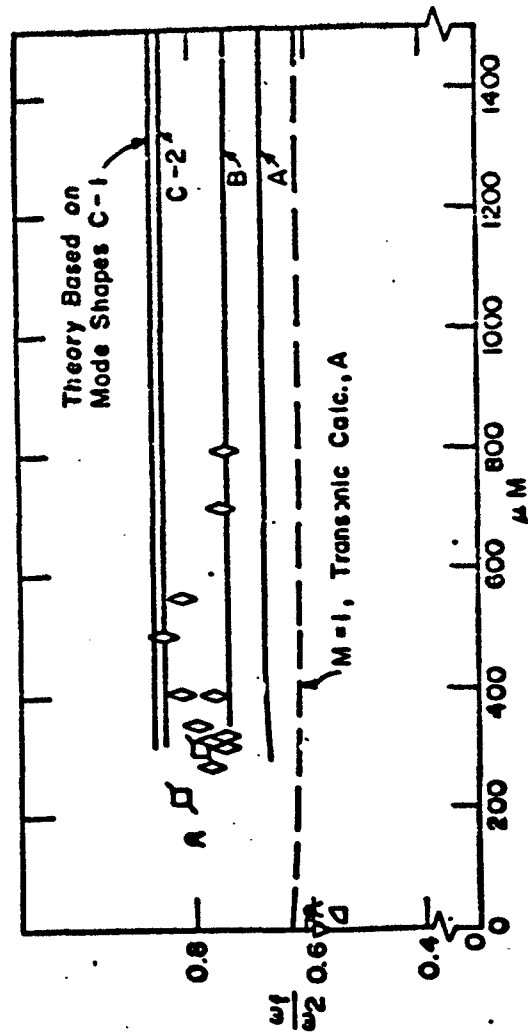


Figure 3.12 Experimental Flutter Frequency Parameter (w_1/w_2) vs M , and Comparison with Theory, for 65-deg Delta-Wing Models at Model Pressure Differentials of $p_d \geq 3$ psig and $\alpha = 0$ deg.

CONFIDENTIAL

CONFIDENTIAL

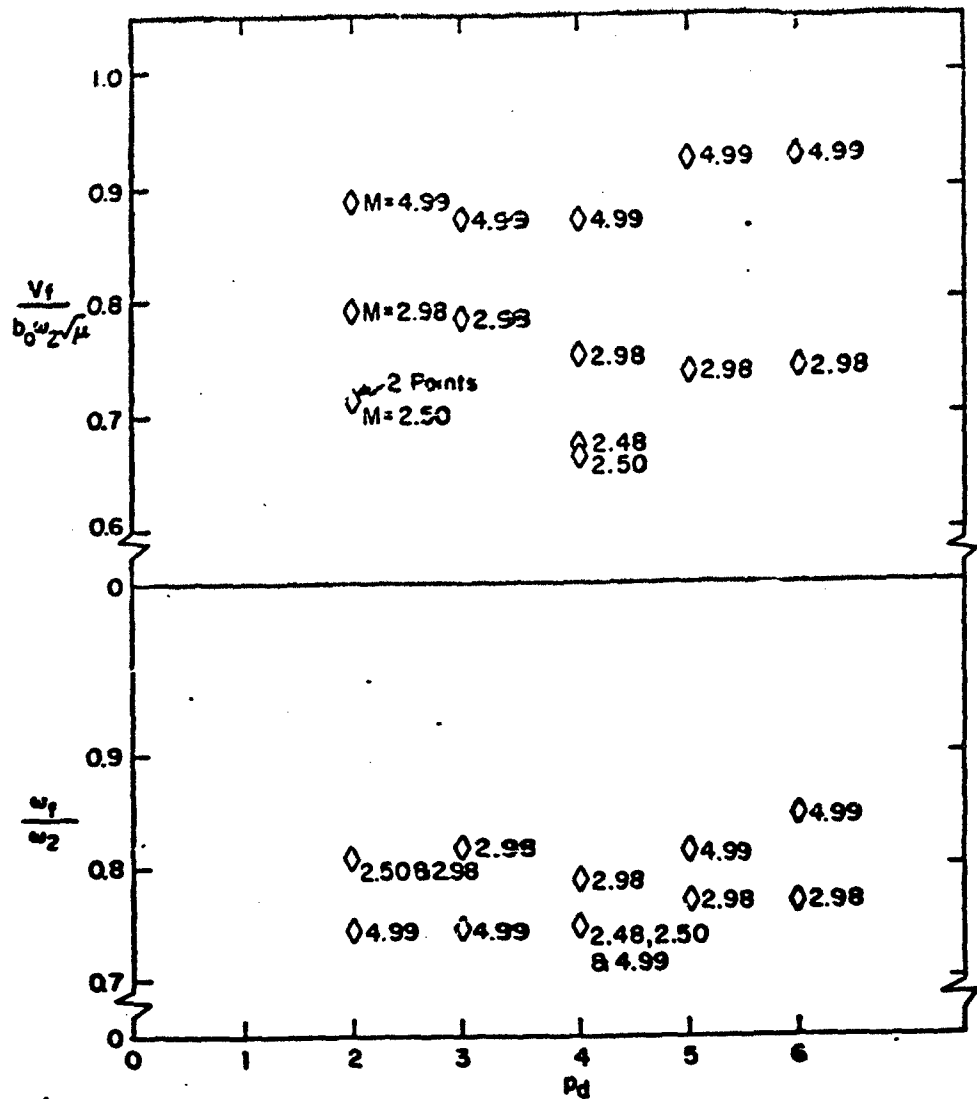


Figure 3.13 Experimental Flutter Index ($V_f / b_0 \omega_2 \sqrt{\mu}$) and Flutter Frequency Parameter (ω_f / ω_2) vs Model Pressure Differential (p_d) at $\alpha = 0$ deg. (All Data for Model 7.)

CONFIDENTIAL

CONFIDENTIAL

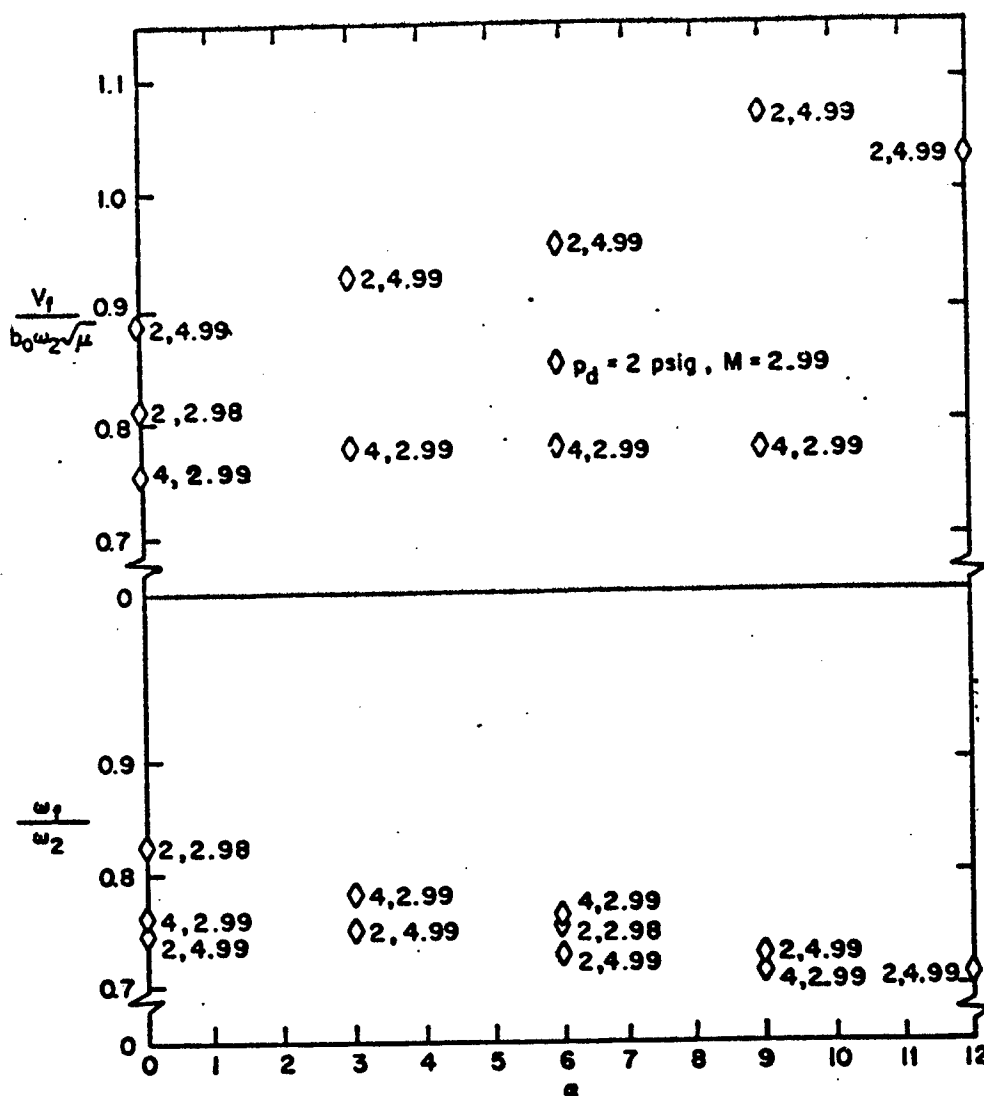


Figure 3.14 Experimental Flutter Index ($V_f / (b_0 \omega_2 \sqrt{\mu})$) and Flutter Frequency Parameter (ω_f / ω_2) vs Angle of Attack (α). (All Data for Model 7.)

CONFIDENTIAL.

CONFIDENTIAL
(THIS PAGE IS UNCLASSIFIED)

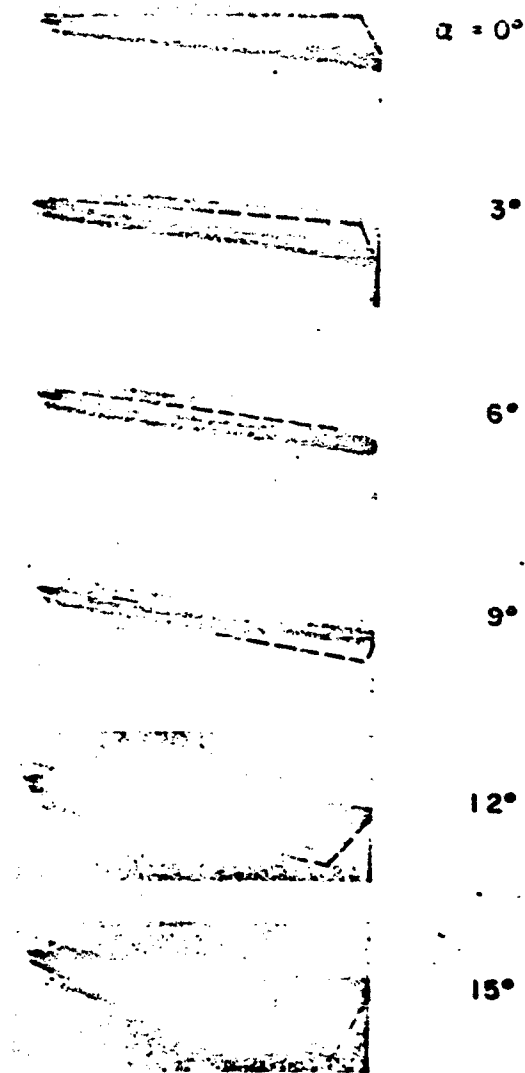


Figure 3.15 Photographs Showing Steady-State Deflections of Model 8 at Several Angles of Attack for $M = 5$. Portions of Root and Trailing Edges are indicated by Dotted Lines.

CONFIDENTIAL
(THIS PAGE IS UNCLASSIFIED)

CONFIDENTIAL

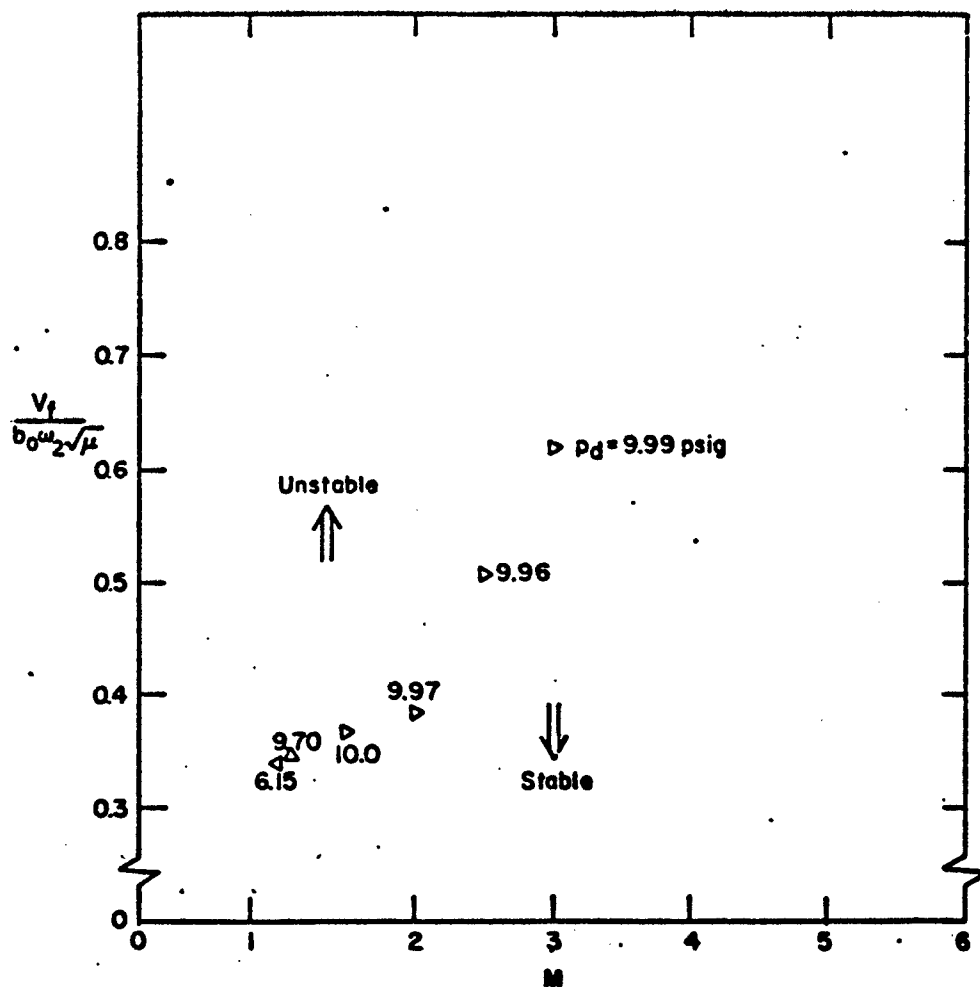


Figure 3.16 Experimental Flutter Index ($V_f/b_0 \omega_2 \sqrt{\mu}$) vs M for 75-deg Delta-Wing Models, at $\alpha = 0$. Low-Frequency Flutter.

CONFIDENTIAL

CONFIDENTIAL

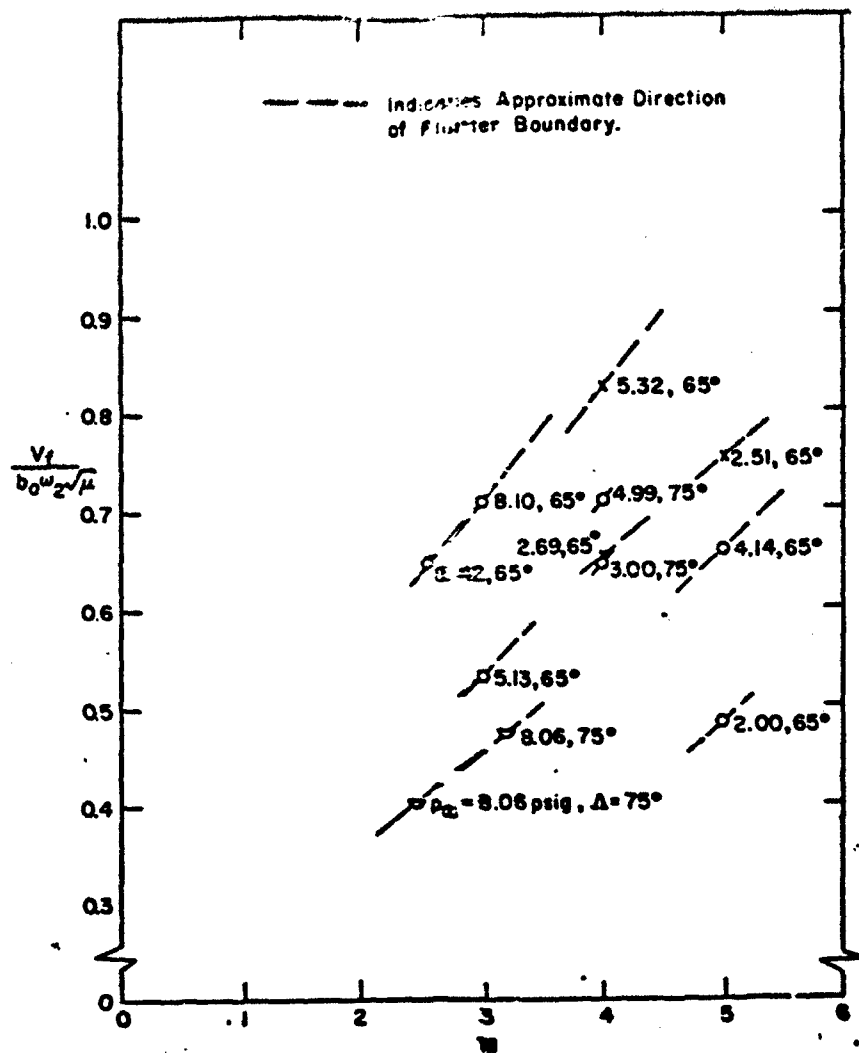


Figure 3.17 Experimental Flutter Index ($V_f/b_0 \omega_2 \sqrt{\mu}$) vs M for 65- and 75-deg Delta-Wing Models at $\alpha = 0$ deg. High-Frequency Flutter.

CONFIDENTIAL

CONFIDENTIAL

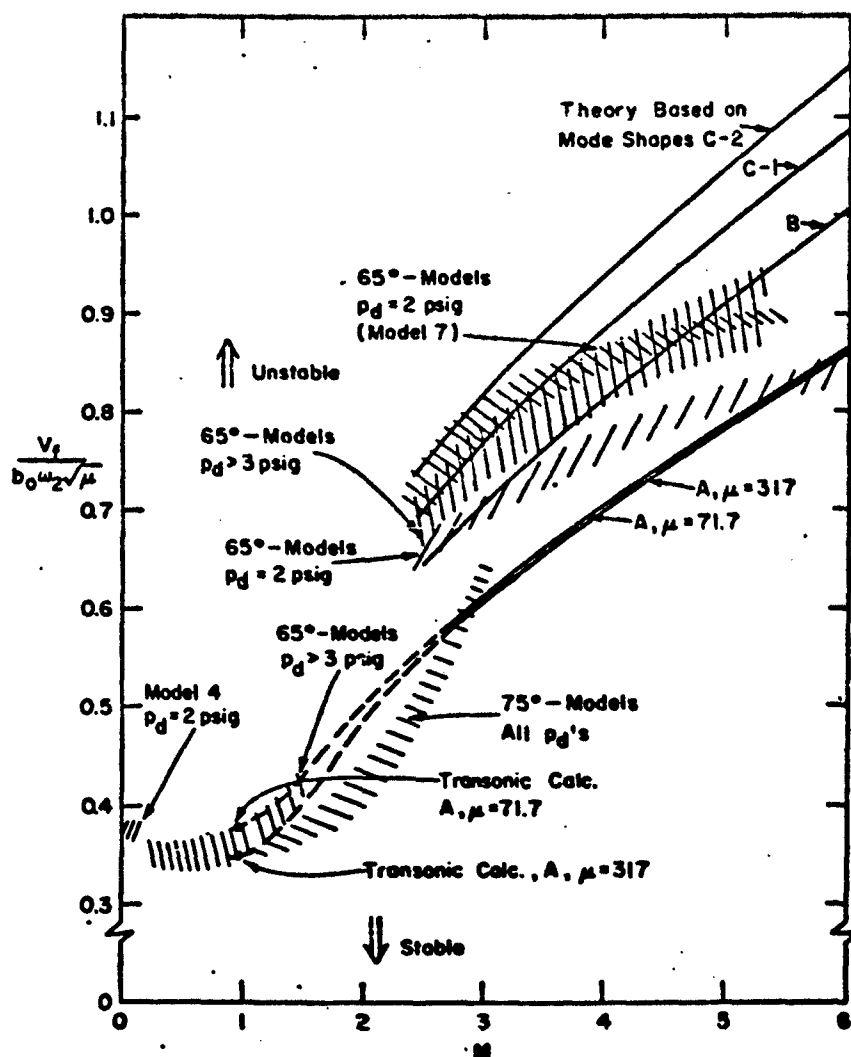


Figure 3.18 Experimental Boundaries ($V_f/b_0\omega_2\sqrt{\mu}$) vs M , and Comparison with Theory for all Low-Frequency Flutter. All Theory Based on 65-deg Model Data at $p_d = 2$ psig.

CONFIDENTIAL

CONFIDENTIAL

TABLE 3.1 EXPERIMENTAL FLUTTER DATA

Flutter Point	Model No.	M	f_p (Hz)	α (deg)	ω_1 (rad/sec)	ω_2	ω_3	$\rho \cdot 10^3$ (g/cm ²)	τ_0 (°)	μ	$\frac{\omega_3}{\omega_2}$	$\frac{V}{b \cdot \omega_2}$	$\frac{V}{b \cdot \omega_3}$	Remarks
1	1	3.00	-	0	-	-	-	0.945	125	116	-	-	-	Model pressure uncertain at flutter
2	3	2.00	4.0	0	108	226	377	0.551	100	205	-	7.71	0.539	Injection flutter; tunnel parameters estimated; no flutter frequency
3	3	2.99	1.96	0	94.2	180	303	0.396	125	235	0.739	11.8	0.700	Repeat of flutter point 3
4	3	2.99	1.98	0	94.2	180	303	0.411	115	275	0.756	11.8	0.710	Repeat of flutter point 3
5	3	3.99	2.02	0	94.2	180	303	0.413	101	273	0.729	12.6	0.763	Repeat of flutter point 3
6	3	3.99	1.96	0	94.2	180	303	0.414	111	273	0.735	12.7	0.770	Repeat of flutter point 3
7	3	3.00	2.00	0	94.2	180	303	0.416	125	271	0.755	13.5	0.817	Repeat of flutter point 3
8	3	3.00	2.00	0	94.2	180	303	0.391	132	239	0.741	13.8	0.810	Strain gages inoperative; flutter frequency obtained from film
9	3	3.98	1.99	0	93.8	182	305	0.403	154	230	0.765	14.0	0.837	Repeat of flutter point 3
10	3	3.98	2.02	0	93.8	182	305	0.401	165	252	0.747	14.1	0.862	Repeat of flutter point 3
11	4	0.116	2.00	0	84.2	186	310	0.238	94	3.67	0.817	0.719	0.375	Low-speed test; Wright Brothers Wind Tunnel, A.I.T.
12	4	2.99	2.15	0	94.2	191	311	0.355	114	247	0.658	11.6	0.701	Frequency and data based on $f_p = 2.0$ pcig
13	7	2.49	4.00	0	117	231	403	0.674	86	136	0.730	7.57	0.674	Repeat of flutter point 14
14	7	2.50	4.01	0	117	231	402	0.652	86	130	0.750	7.60	0.615	Flutter obtained by changing f_p at constant tunnel conditions
15	7	2.50	2.07	0	98.7	204	327	0.497	86	171	0.809	9.35	0.715	Repeat of flutter point 15
16	7	2.50	2.05	0	98.7	204	327	0.498	87	171	0.818	9.36	0.716	Repeat of flutter point 15
17	7	2.98	1.96	0	98.7	204	327	0.533	87	159	0.809	10.0	0.794	Repeat of flutter point 15
18	7	2.98	3.02	0	109	226	368	0.638	86	133	0.817	9.06	0.784	Repeat of flutter point 15
19	7	2.98	4.01	0	117	231	402	0.726	86	117	0.790	8.15	0.753	Repeat of flutter point 15
20	7	2.98	6.99	0	123	270	427	0.810	86	105	0.772	7.56	0.737	Repeat of flutter point 15
21	7	2.98	6.00	0	126	288	451	0.924	85	91.9	0.770	7.11	0.741	Repeat of flutter point 15
22	7	2.98	2.00	0	98.7	204	327	0.560	87	152	0.822	10.0	0.813	Repeat of flutter point 15
23	7	2.98	2.01	0	98.7	204	327	0.613	86	139	0.751	10.0	0.852	Repeat of flutter point 15

CONFIDENTIAL

CONFIDENTIAL

TABLE 3.1 CONTINUED

Flutter Point	Model No.	m	A ($\frac{1}{2}$)	α (deg)	ω ($\frac{rad}{sec}$)	ω_n	ζ	$\beta \cdot 10^3$ ($\frac{1}{sec}$)	T_0 (μsec)	μ	$\frac{\omega}{\omega_n}$	$\frac{V}{b\omega_n}$	$\frac{V}{b\omega_n}$	Remarks
24	7	2.99	2.00	0	94.3	199	314	0.437	127	186	0.776	10.7	0.786	Report of flutter points 17, 22
25	7	2.99	4.00	0	113	241	387	0.645	126	131	0.761	8.82	0.755	
26	7	2.99	4.01	3	113	241	387	0.645	123	125	0.793	8.80	0.778	
27	7	2.99	4.02	6	113	241	387	0.648	120	127	0.762	8.78	0.778	
28	7	2.99	4.01	9	113	241	387	0.649	117	127	0.712	8.76	0.776	
29	7	2.99	1.99	0	94.3	199	314	0.458	121	186	0.765	12.1	0.889	
30	7	2.99	3.01	0	104	222	354	0.530	143	160	0.746	11.0	0.871	
31	7	2.99	4.01	0	113	241	387	0.601	160	141	0.749	10.3	0.870	
32	7	2.99	4.99	0	121	258	420	0.760	174	112	0.815	9.78	0.923	
33	7	2.99	6.00	0	128	273	449	0.865	176	98.3	0.846	9.18	0.926	
34	7	2.99	1.99	3	94.3	199	314	0.465	163	183	0.751	12.5	0.928	
35	7	2.99	1.99	6	94.3	199	314	0.496	161	171	0.726	12.5	0.956	
36	7	2.99	2.02	9	94.3	199	314	0.621	161	137	0.726	12.5	1.070	
37	7	2.99	2.02	12	94.3	199	314	0.576	160	147	0.707	12.5	1.030	
38	8	3.99	1.98	0	99.0	202	320	0.398	143	224	0.739	11.6	0.776	
39	8	3.00	2.05	0	99.0	202	320	0.430	120	207	0.761	11.9	0.828	
40	8	5.98	1.97	0	99.0	202	320	0.415	178	215	0.764	12.8	0.874	
41	9	2.48	8.42	0	220	478	635	2.73	66	37.7	-	3.98	0.648	
42	9	2.99	5.13	0	198	418	523	1.20	88	85.6	-	4.36	0.532	
43	9	2.99	8.10	0	217	471	607	2.72	87	38.0	-	4.92	0.708	
44	9	4.98	2.00	0	165	330	366	0.460	104	224	1.11	7.21	0.482	
45	9	4.98	4.14	0	186	400	460	1.13	144	90.8	1.74	6.28	0.659	
46	10	2.48	8.06	0	370	675	981	2.50	55	48.5	2.98	3.81	0.404	
47	10	2.99	8.04	0	370	675	981	2.95	85	40.8	3.07	3.03	0.474	
48	11	2.79	10.1	0	142	325	317	12.9	70	8.81	0.590	1.03	0.347	
49	11	0.44	10.1	0	162	325	317	3.37	44	21.1	0.609	1.55	0.337	
50	12	0.74	9.64	0	156	356	342	2.42	60	42.6	0.602	1.16	0.340	
51	12	2.50	9.96	0	137	347	343	1.69	80	40.9	0.601	3.48	0.702	

CONFIDENTIAL

CONFIDENTIAL

TABLE 3.1 CONCLUDED

Flutter Point	Model No.	M	P_0 ($\frac{1}{16}$)	α (deg)	ω ($\frac{rad}{sec}$)	ω_k	ω ($\frac{1}{16}$)	μ	$\frac{\omega_k}{\omega}$	$\frac{V_c}{k\omega}$	$\frac{V_c}{k\omega\sqrt{\mu}}$	Remarks
52	13	1.20	10.2	0	225	481				2.56	0.380	Flutter boundary observed visually. No flutter frequency. Gages out.
53	13-1	0.71	10.0	0	171	384				1.99	0.352	
54	14	4.00	9.98	0	159	354				6.26	0.834	
55	14	3.00	10.0	0	159	354				6.72	0.862	
56	15	1.10	9.70	0	347	626				1.84	0.345	Test stable point before model fluttered. Flutter frequency erratic.
57	16	0.99	6.15	0	295	540				2.00	0.340	Flutter boundary observed visually. No flutter frequency. Gages out.
58	17	1.50	10.0	0	324	558				2.52	0.367	Conditions at flutter are approximate except for flutter frequency which is taken from magnetic tape.
59	17	2.00	9.97	0	324	558				3.04	0.385	Persistent, burst-type motion continued under conditions corresponding to lower $\frac{V_c}{k\omega}$.
60	17	2.50	9.96	0	324	558				3.59	0.506	
61	17	3.00	9.99	0	324	558				3.67	0.620	
62	18	4.00	3.00	0	210	361				6.16	0.645	Flutter points 62-66 are based on visual observation of flutter motion. Some non-observable motion still present, as evidenced by attain-gage response
63	18	4.00	4.99	0	248	423				2.52	0.710	
64	20	4.00	2.69	0	116	245				9.03	0.651	
65	20	4.00	3.32	0	141	310				7.19	0.826	
66	20	5.00	2.51	0	114	241				9.75	0.732	

CONFIDENTIAL

CONFIDENTIAL

SECTION 4

CONCLUSIONS AND RECOMMENDATIONS

The main conclusions and recommendations that may be drawn from the experimental and theoretical results of this study are summarized below.

The model construction technique presented here is simple and yields relatively inexpensive models. It is particularly applicable when only a few models are desired and/or when different surface materials are to be used in the individual models.

In general, it is difficult to build duplicate models. Factors which should be given very careful attention are: (1) the orientation of the warp and fill directions of the surface material, for both single and multiple layer models, (2) the type of seams used along the leading and trailing edges, and (3) the number and thickness of the elastomer coatings.

The latex-coated nylon and dacron cloth used as the cover material have been found to be sensitive to both temperature and humidity. Their properties also vary slightly with age. Since the thermal state of a flutter model cannot be predicted accurately and thus compensated for, the variations of model structural behavior with temperature are undesirable from the standpoint of flutter testing to evaluate analytical techniques. Less temperature-sensitive cover materials should be considered for future flutter models of this type.

The procedures used for static and dynamic testing of inflatable models are similar to those used in programs employing more conventional-type models. With the exception of the materials tests and the mirror mode shape tests, no new or special techniques appear to be required.

In vibrating the model with the audio system, care must be

CONFIDENTIAL

CONFIDENTIAL

exercised to not overexcite the models and to properly position the speaker so as to detect all the weak modes.

Due to the lightness of the present models, the apparent mass effect in free-air vibrations is noticeable, amounting to a few per cent for the first mode and decreasing in importance for the higher modes. The effect may be easily estimated and accounted for whenever desirable.

With more effort, the mirror tests can be made to yield mode shapes which will be sufficiently accurate for use in flutter calculations. The particular advantage of mirror mode shapes is that the streamwise slopes, which enter into the calculation of the generalized aerodynamic forces, are obtained directly from the measurements, while the deflections, which are also needed, are obtained by integration.

The measurement of influence coefficients poses no special problem. From influence coefficients, one may calculate the mode shape amplitudes at specified points, and then determine the streamwise slopes by differentiation. For cases where the theoretical results appear particularly sensitive to the choice of assumed modes, a more laborious, but a more accurate approach is recommended. This approach would utilize the streamwise slopes from the mirror mode shape tests and the modal amplitudes from the calculations based on the measured influence coefficients to determine the generalized mass and aerodynamic forces.

Any theoretical calculations used to predict the static or dynamic behavior of inflatable delta-wing models of the type presented here should allow for both shear- and bending-type deformations. The effect of any heavy or stiff seams along the leading and trailing edges should also be accounted for.

The stiffness properties of the model surface material must be accurately determined before the effects of bending-type deformations can be included in vibration or other aeroelastic

CONFIDENTIAL

CONFIDENTIAL

calculations. Dynamic testing methods applied to cylindrical test specimens appear to offer an alternate and better approach than the static methods now being used to determine the extensional and shear moduli.

The predicted flutter speed boundaries are in fair agreement with the experimental results. Various calculated boundaries, based on different sets of assumed modes, give better correlation over different Mach-number ranges; furthermore, they exhibit sufficiently different levels, so as to suggest significant influences from the mode shapes. A quantitative statement as to how well the analysis predicts flutter of inflatable delta wings is precluded by this dependence of the theoretical calculations on the assumed mode shapes. The main problem is one of correctly accounting for the camber effects, which are known to be important, and which are especially dominant in the case of low-aspect-ratio wings (Ref. 10).

Two types of flutter were encountered; the first involved the two lowest vibration modes (low-frequency flutter), while the second involved modes higher than the second (high-frequency flutter). The high-frequency flutter occurred for models having two very close higher frequencies.

The influence of model pressure differential appears to be very slight for the case of low-frequency flutter. In contrast, the effect is much more significant for high-frequency flutter. With increasing pressure differential, higher flutter frequencies are noted, indicating a shift to higher predominating modes. This shift results in a rise of the flutter index $V_f / b_2 \omega_2 \sqrt{\mu}$, until such time as the level reaches that of the low-frequency flutter.

From the experimental tests run at $M = 2.99$ and 4.99 , it appears that the effect of increasing the angle of attack is slightly stabilizing for angles of attack up to 12 degrees. It would be extremely difficult to carry out a theoretical assess-

CONFIDENTIAL

CONFIDENTIAL

ment of the effect of angle of attack, because the typically large deformations experienced by the models, at even low angles of attack, introduce (1) changes in vibration mode shapes and frequencies, and (2) variations in the local angles of attack.

In the transonic range, the experimental results for the 65- and 75-degree models are essentially the same. For the low-supersonic range, the level of the $V_f / b_0 \omega_2 \sqrt{\mu}$ curve is lower for the 75-degree models. Also the rapid rise in the curve, which is evident for all models, occurs at a higher Mach number for the 75-degree models. These results may be partially due to the higher frequency ratios (ω_1 / ω_2) obtained with the 75-degree models. Because of the substantially higher frequencies of the 75-degree models, it was possible to obtain flutter points in the Mach-number range 1.2 to 2.5. For the 65-degree models, flutter points could not be obtained in this Mach number region, the models being unstable even at the lowest tunnel dynamic pressures.

The experimental results are quite consistent, considering the variations encountered between some of the models. All of the supersonic results (for $M \geq 2.5$) lie in a band of ± 8 per cent about a median experimental line (see Fig. 3.18). The region from $M = 1.2$ to 2.5 is not too well covered, but the trend for the 65-degree models is reasonably well defined. It is also clear that the 75-degree boundary lies below that for the 65-degree models over the Mach-number range from, say, 1.2 to 3.0.

CONFIDENTIAL

REFERENCES

1. Rogallo, F. M., Lawry, J. G., Croom, D. R., and Taylor, R. T. Preliminary Investigations of a Paraglider. NASA TN D-443, August 1960.
2. Sandgren, F. B., and Harris, J. T. Application of Inflated, Expandable Structures to Orbital Flight and Re-Entry. American Rocket Society Preprint 1093-60, Paper presented at ARS Meeting on Structural Design of Space Vehicles, Santa Barbara, California, April 6 - 8, 1960.
3. Leonard, R. W., Brooks, G. W., and McComb, H. G. Jr. Structural Considerations of Inflatable Re-Entry Vehicles. NASA TN D-457, September 1960.
4. Olstad, W. B. A Study of the Feasibility of Inflatable Re-Entry Gliders. NASA TN D-538, October 1960.
5. Martuccelli, J. R., Durgin, F. H., and McCallum, R. B. Construction of Testing Techniques of Inflatable Flutter Models. Presented at the Research and Technology Division and Aerospace Industries Association Symposium on Aeroelastic and Dynamic Modeling Technology, 23-25 September 1963, Dayton, Ohio. RTD-TDR-63-4197, Part 1, March 1964.
6. Gristofson, P. N., Stokey, W. F., and Zorowski, C. F.. An Experimental Study of Natural Vibrations of Cantilevered Rectangular Plates. Journal of the Aeronautical Sciences, Vol. 20, 16.5, May 1953, pp. 331-337.
7. Durgin, F. H. A Final Report on Phase I of a Program of Experimental and Theoretical Research on the Use of Quasi-Steady Airloads in Aeroelastic Analysis. Massachusetts Institute of Technology, Naval Supersonic Laboratory TR 360, August 1959.

REFERENCES (Cont'd)

8. Durgin, F. H., and Polutchko, R. J. A Final Report on Part I Phase II of a Program of Experimental and Theoretical Research on the Use of Quasi-Steady Airloads in Aeroelastic Analysis. Massachusetts Institute of Technology, Naval Supersonic Laboratory TR 423, February 1960.
9. Durgin, F. H., and Bartlett, C. J. A Measurement of the Static Aeroelastic Deformation and Loading of a Wing in Supersonic Flow. Massachusetts Institute of Technology, Aerophysics Laboratory TR 19, March 1963.
10. Bisplinghoff, R. L., Ashley, H., and Halfman, R. L. Aeroelasticity. Addison-Wesley Press, Cambridge, Massachusetts, 1955.
11. McComb, H. G. Jr. A Linear Theory for Inflatable Plates of Arbitrary Shape. NASA TN D-930, October 1961.
12. Matlin, R. W. Experimental Natural Frequencies, Damping Coefficients and Mode Patterns of an Inflatable Rectangular Wing. B.S. Thesis, Department of Aeronautics and Astronautics, Massachusetts Institute of Technology, June 1963.
13. Zartarian, G., Heller, A., and Ashley, H. Application of Piston Theory to Certain Elementary Aeroelastic Problems. Proceedings of the Fourth Midwestern Conference on Fluid Mechanics, Purdue University, West Lafayette, Indiana, September 1955.

APPENDIX I

ANALYTICAL PROCEDURES

A. AN APPROXIMATE METHOD OF DEFLECTION AND VIBRATION ANALYSIS

A simplified "strain-energy approach" is derived here to compute the deflection and frequency characteristics of inflatable plates. It is specialized to the case of a plate of uniform thickness, undergoing small deformations, i.e., the linearized formulation. It is considerably simpler than the more general linearized approach of Ref. I.1. The agreement between the two methods is discussed at various stages of the derivation. For this purpose, the notation of Ref. I.1 is adopted insofar as possible.

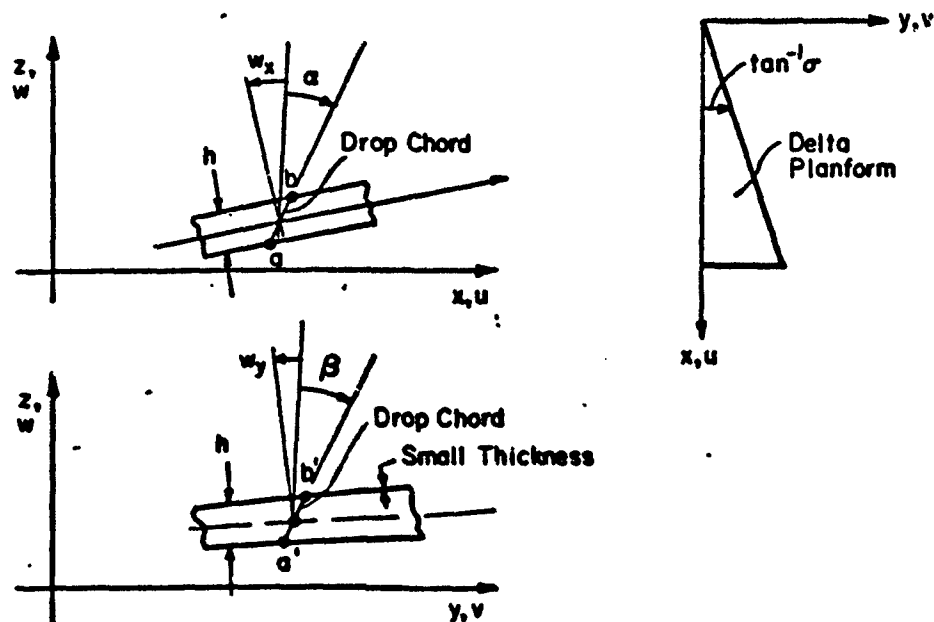


Figure I.1. Coordinate Systems and Deflection Notations for Simplified Analysis.

Consider Fig. 1.1, which depicts elements of the plate as seen in the x-z and y-z planes. Within the framework of small deflection theory with shear deformations present, and assuming small uniform thickness h , the displacements may be expressed as

$$u = z\alpha \quad v = z\beta \quad \text{and} \quad w = w(x, y) \quad (1.1)$$

The strain-displacement relations follow;

$$\begin{aligned} \epsilon_{11} &= \frac{\partial u}{\partial x} = z\alpha_x & \epsilon_{22} &= \frac{\partial v}{\partial y} = z\beta_y \\ \epsilon_{12} &= \frac{\partial u}{\partial y} + \frac{\partial v}{\partial x} = z(\alpha_y + \beta_x) & \epsilon_{13} &= \frac{\partial u}{\partial z} + \frac{\partial w}{\partial x} = \alpha + w_x \end{aligned}$$

and

$$\epsilon_{23} = \frac{\partial v}{\partial z} + \frac{\partial w}{\partial y} = \beta + w_y \quad (1.2)^*$$

The corresponding stress-strain relations for an isotropic plate are given by

$$\begin{aligned} \epsilon_{11} &= \frac{1}{E} (\sigma_{11} - \mu\sigma_{22}) & \epsilon_{22} &= \frac{1}{E} (\sigma_{22} - \mu\sigma_{11}) \\ \epsilon_{12} &= \frac{1}{G} \sigma_{12} & \epsilon_{13} &= \frac{1}{G} \sigma_{13} \quad \text{and} \quad \epsilon_{23} = \frac{1}{G} \sigma_{23} \end{aligned} \quad (1.3a)$$

or inversely,

* Subscripts x, y on α, β, w indicate partial differentiation with respect to x, y .

$$\sigma_{11} = \frac{E}{1-\mu^2} (\epsilon_{11} + \mu \epsilon_{22}) \quad \sigma_{22} = \frac{E}{1-\mu^2} (\epsilon_{22} + \mu \epsilon_{11})$$

$$\sigma_{12} = G \epsilon_{12} = \frac{E}{2(1+\mu)} \epsilon_{12} \quad \sigma_{13} = G \epsilon_{13} \text{ and } \sigma_{23} = G \epsilon_{23} \quad (I.3b)$$

Certain modifications must be made to the stress-strain relations (Eq. (I.3)) before applying them to the inflated, plate-type wing. Firstly, the shear modulus G in the relations

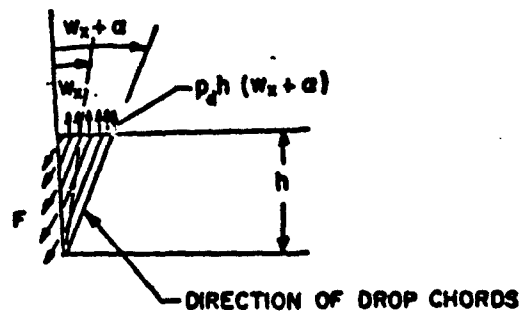
$$\sigma_{13} = G \epsilon_{13} \quad \text{and} \quad \sigma_{23} = G \epsilon_{23}$$

must be replaced by p_d . This can be easily demonstrated. For example, from the sketch below, one has for the shear stress σ_{13} (for small $(w_x + \alpha)$),

$$\sigma_{13} \cong \frac{F}{h} = p_d (w_x + \alpha) \quad \text{or} \quad \sigma_{13} = p_d \epsilon_{13} \quad (I.4a)$$

Similarly,

$$\sigma_{23} = p_d \epsilon_{23} \quad (I.4b)$$



On this basis, and assuming the covers to behave isotropically, the strain energy U_s is given by

$$U_s = \frac{1}{2} \iiint \left\{ \sigma_{11} \epsilon_{11} + \sigma_{22} \epsilon_{22} + \sigma_{12} \epsilon_{12} + \sigma_{13} \epsilon_{13} + \sigma_{23} \epsilon_{23} \right\} dx dy dz \quad (I.5)$$

Secondly, let the stress-strain relations be expressed in the more general form

$$t\sigma_{11} = A_{11}\epsilon_{11} + A_{12}\epsilon_{22} \quad t\sigma_{22} = A_{21}\epsilon_{11} + A_{22}\epsilon_{22} \quad t\sigma_{12} = A_{33}\epsilon_{12} \quad (I.6)$$

which may be applied to orthotropic as well as isotropic situations.

Substitution of Eqs. (I.4a,b) and (I.6) in Eq. (I.5) yields

$$U_s = \frac{1}{2t} \iiint \left\{ A_{11}\epsilon_{11}^2 + A_{22}\epsilon_{22}^2 + (A_{12} + A_{21})\epsilon_{11}\epsilon_{22} + A_{33}\epsilon_{12}^2 \right\} dx dy dz \\ + \frac{1}{2} \iiint p_2 \{ \epsilon_{13}^2 + \epsilon_{23}^2 \} dx dy dz \quad (I.7)$$

The shear stresses σ_{13} and σ_{23} are implicitly assumed to be uniform over the depth h , so that the z -integration for the second of the two triple integrals in (I.7) yields

$$\frac{1}{2} \iiint p_2 \{ \epsilon_{13}^2 + \epsilon_{23}^2 \} dx dy dz = \frac{1}{2} \iint p_2 h (\epsilon_{13}^2 + \epsilon_{23}^2) dx dy \quad (I.8)$$

On the other hand, stresses σ_{11} , σ_{22} , and σ_{12} are carried by the covers, so that the appropriate z -integration is carried out as follows:

$$\int [\iiint \dots] dz = \left[\int_{-\frac{h}{2}-t}^{\frac{h}{2}} + \int_{\frac{h}{2}}^{\frac{h}{2}+t} [\iiint \dots] dz \right] \quad (I.9)$$

Utilizing strain-displacement relations in (I.7) and performing the z-integrations as indicated by Eqs. (I.8) and (I.9), one obtains

$$U_s = \frac{h^2}{4} \iint_S \left\{ A_{11} \alpha_x^2 + A_{22} \beta_y^2 + (A_{12} + A_{21}) \alpha_x \beta_y + A_{33} (\alpha_y + \beta_x)^2 \right\} dx dy \\ + \frac{1}{2} \iint_S p h \left\{ (\alpha + w_x)^2 + (\beta + w_y)^2 \right\} dx dy \quad (I.10)$$

where the double integrals are taken over the planform area S .

The latex-impregnated cloth covers do not behave isotropically; if the covers are treated as orthotropic, and the x- and y-axes are aligned with the principal directions, it follows that

$$A_{11} = \frac{E_1 t}{1 - \mu_{12} \mu_{21}} \quad A_{12} = A_{21} = \frac{\mu_{21} E_1 t}{1 - \mu_{12} \mu_{21}} = \frac{\mu_{12} E_2 t}{1 - \mu_{12} \mu_{21}} \\ A_{22} = \frac{E_2 t}{1 - \mu_{12} \mu_{21}} \quad \text{and} \quad A_{33} = G t \quad (I.11)$$

The structural parameters $E_1 t$ and $E_2 t$ are the extensional stiffnesses in the x- and y-directions, respectively. μ_{12} (or μ_{21}) is the Poisson's ratio associated with a contraction in the y- (or x-) direction caused by a tensile stress in the x- (or y-) direction. The values

of these structural constants depend on the stress levels of the median state, the state about which small additional deflections are assumed to take place. Let W denote the work done by the external forces, which are assumed to act normal to the x-y plane; then

$$W = \iint f w \, dx \, dy \quad (1.12)$$

f being the associated load intensity. According to the principle of minimum potential energy, one must have zero variation of $(U_s - W)$, i.e.,

$$\delta \pi \equiv \delta (U_s - W) = 0 \quad (1.13)$$

With appropriate integrations by parts, and from variations on w, α, β , Eq. (1.13) yields the differential equations

$$p_2 h (w_x + \alpha)_x + p_2 h (w_y + \beta)_y = -f$$

$$\frac{h^2}{2} [A_{11} \alpha_{xx} + A_{12} \beta_{yx} + A_{33} (\alpha_{yy} + \beta_{xy})] - p_2 h (\alpha + w_x) = 0$$

$$\frac{h^2}{2} [A_{21} \alpha_{xy} + A_{22} \beta_{yy} + A_{33} (\alpha_{yx} + \beta_{xx})] - p_2 h (\beta + w_y) = 0 \quad (1.14)$$

These are in agreement with Eqs. (42), Ref. I.1, for the case of time-independent deflections. When motion is included, one must add to the right-hand sides of Eqs. (1.14), the inertia terms $\bar{m} \ddot{w}$, $\bar{m} \frac{h^2}{4} \ddot{\alpha}$ and $\bar{m} \frac{h^2}{4} \ddot{\beta}$, respectively.

Here, \bar{m} represents the mass of the plate for unit area (top and bottom covers included).^{*} From the variational principle, the natural boundary conditions associated with Eqs. (I.14) are, for a rectangular plate,

(1) along an edge where $x = \text{constant}$

$$\begin{array}{ll} \text{either } w = 0 & \text{or } w_x + \alpha = 0 \\ \text{either } \alpha = 0 & \text{or } A_{11}\alpha_x + A_{12}\beta_y = 0 \\ \text{either } \beta = 0 & \text{or } \alpha_y + \beta_x = 0 \end{array}$$

(2) along an edge where $y = \text{constant}$

$$\begin{array}{ll} \text{either } w = 0 & \text{or } w_y + \beta = 0 \\ \text{either } \alpha = 0 & \text{or } \alpha_y + \beta_x = 0 \\ \text{either } \beta = 0 & \text{or } A_{22}\beta_y + A_{12}\alpha_x = 0 \end{array}$$

These boundary conditions assume that no edge forces are being applied; they are slightly different from those given in Eqs. (39) of Ref. I.1. This apparent discrepancy between the two analyses arises from a term

$$\Delta U = \frac{A_2 h^3}{12} \iint_S [\beta_x \alpha_y - \alpha_x \beta_y] dy dx$$

which is included in Ref. I.1, but which is missing from the present derivation. It is worth mentioning that this ΔU -term does not change the system of Eqs. (I.14). Furthermore, this difference can be shown to lead to practically negligible terms in the natural boundary conditions.

For the present application to a delta planform, the method of solution described for a rectangular plate is inconvenient. Instead of solving the differential

^{*} \bar{m} corresponds to the quantity ρ in Ref. I.1.

equations subject to certain boundary conditions, one can return to the original energy equations and use a Rayleigh-Ritz approach. A particularly simple case is one where the bending stiffnesses are assumed so large that the deformations are purely of the shear type. For such a situation, one has

$$\alpha = \beta = 0 \quad U_s = \frac{1}{2} b_d \iint_S h [w_x^2 + w_y^2] dx dy \quad (I.15)$$

To facilitate the ensuing analysis, the dimensionless coordinates \bar{x}, \bar{y} are introduced, where

$$\bar{x} = \frac{x}{C_0} \quad \bar{y} = \frac{y}{C_0} \quad (I.16)$$

and C_0 is the root chord. Also, let

$$\bar{w}(\bar{x}, \bar{y}, t) = \sum_{n=1}^N q_n(t) w_n(\bar{x}, \bar{y}), \quad (I.17)$$

where $w_n(\bar{x}, \bar{y})$ are trial mode shapes (or modal functions), suitable in the sense that each w_n satisfies the geometric boundary conditions. From Eqs. (I.15) - (I.17), one has

$$U_s = \frac{1}{2} b_d \iint_S h [w_x^2 + w_y^2] d\bar{x} d\bar{y} = \frac{1}{2} b_d h \iint_S \left\{ \left(\sum_{n=1}^N q_n \dot{w}_{n\bar{x}} \right)^2 + \left(\sum_{n=1}^N q_n \dot{w}_{n\bar{y}} \right)^2 \right\} d\bar{x} d\bar{y} \quad (I.18)$$

For simplicity, one may consider w_n 's which are single terms in powers of \bar{x} and \bar{y} . For the example presented here, the following power forms are taken:

$$w_1 = \bar{y} \quad w_2 = \bar{x}\bar{y} \quad w_3 = \bar{y}^2 \quad w_4 = \bar{x}^2\bar{y} \quad w_5 = \bar{x}\bar{y}^2 \\ w_6 = \bar{y}^3 \quad w_7 = \bar{x}^2\bar{y}^2 \quad w_8 = \bar{x}\bar{y}^3 \quad \text{and} \quad w_9 = \bar{y}^4$$

The kinetic energy is given by

$$T = \frac{1}{2} \iint_S \bar{m} \left(\sum_1^N \frac{dq_n}{dt} w_n \right)^2 dx dy \\ = \frac{1}{2} \bar{m} c_o^2 \iint_S \left(\sum_1^N \dot{q}_n w_n \right)^2 d\bar{x} d\bar{y} \quad (I.19)$$

where \bar{m} is the mass per unit area, assumed uniform for the present case. Applying Lagrange's equation

$$\frac{d}{dt} \left(\frac{\partial T}{\partial \dot{q}_i} \right) + \frac{\partial U_s}{\partial q_i} = 0,$$

the above equations yield

$$\sum_{n=1}^N q_n (k_{in} - \lambda m_{in}) = 0 \quad i=1, \dots, N \quad (I.20)$$

where

$$\lambda = \frac{\omega^2 \bar{m} c_o^2}{k_d h} \quad (I.21)$$

is the eigenvalue and m_{in} and k_{in} are quantities related to the generalized masses and stiffnesses,

$$m_{in} = \iint_S w_i w_n d\bar{x} d\bar{y}$$

$$k_{in} = \iint_S w_{i\bar{x}} w_{n\bar{x}} d\bar{x} d\bar{y} + \iint_S w_{i\bar{y}} w_{n\bar{y}} d\bar{x} d\bar{y}$$

The double integrals of m_{in} and k_{in} may be easily evaluated, using the relation

$$\iint_S \bar{x}^m \bar{y}^n d\bar{x} d\bar{y} = \int_0^1 \int_0^{\sigma \bar{x}} \bar{x}^m \bar{y}^n d\bar{y} d\bar{x} = \frac{\sigma^{n+1}}{(n+1)(n+m+2)}$$

where σ is the tangent of the semi-apex angle. Equations (I.20) form a set of homogeneous algebraic equations with the eigenvalues $\lambda_1, \dots, \lambda_N$, and may be solved by any one of several well-known techniques, by iteration for instance. To each eigenvalue λ_i is associated an eigenvector $q^{(i)}$ with components $\{q_n^{(i)}; n=1, \dots, N\}$. The eigenvector $q^{(i)}$ defines the mode shape. Since m_{in} and k_{in} are functions of σ only, λ_i 's are fixed once the semi-apex angle is specified. For the 65-degree-sweep deltas* considered here, the first three eigenvalues turn out to be:

$$\lambda_1 = 19.224, \quad \lambda_2 = 77.549, \quad \lambda_3 = 147.32$$

with the associated eigenvectors

* More precisely these results apply to model 1, which has a leading edge very slightly different from 65 degrees. All "65-deg models" have sweeps sufficiently near that for Model 1, so that these results apply to all of them.

$$\begin{aligned}
 \mathbf{g}^{(1)} &= \begin{bmatrix} -0.011, 713 \\ 0.106, 14 \\ -0.197, 51 \\ 0.052, 988 \\ 1.000, 00 \\ -0.873, 19 \\ -0.906, 36 \\ 0.772, 15 \\ 0.031, 149 \end{bmatrix} & \mathbf{g}^{(2)} &= \begin{bmatrix} 0.034, 604 \\ -0.312, 80 \\ -0.167, 02 \\ 0.303, 64 \\ 1.000, 00 \\ -0.253, 30 \\ -0.964, 02 \\ 0.746, 00 \\ -0.566, 77 \end{bmatrix} & \mathbf{g}^{(3)} &= \begin{bmatrix} -0.037, 227 \\ -0.532, 72 \\ 0.641, 80 \\ 0.962, 41 \\ 1.000, 00 \\ -2.942, 5 \\ -2.713, 9 \\ 0.807, 94 \\ 4.851, 1 \end{bmatrix}
 \end{aligned}$$

The natural frequencies, for a particular model, can be determined by inserting the above eigenvalues and the model parameters into Eq. (I.21). The locations of the node lines, which are the same for all models, can be calculated by inserting the assumed modal functions and the associated eigenvectors, given above, into Eq. (I.17), and then setting the left-hand side equal to zero and solving for \bar{x} as a function of \bar{y} (or \bar{y} as a function of \bar{x}).

The deflection of the wing models under a uniform, static load, again based on the assumption of pure shear-type deformations only, can be calculated from the nonhomogeneous Lagrange's equation, which takes the form

$$p_h \sum_{n=1}^N q_n k_{in} = Q_i = c_0^2 f \iint_S \frac{\partial w}{\partial q_i} d\bar{x} d\bar{y}, \quad (i=1, \dots, N) \quad (I.22)$$

where Q_i represents the i -th generalized external force and f is the load intensity. The system of nonhomogeneous equations may be solved to yield the generalized displacements q_i 's, and from these, the deflections. For the 65-degree-sweep delta models, the deflection w turns out to be

$$\omega(\bar{x}, \bar{y}) = \frac{C_0^2 f}{\rho_a h} \left\{ -0.006,3 \bar{y} + 0.690,0 \bar{x} \bar{y} - 0.592,6 \bar{y}^2 - 0.313,9 \bar{x}^2 \bar{y} \right. \\ \left. + 0.397,1 \bar{x} \bar{y}^2 - 0.134,2 \bar{y}^3 - 0.338,3 \bar{x}^2 \bar{y}^2 \right. \\ \left. + 0.342,6 \bar{x} \bar{y}^3 - 0.017,3 \bar{y}^4 \right\} \quad (I.23)$$

B. FLUTTER ANALYSES

1. Equations of Motion

The analytical flutter boundaries presented in this report are based on the expression

$$M_n \ddot{\xi}_n + \sum_{j=1}^N a_{nj} \dot{\xi}_j + M_n \omega_n^2 \xi_n + \sum_{j=1}^N b_{nj} \xi_j = 0 \quad (n=1, N) \quad (I.24)$$

derivable from Lagrange's equation (cf. Ref. I.2, page 407). Here,

ξ_n = generalized coordinate of the n th orthogonal mode,

$$M_n = C_0^2 \iint_S \bar{m} \varphi_n^2 d\bar{x} d\bar{y} = \text{nth generalized mass}$$

a_{nj}, b_{nj} are the out-of-phase and in-phase aerodynamic coefficients which will be discussed below, and

φ_n is the n th orthogonal mode shape.

Parallel static divergence boundaries are also given; they are based on the reduced form of Eq. (I.24)

$$M_n \omega_n^2 \xi_n + \sum_{j=1}^N b_{nj} \xi_j = 0 \quad (I.25)$$

The structural damping may be included in the flutter analyses by applying the factor $(1 + i g_n)$ to the term $M_n \omega_n^2 \xi_n$, where g_n is the structural damping coefficient of the n th mode. The coordinate system is that given in Fig. I.2. In using Eq. (I.24), the following are implicitly assumed:

- (1) The flutter or divergence mode is representable by a linear combination of a finite number of normal (orthogonal) modes. In the applications, combinations of two and three degrees of freedom are considered.
- (2) For the supersonic flutter calculations, the generalized aerodynamic forces are quasi-steady; they may be expressed in terms of two components, one in phase with the displacement, the other in phase with the velocity. For a flat plate, and according to first- or second-order piston theory,

$$a_{nj} = \frac{2\rho V C_o^2}{M} \iint_S \varphi_n \varphi_j d\bar{x} d\bar{y}$$

$$b_{nj} = \frac{2\rho V^2 C_o^2}{M} \iint_S \frac{\partial \varphi_j}{\partial \bar{x}} \varphi_n d\bar{x} d\bar{y} \quad (I.26)$$

where ρ , V , and M are the free-stream density, velocity and Mach number, respectively. For the transonic calculations, the combination of terms

$$\sum_{j=1}^N a_{nj} \dot{\xi}_j + \sum_{j=1}^N b_{nj} \xi_j$$

must be replaced by an appropriate aerodynamic generalized force term. This point is further discussed below.

2. Mode Shapes Used in the Calculations

In all of the analyses presented here, one of the following sets of mode shapes is utilized. All are based on experimental vibration results for a model pressure differential of 2 psig.

Set A

These are analytical modes derived from the vibration data of Model 1. The orthogonal modes are approximated by polynomials of the form:

$$\begin{aligned} \varphi_1^{(A)} &= \bar{x}\bar{y}^2 \\ \varphi_2^{(A)} &= (1+a\bar{x}+b\bar{x}^2)\bar{y}^2+c\bar{y}^4 \end{aligned} \quad (I.27)^*$$

The constants a, b, c in the assumed mode shapes are determined by imposing the orthogonality condition

$$\iint_S \bar{m} \varphi_1^{(A)} \varphi_2^{(A)} d\bar{x}d\bar{y} = 0 \quad (I.28)$$

and by satisfying the node line locations obtained from the Model 1 vibration data. If the mass distribution \bar{m} is assumed uniform, Eq. (I.28) reduces to

$$\iint_S \varphi_1^{(A)} \varphi_2^{(A)} d\bar{x}d\bar{y} = 0 \quad (I.28a)$$

Forcing the node line of the second mode to pass

* Superscripts like A in $\varphi^{(A)}$ designate the sets of mode shapes.

through the leading-edge point ($\bar{x} = 0.83$, $\bar{y} = 0.38$) and to approach the root at the point ($\bar{x} = 0.915$, $\bar{y} = 0$) results in the following mode shapes

$$\varphi_1^{(A)} = \bar{x}\bar{y}^2$$

$$\varphi_2^{(A)} = (1 - 1.9571\bar{x} + 0.9445\bar{x}^2)\bar{y}^2 - 0.1819\bar{y}^4 \quad (I.29)$$

The choice of the above two nodal points is arbitrary. The question arises as to how well Eqs. (I.29) represent the actual vibration modes. This can be answered only by measuring the complete vibration mode shapes. For two of the models, the mirror reflection technique was used to obtain experimental deflection slopes; from the latter, the mode shapes can be calculated, see Sets C-1, C-2 below. A qualitative confirmation of the assumed modes was attempted by visually observing constant deflection lines, using the NASA acceleration technique (cf. Ref. I.3) and comparing these contour lines with those obtained from the assumed modes. The theoretical contour lines for the first mode, $\varphi_1^{(A)} = \bar{x}\bar{y}^2$ are given in Fig. I.3; these agree with the visual observations of "l-g"-lines as the amplitude of motion is varied. Confirmation of the second and particularly higher modes is more difficult, and other modes can be assumed which would agree reasonably well with experimental l-g-lines. Contour lines for the second mode are given in Fig. I.4.

Set B

This set is also comprised of assumed analytical mode shapes. The first mode is identical with that of Set A. The second mode is assumed to be of the form

$$\varphi_2^{(B)} = (1 + a\bar{x})\bar{y}^2 + (b + c\bar{x})\bar{y}^4 \quad (I.30)$$

which involves no chordwise bending. Retaining the first mode, and imposing exactly the same conditions as in Set A, one arrives at the second mode shape.

$$\varphi_2^{(B)} = (1 - 1.092,7\bar{x})\bar{y}^2 + (-4.012,9 + 4.059,7\bar{x})\bar{y}^4 \quad (I.31)$$

The contour lines of $\varphi_2^{(B)}$ are given in Fig. I.5.

Comparison of Figs. I.4 and I.5 shows that the contour lines for $\varphi_2^{(A)}$ and $\varphi_2^{(B)}$ are similar in nature, although $\varphi_2^{(B)}$ exhibits much larger relative deflections at the tip and at the middle of the leading edge. For this set, an expression for the third mode in the polynomial form

$$\varphi_3^{(B)} = (1 + a\bar{x} + b\bar{x}^2)\bar{y}^2 + (c + d\bar{x})\bar{y}^4 \quad (I.32)$$

can also be determined. The constants a, \dots, d are determined by imposing two orthogonality relations

$$\iint_S \varphi_3^{(A)} \varphi_1^{(B)} d\bar{x} d\bar{y} = 0 \quad \iint_S \varphi_3^{(B)} \varphi_2^{(B)} d\bar{x} d\bar{y} = 0$$

and by making the node lines of $\varphi_3^{(B)}$ pass through the points ($\bar{x} = 1, \bar{y} = 0.33$) and ($\bar{x} = 0.5, \bar{y} = 0$). Once more, these points are taken from the experimental node line for Model 1 and their choice is arbitrary. This yields,

$$\varphi_3^{(B)} = (1 - 2.905,3\bar{x} + 1.810,6\bar{x}^2)\bar{y}^2 + (3.329,7 - 2.477,5\bar{x})\bar{y}^4 \quad (I.33)$$

The contour lines for the third mode are given in Fig. I.6.

Sets C-1 and C-2

These sets include three mode shapes derived from the mirror tests on Model 8. Subsection D of Section 2 describes the experimental techniques and the data reduction procedures for obtaining deflections and streamwise slopes. $\varphi_n^{(c)}$ and $\frac{\partial \varphi_n^{(c)}}{\partial x}$ are obtained for some 55 selected points on the planform.* For Sets C-1 and C-2, where the mode shapes are expressed by analytical functions, the mode shape integrals

$$\iint_S \varphi_n \varphi_j dy dx, \quad \iint_S \varphi_n \frac{\partial \varphi_j}{\partial x} dx dy,$$

may be obtained in closed form. For Sets C, inasmuch as the data are furnished at a large number of discrete points, numerical integration techniques are more convenient. In all cases, the rectangular rule is applied. The generalized masses are

$$\begin{aligned} M_{nj} &= c_o^2 \iint \bar{m}(x,y) \varphi_n^{(c)} \varphi_j^{(c)} d\bar{x} d\bar{y} \\ &= \sum_p W_p (\varphi_n^{(c)} \varphi_j^{(c)})_p \end{aligned} \quad (I.34)$$

where the index p denotes the points 1, 1R, . . . , 37. The weighting factor W_p is the mass of that portion of the wing assigned to point p , and $(\varphi_n^{(c)} \varphi_j^{(c)})_p = \varphi_n^{(c)}(\bar{x}_p, \bar{y}_p) \varphi_j^{(c)}(\bar{x}_p, \bar{y}_p)$. The mass distribution is assumed uniform, i.e., $\bar{m} = \text{constant}$, for all areas nonadjacent to the leading and trailing edges. The overlap between top and bottom covers for areas adjacent to the leading and trailing edges is accounted for

* These include the mirror points, augmented by some intermediate points; they do not include the points 1R, 9R, . . . , 37R on Fig. 2.11.

in the mass distribution.

Sets C-1 and C-2 are identical except for the generalized aerodynamic forces. For the aerodynamic integrals, a weighting factor A_p , which is the effective area of the wing assigned to the point p , may be introduced. For example,

$$a_{nj} \sim \iint \varphi_n^{(c)} \varphi_j^{(c)} dx dy = \sum_p A_p (\varphi_n^{(c)} \varphi_j^{(c)})_p \quad (I.35)$$

In general, the A_p is simply the midplane area of the segment of the wing assigned to the point p . For Set C-1, the rounded portions of the leading- and trailing-edge regions associated with the point p are included in the calculation of A_p . For Set C-2, these rounded portions are not included in the calculation of A_p . That is, the A_p is the total midplane area minus the midplane area of the rounded edges (see Fig. I.2). The justification for considering this modified Set C-2 is discussed below.

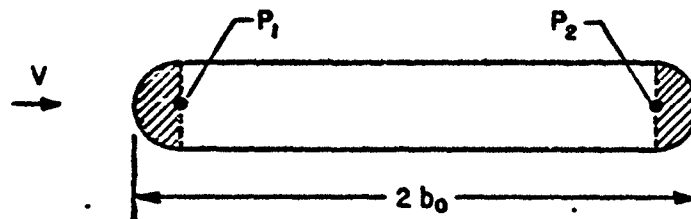
3. Aerodynamic Forces

For the Mach-number range from 2.5 to 6.0, piston theory with and without modifications is used to obtain the generalized aerodynamic forces. For $M = 1$, Landahl's first-order theory for low aspect ratio delta wings is applied.

Unless stated otherwise, the models are assumed to be set at zero angle of attack, and are thus undistorted. Since the model is of uniform thickness over most of the planform, it is reasonable to expect that calculations based on a flat-plate assumption should give adequate estimates for the aerodynamic forces. The errors committed by such an assumption (at least for these slender configurations

at moderate Mach numbers) are confined to the leading- and trailing-edge regions (see Fig. 1.2).

As a simplification, one may arbitrarily neglect the contributions of these blunt regions. Although this may appear quite empirical, one can offer a qualitative physical justification for the two-dimensional case with semicircular edges. Consider the section sketched below. The contributions



of the leading- and trailing-edge shaded regions to the airloads associated with motion come only from the "translation" part. Any rotation about P_1 (or P_2) would give zero total lateral load on the shaded region at P_1 (or P_2) for very small deflections. Consequently, the contributions from the shaded regions are of order $k (= \omega b_0 / V$, the reduced frequency). This means neglect of these regions results in an error in the " ik -terms" of the flutter determinant elements. At the high Mach numbers, the flutter k is very small, (at least for flutter involving the first two or three modes predominantly), and the resultant ik -terms should not influence the flutter results appreciably.

An alternate procedure, which is also somewhat empirical, is based on the use of the simple Newtonian theory for that portion of the airfoil surface near the leading edge where the sine of the flow inclination θ

times M is greater than unity, i.e., $M \sin \theta > 1$. For the rest of the airfoil surface, the piston theory is applied. This method is suggested by Morgan, Runyan and Hickel (Ref. I.4). The slight improvement, afforded by the latter method over the former which neglects entirely these regions, is not significant here, for there are other phases in the dynamic analyses which are equally approximate.

The above arguments apply to the two-dimensional case and thus for zero sweep. Since one would expect a decreasing influence from bluntness with increasing leading-edge sweep, the suggested corrections are excessive. In the analyses presented here for large sweep delta models, one is perhaps justified in neglecting bluntness effects altogether, and in treating the wings as flat plates of the same planforms. A suggested method whereby bluntness and initial angle of attack could be included in the analyses is presented below.

For deriving the unsteady airloads at the sonic speed, Landahl's first-order theory for low aspect ratio delta wings is utilized. Davies (Ref. I.5) presents, in detail, derived results for the airloads associated with some elementary mode shapes of oscillation. However, the mode shapes considered there are insufficient for the present purpose. Generalized aerodynamic forces are derived for additional modes. In particular, the required mode shapes which constitute the elements of the first and second (assumed) mode shapes of Model 1 are (see Eq. (I.27))

$$Z_j = \bar{y}^2, \bar{x}\bar{y}^2, \bar{x}^2\bar{y}^2, \bar{y}^4, \bar{x}\bar{y}^4 \quad (j = 4, 5, 6, 7, 8)$$

They are designated as elementary modes 4, 5, 6, 7, 8, respectively. No attempt is made here to reproduce the lengthy derivations, which essentially parallel those for the simpler modes in Ref. I.5. However, the dimensionless

velocity potentials $\bar{\varphi}_j^{(1)*}$, their streamwise derivatives $\bar{\varphi}_{j,x}^{(1)}$, and the associated generalized forces are summarized below. The notations are those of Fig. 1.2 and k is the reduced frequency $\omega b_0/V$.

Mode 4:

$$\bar{\varphi}^{(1)}(\bar{x}, \bar{y}, 0+) = -2ik \sqrt{s^2 - \bar{y}^2} \left[\frac{s^2}{6} + \frac{\bar{y}^2}{3} \right]$$

$$\bar{\varphi}_x^{(1)}(\bar{x}, \bar{y}, 0+) = -2ik \frac{\sigma}{\sqrt{s^2 - \bar{y}^2}} \left(\frac{s^3}{2} \right)$$

Mode 5:

$$\bar{\varphi}^{(1)}(\bar{x}, \bar{y}, 0+) = -(1 + 2ik\bar{x}) \sqrt{s^2 - \bar{y}^2} \left[\frac{s^2}{6} + \frac{\bar{y}^2}{3} \right]$$

$$\bar{\varphi}_x^{(1)}(\bar{x}, \bar{y}, 0+) = -\frac{\sigma}{\sqrt{s^2 - \bar{y}^2}} \left(\frac{s^3}{2} \right) - 2ik \frac{1}{6\sqrt{s^2 - \bar{y}^2}} [4s^4 + s^2\bar{y}^2 - 2\bar{y}^4]$$

Mode 6:

$$\bar{\varphi}^{(1)}(\bar{x}, \bar{y}, 0+) = -(2\bar{x} + 2ik\bar{x}^2) \sqrt{s^2 - \bar{y}^2} \left[\frac{s^2}{6} + \frac{\bar{y}^2}{3} \right]$$

$$\bar{\varphi}_x^{(1)}(\bar{x}, \bar{y}, 0+) = -\frac{1}{3\sqrt{s^2 - \bar{y}^2}} [4s^4 + s^2\bar{y}^2 - 2\bar{y}^4] - 2ik \frac{\bar{x}}{6\sqrt{s^2 - \bar{y}^2}} [5s^4 + 2s^2\bar{y}^2 - 4\bar{y}^4]$$

Mode 7:

$$\bar{\varphi}^{(1)}(\bar{x}, \bar{y}, 0+) = -2ik \frac{1}{40} \sqrt{s^2 - \bar{y}^2} [8\bar{y}^4 + 4s^2\bar{y}^2 + 3s^4]$$

$$\bar{\varphi}_x^{(1)}(\bar{x}, \bar{y}, 0+) = -2ik \frac{3\sigma}{40\sqrt{s^2 - \bar{y}^2}} [s^5]$$

* Superscript (1) indicates first-order solution, which is essentially the slender body result.

Mode 8:

$$\bar{\varphi}_j^{(1)}(\bar{x}, \bar{y}, 0+) = - \frac{(1+2ik\bar{x})}{40} \sqrt{s^2 - \bar{y}^2} [8\bar{y}^4 + 4s^2\bar{y}^2 + 3s^4]$$

$$\bar{\varphi}_{\bar{x}}^{(1)}(\bar{x}, \bar{y}, 0+) = - \frac{35\sigma}{8\sqrt{s^2 - \bar{y}^2}} - 2ik \frac{1}{40\sqrt{s^2 - \bar{y}^2}} [-8\bar{y}^6 + 4\bar{y}^4 s^2 + s^6 \bar{y}^2 + 18s^6]$$

The generalized aerodynamic forces are defined as

$$\begin{aligned} Q_{ij}^{(1)} = \frac{\bar{Q}_{ij}}{2\rho V^2 C_0^2} &= \frac{1}{2\rho V^2 C_0^2} \iint_S Z_i(\bar{x}, \bar{y}) \{ \Delta p_j(x, y) \} dx dy \\ &= \iint Z_i(\bar{x}, \bar{y}) \left\{ \bar{\varphi}_{j\bar{x}}^{(1)}(\bar{x}, \bar{y}, 0+) + 2ik \bar{\varphi}_j^{(1)}(\bar{x}, \bar{y}, 0+) \right\} d\bar{x} d\bar{y} \end{aligned} \quad (1.36)$$

where $\Delta p_j(x, y)$ is the pressure difference between bottom and top surfaces of the wing undergoing an oscillation in mode j .

$$Q_{44}^{(1)} = \frac{\pi\sigma^6}{48} \left[-2ik + \frac{4k^2}{7} \right] \quad Q_{45}^{(1)} = \frac{\pi\sigma^6}{48} \left[-1 - \frac{16ik}{7} + \frac{k^2}{2} \right]$$

$$Q_{46}^{(1)} = \frac{\pi\sigma^6}{48} \left[-2 - \frac{5ik}{2} + \frac{4k^2}{9} \right] \quad Q_{47}^{(1)} = \frac{3\pi\sigma^6}{256} \left[-2ik + \frac{4k^2}{9} \right]$$

$$Q_{48}^{(1)} = \frac{3\pi\sigma^6}{256} \left[-1 - \frac{20ik}{9} + \frac{2k^2}{5} \right] \quad Q_{54}^{(1)} = \frac{\pi\sigma^6}{48} \left[-\frac{12ik}{7} + \frac{k^2}{2} \right]$$

* The pressure difference Δp is related to $\bar{\varphi}$ in the manner indicated by Eq. (1.36), see Ref. I.5.

$$Q_{55}^{(1)} = \frac{\pi\sigma^6}{48} \left[-\frac{6}{7} - 2ik + \frac{4k^2}{9} \right] \quad Q_{56}^{(1)} = \frac{\pi\sigma^6}{48} \left[-\frac{7}{4} - \frac{20ik}{9} + \frac{2k^2}{5} \right]$$

$$Q_{57}^{(1)} = \frac{3\pi\sigma^8}{256} \left[-\frac{16}{9}ik + \frac{2k^2}{5} \right] \quad Q_{58}^{(1)} = \frac{3\pi\sigma^8}{256} \left[-\frac{8}{9} - 2ik + \frac{4k^2}{11} \right]$$

$$Q_{64}^{(1)} = \frac{\pi\sigma^6}{48} \left[-\frac{3ik}{2} + \frac{4k^2}{9} \right] \quad Q_{65}^{(1)} = \frac{\pi\sigma^6}{48} \left[-\frac{3}{4} - \frac{16ik}{9} + \frac{2k^2}{5} \right]$$

$$Q_{66}^{(1)} = \frac{\pi\sigma^6}{48} \left[-\frac{14}{9} - 2ik + \frac{4k^2}{11} \right] \quad Q_{67}^{(1)} = \frac{3\pi\sigma^8}{256} \left[-\frac{8ik}{5} + \frac{4k^2}{11} \right]$$

$$Q_{68}^{(1)} = \frac{3\pi\sigma^8}{256} \left[-\frac{4}{5} - \frac{20ik}{11} + \frac{k^2}{3} \right] \quad Q_{74}^{(1)} = \frac{3\pi\sigma^8}{256} \left[-2ik + \frac{4k^2}{9} \right]$$

$$Q_{75}^{(1)} = \frac{3\pi\sigma^8}{256} \left[-1 - \frac{20ik}{9} + \frac{2k^2}{5} \right] \quad Q_{76}^{(1)} = \frac{3\pi\sigma^8}{256} \left[-2 - \frac{12ik}{5} + \frac{4k^2}{4} \right]$$

$$Q_{77}^{(1)} = \frac{9\pi\sigma^{10}}{1280} \left[-2ik + \frac{4k^2}{11} \right] \quad Q_{78}^{(1)} = \frac{9\pi\sigma^{10}}{1280} \left[-1 - \frac{24ik}{11} + \frac{k^2}{3} \right]$$

$$Q_{84}^{(1)} = \frac{3\pi\sigma^8}{256} \left[-\frac{16}{9}ik + \frac{2k^2}{5} \right] \quad Q_{85}^{(1)} = \frac{3\pi\sigma^8}{256} \left[-\frac{8}{9} - 2ik + \frac{4k^2}{11} \right]$$

$$Q_{86}^{(1)} = \frac{3\pi\sigma^8}{256} \left[-\frac{9}{5} - \frac{24ik}{11} + \frac{k^2}{3} \right] \quad Q_{87}^{(1)} = \frac{9\pi\sigma^{10}}{1280} \left[-\frac{20ik}{11} + \frac{k^2}{3} \right]$$

$$Q_{88}^{(1)} = \frac{9\pi\sigma^{10}}{1280} \left[-\frac{10}{11} - 2ik + \frac{4k^2}{13} \right]$$

Appropriate linear combinations of the $Q_{ij}^{(n)}$'s yield the generalized aerodynamic forces associated with the assumed modes in the transonic flutter analyses. For example, if the indices 1 and 2 denote the first and second orthogonal vibration modes of Set A (see Eq. (I.29)),

$$Q_{11}^{(1)} = Q_{55}^{(1)}$$

$$Q_{12}^{(1)} = Q_{54}^{(1)} - 1.957,1 Q_{55}^{(1)} + 0.944,5 Q_{56}^{(1)} - 0.181,9 Q_{57}^{(1)}$$

$$Q_{21}^{(1)} = Q_{45}^{(1)} - 1.957,1 Q_{55}^{(1)} + 0.944,5 Q_{65}^{(1)} - 0.181,9 Q_{75}^{(1)}$$

$$\begin{aligned} Q_{22}^{(1)} = & Q_{44}^{(1)} + (-1.957,1)^2 Q_{55}^{(1)} + (0.944,5)^2 Q_{66}^{(1)} + (-0.181,9)^2 Q_{77}^{(1)} \\ & - 1.957,1 (Q_{45}^{(1)} + Q_{54}^{(1)}) + 0.944,5 (Q_{46}^{(1)} + Q_{64}^{(1)}) - 0.181,9 (Q_{47}^{(1)} + Q_{74}^{(1)}) \\ & + (-1.957,1)(0.944,5) [Q_{56}^{(1)} + Q_{65}^{(1)}] + (-1.957,1)(-0.181,9) [Q_{57}^{(1)} + Q_{75}^{(1)}] \\ & + (0.944,5)(-0.181,9) [Q_{67}^{(1)} + Q_{76}^{(1)}] \end{aligned}$$

It can be easily proved that, when using the transonic theory, it is appropriate to replace the a_{ij} - and b_{ij} - terms in the equations of motion (I.24) according to the rule

$$(a_{ij} \dot{\xi}_j + b_{ij} \xi_j) \rightarrow (-\xi_j 2\sigma V C^2 Q_{ij}^{(n)}) \quad (n, j = 1, 2)$$

4. Summary of Calculations

Table I.1 presents a summary and index of the two- and three-degree-of-freedom flutter and divergence analyses that have been carried out. The results are plotted in Figs. I.7 - I.24 and consist primarily of the stability

boundaries $V_f/b_0\omega_2$ (or $V_s/b_0\omega_2$ for the cases of static divergence) vs μM (or μ for the transonic calculations, $M = 1$). μ is the familiar mass ratio parameter, defined conveniently for the present analysis in terms of the total mass of the wing, m , as

$$\mu = \frac{3m}{2\pi\rho b_0^3\sigma}$$

The choice of these parameters as ordinate and abscissa, respectively, is natural, in that it is in this form that the theoretical results are obtained when one uses piston theory or slender-body theory. When comparing theory and experiment, results are reinterpreted in the more common form $V_f/b_0\omega_2\sqrt{\mu}$ vs M . In most instances, dimensionless flutter frequencies, ω_f/ω_2 , are also plotted vs μM .

A portion of these parametric studies were performed early in the program; specifically, the curves utilizing mode shape sets A and B were obtained once the vibration and inertia properties of Model 1 became available. These results were used in the design phases of the other models. The remainder of these calculations were carried out at later times, for purposes of correlation between theoretical and experimental flutter results. For use in the interpretation of the experimental data (Section 3), the important points brought out by these calculations are now briefly discussed.

Figures I.7 and I.8 establish flutter and static divergence boundaries for the typical 65-degree configuration. Two flutter branches are shown in each figure, corresponding to two possible solutions from the flutter determinant. Only the lower branch is of interest here.* The higher speed boundary for static divergence means that the model will flutter before the static divergence condition is reached. This is true in all cases carried

* In the subsequent Figs. I.13 to I.24, only this lower branch is shown whenever two stability boundaries are obtained.

out, with some predicting no divergence at any speed. These plots also indicate that inclusion of equal structural damping is slightly stabilizing, and results in higher flutter frequencies. Similar conclusions are reached when mode shape set B is substituted in the above calculations, as evidenced by the curves of Figs. I.11 and I.12. Figures I.9 and I.10 are included to extend the results with mode shape set A to the sonic Mach number. Figures I.13 and I.14 present the results according to a three-degree-of-freedom analysis. The interesting points about these curves are (1) the lack of a flutter boundary near that associated with modes 1 and 2, and (2) the weak dependence of the higher boundary on mode 1, i.e., modes 1, 2, 3 boundary is nearly the same as that for modes 2, 3 alone. A close examination, using the usual "V-g" type flutter analysis, revealed that the "disappearing branch," with flutter predominantly made up of the first two modes, is very lightly damped. This means that in the analysis, the coupling between modes 2 and 3 are seriously overestimated, a strong possibility considering the extent of the approximations involved in the mode shapes.

For Figs. I.15 to I.24, the calculations are based on the mode shapes C-1 and C-2. Figure I.15 shows the influence of lowering the frequency ratio, ω_1/ω_2 , to be a stabilizing one, but rather small for the range $0.4 \leq \omega_1/\omega_2 \leq 0.6$. Figure I.16 presents the influence on the flutter boundary of the bluntness of the leading and trailing edges, following the approximate technique of Subsection 3 of the present section. This effect is also slightly stabilizing. The influence of the frequency ratio, ω_3/ω_2 , on the higher mode flutter (modes 2 and 3) is brought out in Fig. I.17. It is interesting to note that higher ω_3/ω_2 's are stabilizing. A rapid lowering of the flutter boundary is noted as ω_3/ω_2 approaches unity. At the value of $\omega_3/\omega_2 = \sqrt{1.27}$, this boundary is seen to be below that for flutter involving the first two modes, when one compares it with Fig. I.7. The influ-

ence of the edge bluntness is seen (Fig. I.18) to be stabilizing on the high-frequency flutter, as in the previous case.

Figures I.19 and I.20 show that, with mode shape set C-1, small equal structural damping coefficients for the participating modes have slight destabilizing effects. This destabilizing influence is considerably more with unequal damping coefficients as may be noted from Figs. I.21 and I.22. Finally, Figs. I.23 and I.24 present the results of three-degree-of-freedom analyses utilizing the mode shapes derived from the mirror tests. These results lead to the same conclusions on the effects of edge bluntness and of structural damping as those from the two-degree-of-freedom cases of Figs. I.16 and I.18 to I.20.

C. FLUTTER OF BLUNT WINGS AT LARGE INITIAL ANGLES OF ATTACK

1. General

It is desirable to assess the influence of the initial angle of attack α_0 on the flutter index, as inflatable vehicles are expected to fly at large α_0 's during reentry.

In any reliable analysis, two major modifications must be introduced:

- (1) The changes in the vibration characteristics from those in still air. It is expected that the large deformations due to static lateral loading alter significantly the frequencies and mode shapes.
- (2) Piston theory becomes increasingly inaccurate as $M \sin \alpha$ approaches the values of

1.* For $M = 5$ or 6 , this limit is reached with $\alpha_0 \approx 10$ deg, even without elastic deformations.

Beyond this point, piston theory must be replaced with another aerodynamic theory, such as the simple Newtonian. The latter improves in accuracy with increasing $M \sin \alpha$.

In the initial phases of the program, some analytical work was carried out on the simultaneous effects of α_0 and bluntness on the aerodynamic forces according to Newtonian theory. However, no attempt was made to extend and apply the results of this study to particular model configurations, because (1) the experimental flutter tests were limited to small angles of attack and (2) there exist no reliable and fully-developed techniques for obtaining the vibration characteristics of the deformed models. Nevertheless, this preliminary work is presented below for possible future use; calculations for some simplified, two-dimensional cases are also included, to obtain a qualitative assessment of the effects of bluntness and initial angle of attack.

2. Aerodynamic Forces on a Blunt Deformable Surface at Large Angles of Attack, According to Newtonian Theory

For lifting surfaces at high angles of attack and at high speeds ($M \gg 1$), the simplest way of determining steady or unsteady aerodynamic loads is that following the raw Newtonian theory or the impact theory (Ref. 1.6). Without added complication, one may introduce Lee's modification in the above, wherein all pressures are modified by a constant factor. The justification for the latter is based on experimental results. This factor adjusts the

* More precisely, if $M \sin \theta \rightarrow 1$, where θ is the local surface inclination. Thus piston theory is invalid over certain parts of the blunt leading edge.

stagnation point pressure coefficient C_{p_0} to coincide with the observed C_{p_0} . The pressure coefficient according to Newtonian theory is

$$C_p = C_{p_0} \left[\left(\vec{i} - \frac{\vec{q}_b}{V} \right) \cdot \vec{n} \right]^2 \quad (I.37)$$

\vec{q}_b is the velocity of the body point where the pressure is to be determined, and \vec{n} is the unit normal vector, directed in. The pressure coefficient at the stagnation point is

$$C_{p_0} = \frac{p_0 - p_\infty}{\frac{1}{2} \rho_\infty V^2} \quad (I.38)$$

The observed C_{p_0} varies between 1.8 and 2.0 depending on the configuration. Equation (I.37) is, in a rigorous treatment, applicable only to those regions of the body where the instantaneous local inclination θ of the surface relative to the stream is large, in the sense that

$$M \sin \theta \gg 1 \quad (I.39)$$

However, for lack of a more rational approach, Eq. (I.37) may be utilized, provided that Eq. (I.39) is satisfied over most of the body. For the so-called shadow region, where $\theta < 0$, C_p is assumed to be zero. At high Mach numbers, it is consistent with the above approximations to set

$$p \approx p_0 \left[\left(\vec{i} - \frac{\vec{q}_b}{V} \right) \cdot \vec{n} \right]^2 \quad (I.40)$$

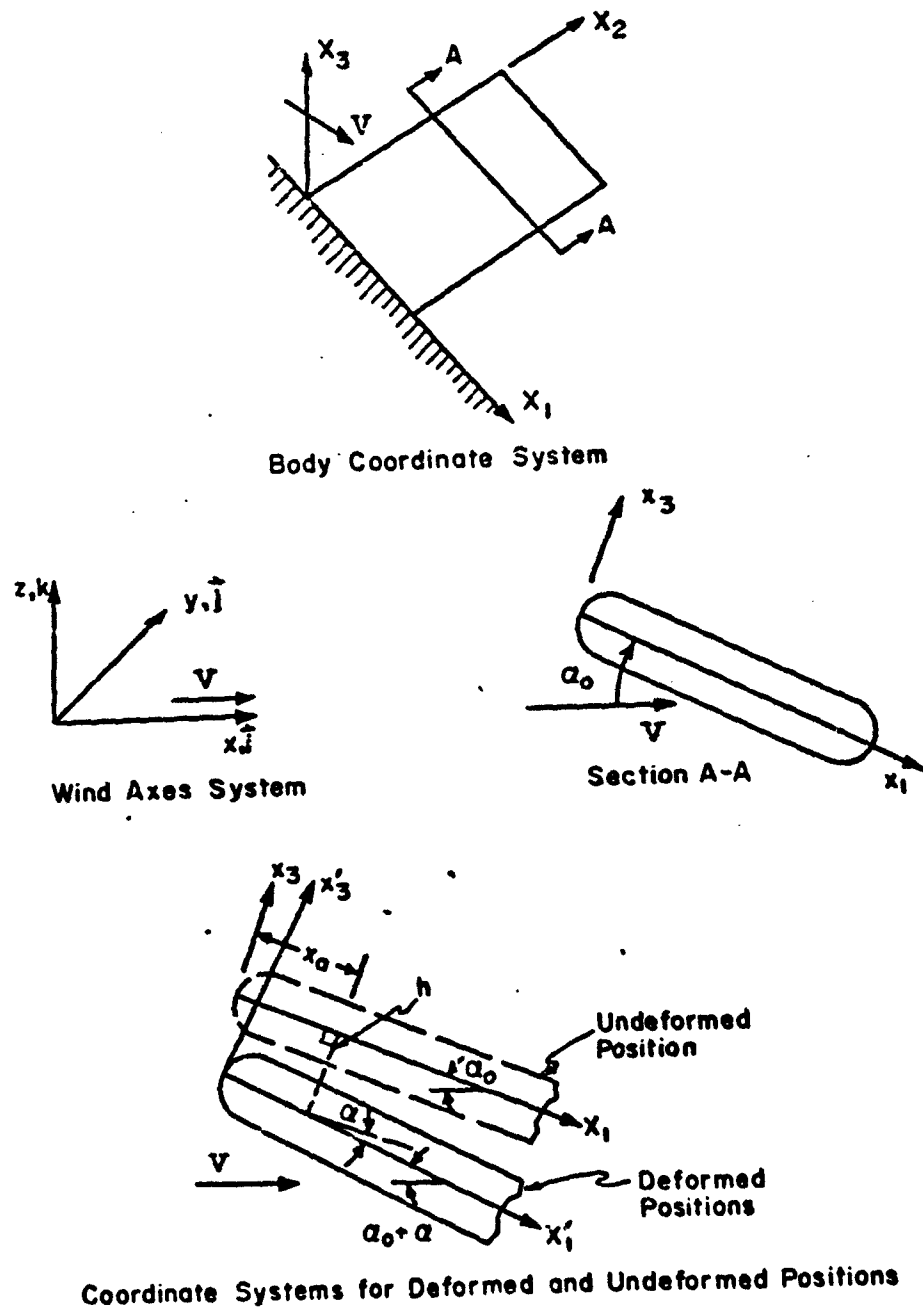
where $p_0 \approx C_{p_0} \left(\frac{1}{2} \rho_\infty V^2 \right)$, since the dynamic pressure will be much larger than p_∞ .

The main task is the determination of \vec{f}_d and \vec{v} . The complexity of this process will depend on the particular problem at hand. It may be possible to treat the steady and unsteady phases simultaneously, or it may have to be carried out in the following two phases:

- (1) Calculating the shape under a static loading, corresponding to steady flight, and
- (2) Proceeding to the unsteady part, using the steady deformed state as the starting point, assuming small (infinitesimal) time-dependent deformations.

Phase (1) may or may not be affected by linear aeroelastic analysis, for even though the structure may behave linearly, the airloads associated with the static deflections may be large. To convey these thoughts, consider the simple model of a cantilever rectangular wing, in its undeformed state. (See sketch below). x_1 is coincident with the "center line" of the cross section, x_3 is normal to the midplane, i.e., $(x_1 - x_2)$ -plane. Under load, the wing is assumed to behave as a beam-rod. Typically, the deformed state at any spanwise station x_2 may be thought of as that due to the sum of (a) a translation $\vec{d} = \vec{d}(x_2, t)$ perpendicular to the midplane, and (b) a rotation $\alpha = \alpha(x_2, t)$ about an axis $x_1 = x_{a_1}$. The shape of the cross section is assumed to remain unaltered under load, or alternately stated, the deformations are describable entirely by the deflection of the center line. Let $x_3 = f(x_1, x_2)$ denote the equation of the surface in its unloaded position. After deformation, assume each section at x_2 remains at x_2 . The equation of the surface in terms of body-fixed axes $x'_1, x'_2 = x_2, x'_3$ is:

$$x'_3 = f(x'_1, x'_2 - x_2) \quad (1.41)$$



Three sets of axes are now considered.

- (1) x, y, z , with x aligned in the free-stream direction, and having unit vectors $\vec{i}, \vec{j}, \vec{k}$
- (2) x_1, x_2, x_3 with unit vectors $\vec{i}_1, \vec{i}_2, \vec{i}_3$ and
- (3) x'_1, x'_2, x'_3 , the body-fixed axes with $\vec{i}'_1, \vec{i}'_2, \vec{i}'_3$.

The following relations hold between the coordinate systems:

$$x'_1 = (x_1 - x_a) \cos \alpha - (x_3 + h) \sin \alpha + x_a \quad (I.42)$$

$$x'_3 = (x_1 - x_a) \sin \alpha + (x_3 + h) \cos \alpha$$

and

$$\vec{i}'_1 = \vec{i} \cos(\alpha_0 + \alpha) - \vec{k} \sin(\alpha_0 + \alpha)$$

$$\vec{i}'_2 = \vec{j}$$

$$\vec{i}'_3 = \vec{i} \sin(\alpha_0 + \alpha) + \vec{k} \cos(\alpha_0 + \alpha) \quad (I.43)$$

The above configuration may be thought of as a "sheared" model, in that during deformation each section stays in its x_2 -plane and keeps its shape. Then the vector \vec{q}_b , which represents the absolute velocity (relative to x, y, z -system) of a point on the body, does not possess a component in the \vec{j} -direction. Since any body point has zero velocity relative to the system (x'_1, x'_2, x'_3) , it follows that

$$\frac{dx'_1}{dt} = 0, \quad \frac{dx'_3}{dt} = 0 \quad (I.44)$$

Differentiated forms of Eqs. (I.42) then yield in conjunction with Eqs. (I.44)

$$\vec{p}_b = \vec{r}_1 [\dot{x}_3' \dot{\alpha} + \dot{h} \sin \alpha] - \vec{r}_3 [(\dot{x}_1' - \dot{x}_a) \dot{\alpha} + \dot{h} \cos \alpha] \quad (I.45)$$

Here the relations

$$\begin{aligned} \vec{r}_1 &= \vec{r}_1' \cos \alpha + \vec{r}_3' \sin \alpha \\ \vec{r}_3 &= -\vec{r}_1' \sin \alpha + \vec{r}_3' \cos \alpha \end{aligned} \quad (I.46)$$

have also been utilized. The unit normal vector \vec{n} may be obtained from

$$\vec{n} = \frac{\nabla B}{|\nabla B|} \quad (I.47)$$

where

$$B = B(x_1', x_2', x_3') = x_3' - f(x_1', x_2') = 0 \quad (I.48)$$

represents the equation of the body shape. Also note that in Eq. (I.45) one may set $\dot{x}_3' = \dot{f}$ since \vec{p}_b refers to the velocity of a body point. After some algebra, there results

$$\vec{r}_1 \cdot \vec{n} = \frac{-f' \cos(\alpha_0 + \alpha) + \sin(\alpha_0 + \alpha)}{\sqrt{1 + (f')^2 + F^2}} \quad (I.49)$$

$$\vec{p}_b \cdot \vec{n} = \frac{-f' \{f \dot{\alpha} + \dot{h} \sin \alpha\} - \{(\dot{x}_1' - \dot{x}_a) \dot{\alpha} + \dot{h} \cos \alpha\}}{\sqrt{1 + (f')^2 + F^2}} \quad (I.50)$$

where

$$f = f(x'_1, x'_2), \quad f' = \frac{\partial f}{\partial x'_1}, \quad F = \frac{\partial f}{\partial x'_2} \quad (1.51)$$

When Eqs. (1.49) and (1.50) are substituted in Eq. (1.40), one obtains

$$p = p_0 \frac{\left[-f' \cos(\alpha_0 + \alpha) + \sin(\alpha_0 + \alpha) + f' \left\{ \frac{f\ddot{\alpha}}{V} + \frac{\dot{h}}{V} \sin \alpha \right\} + \left\{ (x'_1 - x'_2) \frac{\ddot{\alpha}}{V} + \frac{\dot{h}}{V} \cos \alpha \right\} \right]^2}{1 + (f')^2 + F^2} \quad (1.52)$$

for those regions of the body with positive inclination θ .

The latter expression may be linearized with respect to:

- (1) steady and unsteady deformations simultaneously,
- (2) unsteady deformations alone.

Let α and h be split up into two parts, one steady (denoted by subscript s) and one time-dependent (denoted by subscript u).

Case 1: $\alpha_s, \alpha_u, h_s, h_u$ are all small.

$$\cos(\alpha_s + \alpha) \cong \cos \alpha_s - (\alpha_s + \alpha_u) \sin \alpha_s$$

$$\sin(\alpha_s + \alpha) \cong (\alpha_s + \alpha_u) \cos \alpha_s \quad \sin \alpha_s$$

$$\ddot{\alpha} = \ddot{\alpha}_u, \quad \dot{h} = \dot{h}_u, \quad \sin \alpha \cong \alpha_s + \alpha_u, \quad \cos \alpha \cong 1$$

Utilizing these relations, one arrives at

$$p = \frac{p_0}{1+(f')^2+F^2} \left\{ (\sin \alpha_0 - f' \cos \alpha_0)^2 + 2(\sin \alpha_0 - f' \cos \alpha_0) \cdot \left[f'(\alpha_s + \alpha_u) \sin \alpha_0 + (\alpha_s + \alpha_u) \cos \alpha_0 + f f' \frac{\dot{\alpha}_u}{V} (x'_1 - x_u) \frac{\dot{\alpha}_u}{V} + \frac{\dot{h}_u}{V} \right] \right\} \quad (I.53)$$

Case 2: α_u, h_u are small, so that

$$\cos(\alpha_0 + \alpha) \approx \cos(\alpha_0 + \alpha_s) - \alpha_u \sin(\alpha_0 + \alpha_s); \sin(\alpha_0 + \alpha) \approx \alpha_u \cos(\alpha_0 + \alpha_s) + \sin(\alpha_0 + \alpha_s)$$

$$\dot{\alpha} = \dot{\alpha}_u, \dot{h} = \dot{h}_u; \sin \alpha = \sin \alpha_s + \alpha_u \cos \alpha_s; \cos \alpha = \cos \alpha_s - \alpha_u \sin \alpha_s$$

The corresponding pressure is

$$p = \frac{p_0}{1+(f')^2+F^2} \left\{ [\sin(\alpha_0 + \alpha_s) - f' \cos(\alpha_0 + \alpha_s)]^2 + 2[\sin(\alpha_0 + \alpha_s) - f' \cos(\alpha_0 + \alpha_s)] \cdot \left[\alpha_u \left(f' \sin(\alpha_0 + \alpha_s) + \cos(\alpha_0 + \alpha_s) \right) + \frac{\dot{\alpha}_u}{V} \left(f f' + (x'_1 - x_u) \right) + \frac{\dot{h}_u}{V} \left(f' \sin \alpha_s + \cos \alpha_s \right) \right] \right\} \quad (I.54)$$

Appropriate integrations of Eq. (I.53) or Eq. (I.54) lead to the total aerodynamic forces. The choice between Eq. (I.53) and Eq. (I.54) will depend on the particular problem at hand. If α_s is not small, i.e., large initial steady deformations are present, method (2) may have to be used.

The main disadvantage of the above derivation is that it assumes simple deformations of the beam-rod type.

The much more complicated case arises when deflections are not easily describable, as in the plate-type, inflatable delta structures. To make computations tractable, it is necessary to resort to other simplifications. One such case is when one assumes that surface points have only deformations normal to the midplane of the planform, i.e., a point at (x_1, x_2, x_3) goes to the deflected position (under load) at $(x_1, x_2, x_3 - \delta)$, where δ is the deflection, positive down. This approach would be inaccurate in the

blunt regions. Following the previous notation, one may write

$$\begin{aligned}\vec{q}_b &= -\vec{t}_3 \dot{\delta} \\ B &= x_3 - f(x_1, x_2) + \delta(x_1, x_2, t) \\ \vec{n} &= \frac{\vec{t}_1(-f' + \delta') + \vec{t}_2(-F + D) + \vec{t}_3}{\sqrt{1 + (\delta' - f')^2 + (D - F)^2}}\end{aligned}$$

where

$$f' = \frac{\partial f}{\partial x_1} \quad \delta' = \frac{\partial \delta}{\partial x_1} \quad F = \frac{\partial f}{\partial x_2} \quad D = \frac{\partial \delta}{\partial x_2}$$

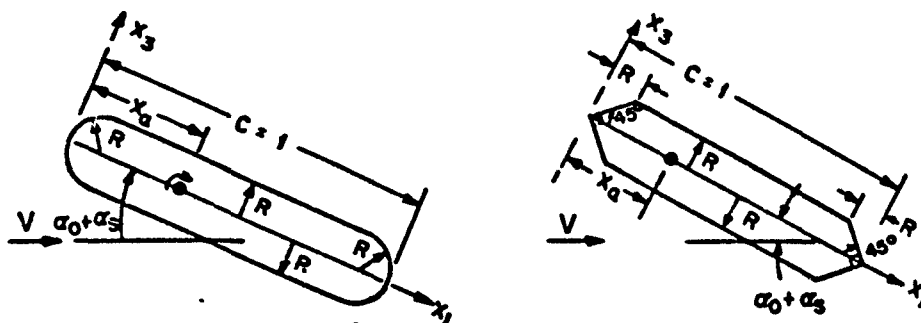
After some manipulation, one finds that

$$b = b_0 \frac{[\cos \alpha_0 (\delta' - f') + \sin \alpha_0 + \frac{\dot{\delta}}{V}]^2}{[1 + (\delta' - f')^2 + (D - F)^2]} \quad (1.55)$$

Since the mid-surface of the structure is required to be plane, δ must be taken to be the sum of the steady and time-dependent deflections. One added source of inaccuracy arises here. Newtonian theory requires high $M \sin \theta$, which means that the initial angles of attack must be large. For the present models, large angles of attack result in excessive model deformations, so that one can no longer assume this type of normal deformation. The preceding Eq. (1.55) is no longer adequate and other methods of analyses must be devised. One possible approach would be to first consider the deformation of the wing under steady load, and then treat the unsteady motion as a perturbation about the steady deformed position.

3. Applications to Two-Dimensional Sections

Some calculations have been carried out on the typical section (corresponding to the spanwise sections of the beam-rod-type structure) to obtain qualitative assessment of the effects of bluntness and initial angle of attack. Specifically, the cases treated are those given in the sketch below.



(a) Circular Nose

(b) Pointed Nose

As shown in the sketch, the sections are situated in their deformed state under steady aerodynamic loads only. Expressions were obtained for the unsteady airloads associated with a translation $\bar{h}_a e^{i\omega t}$ (perpendicular to x_1 -axis), and a rotation $\bar{\alpha}_a e^{i\omega t}$ (about $x = x_a$). The aerodynamic loads of interest are:

L Force perpendicular to x_1 , positive in the $-x_3$ -direction,

M_m Moment about any axis $x_1 = x_m$, positive nose up. It is noted that in the derivations of L and M_m (M_m for $x_m = x_a$), the axial force A , in the direction of x_1 , is also required, although it does not explicitly appear in the final equations. These expressions are not reproduced here, for

they are rather lengthy and do not bear directly on the discussions to follow.

Some observations can be made as to the behavior of the "center of pressure" movement due to initial angle of attack and leading and trailing edge bluntness. In the limit as the oscillation frequency $\omega \rightarrow 0$, the A_u -motion effects vanish and the center of rotation x_a becomes immaterial.

The point $x_i = x_m$ about which the moment M vanishes is denoted by x_c , the center of pressure. For slow oscillations, the center-of-pressure location relative to x_a may be important in flutter calculations. $(x_c - x_a)$ gives a measure of the real part of the complex M_a due to the rotation $\bar{a}_u e^{i\omega t}$.

The variation in center-of-pressure location, as calculated for the circular nose and pointed nose sections at various angles of attack, is presented in Fig. I.25a. A measure of bluntness is the ratio $\frac{R}{c}$ ($\frac{R}{c} = R$, if the chord is taken to be unity). For $R \rightarrow 0$, the section becomes a flat plate and $x_c = 0.5$, regardless of α_0 , as one would expect. $R \rightarrow 1/2$ corresponds to circular and square cylinders for the circular and pointed noses, respectively. For the case of $\alpha_0 = 45$ deg, x_c remains at 0.50 regardless of the bluntness R . For lower α_0 's, x_c is forward of the 50-per-cent.chord, while the reverse is true for larger α_0 's. Also the x_c -movements are less for the circular than for the pointed nose.

The above calculations are essentially those of a small steady angle of attack superimposed on the median angle ($\alpha_0 + \alpha_s$). For this case, another interesting comparison can be made between the force L for various R 's and $(\alpha_0 + \alpha_s)$'s. The plots given in Fig. I.25b

correspond to the expressions:

$$\frac{L}{\rho \alpha c} = \sin 2(\alpha_o + \alpha_s) \quad \text{for flat plate} \quad (I.56)$$

$$= (1-2R) \sin 2(\alpha_o + \alpha_s) \quad \text{for circular nose} \quad (I.57)$$

$$= (1-3R) \sin 2(\alpha_o + \alpha_s) \quad \text{for pointed nose with } (\alpha_o + \alpha_s) \geq 45 \text{ deg}$$

$$= (1-2R) \sin 2(\alpha_o + \alpha_s) + R(1-2\cos 2(\alpha_o + \alpha_s)) \quad \text{for pointed nose with } (\alpha_o + \alpha_s) \leq 45 \text{ deg}$$

The delta wings, such as those considered in the experimental program, have sparwise cross sections which are similar to the circular nose typical section. $\frac{R}{c}$ however is variable, increasing as one takes sections further away from the root. The above results (Eqs. (I.56) - (I.57)) suggest that perhaps one can account approximately for the leading- and trailing-edge bluntnesses by discarding from aerodynamic consideration the rounded portions of the leading and trailing edges. A similar conclusion was reached in Section B of this appendix, based on physical considerations.

REFERENCES FOR APPENDIX I

1. McComb, H. G., Jr. A Linear Theory for Inflatable Plates of Arbitrary Shape. NASA TN D-930, October 1961.
2. Bisplinghoff, R. L. and Ashley, H. Principles of Aeroelasticity. John Wiley and Sons, Inc., New York, 1962.
3. Hanson, P. W. and Tuovila, W. J. Experimentally Determined Natural Vibration Modes of Some Cantilever-Wing Flutter Models by Using an Acceleration Method. NACA TN 4010, April 1957.
4. Morgan, H. G., Runyan, H. L. and Huckel, V. Theoretical Considerations of Flutter at High Mach Numbers. Journal of the Aeronautical Sciences, Vol. 25, No. 6, June 1958, pp. 371-381.
5. Davies, D. E. Three-Dimensional Sonic Theory. Chapter 4, Vol. II, Manual on Aeroelasticity, NATO Advisory Group for Aeronautical Research and Development, W. P. Jones, Editor.
6. Zartarian, G. Unsteady Airloads on Pointed Airfoils and Slender Bodies at High Mach Numbers. WADC-TR-59-583, August 1959, Appendix A.

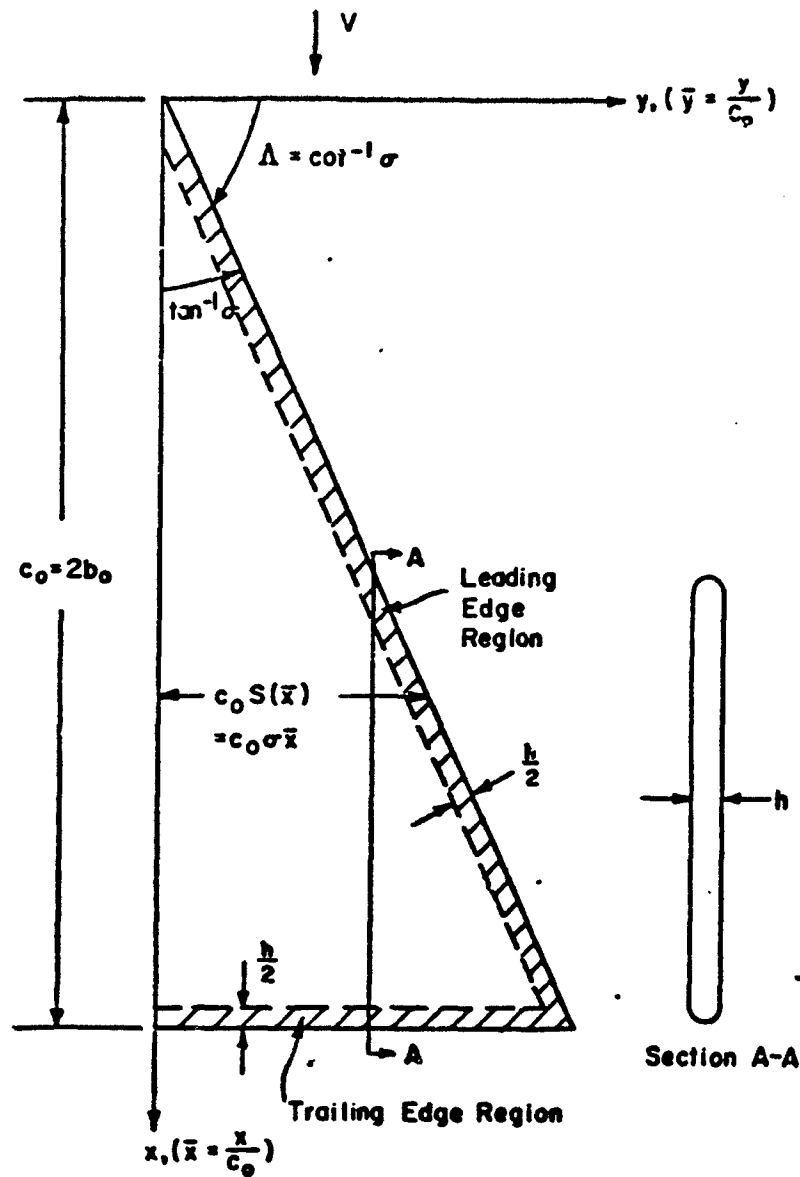


Figure I.2. Coordinate System and Notation for the Delta Models.

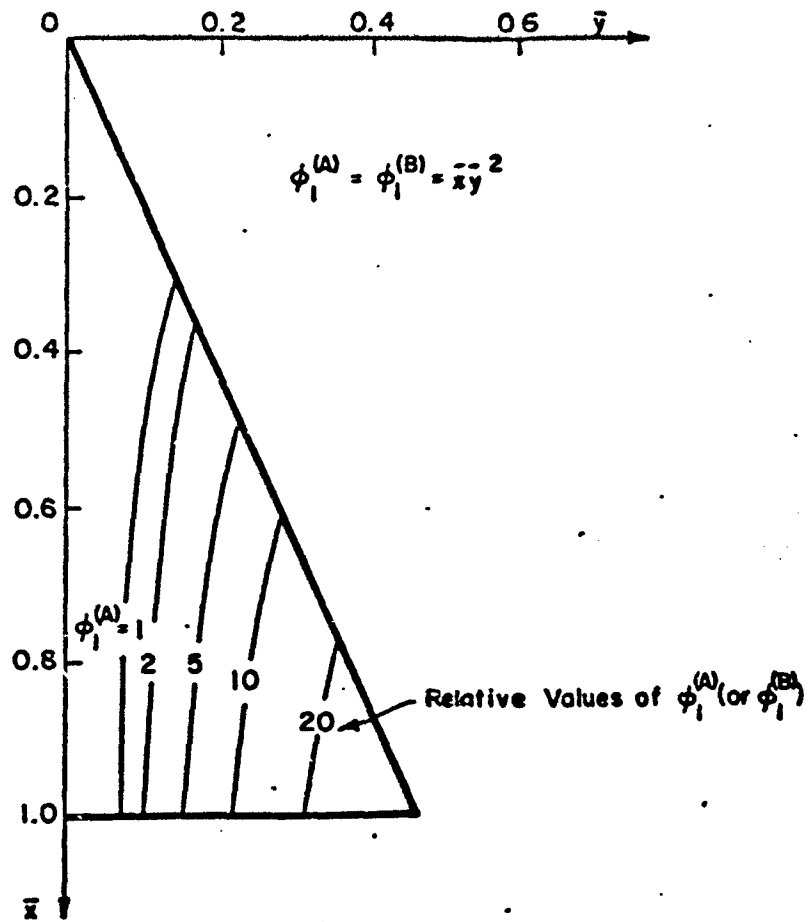


Figure I.3. Equal Deflection Lines for First Mode Shapes of Sets A and B.

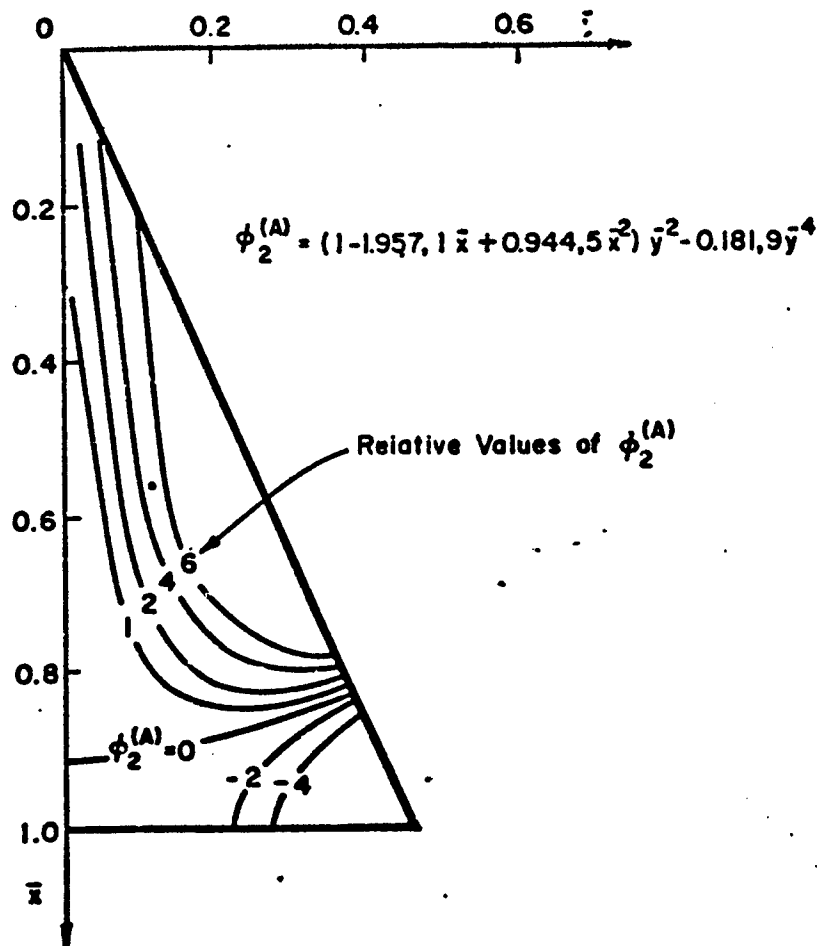


Figure 1.4. Equal Deflection Lines for Second Mode Shape of Set A.

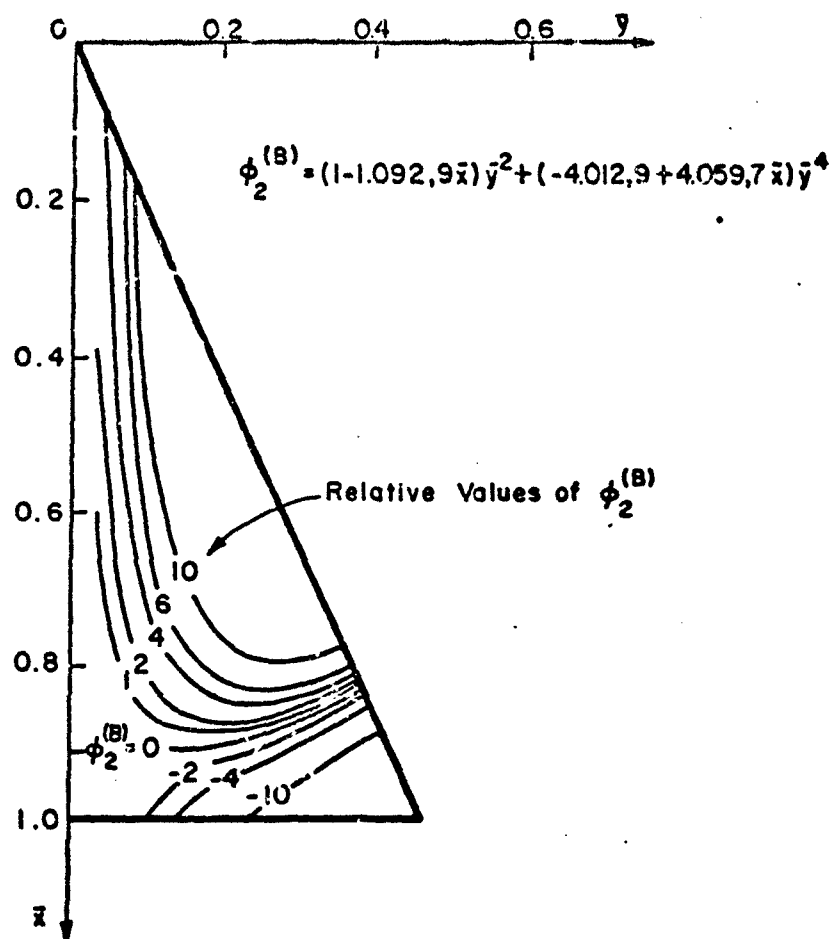


Figure I.5. Equal Deflection Lines for Second Mode Shape of Set B.

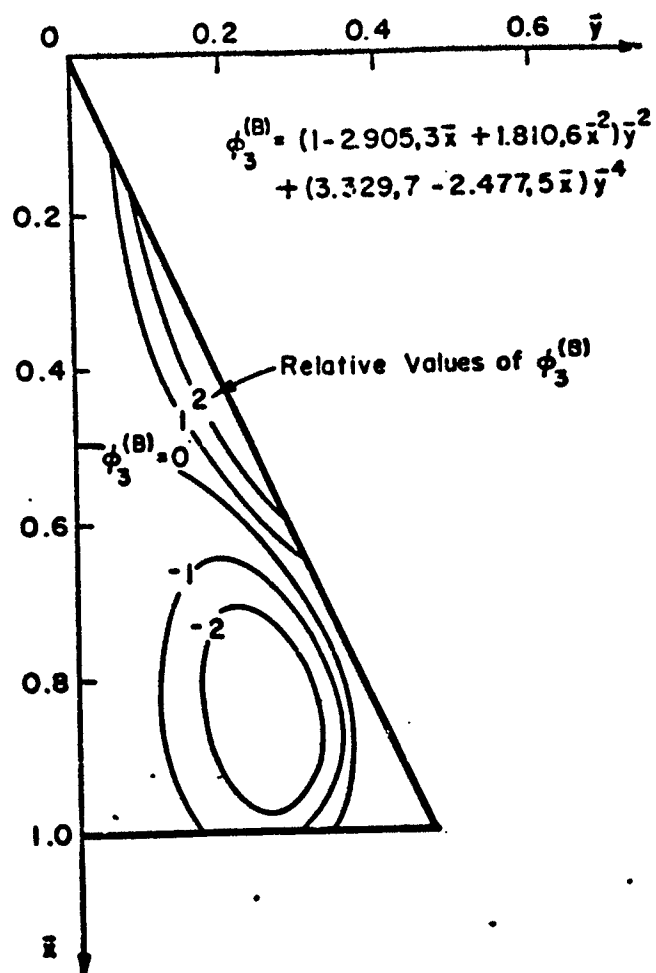


Figure I.6. Equal Deflection Lines for Third Mode Shape of Set B.

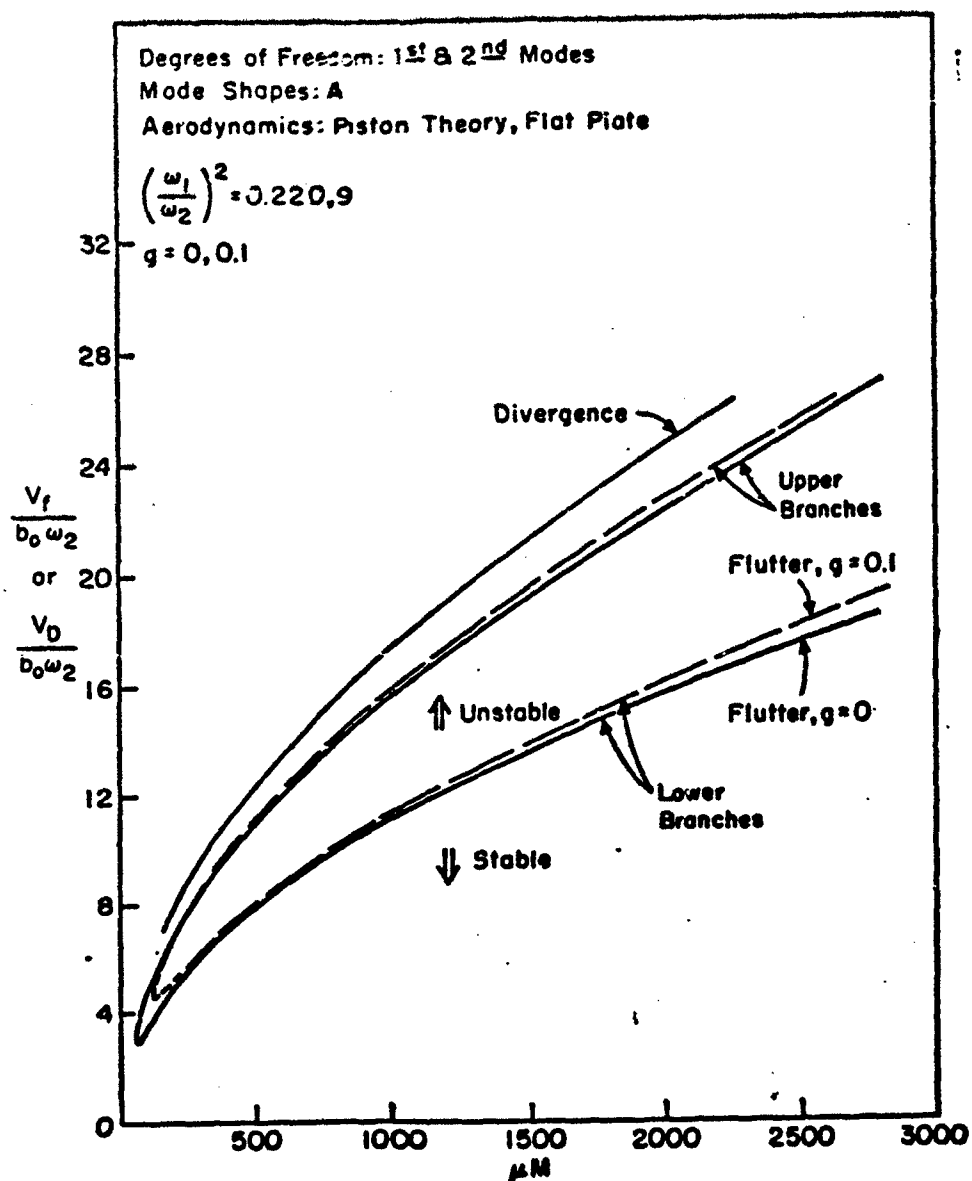


Figure I.7. Theoretical Flutter Parameter ($V_f/b_o \omega_2$) and Static Divergence Parameter ($V_D/b_o \omega_2$) vs μM for Stated Conditions.

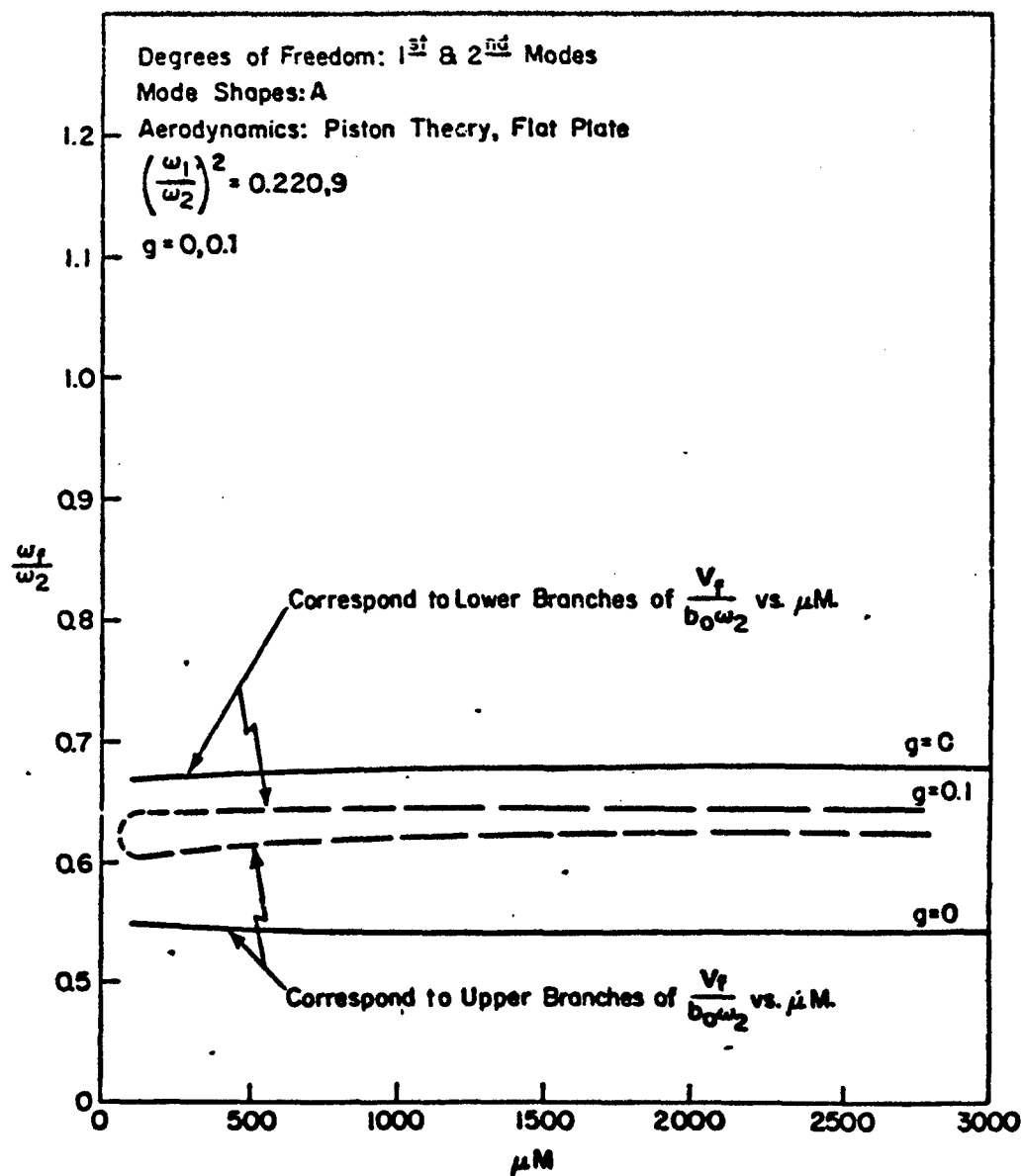


Figure I.8. Theoretical Flutter Frequency Parameter (ω_f/ω_2) vs μM for Stated Conditions.

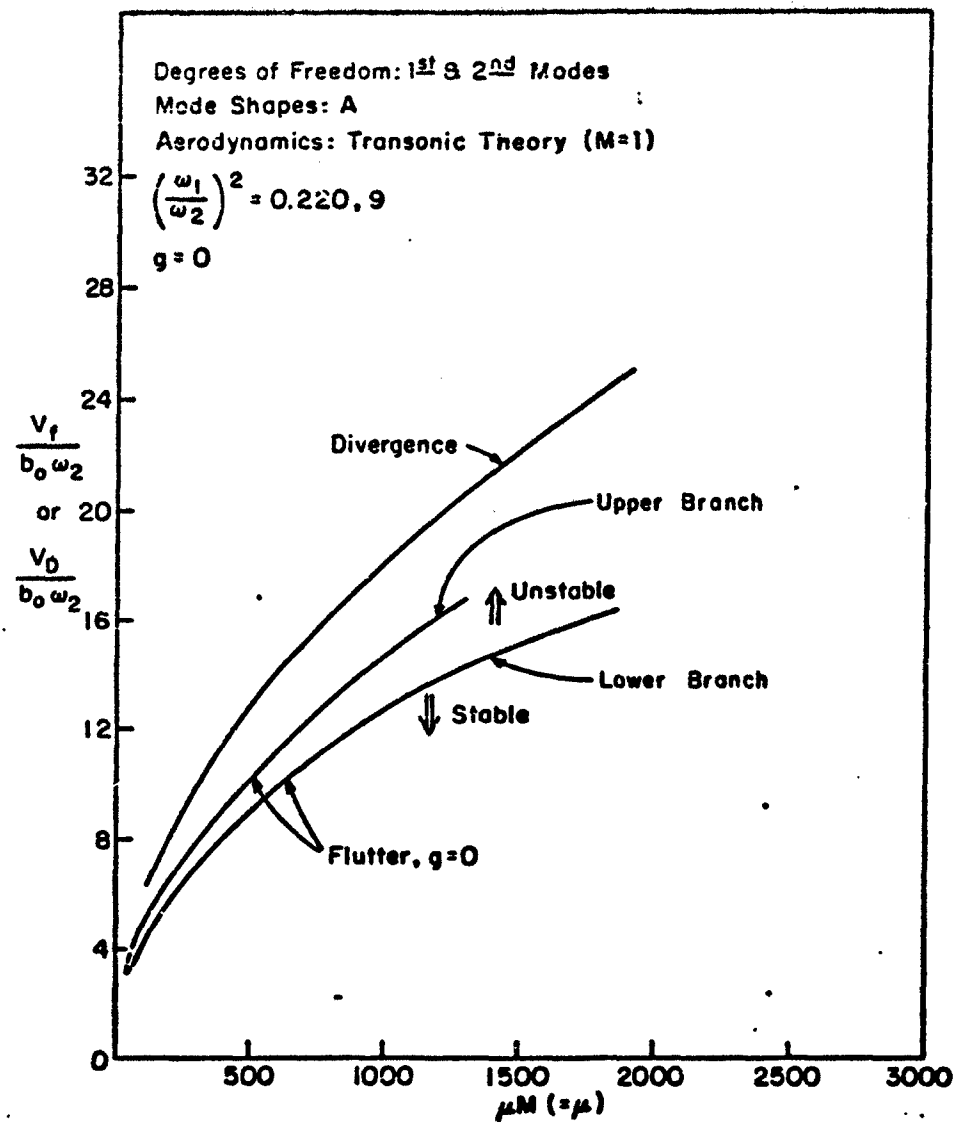


Figure I.9. Theoretical Flutter Parameter ($V_f/b_o \omega_2$) and Static Divergence Parameter ($V_D/b_o \omega_2$) vs μM for Stated Conditions.

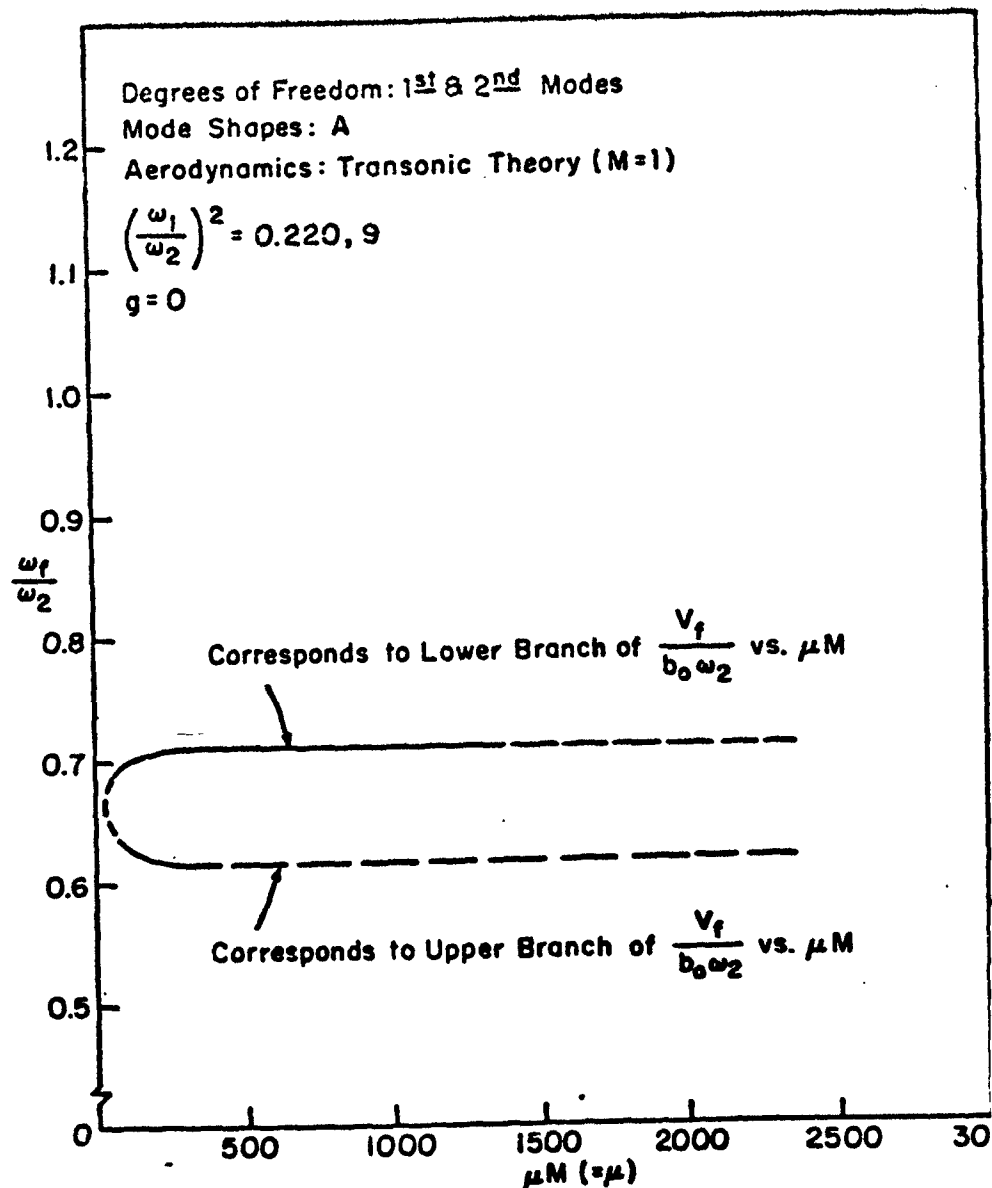


Figure I.10. Theoretical Flutter Frequency Parameter (ω_f/ω_2) vs μM for Stated Conditions.

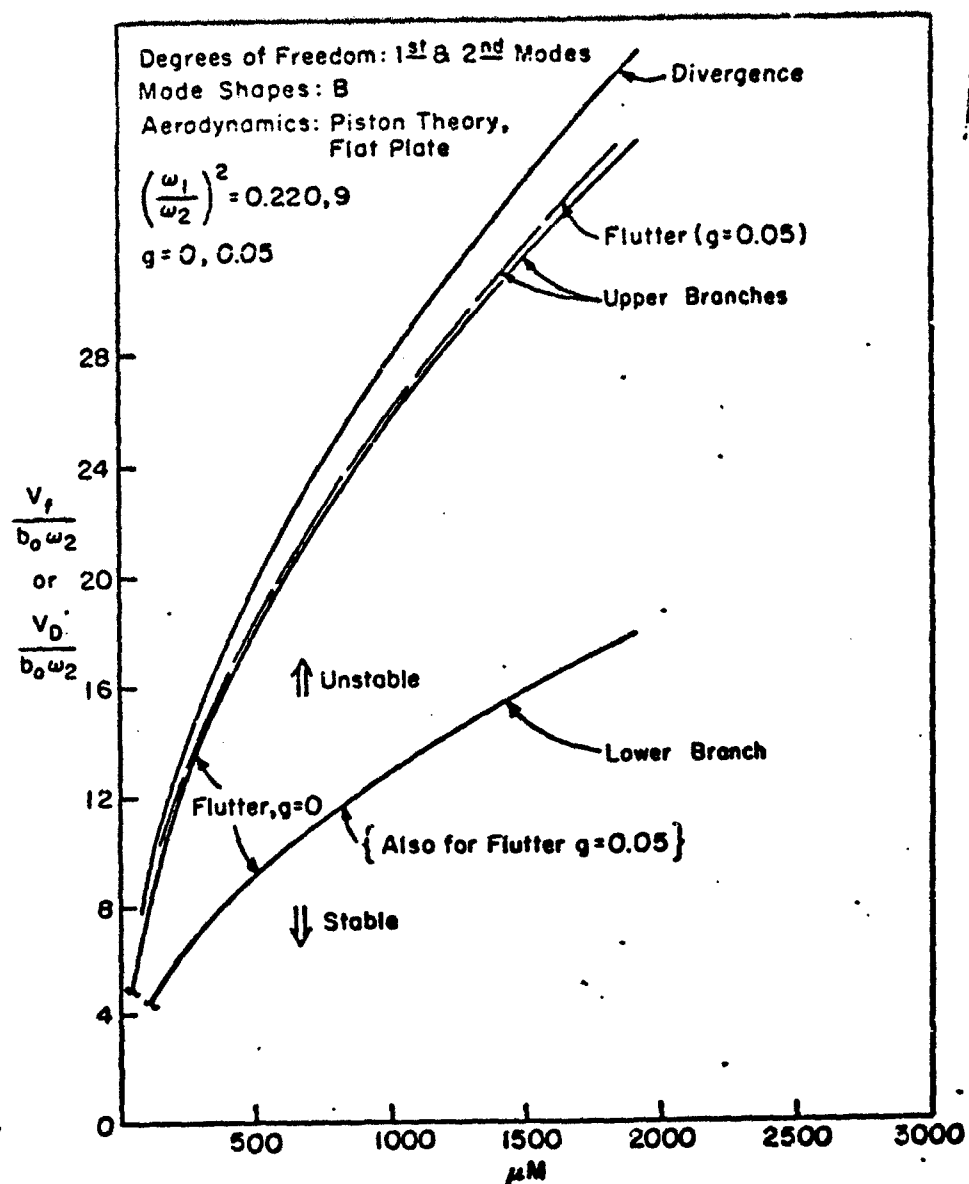


Figure I.11. Theoretical Flutter Parameter ($V_f/b_0 \omega_2$) and Static Divergence Parameter ($V_D/b_0 \omega_2$) vs μM for Stated Conditions.

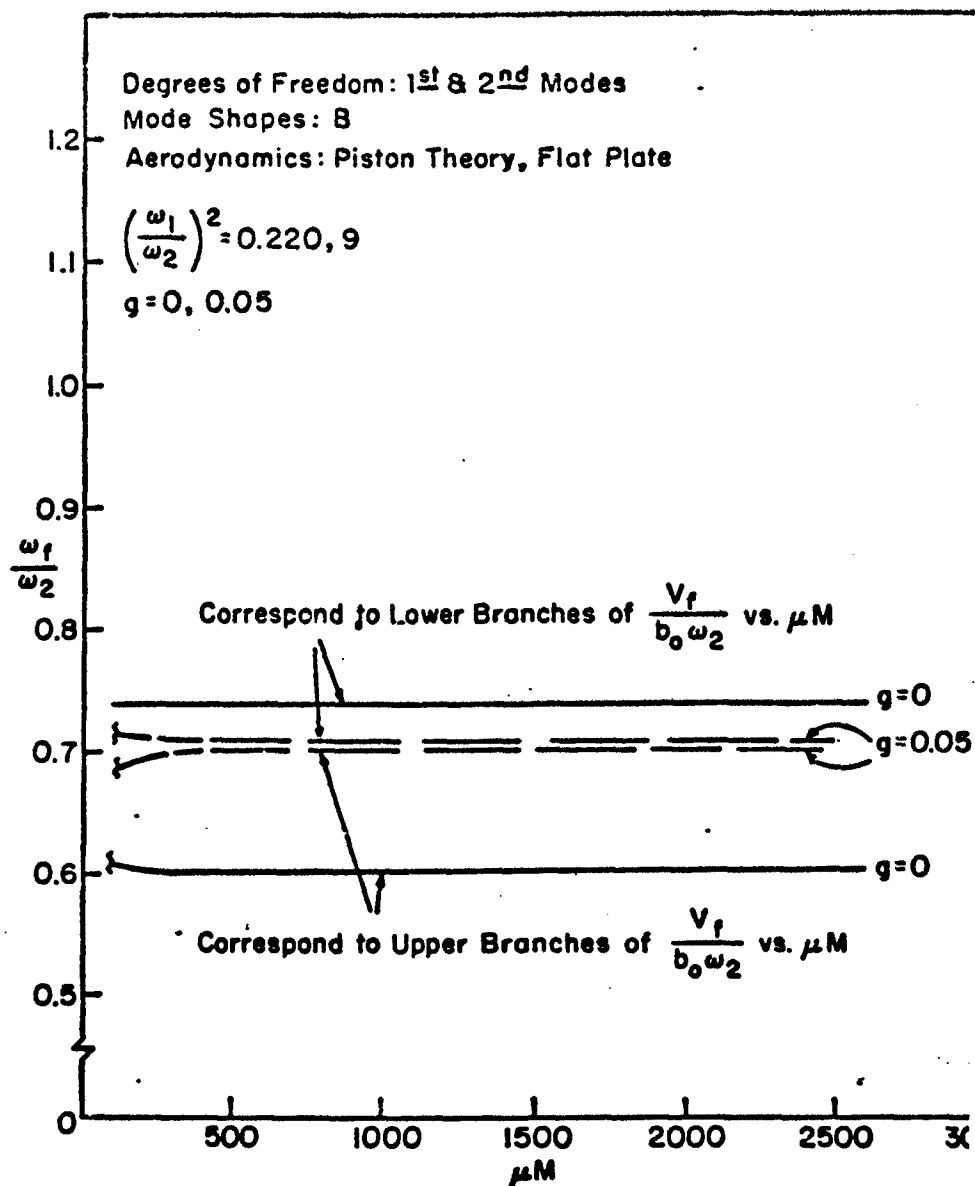


Figure I.12. Theoretical Flutter Frequency Parameter (ω_f/ω_2) vs μM for Stated Conditions.

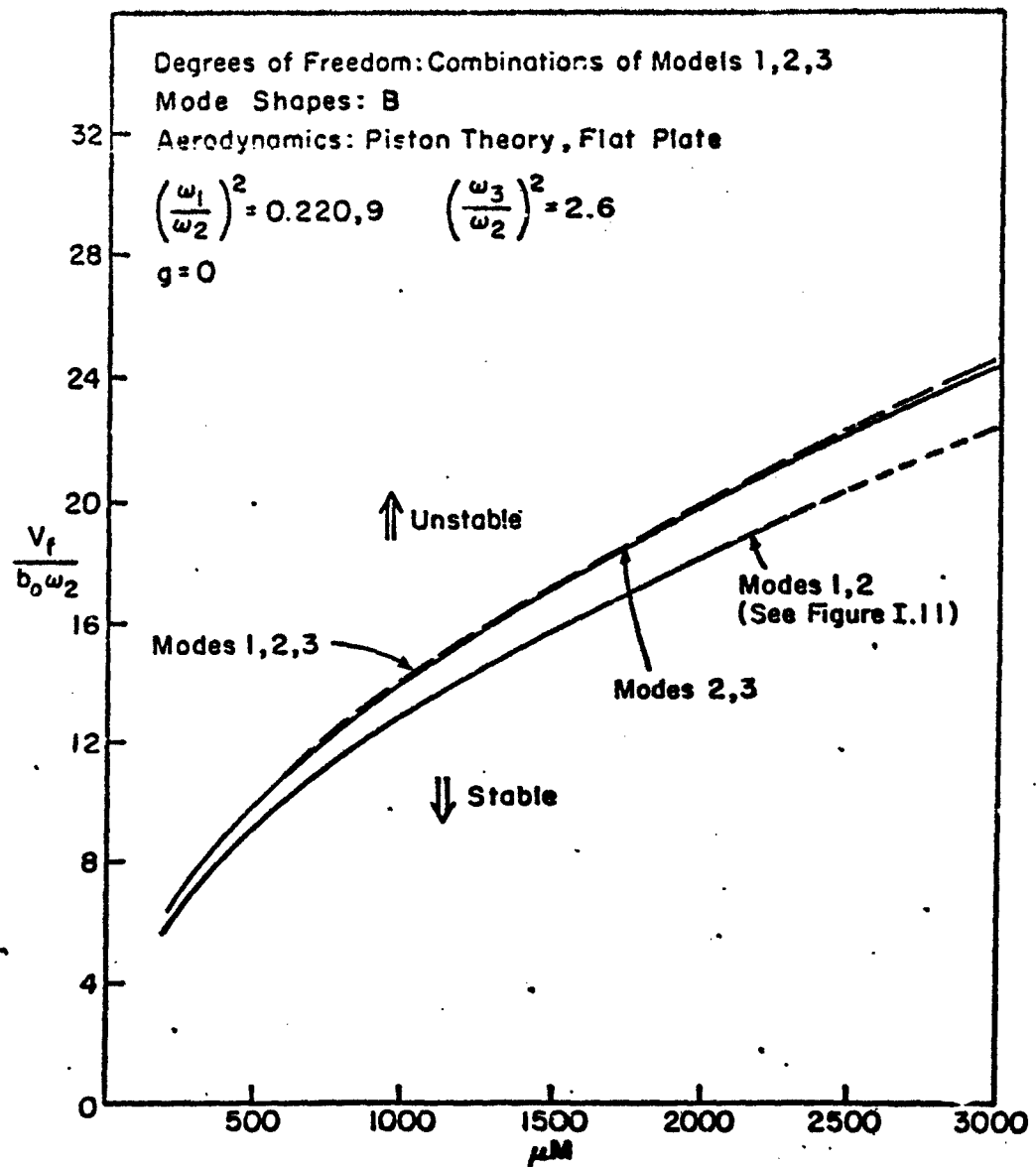


Figure I.13. Theoretical Flutter Parameter ($V_f/b_0 \omega_2$) vs μM for Stated Conditions.

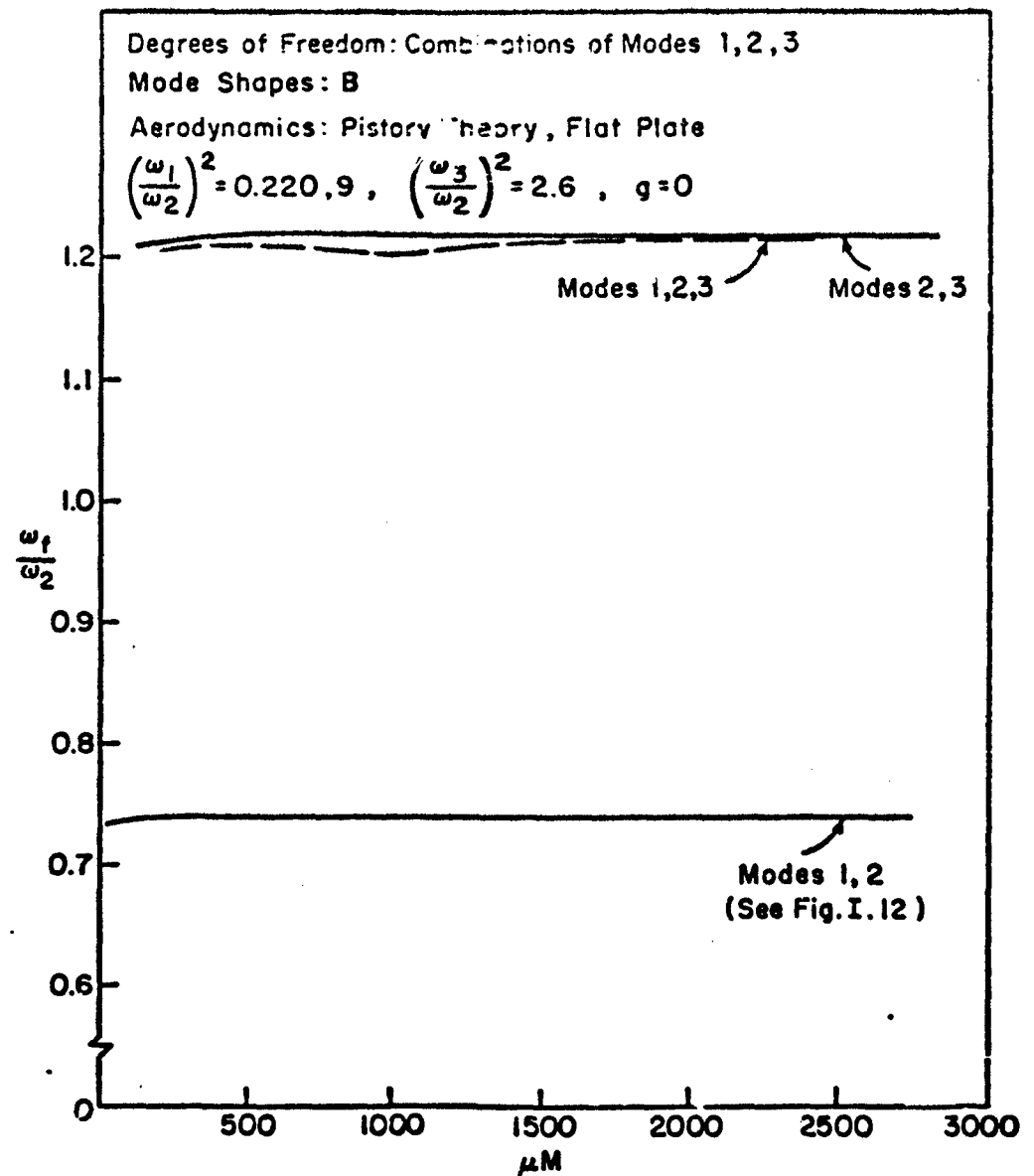


Figure I.14. Theoretical Flutter Frequency Parameter (ω_f/ω_2) vs μM for Stated Conditions.

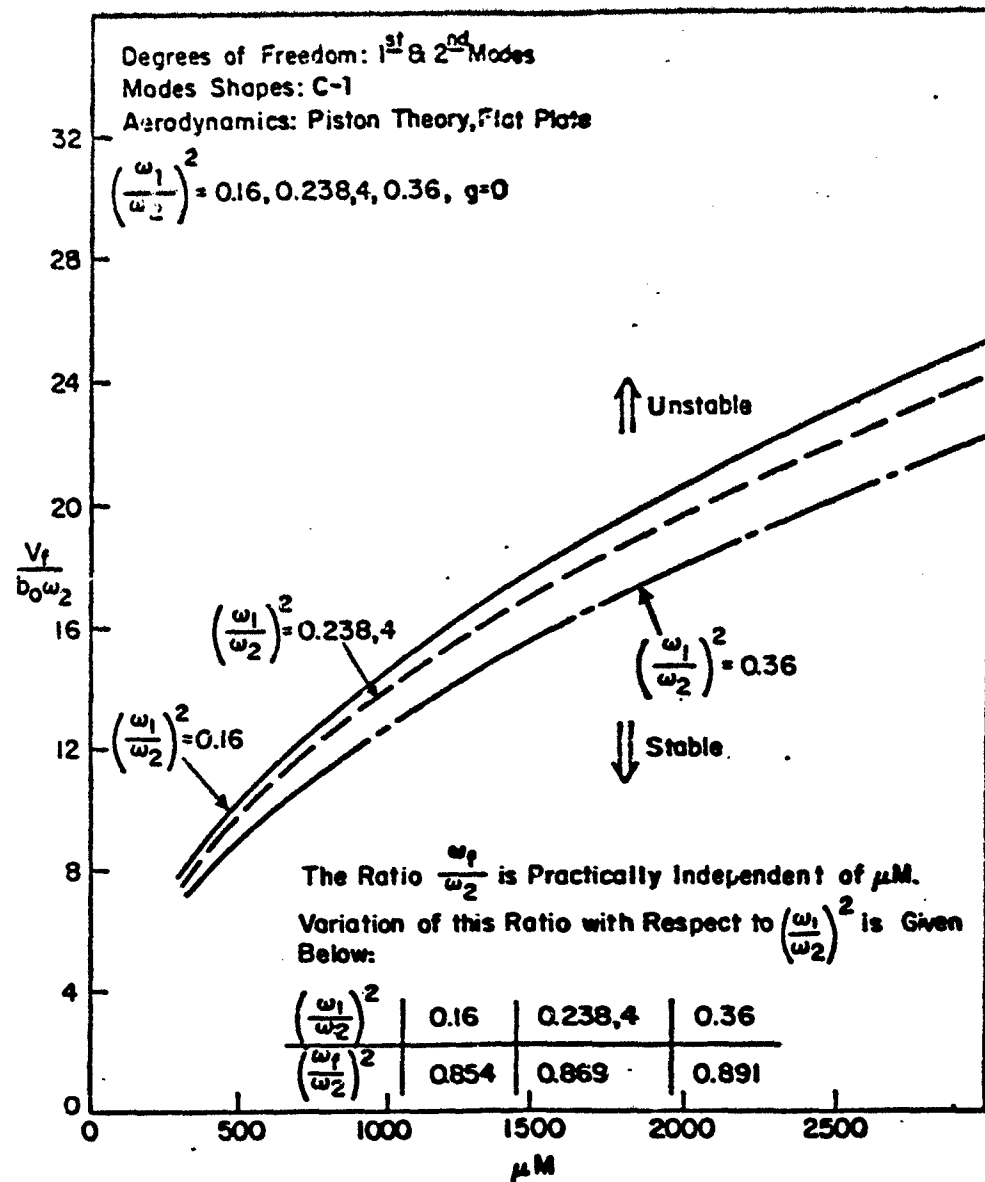


Figure I.15. Theoretical Flutter Parameter ($V_f/b_0\omega_2$) and Flutter Frequency Parameter (ω_f/ω_2) vs μM for Stated Conditions.

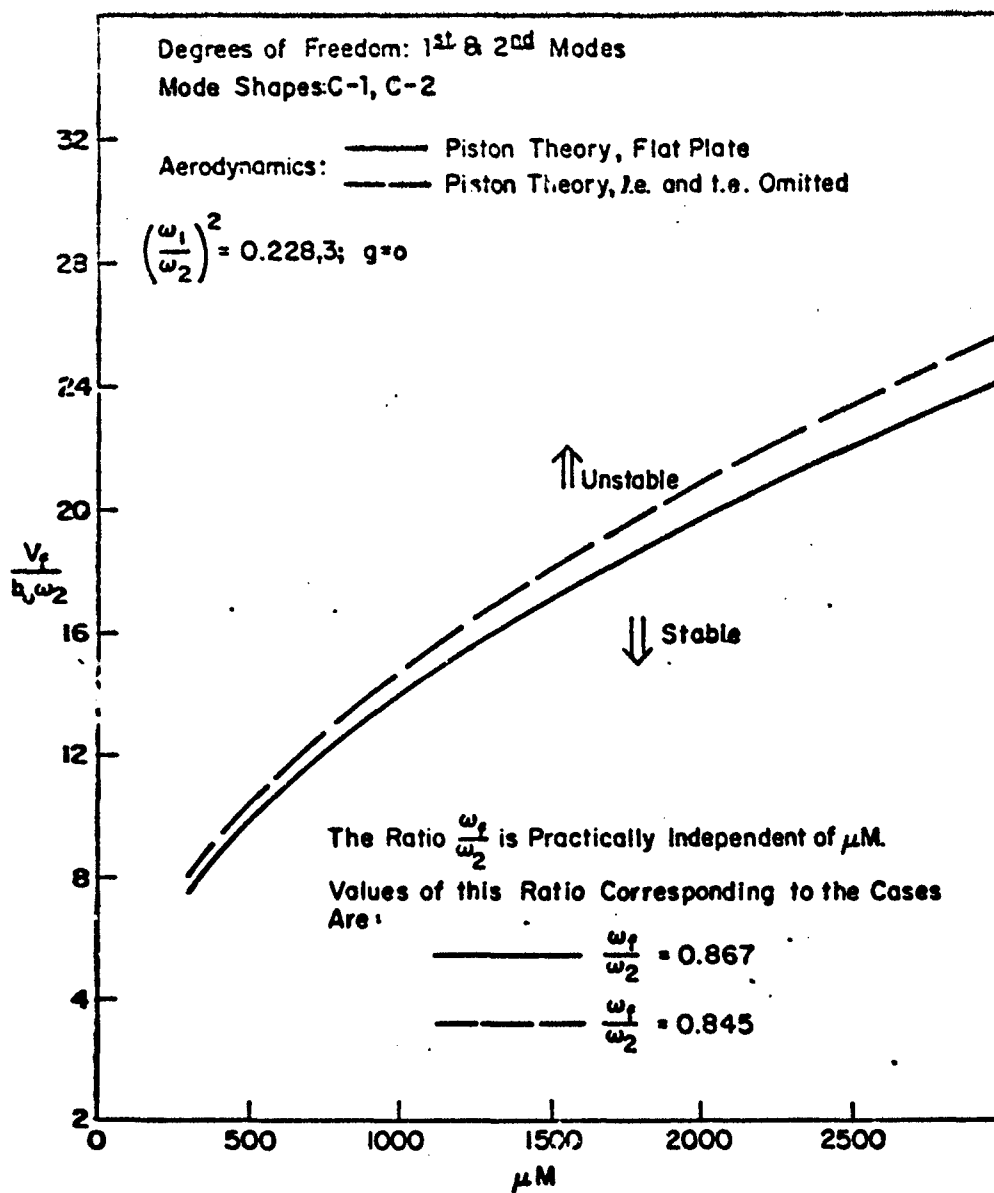


Figure I.16. Theoretical Flutter Parameter ($V_F/b\omega_2$) and Flutter Frequency Parameter (ω_F/ω_2) vs μM for Stated Conditions.

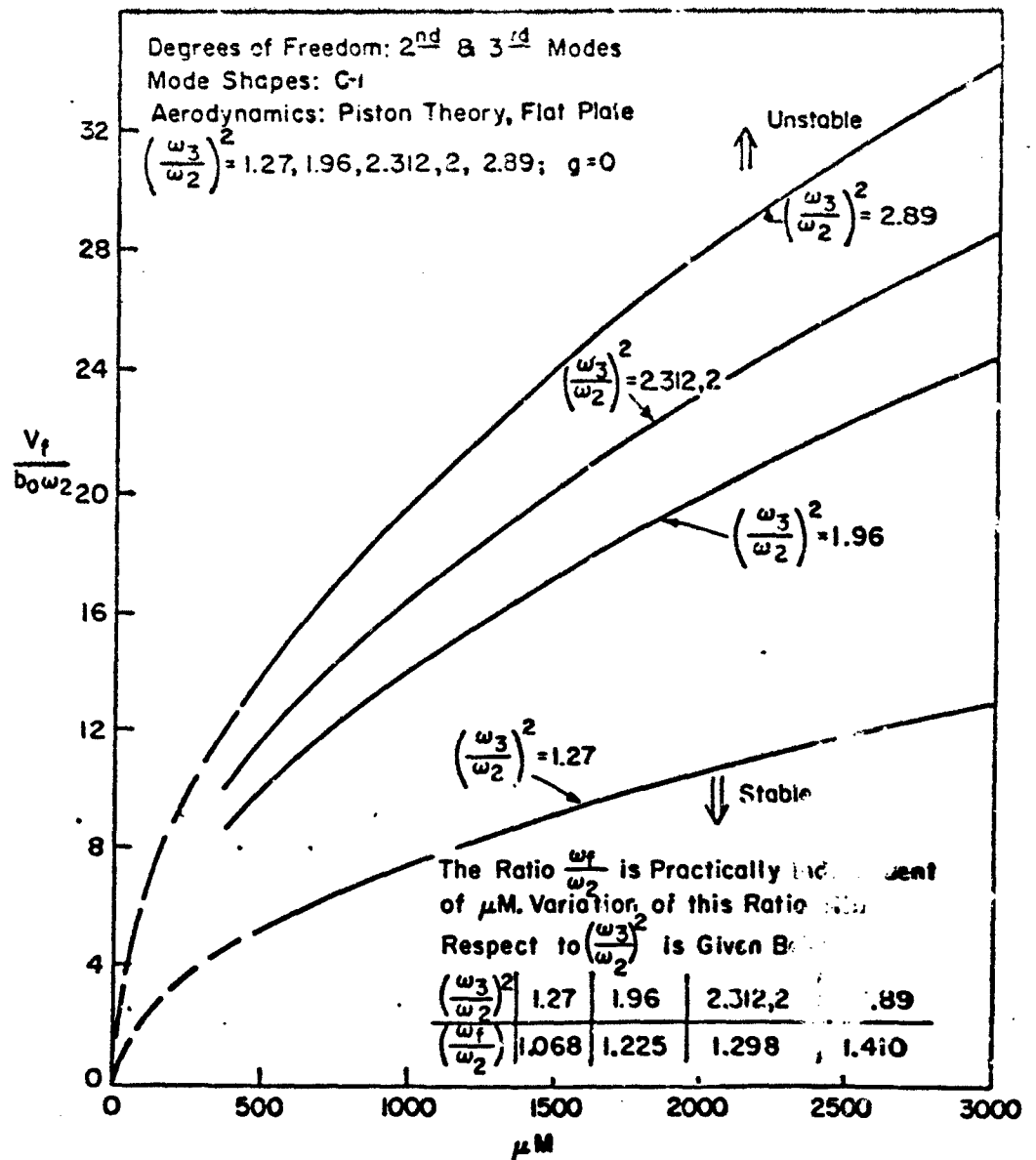


Figure I.17. Theoretical Flutter Parameter ($V_f/b_0\omega_2$) and Flutter Frequency Parameter (ω_f/ω_2) vs μM for Stated Conditions.

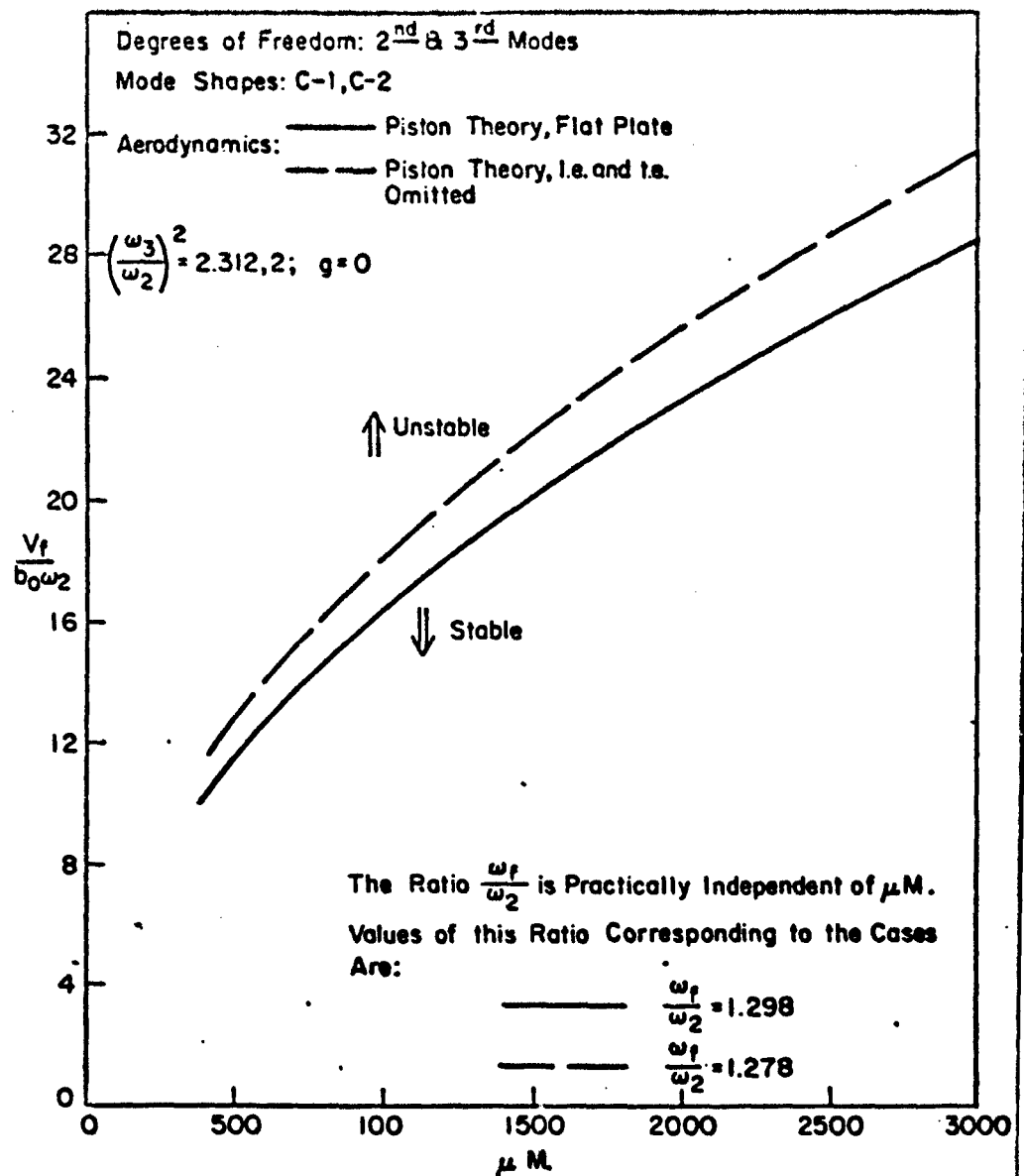


Figure I.18. Theoretical Flutter Parameter ($V_f/b_0\omega_2$) and Flutter Frequency Parameter (ω_f/ω_2) vs μM for Stated Conditions.

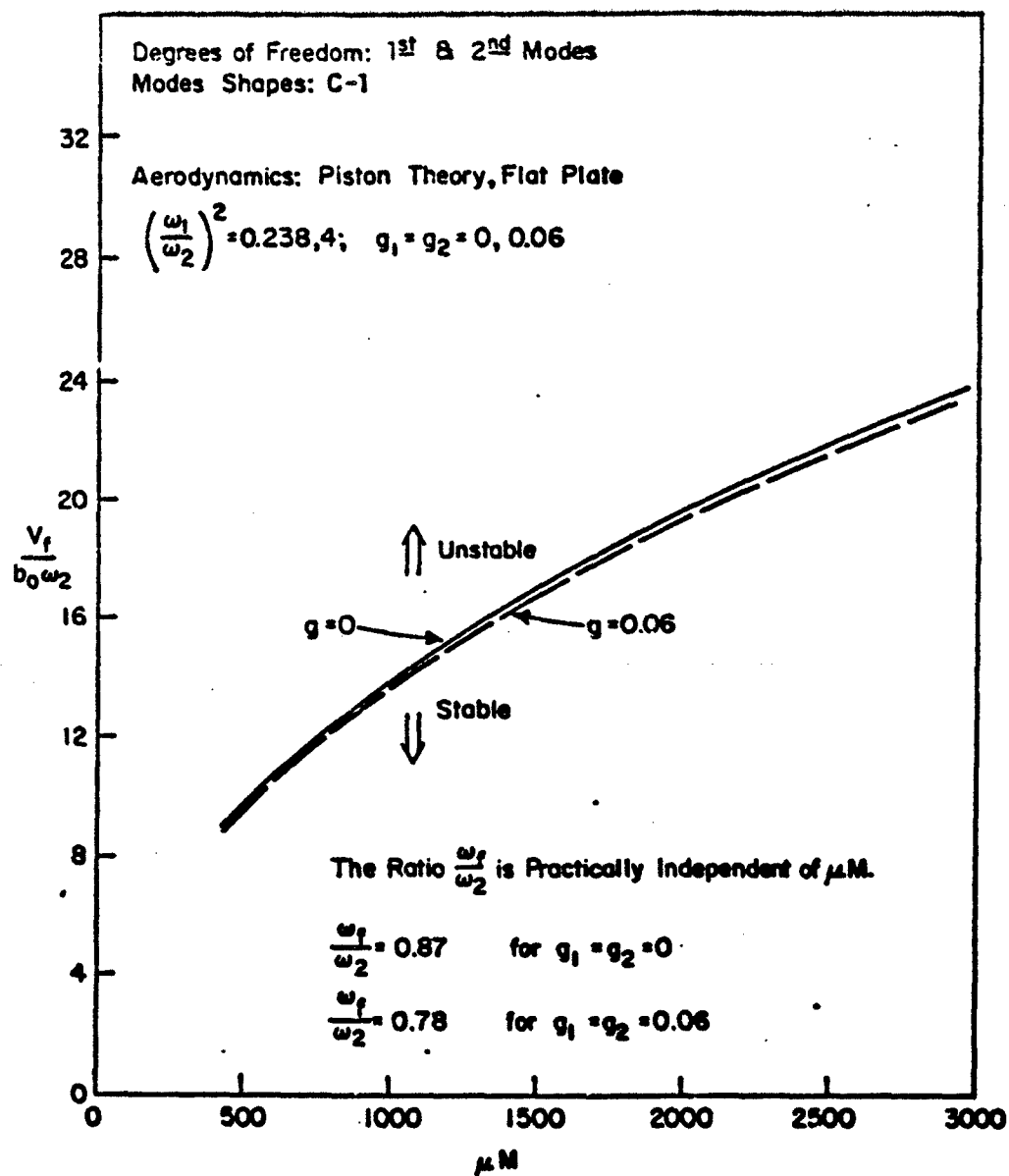


Figure I.19. Theoretical Flutter Parameter ($V_f/b_0\omega_2$) and Flutter Frequency Parameter (ω_f/ω_2) vs μM for Stated Conditions.

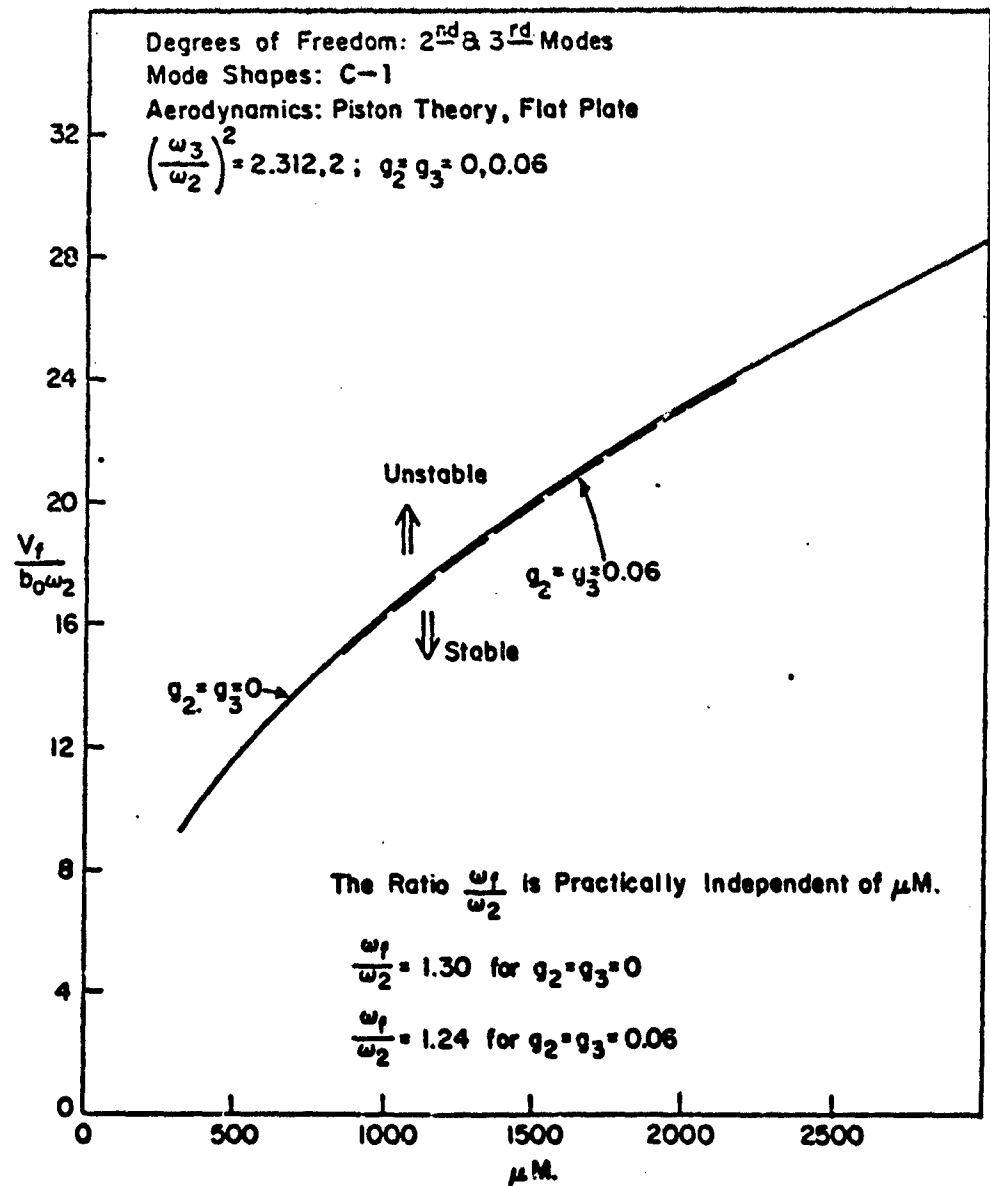


Figure I.20. Theoretical Flutter Parameter ($V_f/b_0\omega_2$) and Flutter Frequency Parameter (ω_f/ω_2) vs μM for Stated Conditions.

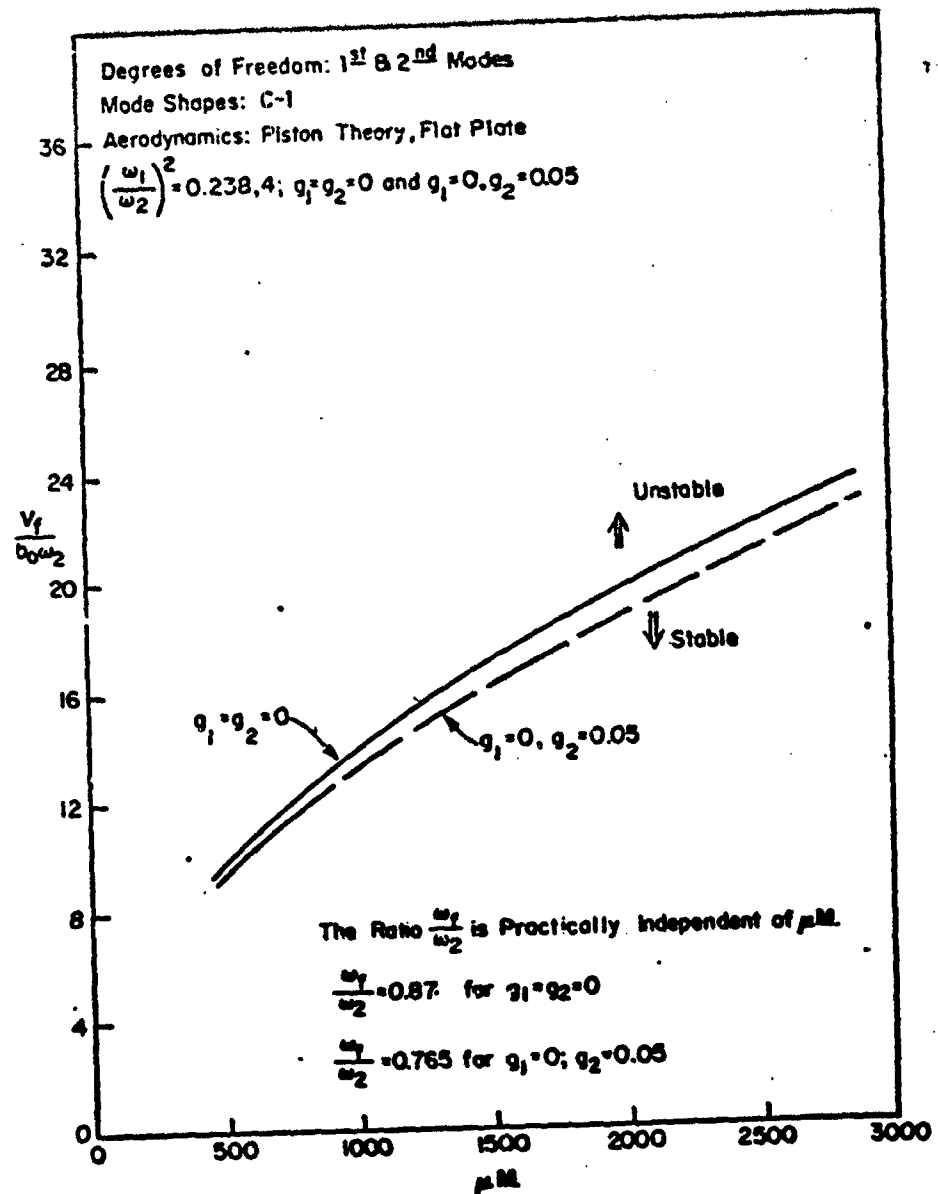


Figure I.21. Theoretical Flutter Parameter ($V_f/b_0\omega_2$) and Flutter Frequency Parameter (ω_f/ω_2) vs μM for Stated Conditions.

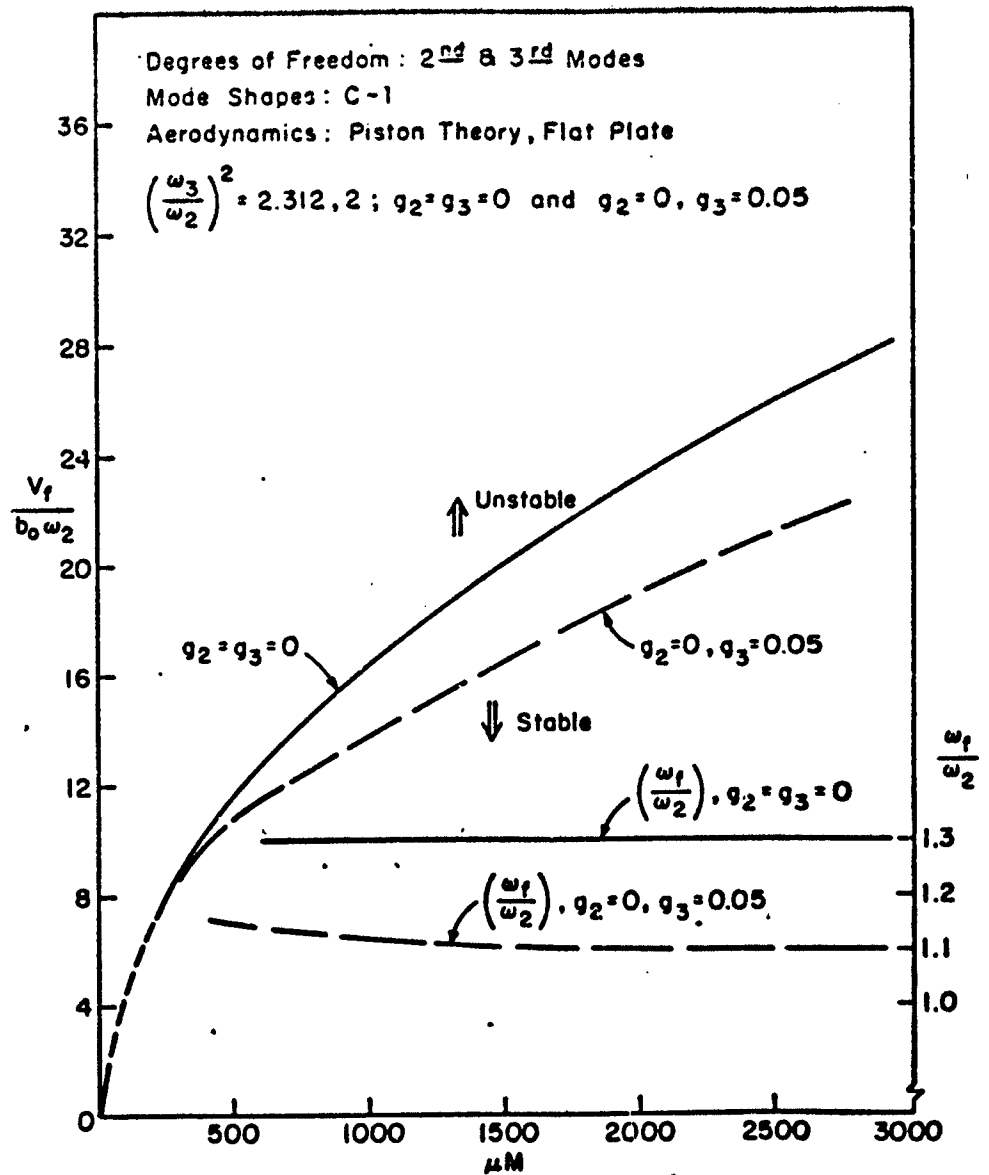


Figure I.22. Theoretical Flutter Parameter ($V_f/b_0\omega_2$) and Flutter Frequency Parameter (ω_f/ω_2) vs μM for Stated Conditions.

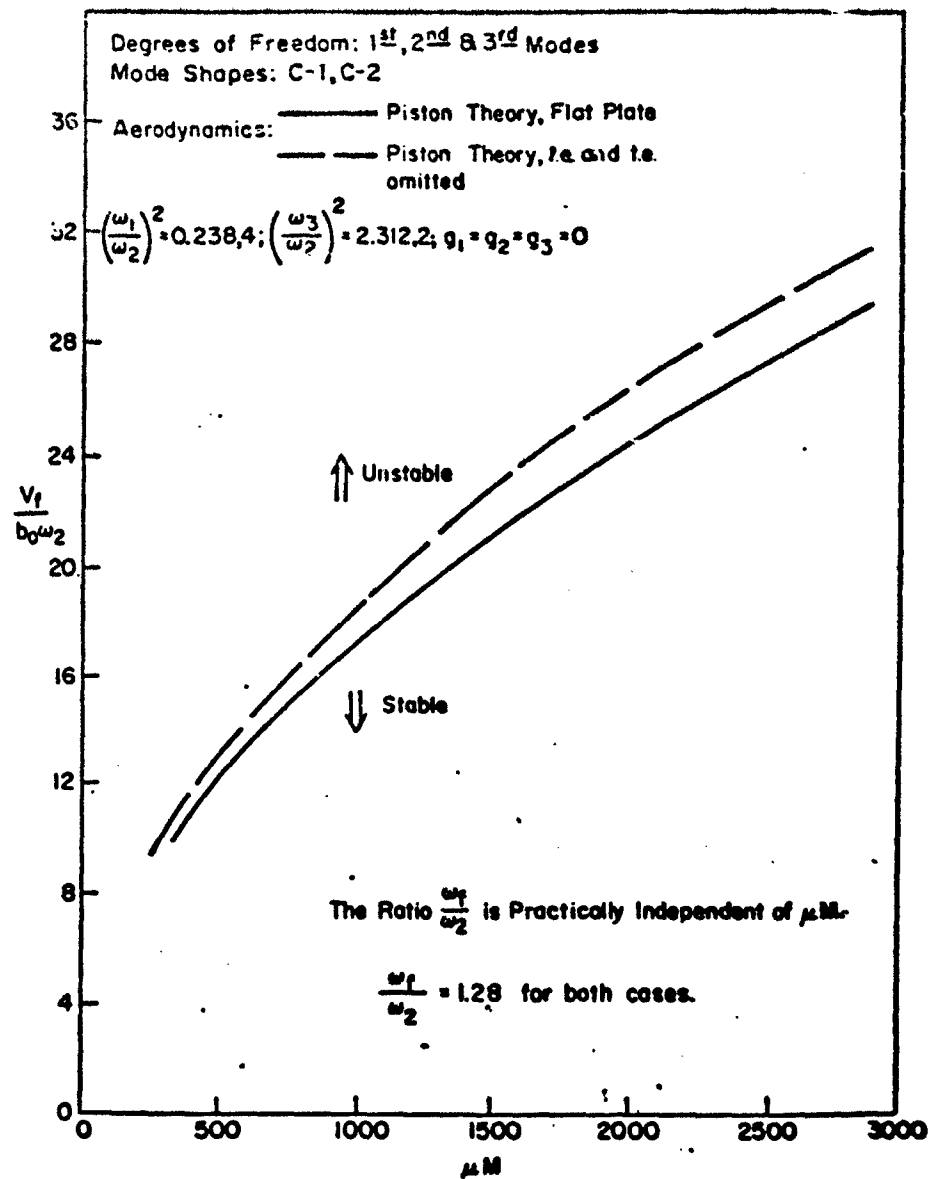


Figure I.23. Theoretical Flutter Parameter ($V_f/b_0 \omega_2$) and Flutter Frequency Parameter (ω_f/ω_2) vs μM for Stated Conditions.

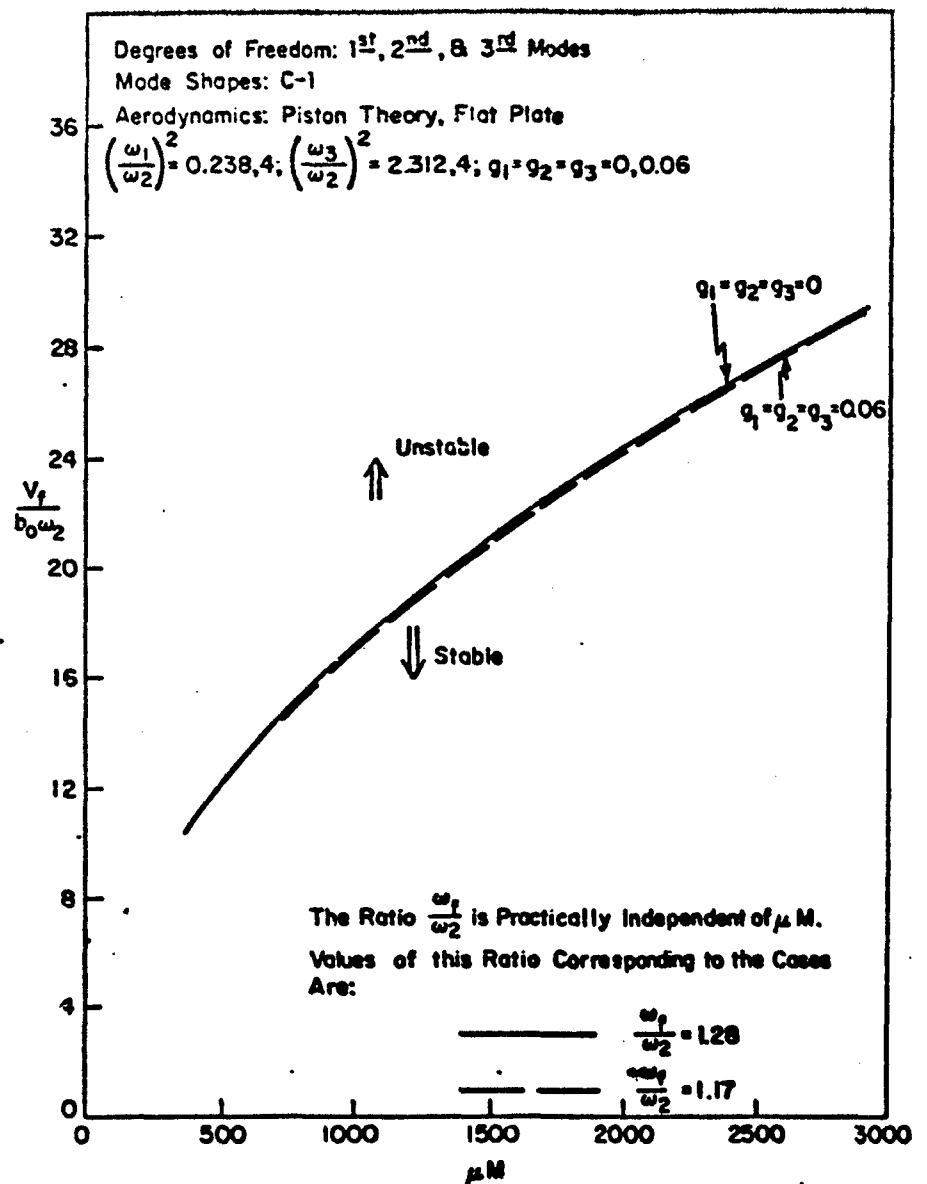


Figure I.24. Theoretical Flutter Parameter ($V_f/b_0\omega_2$) and Flutter Frequency Parameter (ω_f/ω_2) vs μM for Stated Conditions.

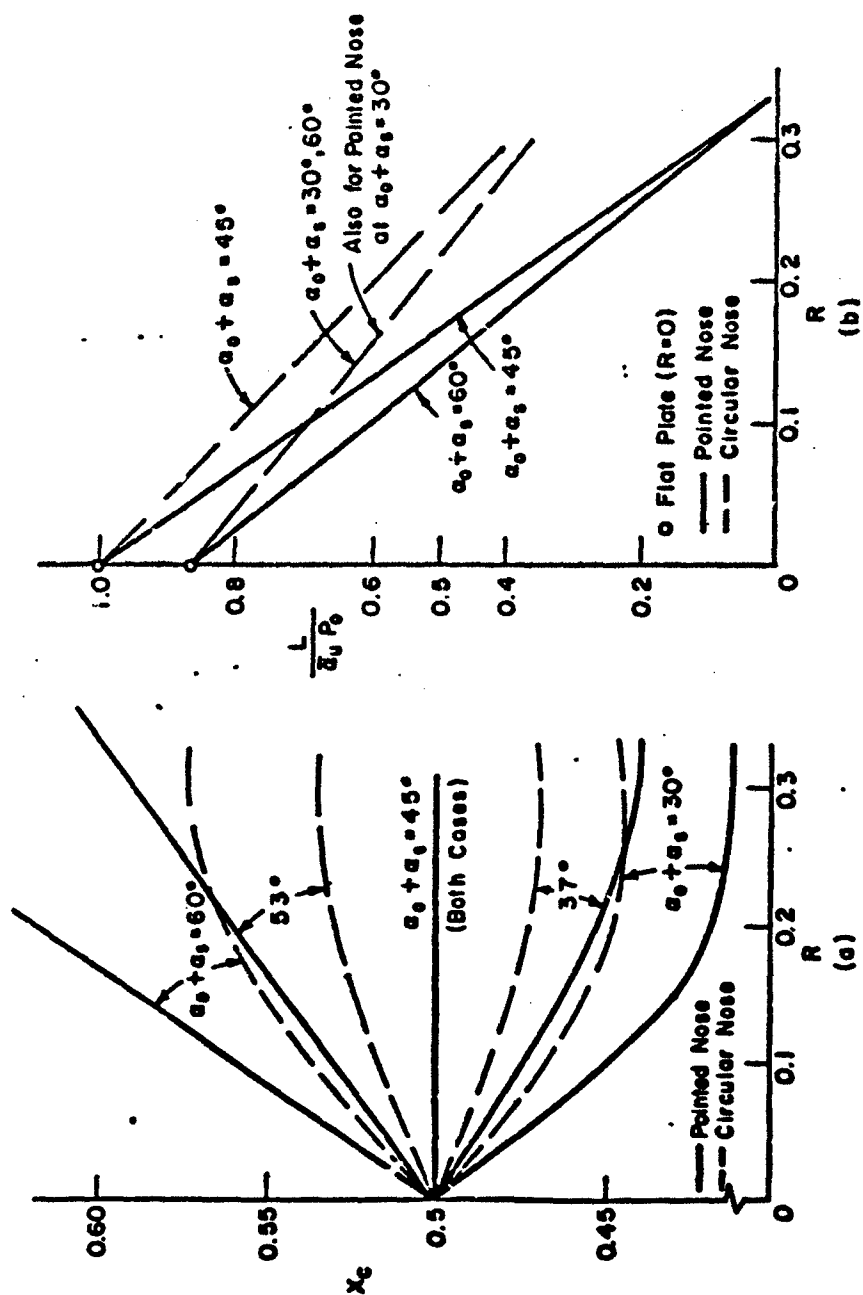


Figure I.25. Variations of Center-of-Pressure Location and Force L with Bluntness and Initial Angle of Attack, for Various Two-Dimensional Sections.

TABLE I.1 SUMMARY AND INDEX OF FLUTTER AND DIVERGENCE ANALYSES

Modes Considered	Node Shape Set	Damping Coefficient δ	Frequency		Aerodynamic Theory*	Location of Flutter Results		Location of Static Divergence Results
			$\left(\frac{\omega}{\omega_0}\right)^2$	Ratio $\left(\frac{\omega}{\omega_0}\right)^2$		$\frac{V_f}{V_D}$ vs $\frac{\omega}{\omega_0}$	$\frac{\omega_f}{\omega_D}$ vs $\frac{\omega}{\omega_0}$	
1,2	A	$\delta = 0, 0.1$	0.220, 9	--	P	Fig. 1.7	Fig. 1.7	Fig. 1.7
1,2	A	$\delta = 0$	0.220, 9	--	T	Fig. 1.9	Fig. 1.8	Fig. 1.5
1,2	B	$\delta = 0, 0.05$	0.220, 9	--	P	Fig. 1.11	Fig. 1.10	Fig. 1.10
2,3	B	$\delta = 0$	--	2.6	P	Fig. 1.13	Fig. 1.14	No divergence
1,2,3	B	$\delta = 0$	0.220, 9	2.6	P	Fig. 1.13	Fig. 1.14	No divergence
1,2	C-1	$\delta = 0$	Variable	--	P	Fig. 1.15	Fig. 1.15	No divergence
1,2	C-1, -2	$\delta = 0$	0.228, 3	--	P, PM	Fig. 1.16	Fig. 1.16	--
2,3	C-1	$\delta = 0$	--	Variable	P	Fig. 1.17	Fig. 1.17	--
2,3	C-1, -2	$\delta = 0$	--	2.312, 2	P, PM	Fig. 1.18	Fig. 1.18	--
1,2	C-1	$\delta_1 = \delta_2 = 0, 0.06$	0.238, 4	--	P	Fig. 1.19	Fig. 1.19	--
2,3	C-1	$\delta_2 = \delta_3 = 0, 0.06$	--	2.312, 2	P	Fig. 1.20	Fig. 1.20	--
1,2	C-1	Variable	0.238, 4	--	P	Fig. 1.21	Fig. 1.21	--
2,3	C-1	$\delta_1 = \delta_2 = 0$ and $\delta_1 - \delta_2 = 0.05$	--	2.312, 2	P	Fig. 1.22	Fig. 1.22	--
1,2,3	C-1, -2	$\delta_2 = \delta_3 = 0$ and $\delta_2 - \delta_3 = 0.05$	0.238, 4	2.312, 2	P, PM	Fig. 1.23	Fig. 1.23	No divergence
1,2,3	C-1	$\delta = 0, 0.06$	0.238, 4	2.312, 2	P	Fig. 1.24	Fig. 1.24	--

* P - Piston theory; PM - Piston theory omitting leading and trailing-edge region; T - Transonic theory.

APPENDIX II

MEMBRANE-TYPE FLUTTER OF AN INFLATABLE PANEL

by Marten T. Landahl

A. SIMPLIFIED MATHEMATICAL MODEL

Following Miles (Ref. II.1) we will consider the stability of two-dimensional waves travelling on a stationary panel of infinitive length with a deformation of the form

$$w = \text{Re} \{ \bar{w} e^{ik(x-ct)} \} \quad (\text{II.1})$$

where w is the instantaneous deformation (assumed infinitesimal), $k = (2\pi/\lambda)$ is the wave number, c is the wave velocity, and λ the wave length. It will be assumed that the panel is exposed to flow of a constant Mach number $M = (V/a)$ and density ρ on both sides (Fig. II.1):

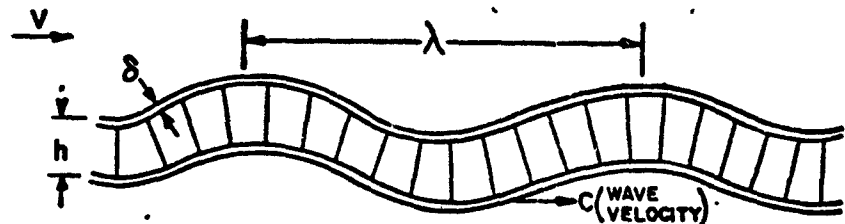


Figure II.1

This model will be useful for an approximate analysis of waves of short wave length so that edge effects may be neglected. Also, it can be used as an approximation for nonuniform outside flow (as would be created by

the disturbances due to the vehicle itself), provided the wave-length λ is so small that flow parameters vary little over the distance of one wave length. A more general analysis would require different flows on the two sides of the panel, but this would unduly complicate the analysis. For the case of vacuum, or very low velocity on one side the present analysis will hold if the aerodynamic forcing term in the equations below is reduced by one half its value.

B. AERODYNAMIC CONSIDERATIONS

The disturbance pressure created by a small amplitude travelling wave of the form (II.1) may easily be calculated, since it must be the same as that on a steady wavy wall in a stream of velocity $(V-c)$. One thus easily finds that the pressure induced on the upper surface of the panel is

$$p - p_{\infty} = - \frac{\rho k (V-c)^2 \bar{w} e^{ik(x-ct)}}{\sqrt{1 - M^2 \left(1 - \frac{c}{V}\right)^2}} \quad (\text{II.2})$$

(The denominator is simply the Prandtl-Glauert correction). Similarly, for a wave that is supersonic with respect to the stream $[(V-c) > a]$ one obtains

$$p - p_{\infty} = \frac{i \rho k (V-c)^2 \bar{w} e^{ik(x-ct)}}{\sqrt{M^2 \left(1 - \frac{c}{V}\right)^2 - 1}} \quad (\text{II.3})$$

Since there is an equal pressure disturbance, but with opposite sign, on the lower surface, the total aerodynamic loading on the panel is

$$q_A = \bar{q}_A e^{ik(x-ct)} = \frac{2\rho k(V-c)^2}{\sqrt{1-M^2(1-\frac{c}{V})^2}} \bar{w} e^{ik(x-ct)} \quad (II.4)$$

for a subsonic wave, and

$$q_A = \bar{q}_A e^{ik(x-ct)} = -\frac{2\rho k(V-c)^2}{\sqrt{M^2(1-\frac{c}{V})^2-1}} \bar{w} e^{ik(x-ct)} \quad (II.5)$$

for a supersonic wave.

These loadings are conveniently expressed in form of an "aerodynamic impedance"

$$Z_A = \frac{\bar{q}_A}{\bar{w}}$$

$$= \begin{cases} \frac{2\rho k(V-c)^2}{\sqrt{1-M^2(1-\frac{c}{V})^2}} & \text{for subsonic wave} \\ -\frac{2\rho k(V-c)^2}{\sqrt{M^2(1-\frac{c}{V})^2-1}} & \text{for supersonic wave} \end{cases} \quad (II.6)$$

C. STRUCTURAL CONSIDERATIONS

The two-dimensional inflatable panel possesses shear deformation and rotary inertia, and as such can be represented as a Timoshenko beam (see for example, Ref. II.2, Chap. 3, Eqs. 3-4 to 3-6). The governing panel equation would then be

$$D w_{xxxx} - \left(I + \frac{Dm}{p_2 h} \right) \ddot{w}_{xx} + m \ddot{w} + \frac{mI}{p_2 h} \ddot{\bar{w}} = q + \frac{I}{p_2 h} \ddot{\bar{q}} - \frac{D}{p_2 h} q_{xx} \quad (\text{II.7})$$

where $D = E\delta h^2/2$ is the overall panel bending stiffness, $I = mh^2/4$ is the rotary inertia, m is the mass per unit length, $p_2 h$ is the shear stiffness due to internal pressure and q is loading per unit length. The contribution of drop chord mass to I and m may be neglected.

To give the panel the travelling wave deflection w of Eq. (II.1) would require a loading q of the type

$$q = \bar{q} e^{ik(x-ct)} \quad (\text{II.8})$$

Upon introduction of this and Eq. (II.1) into Eq. (II.7), one obtains

$$\bar{q} = k^2 m \bar{w} \frac{c^4 - \left(\frac{p_2 h}{m} + \frac{D}{I} + \frac{p_2 h}{I k^2} \right) c^2 + \frac{D p_2 h}{I m}}{\left(\frac{D}{I} + \frac{p_2 h}{I k^2} - c^2 \right)} \quad (\text{II.9})$$

As with the aerodynamic forcing term we write this result in form of a "structural impedance" Z_s , given by

$$Z_s = \frac{\bar{F}}{w} = k^2 m \frac{C^4 - \left(\frac{p_d h}{m} + \frac{D}{I} + \frac{p_d h}{I k^2} \right) C^2 + \frac{D p_d h}{I m}}{\left(\frac{D}{I} + \frac{p_d h}{I k^2} - C^2 \right)} \quad (\text{II.10})$$

It is instructive to express this as follows:

$$Z_s = k^2 m \frac{(C_1^2 - C^2)(C_2^2 - C^2)}{(C_0^2 - C^2)} \quad (\text{II.11})$$

where

$$C_1^2 = \frac{1}{2} \left(\frac{p_d h}{m} + \frac{D}{I} + \frac{p_d h}{I k^2} \right) - \sqrt{\frac{1}{4} \left(\frac{p_d h}{m} + \frac{D}{I} + \frac{p_d h}{I k^2} \right)^2 - \frac{p_d h D}{I m}} \quad (\text{II.12})$$

$$C_2^2 = \frac{1}{2} \left(\frac{p_d h}{m} + \frac{D}{I} + \frac{p_d h}{I k^2} \right) + \sqrt{\frac{1}{4} \left(\frac{p_d h}{m} + \frac{D}{I} + \frac{p_d h}{I k^2} \right)^2 - \frac{p_d h D}{I m}} \quad (\text{II.13})$$

$$C_0^2 = \frac{D}{I} + \frac{p_d h}{I k^2} \quad (\text{II.14})$$

The impedance of the structure is thus zero when excited at the wave velocities $C = \pm C_1$, and $C = \pm C_2$. Hence, these are the phase velocities for free surface waves

(in vacuum). At $C=C_0$ the structure has infinite rigidity, i.e., it acts as a "dynamic vibration damper." It turns out that

$$C_1 < C_0 < C_2 \quad (\text{II.15})$$

so that, in principle, the structural impedance varies with wave velocity as shown in Fig. II.2.

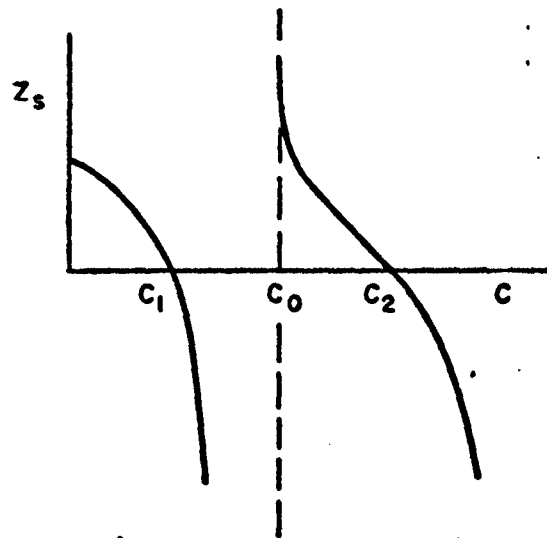


Figure II.2

To simplify the discussion we will consider the following two extreme cases:

a) Pure Shear

Pure shear deformation is obtained for $D \rightarrow \infty$ with h finite. Then, (II.12) - (II.14) give

$$C_1^2 \rightarrow \frac{p_d h}{m} \quad (\text{II.16})$$

$$C_2^2 \rightarrow C_0^2 \rightarrow \frac{D}{I} \rightarrow \infty \quad (\text{II.16a})$$

Hence

$$Z_S \rightarrow m k^2 \left(\frac{p_d h}{m} - C^2 \right) \quad (\text{II.17})$$

b) Pure Bending

In this case we let $p_d h \rightarrow \infty$ keeping D finite. This gives

$$C_1^2 \rightarrow \frac{D k^2}{I k^2 + m} \quad (\text{II.18})$$

$$C_2^2 \rightarrow \frac{p_d h}{m} + \frac{p_d h}{I k^2} \rightarrow \infty \quad (\text{II.19})$$

$$C_0^2 \rightarrow \frac{p_d h}{I k^2} \rightarrow \infty \quad (\text{II.20})$$

which in turn leads to

$$Z_S \rightarrow m k^2 \left(1 + \frac{I k^2}{m} \right) \left[\frac{k^2 D}{m + I k^2} - C^2 \right] \quad (\text{II.21})$$

Practical configurations tend to lie between these two extremes, perhaps closer to the shear case.

In both cases, the structural impedance is of the

form

$$Z_s = m_e k^2 (C_e^2 - C^2) \quad (\text{II.22})$$

where, for pure shear,

$$m_e = m \quad (\text{II.23})$$

$$C_e^2 = \frac{k_2 h}{m} \quad (\text{II.24})$$

whereas, for pure bending,

$$m_e = m + I k^2 \quad (\text{II.25})$$

$$C_e^2 = \frac{k^2 D}{m + I k^2} \quad (\text{II.26})$$

The expression (II.22) will be used in the following discussion. By inserting typical parameter values it turns out that C_e is of the order 100 - 200 ft/sec., i.e., rather small compared to flight velocities of interest. This is of crucial importance for the instability problem as will be seen below.

D. STRUCTURAL DAMPING

To avoid complications, structural damping will be introduced, without consideration of how it originates physically, simply by replacing C_e by

$$C_e (1 - i\epsilon_e) \quad (\text{II.27})$$

where \mathcal{E}_e is an equivalent "damping ratio" such that the free surface waves are reduced in amplitude by the factor

$$e^{-2\pi\mathcal{E}_e} \quad (\text{II.28})$$

over each cycle of an oscillation. In principle, \mathcal{E}_e could be obtained from experiments. It will be assumed that the damping is small so that terms that are quadratic in \mathcal{E}_e may be neglected.

With damping, the impedance (II.22) that before was purely real now becomes complex, so that

$$Z_s = Z_{sR} + iZ_{sI} \quad (\text{II.29})$$

where

$$Z_{sR} = m_e k^2 (c_e^2 - c^2) \quad (\text{II.30})$$

$$Z_{sI} = -m_e k^2 c_e \mathcal{E}_e \quad (\text{II.31})$$

E. EIGENVALUE PROBLEM

Self-sustained motion can occur when the aerodynamic and structural impedances match, i.e., when

$$Z_A(c) = Z_s(c) \quad (\text{II.32})$$

where Z_A is given by (II.6), and (II.22) will be used for Z_s . This equation can then be solved for the (generally complex) eigenvalue (s) C of the problem for a given set of system parameters and k . If the imaginary part of the eigenvalue C is positive, the waves will

grow exponentially with time, i.e., flutter sets in. In view of the fact that the aerodynamic impedance changes from purely real (for real C) for a subsonic wave to purely imaginary for a supersonic wave, the two cases are best discussed separately.

F. STABILITY OF SUBSONIC WAVES

The simplest approach for a wave that is subsonic relative to the stream is to first consider a panel with zero structural damping for which the eigenvalue relation (II.32) takes the form

$$\frac{2\rho k(V-c)^2}{\sqrt{1-M^2(1-\frac{c}{V})^2}} = m_e k^2(C_e^2 - C^2) \quad (\text{II.33})$$

The arch type of a subsonic wave is the incompressible one, $M=0$. The incompressible cases have been thoroughly discussed by Landahl (Ref. II.3) and by Brooke Benjamin (Ref. II.4).

For real C , (II.33) is purely real and expresses a balance between the aerodynamic stiffness (on the left-hand side of the equation) and the mechanical stiffness - inertial reaction (right-hand side). It was shown in Ref. II.3 that, for $M=0$, the two roots of (II.33) are real for sufficiently low V and thus correspond to two neutrally stable waves labelled Class A and Class B, respectively. The Class A wave speed is essentially the root $C=-C_e$ for $\rho=0$, modified by the presence of the air flow and thus increased. The Class B wave speed corresponds to the free-surface wave speed $C=C_e$, modified (lowered) by the flow. For increasing forward speeds or densities, there may eventually be no wave speed for which the two

sides of (II.33) balance, and the resultant mechanical stiffness will consequently always be insufficient to balance the aerodynamic forces. In such a case, the two eigenvalues for C become complex conjugates indicating the onset of a violent Class C or Kelvin-Helmholtz-type instability. This was the type of flutter considered by Miles (Ref. II.1).

The effect of (small) structural damping on stability was considered in detail by Landahl (Ref. II.3). He demonstrated that damping may make the Class A wave (mildly) unstable, but stabilizes the Class B wave. In contrast it has very little effect on the Class C wave. It was also shown by Brooke Benjamin (Ref. II.4) that for high density ratios $\mu = \rho_0/\rho$, the speed margin between the onset of Class A and Class C instabilities is inversely proportional to μ . It would therefore seem that Class C instability is the type of primary technical interest.

It also follows from (II.33) that the wave velocity for either Class A or Class C is always less than C_e . Since C_e for cases of practical interest for the present problem is likely to be small (< 200 ft/sec, say) a subsonic-type wave cannot be maintained for free stream speeds much beyond sonic, say beyond $M \approx 1.2$. From a practical standpoint, the stability of supersonic waves is therefore more of interest.

G. STABILITY OF SUPERSONIC WAVES .

For a wave that is supersonic with respect to the free stream the eigenvalue relation (II.32) becomes

$$\frac{-2i\rho k(V-c)^2}{\sqrt{M^2(1-\frac{c}{V})^2-1}} = m_e k^2 [C_e^2(1-i\varepsilon_e)^2 - C^2] \quad (\text{II.34})$$

Here we have included structural damping because without it no neutrally stable wave can exist. By separating the real and imaginary parts of (II.34) we find that flutter sets in for

$$C = C_e \quad (\text{II.35})$$

$$\frac{\rho (V_F - C_e)^2}{\sqrt{M^2 (1 - \frac{C_e}{V_F})^2 - 1}} = m_e k C_e^2 \epsilon_e \quad (\text{II.36})$$

Here we have neglected terms quadratic in ϵ_e . For Mach numbers well into the supersonic region (transonic Mach numbers will be considered later) C_e may be neglected compared to V_F and we thus obtain from (II.36)

$$V_F = C_e \sqrt{\mu_e \epsilon_e \beta} \quad (\text{II.37})$$

where

$$\mu_e = \frac{m_e k}{\rho}, \quad \beta = \sqrt{M^2 - 1}$$

It follows from (II.37) that since the flutter velocity is proportional to the \sqrt{k} , the long waves are more unstable than short ones. However, the analysis was based on the assumption that the wave length is much smaller than the chord. This is due to the fact that the structural damping decreases faster with decreasing wave number (as k^2) than does the aerodynamic out-of-phase forcing pressure. It is therefore unlikely that membrane type flutter will occur before ordinary-type flutter.

H. EFFECT OF BOUNDARY LAYER

Equation (II.37) indicates that for $M \rightarrow 1$ the flutter velocity goes to zero. It was shown by McClure (Ref. II.5) that this conservative result is due to the neglect of the boundary layer. McClure's calculations were based on shear-flow stability concepts and are too complicated to be reproduced here. However, the basic features may be studied by using a very simple flow model proposed by Fung (Ref. II.6). In this, the boundary layer is represented by a layer of constant velocity less than the free-stream velocity (see Figure II.3).

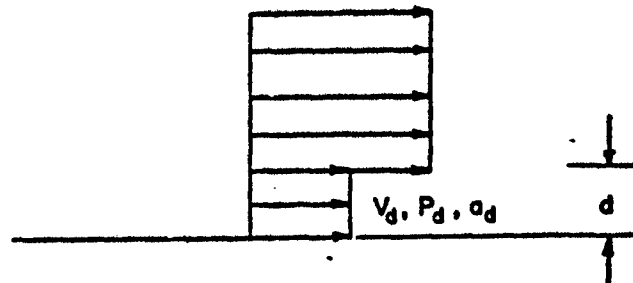


Figure II.3

Assuming that the wave length is much longer than the thickness of the boundary layer, we may treat the flow in the boundary layer as one-dimensional. One then finds by matching pressures and deformations across the slip line that

$$Z_A = \frac{-2ik\rho(V-c)^2}{\sqrt{M^2(1-\frac{c}{V})^2-1} - ikd \frac{\rho}{\rho_d} \frac{(V-c)^2}{(V_d-c)^2} \left[1 - \frac{(V_d-c)^2}{a_d^2}\right]} \quad (\text{II.38})$$

This result reduces to the previous one, e.g., (II.6), for

$kd=0$. Again, it has been assumed that there is an identical flow over the lower panel surface. Since the impedance (II.38) now has both a real and imaginary part, the eigenvalue problem becomes much more complicated. However, considerable insight might be gained by a simplified treatment along the following lines:

Since the negative of the imaginary part of Z_A represents the force component in phase with the transverse plate velocity, it gives a measure of the energy input per unit area which, for a neutrally stable wave, must be balanced by the structural energy dissipation in the panel which is proportional to \mathcal{E} . Whereas according to (II.6) this energy input is infinite when the wave travels at sonic speed, (II.38) shows that, in fact, for this speed the boundary layer will make it zero. By separating the real and imaginary parts of Z_A , one finds that, for given $\rho, V, c, k, d, V_d, \rho_d$ and a_d , the imaginary part, Z_{AI} is minimum for a Mach number given by

$$\sqrt{M^2 \left(1 - \frac{c}{V}\right)^2 - 1} = kd \frac{\rho(V-c)^2}{\rho_d(V_d-c)^2} \left[1 - \frac{(V_d-c)^2}{a_d^2}\right] \quad (\text{II.39})$$

The minimum value is then found to be

$$(Z_{AI})_{\min} = - \frac{\rho_d (V_d - c)^2}{d \left[1 - \frac{(V_d - c)^2}{a_d^2}\right]} \quad (\text{II.40})$$

with the associated real part being equal but with opposite sign, thus

$$(Z_{AR})_{at\ min.} = \frac{\rho_d (V_d - c)^2}{d \left[1 - \frac{(V_d - c)^2}{a_d^2} \right]} \quad (II.41)$$

The boundary-layer model would require that

$$V_d = \mathcal{L} V \quad (II.42)$$

where \mathcal{L} is some constant less than unity but probably greater than 0.5. Since the wave velocity is mainly controlled by C_e , the propagation velocity of free surface waves in vacuum, we may therefore, using the same arguments as before, assume that c may be neglected compared to V , and hence also compared to V_d . Then (II.40) and (II.41) simplify to

$$(Z_{AI})_{min} \equiv - \frac{\rho \mathcal{L}^2 V^2}{d (1 - M_d^2)} = - (Z_{AR})_{at\ min.} \quad (II.43)$$

where

$$M_d = \frac{V_d}{a_d}$$

Now substituting these back into the eigenvalue relation (II.32) we find that, at the maximum energy input condition,

$$\frac{\rho \mathcal{L}^2 V_F^2}{d (1 - M_d^2)} = 2 m_e \hbar^2 C_e^2 \epsilon_e \quad (II.44)$$

and

$$\frac{\rho k^2 V_F^2}{d(1-M_d^2)} = m_e k^2 (C_e^2 - C^2) \quad (\text{II.45})$$

The second of these, (II.45), merely shows that, for high mass ratios, the wave velocity will be slightly below C_e . The first relation is the interesting one and represents an energy balance at the condition of maximum aerodynamic energy input. Solving it for the flutter velocity V_F we obtain

$$V_F = \frac{C_e}{k} \sqrt{2\mu_e d k \varepsilon_e (1-M_d^2)} \quad (\text{II.46})$$

which, again, shows that the low wave numbers, i.e., large wave lengths are the most unstable one. It is also interesting to note that thickening of the boundary layer can stabilize membrane-type flutter at transonic speeds. This should also hold for panel flutter in general, the physical explanation being that the low-speed boundary-layer flow acts as a "cushion" to lower the aerodynamic forces exerted by the free stream due to panel deflections.

I. CONCLUSIONS

A simplified analysis of the stability of travelling waves over a flat two-dimensional inflatable panel indicates that short-wave instability is not likely to occur. The reason is that the stiffness and resistance of the structure decreases faster (as k^2) than does the aerodynamic forcing term (as k). Therefore, the longest waves would be most

unstable (i.e., have lowest flutter velocity) which points to the ordinary type (bending-torsion) flutter as being the most critical. The situation would be different for a curved inflatable panel, or membrane, because then the hoop stresses generated by the travelling waves would act as a distributed elastic support and the structural stiffness would go to a constant as $t \rightarrow 0$, thus making possible for instability to occur at some intermediate wave number. The situation would then be similar to that realized by Dugundji, Dowell, and Perkin (Ref. II.7) in their experiments with a panel on continuous elastic foundations, in which travelling-wave-type flutter indeed was found.

The very simple and crude analysis of the effect of a boundary layer shows, as previously demonstrated by McClure (Ref. II.5) that the boundary layer removes the singularity in pressure predicted by linearized inviscid theory for a wave travelling at sonic velocity relative to the air. Hence, thickening of the boundary layer has a stabilizing effect on waves travelling at transonic speeds.

REFERENCES FOR APPENDIX II

1. Miles, J. W. On the Aerodynamic Instability of Thin Panels. Journal of the Aeronautical Sciences, Vol. 23, No. 8, August 1956, pp. 771-780.
2. Disalvinghoff, A., Ashley, H., Halfman, R. Aeroelasticity. Addison-Wesley Publishing Co., Inc., 1955.
3. Landahl, M. T. On the Stability of a Laminar Incompressible Boundary Layer over a Flexible Surface. Journal of Fluid Mechanics, Vol. 13, part 4, August 1962, pp. 609-632.
4. Brooke Benjamin, T. The Threefold Classification of Unstable Disturbances in Flexible Surfaces Bounding Inviscid Flows. Journal of Fluid Mechanics, Vol. 16, part 3, pp. 436-450, July 1963.
5. McClure, J. D. On Perturbed Boundary Layer Flows. Massachusetts Institute of Technology, Fluid Dynamics Research Laboratory Report No. 62-2, June 1962.
6. Fung, Y. C. Some Recent Contributions to Panel Flutter Research. AIAA Journal, Vol. I, No. 4, pp. 898-909, April 1963.
7. Dugundji, J., Dowell, E., Perkin, B. Subsonic Flutter of Panels on Continuous Elastic Foundations. AIAA Journal, Vol. I, No. 5, pp. 1146-1154, May 1963. See also Massachusetts Institute of Technology, Aeroelastic and Structures Research Laboratory TR 74-4.

LIST OF SYMBOLS FOR APPENDIX II

a	Speed of sound
c	Wave velocity
c_0, c_1, c_2	Functions defined by Eqs. (II.12) - (II.14)
h	Depth of panel, see Fig. II.1
i	($= \sqrt{-1}$)
k	Wave number ($= 2\pi/\lambda$)
m	Mass per unit length
p	Pressure
p_2	Differential pressure (p_2/h is shear stiffness due to internal pressure)
t	Time
w	Time-dependent lateral deflection of panel
x	Streamwise coordinate
D	Panel bending stiffness ($= E\delta h^2/2$)
E	Young's modulus
M	Mach number ($= V/a$)
V	Free-stream velocity
Z	Impedance
β	Related to M according to ($\beta = \sqrt{M^2 - 1}$)
δ	Thickness of cover
ϵ	Damping ratio
λ	Wave length
μ	Relative mass parameter, see Eq. (II.37)
ρ	Free-stream density
α	Constant in Eq. (II.42)

Subscripts, etc.

d	Quantities at base of boundary layer, except for the case of p_2 , see Fig. II.3
-----	--

e	"Effective" values, see Eqs. (II.22) - (II.27)
A	Aerodynamic
F	At flutter
I	Imaginary part
R or Re	Real part
S	Structural
∞	Free-stream conditions
$(-)$	Denotes amplitude
$()_x$	Differentiation with respect to x
(\cdot)	Differentiation with respect to time

APPENDIX III

STRUCTURAL ANALYSIS OF AN INFLATED, AIRMAT-TYPE STRUCTURE

by James W. Mar

A. INTRODUCTION

The equations governing the behavior of a sandwich-type shell structure consisting of two membranes held apart by internal pressure and shear chords will be developed. Details of the construction are shown in Fig. III.1.

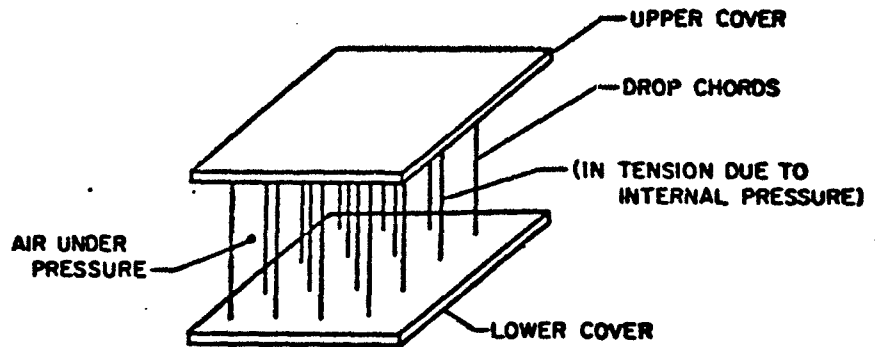


Figure III.1

The development presented herein forms the basis for the analysis of inflated structures. Specialization and simplifications will be presented in a subsequent report.

B. THE GEOMETRY OF THE DEFORMED MIDDLE SURFACE

The initial undeformed middle surface of the shell is described by the equation

$$\vec{r}_0 = \vec{r}_0(\xi^1, \xi^2) \quad (\text{III.1})$$

where \vec{r}_0 is the position vector to points on the middle surface and ξ^1, ξ^2 are coordinates on the middle surface

(see Fig. III.2)

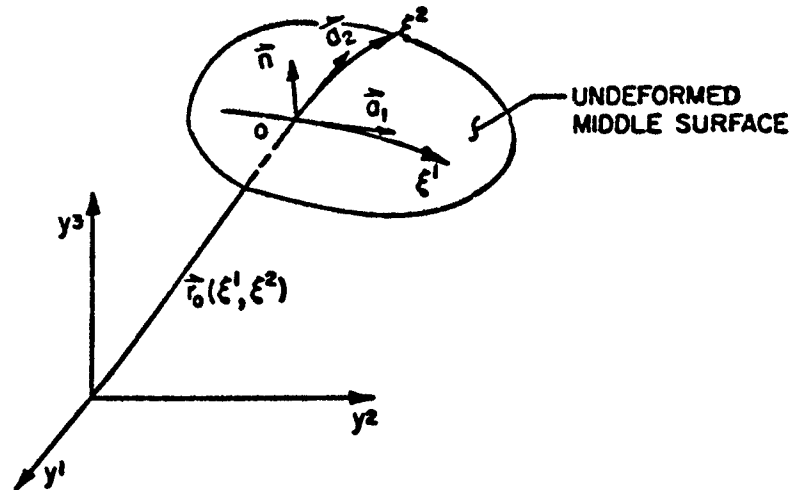


Figure III.2

Other parameters of the middle surface are listed as follows:

covariant base vectors: $\vec{a}_\alpha = \frac{\partial \vec{r}_0}{\partial \xi^\alpha}$ (III.2)

unit normal: $\vec{n} = \frac{\vec{a}_1 \times \vec{a}_2}{\sqrt{a}}$ (III.3)

discriminant: $a = a_{11}a_{22} - (a_{12})^2$ (III.4)

first fundamental tensor: $a_{\alpha\beta} = \vec{a}_\alpha \cdot \vec{a}_\beta$ (III.5)

second fundamental tensor: $b_{\alpha\beta} = \vec{n} \cdot \frac{\partial \vec{a}_\alpha}{\partial \xi^\beta}$ (III.6)

In the above formulae and in the subsequent derivations the indicial and summation conventions of tensor analysis will be used. Thus, Greek letter indices imply the numbers one or two and a repeated index is to be summed from one to two. Also, the vector product of two vectors (as in Eq. (III.3)) will be symbolized by an 'x' and the scalar product of two vectors (as in Eq. (III.5)) will be symbolized by a dot).

The deformed middle surface is located by the position vector $\vec{R}_o(\xi^1, \xi^2)$ as depicted in Fig. III.3.

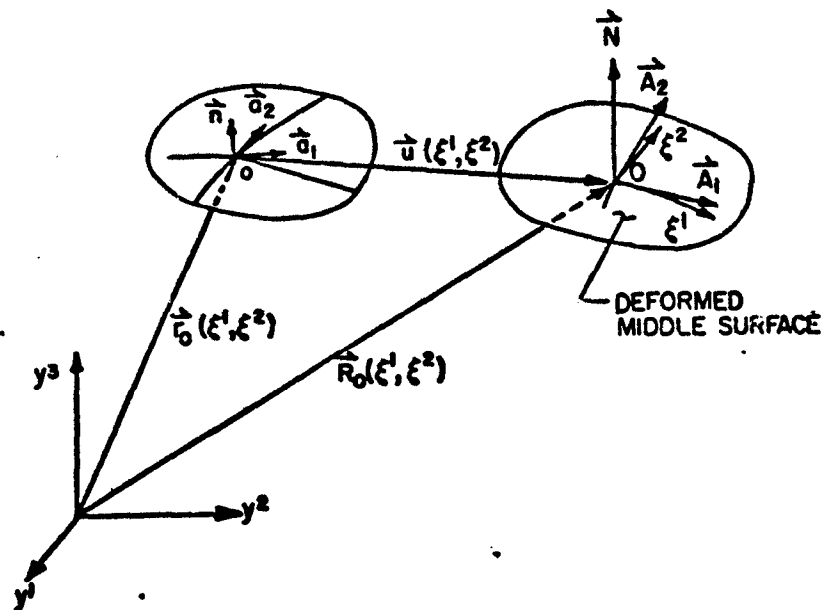


Figure III.3

Point o on the undeformed middle surface is displaced to the point labeled O after deformation. This is expressed as

$$\vec{R}_o(\xi^1, \xi^2) = \vec{r}_o(\xi^1, \xi^2) + \vec{u}(\xi^1, \xi^2) \quad (\text{III.7})$$

Other parameters of the deformed middle surface which will be of interest are listed as follows:

$$\text{covariant base vectors: } \vec{A}_\alpha = \frac{\partial \vec{r}}{\partial \xi^\alpha} = \vec{a}_\alpha + \frac{\partial \vec{u}}{\partial \xi^\alpha} \quad (\text{III.8})$$

$$\text{unit normal: } \vec{N} = \frac{\vec{A}_1 \times \vec{A}_2}{\sqrt{A}} \quad (\text{III.9})$$

$$\text{discriminant: } A = A_{11}A_{22} - (A_{12})^2 \quad (\text{III.10})$$

$$\text{first fundamental tensor: } A_{\alpha\beta} = \vec{A}_\alpha \cdot \vec{A}_\beta \quad (\text{III.11})$$

$$\text{second fundamental tensor: } B_{\alpha\beta} = \vec{N} \cdot \frac{\partial \vec{A}_\alpha}{\partial \xi^\beta} \quad (\text{III.12})$$

$$\text{contravariant base vectors: } \vec{A}^\beta = \vec{N} \times \vec{A}_\alpha \quad (\text{III.13})$$

$$\text{contravariant metric tensor: } A^{\alpha\beta} A_{\beta\gamma} = \delta^\alpha_\gamma \quad (\text{III.14})$$

$$\text{Christoffel symbols of the second kind: } \left\{ \begin{matrix} \alpha \\ \beta\gamma \end{matrix} \right\} = \vec{A}^\alpha \cdot \frac{\partial \vec{A}_\gamma}{\partial \xi^\beta} \quad (\text{III.15})$$

$$\text{Weingarten formulae: } \frac{\partial \vec{N}}{\partial \xi^\alpha} = -A^{\beta\gamma} B_{\gamma\alpha} \vec{A}_\beta \quad (\text{III.16})$$

$$\text{Gauss relations: } \frac{\partial \vec{A}_\alpha}{\partial \xi^\beta} = B_{\alpha\beta} \vec{N} + \left\{ \begin{matrix} \gamma \\ \alpha\beta \end{matrix} \right\} \vec{A}_\gamma \quad (\text{III.17})$$

The covariant surface permutation tensor, $\vec{e}_{\alpha\beta}$, introduced in Eq. (III.13), and its contravariant counterpart are defined to have the following values:

$$\begin{aligned}\bar{\epsilon}_{11} = \bar{\epsilon}_{22} &= 0 \\ \bar{\epsilon}_{12} = \bar{\epsilon}_{21} &= 0\end{aligned}\quad (\text{III.18})$$

$$\begin{aligned}\bar{\epsilon}_{12} = -\bar{\epsilon}_{21} &= \sqrt{A} \\ \bar{\epsilon}^{12} = -\bar{\epsilon}^{21} &= \frac{1}{\sqrt{A}}\end{aligned}\quad (\text{III.19})$$

The symbol δ_{β}^{α} is a Kronecker delta with the values

$$\delta_2^1 = \delta_1^2 = 0 \quad (\text{III.20})$$

$$\delta_1^1 = \delta_2^2 = 1 \quad (\text{III.21})$$

C. THE GEOMETRY OF THE DEFORMED SHELL: THE STRAIN TENSOR

The geometries of the undeformed and deformed shell are taken with reference to imaginary middle surfaces which are defined as the locus of all points midway between the upper and lower membranes.

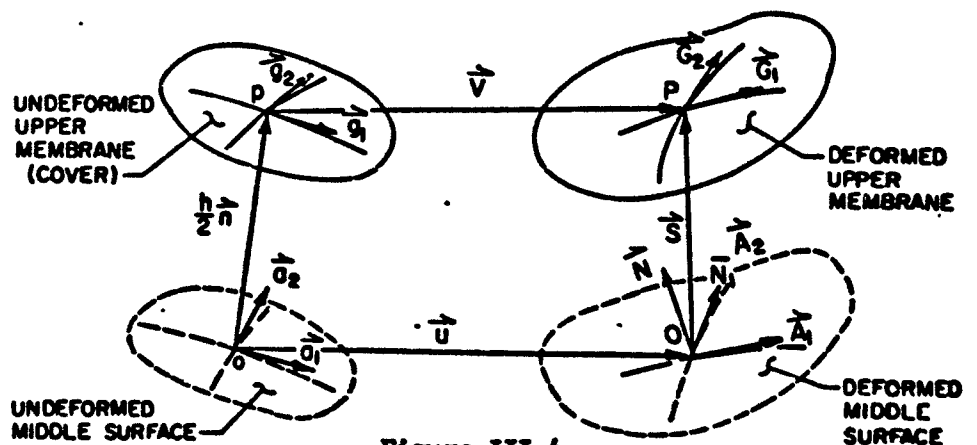


Figure III.4

An examination of Fig. III.1 discloses the following geometrical parameters:

$\vec{op} = \frac{h}{2} \vec{n}$	vector along shear chord from point o on the middle surface to a point p on the upper membrane of undeformed shell
h	length of shear chord in undeformed shell, i.e., spacing of membranes in undeformed shell
$\vec{s} = \vec{OP}$	vector along shear chord in deformed shell, i.e., \vec{s} is the orientation of the drop chord after deformation
$2s = 2 \vec{s} $	length of shear chord in deformed shell (note that this is <u>not</u> spacing of the membrane in the deformed shell)
Point P	location of material point p after deformation
Point O	location of point o after deformation
h^*	spacing of membranes in deformed shell
$\vec{u}(\xi', \xi^2)$	displacement vector of middle surface
$\vec{v}(\xi', \xi^2, \frac{h^*}{2})$	displacement vector of upper membrane
\vec{g}_1, \vec{g}_2	base vectors on undeformed upper membrane
\vec{G}_1, \vec{G}_2	base vectors on deformed upper membrane associated with \vec{v}

ds_u element of arc length on undeformed upper membrane

dS_u element of arc length on deformed upper membrane

The base vectors on the undeformed and deformed upper surface are expressed as

$$\vec{g}_\alpha = \frac{\partial \vec{r}}{\partial \xi^\alpha} + \frac{h}{2} \frac{\partial \vec{n}}{\partial \xi^\alpha} = \vec{a}_\alpha - \frac{h}{2} b_\alpha^\sigma \vec{a}_\sigma \quad (\text{III.22})$$

$$\vec{G}_\alpha = \vec{g}_\alpha + \frac{\partial \vec{v}}{\partial \xi^\alpha} \quad (\text{III.23})$$

We define the strain tensor for the upper surface in the usual manner

$$(dS_u)^2 - (ds_u)^2 = 2\gamma_{\alpha\beta} d\xi^\alpha d\xi^\beta \quad (\text{III.24})$$

Thus

$$\gamma_{\alpha\beta} = \frac{1}{2} [\vec{G}_\alpha \cdot \vec{G}_\beta - \vec{g}_\alpha \cdot \vec{g}_\beta] \quad (\text{III.25})$$

It will be convenient to express \vec{S} in terms of \vec{A}_α and \vec{N}

$$\vec{S} = s^\alpha \vec{A}_\alpha + s^3 \vec{N} \quad (\text{III.26})$$

Then the following relations can be obtained

$$\frac{\partial \vec{S}}{\partial \xi^\alpha} = (s^\sigma|_\alpha - B_\alpha^\sigma s^3) \vec{A}_\sigma + (s^\sigma B_{\sigma\alpha} + s^3|_\alpha) \vec{N} \quad (\text{III.27})$$

$$\gamma_{\alpha\beta} = \frac{1}{2} \left[\vec{g}_\alpha \cdot \frac{\partial \vec{v}}{\partial \xi^\beta} + \vec{g}_\beta \cdot \frac{\partial \vec{v}}{\partial \xi^\alpha} + \frac{\partial \vec{v}}{\partial \xi^\alpha} \cdot \frac{\partial \vec{v}}{\partial \xi^\beta} \right] \quad (\text{III.28})$$

where the vertical bar before the α signifies covariant differentiation with respect to ξ^α in the metric of the middle surface of the deformed shell.

Relative elongations, or extensional strain in the usual engineering sense, are defined along the two coordinate curves as

$$E_\alpha = \frac{|\bar{G}_\alpha d\xi^\alpha| - |\bar{g}_\alpha d\xi^\alpha|}{|\bar{g}_\alpha d\xi^\alpha|} \quad (\text{no sum on } \alpha) \quad (\text{III.29})$$

This leads to the result

$$E_\alpha = \sqrt{1 + \frac{2\gamma_{\alpha\alpha}}{g_{\alpha\alpha}}} - 1 \quad (\text{no sum on } \alpha) \quad (\text{III.30})$$

In what follows, the relative elongations will be assumed to be small relative to unity. Thus

$$E_\alpha \approx \frac{\gamma_{\alpha\alpha}}{g_{\alpha\alpha}} \quad (\text{no sum on } \alpha) \quad (\text{III.31})$$

The shearing deformation is defined as the change in angle formed by the base vectors \bar{g}_α and \bar{G}_α . Let π_{12} be the angle between \bar{g}_1 and \bar{g}_2 , and let $\pi_{12} - \phi_{12}$ be the angle between \bar{G}_1 and \bar{G}_2 . Then

$$\cos(\pi_{12} - \phi_{12}) = \frac{\bar{G}_1 \cdot \bar{G}_2}{|\bar{G}_1| |\bar{G}_2|} \quad (\text{III.32})$$

This leads to the result

$$\cos(\pi_{12} - \phi_{12}) = \frac{g_{12} + 2\gamma_{12}}{(1+E_1)(1+E_2)\sqrt{g_{11}g_{22}}} \quad (\text{III.33})$$

If the base vectors \vec{g}_α are orthogonal (and generally the ξ^α are chosen such that this is true), then $\pi_{12} = \frac{\pi}{2}$ and $g_{12} = 0$. The angle ϕ_{12} will also be assumed to be small such that $\sin \phi_{12} \cong \phi_{12}$. Thus for orthogonal coordinates on the undeformed membrane the shearing angle ϕ_{12} is approximated for the case of small strains by

$$\phi_{12} \cong \frac{2\gamma_{12}}{\sqrt{g_{11}g_{22}}} \quad (\text{III.34})$$

The transverse shearing deformations of the shell is defined by considering the shear chords (see Fig. III.5).

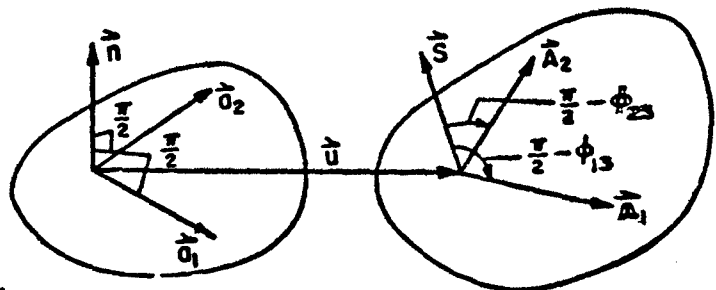


Figure III.5

The angle between the base vectors \vec{g}_α and \vec{S} will be denoted by $\frac{\pi}{2} - \phi_{\alpha 3}$ because the original angles are 90 deg, since the normal vector \vec{n} is perpendicular to \vec{g}_α . Proceeding as before

$$\cos\left(\frac{\pi}{2} - \phi_{\alpha 3}\right) = \frac{\vec{A}_\alpha \cdot \vec{S}}{|\vec{S}| |\vec{A}_\alpha|} \quad (\text{no sum on } \alpha) \quad (\text{III.35})$$

By definition (see Eq. (III.33)) the shearing components of the strain tensor are expressed as

$$\cos\left(\frac{\pi}{2} - \phi_{\alpha 3}\right) = \frac{2\gamma_{\alpha 3}}{|\vec{S}| |\vec{A}_\alpha|} \quad (\text{III.36})$$

Thus there is obtained

$$\gamma_{\alpha 3} = \frac{1}{2} (\vec{A}_{\alpha} \cdot \vec{s}) \quad (\text{III.37})$$

Since the shear rigidity of the pressurized sandwich is relatively low, the transverse shearing angles $\phi_{\alpha 3}$ will not be assumed to be small at this stage in the development.

It is interesting to note that Eq. (III.37) represents the usual first approximation to transverse shear deformations in shell theory. However, in the case of the shell construction under consideration, Eq. (III.37) is the exact expression because the shear chords remain straight.

D. DEFINITION OF FORCE AND MOMENT RESULTANTS

It will be found convenient to define force and moment resultant tensors. These are obtained by summing the stresses across the thickness of the shell to obtain a set of equipollent forces and moments which are assumed to act at the mid-surface of the shell. An isolated element of volume of the deformed shell will be acted upon by the following kinds of forces:

- (a) Membrane stresses in the upper and lower membrane
- (b) The pressure of the gas
- (c) The stresses in the shear chords

Each of these will be separately discussed.

The isolated element of volume is carved out of the shell by the vectors $\vec{A}_1 d\xi^1$, $\vec{A}_2 d\xi^2$ and $\pm \frac{A}{2} \vec{N}$ as depicted in Fig. III.6. On the upper and lower membranes, the edges of the element of volume are defined by the vectors $\vec{H}_1^{(u)} d\xi^1$, $\vec{H}_2^{(u)} d\xi^2$, $\vec{H}_1^{(l)} d\xi^1$, and $\vec{H}_2^{(l)} d\xi^2$, where the enclosed sub-

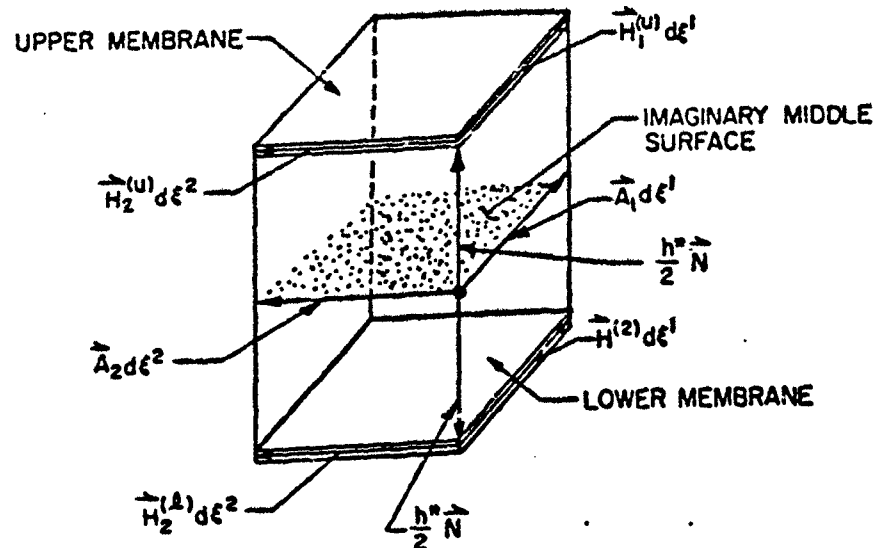


Figure III.6

scripts (u) and (l) are tags identifying the 'upper' and 'lower' membranes, respectively. These vectors, which are in reality another set of base vectors for the upper and lower membranes, are defined by the equations

$$\vec{H}_\sigma^{(u)} = \vec{A}_\sigma + \frac{\kappa^*}{2} \frac{\partial \vec{N}}{\partial \xi^\sigma} + \frac{1}{2} \frac{\partial \kappa^*}{\partial \xi^\sigma} \vec{N} \quad (\text{III.38})$$

$$\vec{H}_\sigma^{(l)} = \vec{A}_\sigma - \frac{\kappa^*}{2} \frac{\partial \vec{N}}{\partial \xi^\sigma} - \frac{1}{2} \frac{\partial \kappa^*}{\partial \xi^\sigma} \vec{N} \quad (\text{III.39})$$

It should be borne in mind that these base vectors are different from those used in subsection C of this Appendix.

The membrane stress vectors associated with the upper

and lower membranes are shown acting on the volume element of Fig. III.6 in Fig. III.7. These are depicted as $\vec{\sigma}_{(u)}^{\alpha}$ and $\vec{\sigma}_{(l)}^{\alpha}$ acting on the upper and lower membranes, respectively

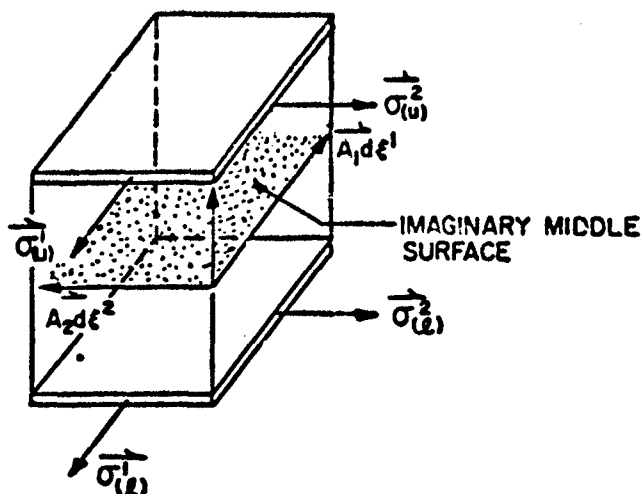


Figure III.7

Since it is assumed that there exists a membrane state of stress in the membranes, the stress vectors on the upper membrane are written in component form as

$$\vec{\sigma}_{(u)}^{\alpha} = \frac{1}{\sqrt{H_{(u)}^{\alpha\alpha}}} \tau_{(u)}^{\alpha\sigma} \vec{H}_{\sigma}^{(u)} \quad (\text{no sum on } \alpha) \quad (\text{III.40})$$

With the introduction of the Weingarten relations the base vectors become

$$\vec{H}_{\sigma}^{(u)} = \left(\delta_{\sigma}^{\gamma} - \frac{k^{\sigma}}{2} B_{\sigma}^{\gamma} \right) \vec{A}_{\gamma} + \frac{1}{2} \frac{\partial k^{\sigma}}{\partial \xi^{\sigma}} \vec{N} \quad (\text{III.41})$$

and hence

$$\vec{\sigma}_{(u)}^{\alpha\sigma} = \frac{\tau_{(u)}^{\alpha\sigma}}{\sqrt{H_{(u)}^{\alpha\alpha}}} \left[\left(\delta_{\sigma}^{\gamma} - \frac{k^{\alpha}}{2} B_{\sigma}^{\gamma} \right) \vec{A}_{\gamma} + \frac{1}{2} \frac{\partial k^{\alpha}}{\partial \xi^{\sigma}} \vec{N} \right] \quad \begin{matrix} \text{(no sum} \\ \text{on } \alpha) \end{matrix} \quad \text{(III.42)}$$

Similarly for the lower membrane

$$\vec{\sigma}_{(l)}^{\alpha\sigma} = \frac{\tau_{(l)}^{\alpha\sigma}}{\sqrt{H_{(l)}^{\alpha\alpha}}} \left[\left(\delta_{\sigma}^{\gamma} + \frac{k^{\alpha}}{2} B_{\sigma}^{\gamma} \right) \vec{A}_{\gamma} - \frac{1}{2} \frac{\partial k^{\alpha}}{\partial \xi^{\sigma}} \vec{N} \right] \quad \begin{matrix} \text{(no sum} \\ \text{on } \alpha) \end{matrix} \quad \text{(III.43)}$$

The equipollent force resultant vector for the membrane stresses acting on the length $\sqrt{A_{22}} d\xi^2$ is defined by the relation

$$\vec{I}' \sqrt{A_{22}} d\xi^2 = \vec{\sigma}_{(u)}^{\alpha\sigma} t_{(u)} \sqrt{H_{(u)}^{\alpha\alpha}} d\xi^2 + \vec{\sigma}_{(l)}^{\alpha\sigma} t_{(l)} \sqrt{H_{(l)}^{\alpha\alpha}} d\xi^2 \quad \text{(III.44)}$$

where $t_{(u)}$ and $t_{(l)}$ are the thickness of the upper and lower membranes, respectively. Substituting Eqs. (III.42) and (III.43) into Eq. (III.44) yields

$$\vec{I}' \sqrt{A_{22}} = \left(T'^{\alpha\sigma} - V'^{\alpha\sigma} \frac{k^{\alpha}}{2} B_{\sigma}^{\gamma} \right) \vec{A}_{\gamma} + V'^{\alpha\sigma} \frac{1}{2} \frac{\partial k^{\alpha}}{\partial \xi^{\sigma}} \vec{N} \quad \text{(III.45)}$$

where there has been introduced

$$T'^{\alpha\sigma} = \sqrt{H_{(u)}} t_{(u)} \tau_{(u)}^{\alpha\sigma} + \sqrt{H_{(l)}} t_{(l)} \tau_{(l)}^{\alpha\sigma} \quad \text{(III.46)}$$

$$V'^{\alpha\sigma} = \sqrt{H_{(u)}} t_{(u)} \tau_{(u)}^{\alpha\sigma} - \sqrt{H_{(l)}} t_{(l)} \tau_{(l)}^{\alpha\sigma} \quad \text{(III.47)}$$

and it is known that

$$H = \frac{H_{22}}{H''} \quad (\text{III.48})$$

The components of the force resultant tensor are defined by writing

$$\vec{\ell}' \sqrt{A''} = \ell'^{\sigma} \vec{A}_{\sigma} + q' \vec{N} \quad (\text{III.49})$$

$$\vec{\ell}^2 \sqrt{A^{22}} = \ell^{2\sigma} \vec{A}_{\sigma} + q^2 \vec{N} \quad (\text{III.50})$$

By comparing Eq. (III.49) with Eq. (III.45), there is obtained

$$\ell'' = \frac{1}{\sqrt{A}} \left\{ T'' - V'^{\gamma} \frac{\ell^{\sigma}}{2} B_{\gamma}^{\sigma} \right\} \quad (\text{III.51})$$

$$\ell'^2 = \frac{1}{\sqrt{A}} \left\{ T'^2 - V'^{\gamma} \frac{\ell^{\sigma}}{2} B_{\gamma}^{\sigma} \right\} \quad (\text{III.52})$$

$$q' = \frac{1}{\sqrt{A}} \left\{ V'^{\gamma} \frac{1}{2} \frac{\partial \ell^{\sigma}}{\partial \xi^{\gamma}} \right\} \quad (\text{III.53})$$

In a similar manner the remaining components can be determined.

$$\ell^{22} = \frac{1}{\sqrt{A}} \left\{ T^{22} - V^{2\gamma} \frac{\ell^{\sigma}}{2} B_{\gamma}^{\sigma} \right\} \quad (\text{III.54})$$

$$\ell^{21} = \frac{1}{\sqrt{A}} \left\{ T^{21} - V^{2\gamma} \frac{\ell^{\sigma}}{2} B_{\gamma}^{\sigma} \right\} \quad (\text{III.55})$$

$$q^2 = \frac{1}{\sqrt{A}} \left\{ V^{2\gamma} \frac{1}{2} \frac{\partial h^{\alpha}}{\partial \xi^{\gamma}} \right\} \quad (\text{III.56})$$

The equipollent moment resultant vector is defined as

$$\vec{m}' \sqrt{A_{22}} d\xi^2 = \frac{h^{\alpha}}{2} \vec{N} \times \left\{ t_{(u)} \vec{\sigma}'_{(u)} \sqrt{H_{22}^{(u)}} - t_{(u)} \vec{\sigma}'_{(u)} \sqrt{H_{22}^{(u)}} \right\} d\xi^2 \quad (\text{III.57})$$

which becomes with the introduction of Eqs. (III.42), (III.43), (III.46) and (III.47),

$$\vec{m}' \sqrt{A_{22}} = \frac{h^{\alpha}}{2} \vec{N} \times \left\{ (V^{1\sigma} - T^{1\gamma} \frac{h^{\sigma}}{2} B_{\gamma}^{\sigma}) \vec{A}_{\sigma} + T^{1\gamma} \frac{1}{2} \frac{\partial h^{\alpha}}{\partial \xi^{\gamma}} \vec{N} \right\} \quad (\text{III.58})$$

This leads to the following definitions for the moment resultant tensor

$$\vec{m}' \sqrt{A^{11}} = \sqrt{A} m^{11} \vec{A}^1 - \sqrt{A} m^{12} \vec{A}^2 \quad (\text{III.59})$$

$$\vec{m}' \sqrt{A^{22}} = \sqrt{A} m^{21} \vec{A}^1 - \sqrt{A} m^{22} \vec{A}^2 \quad (\text{III.60})$$

A comparison of Eqs. (III.59) and (III.58) leads to the following components

$$m^{11} = \frac{h^{\alpha}}{2\sqrt{A}} \left[V^{11} - T^{1\gamma} \frac{h^{\alpha}}{2} B_{\gamma}^1 \right] \quad (\text{III.61})$$

$$m^{12} = \frac{h^{\alpha}}{2\sqrt{A}} \left[V^{12} - T^{1\gamma} \frac{h^{\alpha}}{2} B_{\gamma}^2 \right] \quad (\text{III.62})$$

$$m^{21} = \frac{h^{\alpha}}{2\sqrt{A}} \left[V^{21} - T^{2\gamma} \frac{h^{\alpha}}{2} B_{\gamma}^1 \right] \quad (\text{III.63})$$

$$q^2 = \frac{1}{\sqrt{A}} \left\{ V^{2j} \frac{1}{2} \frac{\partial h^a}{\partial \xi^j} \right\} \quad (\text{III.56})$$

The equipollent moment resultant vector is defined as

$$\vec{m}' \sqrt{A_{22}} d\xi^2 = \frac{h^a}{2} \vec{N} \times \left\{ t_{(u)} \vec{\sigma}_{(u)}' \sqrt{H_{22}^{(u)}} - t_{(l)} \vec{\sigma}_{(l)}' \sqrt{H_{22}^{(l)}} \right\} d\xi^2 \quad (\text{III.57})$$

which becomes with the introduction of Eqs. (III.42), (III.43), (III.46) and (III.47),

$$\vec{m}' \sqrt{A_{22}} = \frac{h^a}{2} \vec{N} \times \left\{ (V^{1\sigma} - T^{1\sigma} \frac{h^a}{2} B_{\sigma}^a) \vec{A}_{\sigma} + T^{1\sigma} \frac{1}{2} \frac{\partial h^a}{\partial \xi^j} \vec{N} \right\} \quad (\text{III.58})$$

This leads to the following definitions for the moment resultant tensor

$$\vec{m}' \sqrt{A^{11}} = \sqrt{A} m^{11} \vec{A}^2 - \sqrt{A} m^{12} \vec{A}^1 \quad (\text{III.59})$$

$$\vec{m}^2 \sqrt{A^{22}} = \sqrt{A} m^{21} \vec{A}^2 - \sqrt{A} m^{22} \vec{A}_1 \quad (\text{III.60})$$

A comparison of Eqs. (III.59) and (III.58) leads to the following components

$$m^{11} = \frac{h^a}{2\sqrt{A}} \left[V^{11} - T^{1\sigma} \frac{h^a}{2} B_{\sigma}^a \right] \quad (\text{III.61})$$

$$m^{12} = \frac{h^a}{2\sqrt{A}} \left[V^{12} - T^{1\sigma} \frac{h^a}{2} B_{\sigma}^a \right] \quad (\text{III.62})$$

$$m^{21} = \frac{h^a}{2\sqrt{A}} \left[V^{21} - T^{2\sigma} \frac{h^a}{2} B_{\sigma}^a \right] \quad (\text{III.63})$$

$$m^{22} = \frac{\hbar^2}{2\sqrt{A}} \left[V^{22} - T^{2j} \frac{\hbar^2}{2} B_j^2 \right] \quad (\text{III.64})$$

The pressure of the gas on the element of volume is depicted in Fig. III.8 where, for purposes of clarity, the pressure is shown acting on only one face.

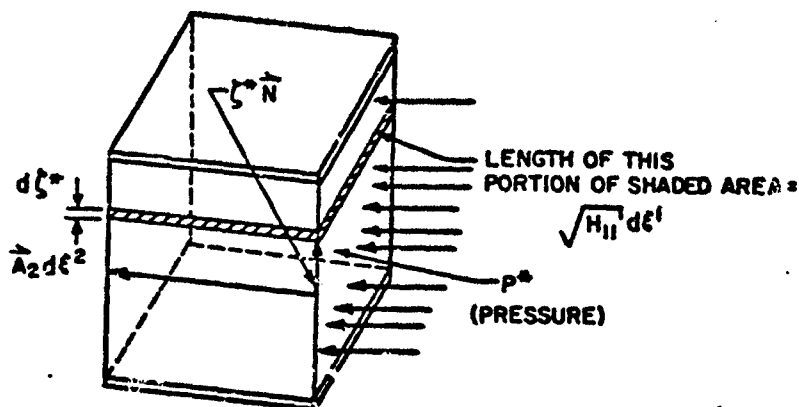


Figure III.8

It will be necessary to define vectors

$$\vec{H}_\alpha = \vec{A}_\alpha + \zeta^* \frac{\partial \vec{N}}{\partial \zeta^\alpha} - (\delta_\alpha^j - \zeta^* B_\alpha^j) \vec{A}_j \quad (\text{III.65})$$

in order to delineate the areas on which the pressures are acting. Since the pressure is a force which acts perpendicular to a surface, the equipollent force resultant acting on the right face of the volume element shown in Fig. III.8 is defined from the equation

$$\vec{p}^2 \sqrt{A_1} d\xi' = \int_{-\frac{\xi^0}{2}}^{\frac{\xi^0}{2}} p_0^* \frac{\vec{H}^2}{\sqrt{H^2}} \sqrt{H_{11}} d\xi' d\zeta^0 \quad (\text{III.66})$$

where it should be recognized that the vector $\vec{H}^2/\sqrt{H^2}$ is the unit vector which is perpendicular to the shaded area $\sqrt{H_{11}} d\xi'$. The vector \vec{H}^2 is obtained from the vector product of \vec{N} and \vec{H}_1 :

$$\vec{H}^2 = \frac{1}{\sqrt{H}} \vec{N} \times \vec{H}_1 = \sqrt{\frac{A}{H}} \epsilon^{\alpha 2} \epsilon_{\gamma \sigma} (\delta_\alpha^\beta - \zeta^\alpha B_\alpha^\beta) \vec{A}^\sigma \quad (\text{III.67})$$

The substitution of Eq. (III.67) into Eq. (III.66) leads to

$$\vec{p}^2 \sqrt{A_{11}} = - \int_{-\frac{\xi^0}{2}}^{\frac{\xi^0}{2}} \sqrt{A} p_0^* \epsilon^{\alpha 2} \epsilon_{\gamma \sigma} (\delta_\alpha^\beta - \zeta^\alpha B_\alpha^\beta) \vec{A}^\sigma d\zeta^0 \quad (\text{III.68})$$

In a manner analogous to the treatment of the membrane stresses we write

$$\vec{p}^2 \sqrt{A^2} = \sqrt{A} p_1^2 \vec{A}^1 + \sqrt{A} p_2^2 \vec{A}^2 \quad (\text{III.69})$$

$$\vec{p}_1^2 \sqrt{A^2} = \sqrt{A} p_1^1 \vec{A}^1 + \sqrt{A} p_2^1 \vec{A}^2 \quad (\text{III.70})$$

By comparing Eqs. (III.68) and (III.69), we arrive at

$$p_1^2 = \int_{-\frac{\xi^0}{2}}^{\frac{\xi^0}{2}} \frac{p_0^*}{\sqrt{A}} \zeta^\alpha B_\alpha^2 d\zeta^0 = 0 \quad (\text{III.71})$$

$$p_2^* = \int_{-\frac{h^*}{2}}^{\frac{h^*}{2}} \frac{p_0^*}{\sqrt{A}} (1 - \zeta^* B_1') d\zeta^* = \frac{p_0^* h^*}{\sqrt{A}} \quad (\text{III.72})$$

Similarly

$$p_1' = \int_{-\frac{h^*}{2}}^{\frac{h^*}{2}} \frac{p_0^*}{\sqrt{A}} (1 - \zeta^* B_2^2) d\zeta^* = \frac{p_0^* h^*}{\sqrt{A}} \quad (\text{III.73})$$

$$p_2' = \int_{-\frac{h^*}{2}}^{\frac{h^*}{2}} \frac{p_0^*}{\sqrt{A}} \zeta^* B_2' d\zeta^* = 0 \quad (\text{III.74})$$

The shear chords are in a state of uniaxial tension caused by the pressurized gas and their orientation in space is along the vector \vec{S} . This means, since the element of volume (see Fig. III.6) is carved out with edges orthogonal to the middle surface, that many of the shear chords are cut by the creation of the element of volume. We can visualize the several shear chords as a thicket of wires with ends on the surface (see Fig. III.9). There must be placed on these ends the forces representing the stresses in the shear chords. It will be assumed that there are a sufficient density of shear chords such that their effect can be replaced by an effective stress, σ^* , with a line of action along \vec{S} .

Let us isolate a tetrahedron from the thicket of shear chords (see Fig. III.10). The tetrahedron has as a base, the vectors $\vec{A}_1 d\xi^1$ and $\vec{A}_2 d\xi^2$ and an altitude along the vector \vec{N} .

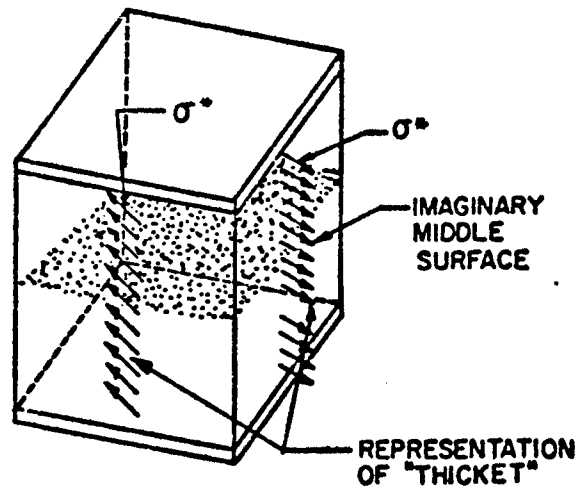


Figure III.9

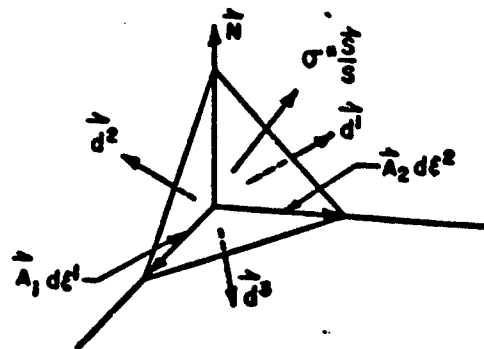


Figure III.10

The fourth face (canted face) is taken perpendicular to $\vec{\sigma}$, i.e., it is orthogonal to the shear chords. On this fourth face the stress vector is that caused by the tension

in the shear chords and is shown as $\sigma^s \frac{\vec{s}}{s}$ where $\frac{\vec{s}}{s}$ is the unit vector taken along the shear chords. The tetrahedron is in equilibrium and this is represented by the equation

$$\frac{\sigma^s}{s} \vec{s} dA_s = \vec{d}' dA_1 + \vec{d}^2 dA_2 + \vec{d}^3 dA_3 \quad (\text{III.75})$$

where $\vec{d}', \vec{d}^2, \vec{d}^3$ are stress vectors acting on the faces of the tetrahedron which are perpendicular to \vec{A}^1, \vec{A}^2 and \vec{N} respectively (see Fig. III.10). Note also that $\vec{d}' k^1$ and $\vec{d}^2 k^2$ are the forces (per unit length of the mid-surface) which are equipollent to the stresses in the severed shear chords between the upper and lower membranes of the element of volume (see Fig. III.9). The areas of the faces on which these vectors are acting are represented as dA_1, dA_2, dA_3 with dA_s as the area of the fourth face. Geometrically

$$dA_s \frac{\vec{s}}{s} = dA_1 \frac{\vec{A}^1}{\sqrt{A^{11}}} + dA_2 \frac{\vec{A}^2}{\sqrt{A^{22}}} + dA_3 \vec{N} \quad (\text{III.76})$$

We can express \vec{s} (see Eq. (III.26)) in terms of the contravariant base vectors:

$$\vec{s} = s_1 \vec{A}^1 + s_2 \vec{A}^2 + s_3 \vec{N} \quad (\text{III.77})$$

and hence it is seen that

$$\frac{dA_1}{dA_s} = \sqrt{A^{11}} \frac{s_1}{s} \quad (\text{III.78})$$

$$\frac{dA_2}{dA_s} = \sqrt{A^{22}} \frac{s_2}{s} \quad (\text{III.79})$$

$$\frac{dA_3}{dA_s} = \frac{s_3}{s} \quad (\text{III.80})$$

Then the equilibrium equation becomes

$$\sigma^* \vec{s} = \vec{d}^1 \sqrt{A^1} s_1 + \vec{d}^2 \sqrt{A^2} s_2 + \vec{d}^3 s_3 \quad (\text{III.81})$$

This last expression gives us license to write

$$\vec{d}^1 \sqrt{A^1} = d^{1\alpha} \vec{A}_\alpha + d^{(3)1} \vec{N} \quad (\text{III.82})$$

$$\vec{d}^2 \sqrt{A^2} = d^{2\alpha} \vec{A}_\alpha + d^{(3)2} \vec{N} \quad (\text{III.83})$$

Next we isolate an element of volume from the thicket with one edge along \vec{s} and two other edges perpendicular to \vec{s} (see Fig. III.11).

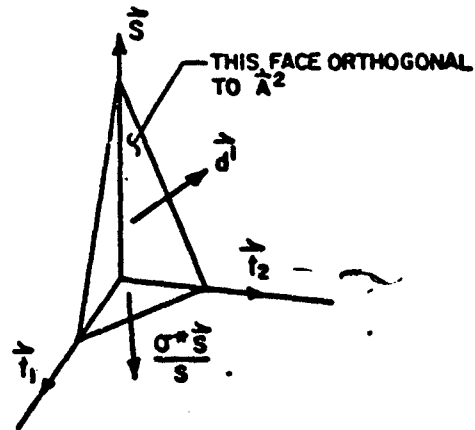


Figure III.11

The vectors \vec{t}_1 and \vec{t}_2 are unit vectors which together with \vec{s} form a mutually orthogonal set. The fourth or

canted face is chosen to be orthogonal to \vec{A}' , i.e., stress vector \vec{J}' acts on this face (see Fig. III.9). Note that two of the four faces, being parallel to the shear chords, are stress free. The stress vectors acting on the bottom surface (which is perpendicular to \vec{S}) and on the fourth face are $\sigma^* \frac{\vec{S}}{S}$ and \vec{J}' , respectively. Then, for equilibrium we must have

$$\vec{J}' dA_1 = \frac{\sigma^*}{S} \vec{S} dA_3 \quad (\text{III.84})$$

Geometrically

$$dA_1 \frac{\vec{A}'}{\sqrt{A''}} = dA_3 \frac{\vec{S}}{S} + dA_2 \vec{T}_2 + dA_1 \vec{T}_1 \quad (\text{III.85})$$

By forming the scalar product of Eq. (III.85) with \vec{S} we obtain

$$\frac{dA_3}{dA_1} = \frac{\vec{A}' \cdot \vec{S}}{\sqrt{A''} S} \quad (\text{III.86})$$

Then by using Eq. (III.26) we obtain

$$\frac{dA_3}{dA_1} = \frac{SS'}{\sqrt{A''}} \quad (\text{III.87})$$

Similarly

$$\frac{dA_2}{dA_1} = \frac{SS^2}{\sqrt{A''}} \quad (\text{III.88})$$

Thus Eq. (III.84) yields

$$\vec{J}^1 = \sigma^* \frac{s^1}{\sqrt{A^{11}}} \vec{S} \quad (\text{III.89})$$

In a similar fashion

$$\vec{J}^2 = \sigma^* \frac{s^2}{\sqrt{A^{22}}} \vec{S} \quad (\text{III.90})$$

By combining Eqs. (III.89) and (III.90) with Eqs. (III.82) and (III.83) we obtain

$$\sigma^* s^\beta \vec{S} = d^{\beta\alpha} \vec{A}_\alpha + d^{(3)\beta} \vec{N} \quad (\text{III.91})$$

Thus, by using Eq. (III.26), we obtain

$$d^{\beta\alpha} = \sigma^* s^\beta s^\alpha \quad (\text{III.92})$$

$$d^{(3)\beta} = \sigma^* s^\beta s^3 \quad (\text{III.93})$$

E. EQUATIONS OF EQUILIBRIUM

There has been defined in the previous section force resultants and moment resultants which are equipollent to the stresses in the two membranes, the internal pressure, and the shear chords. This equipollent system is defined for the middle surface of the shell and, therefore, the equilibrium equations are written for an element of area on the imaginary middle surface. It is convenient to define quasi-force and moment vectors as follows:

$$\vec{L}^\sigma = \sqrt{A} (l^{\sigma\alpha} \vec{A}_\alpha + g^\sigma \vec{N}) \quad (\text{III.94})$$

$$\vec{M}^{\sigma} = \sqrt{A} \, \vec{e}_{\alpha\sigma} \, m^{\alpha\sigma} \vec{A}^{\sigma} \quad (\text{III.95})$$

$$\vec{P}^{\sigma} = \sqrt{A} \, p_n^{\sigma} \, h^{\sigma} \vec{A}^{\sigma} \quad (\text{III.96})$$

$$\vec{D}^{\sigma} = \sqrt{A} \, h^{\sigma} \left(d^{\sigma\alpha} \vec{A}_{\alpha} + d^{(3)\sigma} \vec{N} \right) \quad (\text{III.97})$$

The conversion of the preceding vectors to forces is accomplished simply by multiplying the appropriate $d\xi^{\alpha}$ e.g., the force acting on the mid-surface due to \vec{L}^{σ} is $\vec{L}^{\sigma} d\xi^{\sigma}$. We also define a loading force vector \vec{F} as

$$\vec{F} = \sqrt{A} \left[F^{\alpha} \vec{A}_{\alpha} + F^3 \vec{N} \right] \quad (\text{III.98})$$

All of these are shown in Figs. III.12 and III.13 (two figures are used for purposes of clarity).

The vector equation of force equilibrium is obtained by summing all the force vectors in Figs. III.12 and III.13. There results

$$\frac{\partial \vec{L}^{\sigma}}{\partial \xi^{\sigma}} + \frac{\partial \vec{D}^{\sigma}}{\partial \xi^{\sigma}} - \frac{\partial \vec{P}^{\sigma}}{\partial \xi^{\sigma}} + \vec{F} \sqrt{A} = 0 \quad (\text{III.99})$$

The vector equation of moment equilibrium is obtained by summing the moment vectors (represented by double-headed arrows in Fig. III.13) and taking moments of all the force vectors about point o. The result is

$$\frac{\partial \vec{M}^{\sigma}}{\partial \xi^{\sigma}} + \vec{A}_{\sigma} \times (\vec{L}^{\sigma} + \vec{D}^{\sigma} - \vec{P}^{\sigma}) = 0 \quad (\text{III.100})$$

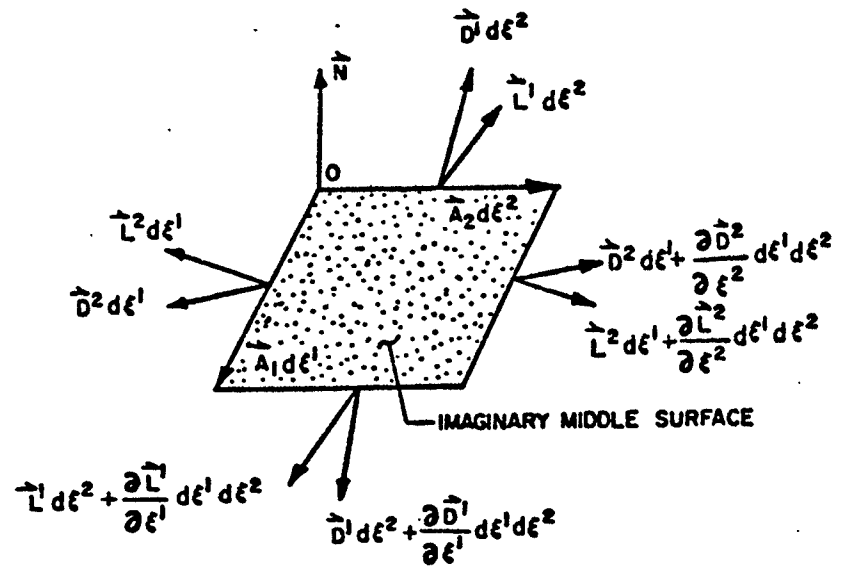


Figure III.12

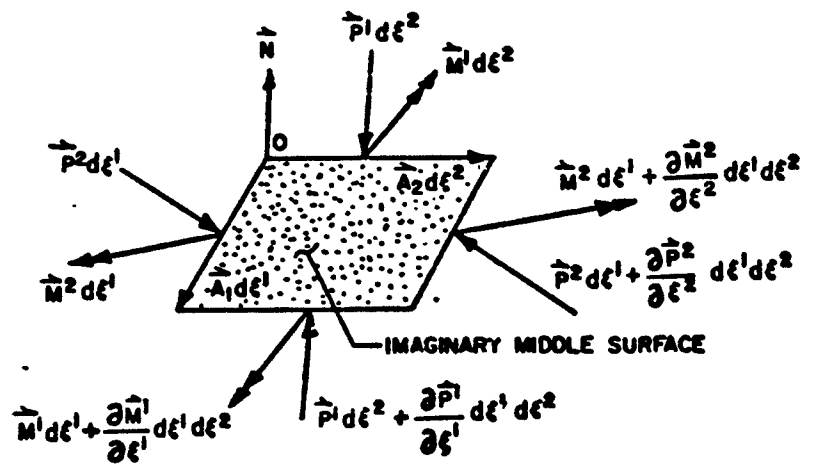


Figure III.13

We make use of the following auxiliary relations:

$$\frac{\partial \vec{L}^\sigma}{\partial \xi^\sigma} = \sqrt{A} \left\{ \left(l^{\sigma\alpha} \Big|_\sigma - q^\sigma B_\sigma^\alpha \right) \vec{A}_\alpha + \left(q^\sigma \Big|_\sigma + l^{\sigma\alpha} B_{\alpha\sigma} \right) \vec{N} \right\} \quad (\text{III.101})$$

$$\begin{aligned} \frac{\partial \vec{D}^\sigma}{\partial \xi^\sigma} = & \sqrt{A} h^* \left\{ \left(d^{\sigma\alpha} \Big|_\sigma - d^{(\sigma\sigma} B_\sigma^\alpha \right) \vec{A}_\alpha + \left(d^{(\sigma\sigma} \Big|_\sigma + d^{\sigma\alpha} B_{\alpha\sigma} \right) \vec{N} \right\} \\ & + \sqrt{A} \frac{\partial h^*}{\partial \xi^\sigma} \left(d^{\sigma\alpha} \vec{A}_\alpha + d^{(\sigma\sigma} \vec{N} \right) \end{aligned} \quad (\text{III.102})$$

$$\frac{\partial \vec{P}^\sigma}{\partial \xi^\sigma} = \sqrt{A} \left\{ p_\sigma^* h^* B_\sigma^\sigma \vec{N} + p_\sigma^* \frac{\partial h^*}{\partial \xi^\sigma} \vec{A}^\sigma \right\} \quad (\text{III.103})$$

$$\frac{\partial \vec{M}^\sigma}{\partial \xi^\sigma} = \sqrt{A} \left\{ \mathcal{E}_{\alpha\sigma} m^{\beta\alpha} \Big|_\beta \vec{A}^\sigma + \mathcal{E}_{\alpha\sigma} m^{\beta\alpha} B_\beta^\sigma \vec{N} \right\} \quad (\text{III.104})$$

$$\vec{A}_\sigma \times \vec{D}^\sigma = \sqrt{A} h^* \left\{ d^{\alpha\sigma} \mathcal{E}_{\alpha\sigma} \vec{N} + d^{(\sigma\alpha} \mathcal{E}_{\sigma\alpha} \vec{A}^\sigma \right\} \quad (\text{III.105})$$

$$\vec{A}_\sigma \times \vec{L}^\sigma = \sqrt{A} \left\{ l^{\alpha\sigma} \mathcal{E}_{\alpha\sigma} \vec{N} + q^\alpha \mathcal{E}_{\sigma\alpha} \vec{A}^\sigma \right\} \quad (\text{III.106})$$

$$\vec{A}_\sigma \times \vec{P}^\sigma = 0 \quad (\text{III.107})$$

These latter relations lead, when substituted into the vector Eqs. (III.99) and (III.100), to the following tensor equations of force and moment equilibrium:

$$l^{\sigma\alpha} \Big|_\sigma - q^\sigma B_\sigma^\alpha + h^* \left(l^{\sigma\alpha} \Big|_\sigma - d^{(\sigma\sigma} B_\sigma^\alpha \right) + \frac{\partial h^*}{\partial \xi^\sigma} d^{\sigma\alpha} - \mathcal{E}_{\sigma\alpha} \frac{\partial h^*}{\partial \xi^\sigma} \vec{A}^\sigma + F^\alpha = 0. \quad (\text{III.108})$$

$$q^\sigma|_\sigma + l^{\sigma\alpha} B_{\alpha\sigma} + h^* (d^{(3)\sigma}|_\sigma + d^{\sigma\alpha} B_{\alpha\sigma}) + \frac{\partial h^*}{\partial \xi^\sigma} d^{(3)\sigma} + F^3 = 0 \quad (\text{III.109})$$

$$m^{\beta\alpha}|_\beta - q^\alpha - h^* d^{(3)\alpha} = 0 \quad (\text{III.110})$$

$$\frac{\partial}{\partial \sigma} (m^{\beta\alpha} B_\beta^\sigma + l^{\alpha\sigma} + h^* d^{\alpha\sigma}) = 0 \quad (\text{III.111})$$

F. STRESS-STRAIN RELATIONS FOR SMALL STRAIN

The upper and lower membranes of an inflated shell will most likely be constructed of a woven fabric. Although the microscopic behavior of such a material is very difficult to specify, the gross macroscopic behavior can be satisfactorily approximated by treating the membrane as a material with two axes of symmetry. The stress-strain relation can then be written in the general form

$$\tau^{\alpha\beta} = E^{\alpha\beta\theta\tau} \gamma_{\theta\tau} \quad (\text{III.112})$$

for general curvilinear coordinates. We will call the $E^{\alpha\beta\theta\tau}$ the elasticity tensor and it obeys the symmetry relations

$$E^{\alpha\beta\theta\tau} = E^{\beta\alpha\theta\tau} = E^{\alpha\beta\tau\theta} = E^{\theta\tau\alpha\beta} \quad (\text{III.113})$$

If we choose a set of local rectangular cartesian coordinates to coincide with the axes of orthotropy, the stress-strain relations become

$$\sigma^{\alpha\beta} = \hat{E}^{\alpha\beta\theta\tau} \epsilon_{\theta\tau} \quad (\text{III.114})$$

$$q^\sigma|_\sigma + l^{\sigma\alpha} B_{\alpha\sigma} + h^* (d^{(3)\sigma}|_\sigma + d^{\sigma\alpha} B_{\alpha\sigma}) + \frac{\partial h^*}{\partial \xi^\sigma} d^{(3)\sigma} + F^3 = 0 \quad (\text{III.109})$$

$$m^{\beta\alpha}|_\beta - q^\alpha - h^* d^{(3)\alpha} = 0 \quad (\text{III.110})$$

$$\mathcal{L}_{\alpha\sigma} (m^{\beta\alpha} B_\beta^\sigma + l^{\alpha\sigma} + h^* d^{\alpha\sigma}) = 0 \quad (\text{III.111})$$

F. STRESS-STRAIN RELATIONS FOR SMALL STRAIN

The upper and lower membranes of an inflated shell will most likely be constructed of a woven fabric. Although the microscopic behavior of such a material is very difficult to specify, the gross macroscopic behavior can be satisfactorily approximated by treating the membrane as a material with two axes of symmetry. The stress-strain relation can then be written in the general form

$$\tau^{\alpha\beta} = E^{\alpha\beta\theta\tau} \gamma_{\theta\tau} \quad (\text{III.112})$$

for general curvilinear coordinates. We will call the $E^{\alpha\beta\theta\tau}$ the elasticity tensor and it obeys the symmetry relations

$$E^{\alpha\beta\theta\tau} = E^{\beta\alpha\theta\tau} = E^{\alpha\beta\tau\theta} = E^{\theta\tau\alpha\beta} \quad (\text{III.113})$$

If we choose a set of local rectangular cartesian coordinates to coincide with the axes of orthotropy, the stress-strain relations become

$$\sigma^{\alpha\beta} = \hat{E}^{\alpha\beta\theta\tau} \epsilon_{\theta\tau} \quad (\text{III.114})$$

where $\sigma^{\alpha\beta}$ and $\epsilon_{\theta\tau}$ are physical components. Since the material is assumed orthotropic, there are only five independent components of the elasticity tensor.

$$\hat{E}^{\alpha\beta\theta\tau} = \begin{bmatrix} \hat{E}^{1111} & \hat{E}^{1122} & 0 \\ \hat{E}^{2211} & \hat{E}^{2222} & 0 \\ 0 & 0 & \hat{E}^{1212} \end{bmatrix} \quad (\text{III.115})$$

If we indicate the transformation from rectangular cartesian coordinates y^{α} , to general curvilinear coordinates ξ^{α} , as

$$\xi^{\alpha} = \xi^{\alpha}(y^1, y^2) \quad (\text{III.116})$$

then the elasticity tensor in the y^{α} coordinates is transformed to the ξ^{α} coordinates as

$$E^{\alpha\beta\theta\tau} = \frac{\partial \xi^{\alpha}}{\partial y^{\sigma}} \frac{\partial \xi^{\beta}}{\partial y^{\eta}} \frac{\partial \xi^{\theta}}{\partial y^{\delta}} \frac{\partial \xi^{\tau}}{\partial y^{\omega}} \hat{E}^{\sigma\eta\delta\omega} \quad (\text{III.117})$$

For an isotropic material the elasticity tensor takes on the form

$$E^{\alpha\beta\theta\tau} = \mu \left\{ g^{\alpha\theta} g^{\beta\tau} + g^{\alpha\tau} g^{\beta\theta} + \frac{2\nu}{1-\nu} g^{\alpha\beta} g^{\theta\tau} \right\} \quad (\text{III.118})$$

where

$$\mu = \frac{E}{2(1+\nu)}$$

with E and ν being the usual Young's modulus and Poisson's ratio, respectively. The $g^{\alpha\theta}$ are the metric tensors of the membrane surface.

G. INCREMENTAL THEORY LEADING TO LARGE DISPLACEMENTS

The equations which have been developed for the large deformations of an inflated shell are much too difficult to solve explicitly. We will propose a method of solution which arrives at the final result by a series of linearized equations.

In Fig. III.14 the imaginary middle surfaces at three different stages of deformation are shown. The first stage is the undeformed, the second will be called the deformed, and the third will be called the further-deformed. It will be assumed that the additional displacements leading to the further-deformed shell are sufficiently small so that the squares and products of changes in all quantities can be neglected.

Let us first define and calculate the geometric parameters of the imaginary middle surface of the further-deformed shell. The displacement vector connecting the deformed and further-deformed middle surfaces will be denoted by $\Delta \vec{u}(\xi^1, \xi^2)$ where the Δ signifies a small change. All vectors and tensors will be denoted as the tensor of the deformed shell plus a Δ change, e.g., the base vectors are denoted by $\vec{A}_\alpha + \Delta \vec{A}_\alpha$, the fundamental metric tensor by $A_{\alpha\beta} + \Delta A_{\alpha\beta}$, etc. We assume that squares of Δ changes are negligible.

Our primary interest lies in the Δ changes. For

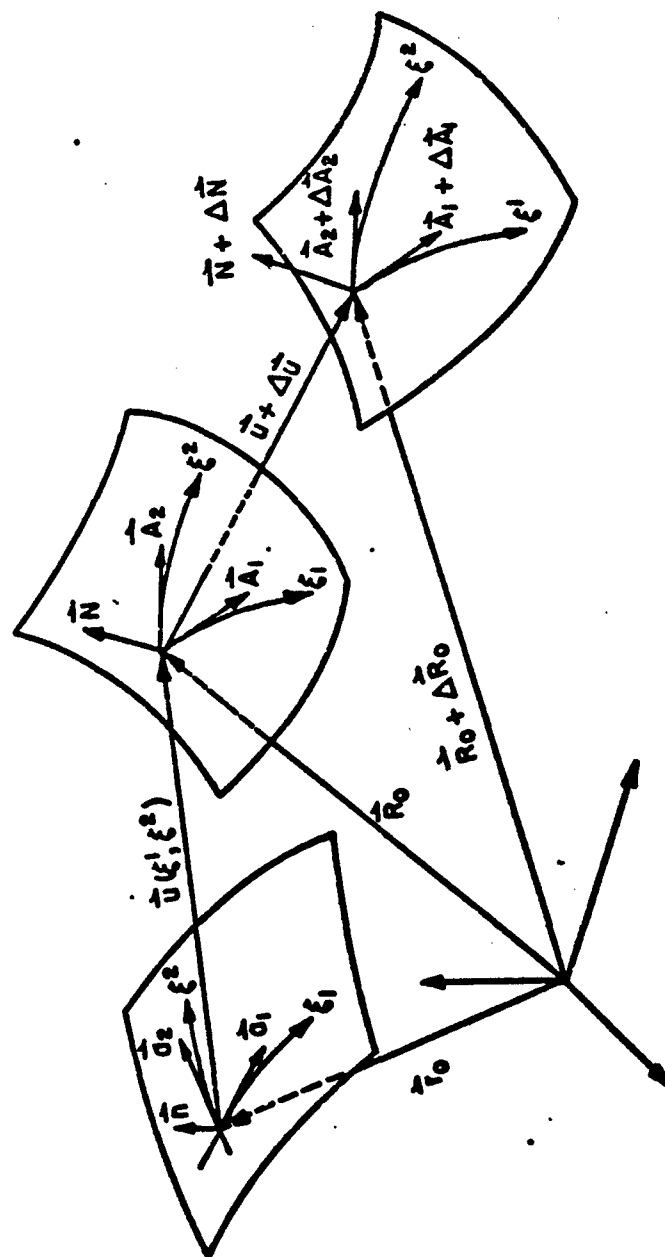


Figure III.14

example

$$\vec{A}_\alpha + \Delta \vec{A}_\alpha = \frac{\partial \vec{R}_\alpha}{\partial \xi^\alpha} + \frac{\partial \vec{u}}{\partial \xi^\alpha} + \frac{\partial \Delta \vec{u}}{\partial \xi^\alpha} \quad (\text{III.119})$$

and hence

$$\Delta \vec{A}_\alpha = \frac{\partial \Delta \vec{u}}{\partial \xi^\alpha} \quad (\text{III.120})$$

We will write $\Delta \vec{u}$ in terms of components with respect to vector directions of the deformed middle surface

$$\Delta \vec{u} = \Delta u^\beta \vec{A}_\beta + \Delta w \vec{N} \quad (\text{III.121})$$

This leads to the following relation for $\Delta \vec{A}_\alpha$

$$\Delta \vec{A}_\alpha = \left[\Delta u^\sigma \right]_\alpha - B_\alpha^\sigma \Delta w \Big] \vec{A}_\sigma + \left[\Delta u^\sigma B_{\sigma\alpha} + \frac{\partial \Delta w}{\partial \xi^\alpha} \right] \vec{N} \quad (\text{III.122})$$

where the vertical bar signifies covariant differentiation with respect to the metric of the deformed middle surface.

We recall the basic definition for the base vectors

$$A_{\alpha\beta} + \Delta A_{\alpha\beta} = (\vec{A}_\alpha + \Delta \vec{A}_\alpha) \cdot (\vec{A}_\beta + \Delta \vec{A}_\beta) \quad (\text{III.123})$$

As a consequence of the assumption regarding the magnitude of the Δ changes, we neglect the term $\Delta \vec{A}_\alpha \cdot \Delta \vec{A}_\beta$ and approximate $\Delta A_{\alpha\beta}$ as follows:

$$\Delta A_{\alpha\beta} \approx \Delta \vec{A}_\alpha \cdot \vec{A}_\beta + \vec{A}_\alpha \cdot \Delta \vec{A}_\beta \quad (\text{III.124})$$

In a similar fashion, the changes in the parameters of the strained middle surface can be found.

$$\Delta A^{\alpha\sigma} = -A^{\gamma\sigma} A^{\alpha\beta} \Delta A_{\beta\gamma} \quad (\text{III.125})$$

$$\Delta A = A A^{\sigma\alpha} \Delta A_{\sigma\alpha} \quad (\text{III.126})$$

$$\Delta \vec{N} \approx \frac{1}{\sqrt{A}} \left[\Delta \vec{A}_1 \times \vec{A}_2 + \vec{A}_1 \times \Delta \vec{A}_2 \right] \quad (\text{III.127})$$

$$\Delta \vec{A}^\alpha \approx A^{\alpha\beta} \Delta \vec{A}_\beta + \Delta A^{\alpha\beta} \vec{A}_\beta \quad (\text{III.128})$$

$$\Delta B_{\alpha\beta} \approx \Delta \vec{N} \cdot \frac{\partial \vec{A}_\alpha}{\partial \xi^\beta} + \vec{N} \cdot \frac{\partial \Delta \vec{A}_\alpha}{\partial \xi^\beta} \quad (\text{III.129})$$

$$\Delta B_\sigma^\alpha \approx A^{\alpha\beta} \Delta B_{\beta\sigma} + \Delta A^{\alpha\beta} B_{\beta\sigma} \quad (\text{III.130})$$

$$\Delta \left\{ \begin{matrix} \alpha \\ \beta\gamma \end{matrix} \right\} \approx \Delta \vec{A}^\alpha \cdot \frac{\partial \vec{A}_\gamma}{\partial \xi^\beta} + \vec{A}^\alpha \cdot \frac{\partial \Delta \vec{A}_\gamma}{\partial \xi^\beta} \quad (\text{III.131})$$

The increments in the components of strain on the upper membrane are defined in the traditional manner:

$$(dS_u)_{\text{further strained}}^2 - (dS_u)_{\text{strained}}^2 = 2 \Delta \gamma_{\alpha\beta}^{(u)} d\xi^\alpha d\xi^\beta \quad (\text{III.132})$$

where the index u denotes the upper membrane. A similar expression can be written for the lower membrane.

The relationships of the various vectors connecting on the upper membrane of the deformed shell to the same

point on P' of the further-deformed shell are depicted in Fig. III.15.

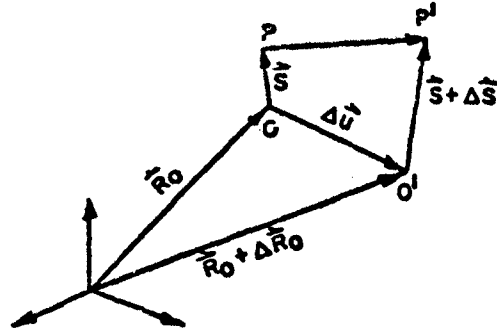


Figure III.15

The vector joining O' on the imaginary middle surface to P' is seen to be denoted by $\vec{S} + \Delta\vec{S}$ where

$$\Delta\vec{S} = \Delta S \vec{A}_r + \Delta S^3 \vec{N} \quad (\text{III.133})$$

We observe that the position vector to P' is given by

$$\vec{R}_u + \Delta\vec{R}_u = \vec{R}_o + \Delta\vec{R}_o + \vec{S} + \Delta\vec{S} \quad (\text{III.134})$$

and hence

$$d(\vec{R}_u + \Delta\vec{R}_u) = d(\vec{R}_o + \vec{S}) + d(\Delta\vec{R}_o + \Delta\vec{S}) \quad (\text{III.135})$$

This, when substituted into Eq. (III.132), leads to the following expression for the increments in the components of strain on the upper membrane

$$\Delta \gamma_{\alpha\beta}^{(u)} = \frac{1}{2} \left\{ \left[\vec{A}_\alpha + \frac{\partial \vec{S}}{\partial \xi^\alpha} \right] \cdot \left[\frac{\partial \Delta \vec{u}}{\partial \xi^\beta} + \frac{\partial \Delta \vec{S}}{\partial \xi^\beta} \right] + \left[\vec{A}_\beta + \frac{\partial \vec{S}}{\partial \xi^\beta} \right] \cdot \left[\frac{\partial \Delta \vec{u}}{\partial \xi^\alpha} + \frac{\partial \Delta \vec{S}}{\partial \xi^\alpha} \right] \right\} \quad (\text{III.136})$$

wherein we have dropped terms involving products of Δ changes.

In a similar manner the components on the lower membrane can be obtained

$$\Delta \gamma_{\alpha\beta}^{(l)} = \frac{1}{2} \left\{ \left[\vec{A}_\alpha - \frac{\partial \vec{S}}{\partial \xi^\alpha} \right] \cdot \left[\frac{\partial \Delta \vec{u}}{\partial \xi^\beta} - \frac{\partial \Delta \vec{S}}{\partial \xi^\beta} \right] + \left[\vec{A}_\beta - \frac{\partial \vec{S}}{\partial \xi^\beta} \right] \cdot \left[\frac{\partial \Delta \vec{u}}{\partial \xi^\alpha} - \frac{\partial \Delta \vec{S}}{\partial \xi^\alpha} \right] \right\} \quad (\text{III.137})$$

It will be convenient to define an average strain $\Delta \gamma_{\alpha\beta}^o$ and a curvature strain $\Delta \kappa_{\alpha\beta}^o$:

$$\Delta \gamma_{\alpha\beta}^o = \frac{1}{2} (\Delta \gamma_{\alpha\beta}^{(u)} + \Delta \gamma_{\alpha\beta}^{(l)}) \quad (\text{III.138})$$

$$\Delta \kappa_{\alpha\beta}^o = \frac{1}{2} (\Delta \gamma_{\alpha\beta}^{(u)} - \Delta \gamma_{\alpha\beta}^{(l)}) \quad (\text{III.139})$$

The substitution of Eqs. (III.136) and (III.137) into Eqs. (III.138) and (III.139) yields

$$\Delta \gamma_{\alpha\beta}^{\circ} = \frac{1}{2} \left\{ \vec{A}_{\alpha} \cdot \frac{\partial \Delta \vec{u}}{\partial \xi^{\beta}} + \vec{A}_{\beta} \cdot \frac{\partial \Delta \vec{u}}{\partial \xi^{\alpha}} + \frac{\partial \vec{s}}{\partial \xi^{\alpha}} \cdot \frac{\partial \Delta \vec{s}}{\partial \xi^{\beta}} + \frac{\partial \vec{s}}{\partial \xi^{\beta}} \cdot \frac{\partial \Delta \vec{s}}{\partial \xi^{\alpha}} \right\} \quad (\text{III.140})$$

$$\Delta k_{\alpha\beta}^{\circ} = \frac{1}{2} \left\{ \vec{A}_{\alpha} \cdot \frac{\partial \Delta \vec{s}}{\partial \xi^{\beta}} + \vec{A}_{\beta} \cdot \frac{\partial \Delta \vec{s}}{\partial \xi^{\alpha}} + \frac{\partial \vec{s}}{\partial \xi^{\alpha}} \cdot \frac{\partial \Delta \vec{u}}{\partial \xi^{\beta}} + \frac{\partial \vec{s}}{\partial \xi^{\beta}} \cdot \frac{\partial \Delta \vec{u}}{\partial \xi^{\alpha}} \right\} \quad (\text{III.141})$$

wherein the nonlinear terms have been omitted from Eq. (III.140).

The derivatives of \vec{s} , $\Delta \vec{u}$, and $\Delta \vec{s}$ are as follows:

$$\frac{\partial \vec{s}}{\partial \xi^{\alpha}} = \left[s^{\sigma} \right]_{\alpha} - B_{\alpha}^{\sigma} s^{\beta} \vec{A}_{\sigma} + \left[s^{\sigma} B_{\sigma\alpha} + \frac{\partial s^{\beta}}{\partial \xi^{\alpha}} \right] \vec{N} \quad (\text{III.142})$$

$$\frac{\partial \Delta \vec{u}}{\partial \xi^{\alpha}} = \left[\Delta u^{\sigma} \right]_{\alpha} - B_{\alpha}^{\sigma} \Delta u^{\beta} \vec{A}_{\sigma} + \left[\Delta u^{\sigma} B_{\sigma\alpha} + \frac{\partial \Delta u^{\beta}}{\partial \xi^{\alpha}} \right] \vec{N} \quad (\text{III.143})$$

$$\frac{\partial \Delta \vec{s}}{\partial \xi^{\alpha}} = \left[\Delta s^{\sigma} \right]_{\alpha} - B_{\alpha}^{\sigma} \Delta s^{\beta} \vec{A}_{\sigma} + \left[\Delta s^{\sigma} B_{\sigma\alpha} + \frac{\partial \Delta s^{\beta}}{\partial \xi^{\alpha}} \right] \vec{N} \quad (\text{III.144})$$

There results for the components of strain

$$\begin{aligned}
\Delta Y_{\alpha\beta}^{\circ} = \frac{1}{2} \bigg\{ & \Delta u_{\alpha}|_{\beta} + \Delta u_{\beta}|_{\alpha} - 2 B_{\alpha\beta} \Delta w \\
& + [s^{\sigma}|_{\alpha} - B_{\alpha}^{\sigma} s^3] [\Delta s^{\gamma}|_{\beta} - B_{\beta}^{\gamma} \Delta s^3] A_{\sigma\gamma} \\
& + [s^{\sigma}|_{\beta} - B_{\beta}^{\sigma} s^3] [\Delta s^{\gamma}|_{\alpha} - B_{\alpha}^{\gamma} \Delta s^3] A_{\sigma\gamma} \\
& + [s^{\sigma} B_{\sigma\alpha} + \frac{\partial s^3}{\partial \xi^{\alpha}}] [\Delta s^{\gamma} B_{\gamma\beta} + \frac{\partial \Delta s^3}{\partial \xi^{\beta}}] \\
& + [s^{\sigma} B_{\sigma\beta} + \frac{\partial s^3}{\partial \xi^{\beta}}] [\Delta s^{\gamma} B_{\gamma\alpha} + \frac{\partial \Delta s^3}{\partial \xi^{\alpha}}] \bigg\} \quad (\text{III.145})
\end{aligned}$$

$$\begin{aligned}
\Delta K_{\alpha\beta}^{\circ} = \frac{1}{2} \bigg\{ & \Delta s_{\alpha}|_{\beta} + \Delta s_{\beta}|_{\alpha} - 2 B_{\alpha\beta} \Delta s^3 \\
& + [s^{\sigma}|_{\alpha} - B_{\alpha}^{\sigma} s^3] [\Delta u^{\gamma}|_{\beta} - B_{\beta}^{\gamma} \Delta w] A_{\sigma\gamma} \\
& + [s^{\sigma}|_{\beta} - B_{\beta}^{\sigma} s^3] [\Delta u^{\gamma}|_{\alpha} - B_{\alpha}^{\gamma} \Delta w] A_{\sigma\gamma} \\
& + [s^{\sigma} B_{\sigma\alpha} + \frac{\partial s^3}{\partial \xi^{\alpha}}] [\Delta u^{\gamma} B_{\gamma\beta} + \frac{\partial \Delta w}{\partial \xi^{\beta}}] \\
& + [s^{\sigma} B_{\sigma\beta} + \frac{\partial s^3}{\partial \xi^{\beta}}] [\Delta u^{\gamma} B_{\gamma\alpha} + \frac{\partial \Delta w}{\partial \xi^{\alpha}}] \bigg\} \quad (\text{III.146})
\end{aligned}$$

The first three terms for $\Delta\gamma_{\alpha\beta}^{\circ}$ in Eq. (III.145) are recognizable as of the same form as those appearing in the infinitesimal theory of thin shells. The remainder of the terms in Eq. (III.145) can be shown to be proportional to the square of the spacing between the membranes. Again, these terms are usually omitted from thin shell theory. It is not clear at this stage that omission from the theory of inflated shells is justified since some of the proposed configurations are not "thin." Similarly, only the first two terms for $\Delta k_{\alpha\beta}^{\circ}$ in Eq. (III.146) are retained in thin shell theory.

The increment in the transverse shearing strain (see Eq. (III.37)) is defined by the equation

$$\gamma_{\alpha 3} + \Delta\gamma_{\alpha 3} = \frac{1}{2} (\vec{A}_{\alpha} + \Delta\vec{A}_{\alpha}) \cdot (\vec{S} + \Delta\vec{S}) \quad (\text{III.147})$$

from which there is obtained

$$\Delta\gamma_{\alpha 3} = \frac{1}{2} (\vec{A}_{\alpha} \cdot \Delta\vec{S} + \Delta\vec{A}_{\alpha} \cdot \vec{S}) \quad (\text{III.148})$$

In terms of the increments in \vec{S} and \vec{u} , Eq. (III.148) becomes

$$\Delta\gamma_{\alpha 3} = \frac{1}{2} \left\{ (\Delta u_{,\alpha} - B_{\alpha\alpha} \Delta w) S^{\alpha} + \left(\Delta u^{\alpha} B_{\alpha\alpha} + \frac{\partial \Delta w}{\partial x^{\alpha}} \right) S^{\alpha} + \Delta S_{\alpha} \right\} \quad (\text{III.149})$$

The inflated sandwich shell remains in equilibrium in its further-deformed state. We express the force and moment resultants acting on the middle surface in the further-deformed state as the force and moment, respectively,

in the deformed state plus a small increment. Thus, the two equilibrium equations given by Eq. (III.108) become

$$\begin{aligned}
 & (\ell^{\sigma\alpha} + \Delta\ell^{\sigma\alpha}) \parallel_{\sigma} - (\ell^{\sigma} + \Delta\ell^{\sigma}) (B_{\sigma}^{\alpha} + \Delta B_{\sigma}^{\alpha}) + (d^{\sigma\alpha} + \Delta d^{\sigma\alpha}) \parallel_{\sigma} \\
 & - (d^{(3)\sigma} + \Delta d^{(3)\sigma}) (B_{\sigma}^{\alpha} + \Delta B_{\sigma}^{\alpha}) + \frac{\partial(\ell^{\sigma} + \Delta\ell^{\sigma})}{\partial \xi^{\sigma}} (d^{\sigma\alpha} + \Delta d^{\sigma\alpha}) \\
 & - (b_{\sigma}^{\alpha} + \Delta b_{\sigma}^{\alpha}) \left(\frac{\partial(\ell^{\sigma} + \Delta\ell^{\sigma})}{\partial \xi^{\sigma}} \right) (A^{\sigma\alpha} + \Delta A^{\sigma\alpha}) + F^{\alpha} + \Delta F^{\alpha} = 0
 \end{aligned} \tag{III.150}$$

wherein the double vertical bars preceding a subscript signifies covariant differentiation with respect to the metric of the further-deformed middle surface. For example, the covariant derivative of the force resultant, $\ell^{\sigma\alpha} + \Delta\ell^{\sigma\alpha}$ with respect to the metric of the further-deformed state is given by

$$\begin{aligned}
 (\ell^{\sigma\alpha} + \Delta\ell^{\sigma\alpha}) \parallel_{\sigma} &= \frac{\partial(\ell^{\sigma\alpha} + \Delta\ell^{\sigma\alpha})}{\partial \xi^{\sigma}} + \left(\left\{ \begin{matrix} \gamma \\ \delta \sigma \end{matrix} \right\} + \Delta \left\{ \begin{matrix} \gamma \\ \delta \sigma \end{matrix} \right\} \right) (\ell^{\sigma\alpha} + \Delta\ell^{\sigma\alpha}) \\
 &+ \left(\left\{ \begin{matrix} \alpha \\ \delta \sigma \end{matrix} \right\} + \Delta \left\{ \begin{matrix} \alpha \\ \delta \sigma \end{matrix} \right\} \right) (\ell^{\gamma\sigma} + \Delta\ell^{\gamma\sigma})
 \end{aligned} \tag{III.151}$$

If Eq. (III.151) is substituted into Eq. (III.150) together with an analogous expression for $(d^{\sigma\alpha} + \Delta d^{\sigma\alpha}) \parallel_{\sigma}$, there will result, since Eq. (III.108) can be factored out,

$$\begin{aligned}
& \Delta l^{\sigma\alpha} \Big|_{\sigma} - \Delta q^{\sigma} B_{\sigma}^{\alpha} + \Delta d^{\sigma\alpha} \Big|_{\sigma} - \Delta d^{(1)\sigma} B_{\sigma}^{\alpha} - \Delta d^{(2)\sigma} B_{\sigma}^{\alpha} - \Delta d^{(3)\sigma} B_{\sigma}^{\alpha} \\
& + \Delta \left\{ \frac{\sigma}{\gamma\sigma} \right\} l^{\sigma\alpha} + \Delta \left\{ \frac{\alpha}{\gamma\sigma} \right\} l^{\gamma\sigma} - \Delta B_{\sigma}^{\alpha} q^{\sigma} + d^{\sigma\alpha} \Delta \left\{ \frac{\sigma}{\gamma\sigma} \right\} + d^{\gamma\sigma} \Delta \left\{ \frac{\alpha}{\gamma\sigma} \right\} - d^{\gamma\sigma} \Delta B_{\sigma}^{\alpha} \\
& + \frac{\partial \Delta l^{\sigma\alpha}}{\partial \xi^{\sigma}} \Delta d^{\sigma\alpha} + \frac{\partial \Delta l^{\sigma\alpha}}{\partial \xi^{\sigma}} d^{\sigma\alpha} - \rho_0^{\alpha} \left[\frac{\partial \Delta l^{\sigma\alpha}}{\partial \xi^{\sigma}} \Delta A^{\sigma\alpha} + \frac{\partial \Delta l^{\sigma\alpha}}{\partial \xi^{\sigma}} A^{\sigma\alpha} \right] = 0 \quad (\text{III.152})
\end{aligned}$$

Similarly, the equation of force equilibrium in the normal direction (see Eq. (III.109)) and the moment equilibrium equations (see Eq. (III.110)) become

$$\begin{aligned}
& \Delta q^{\sigma} \Big|_{\sigma} - \Delta l^{\sigma\alpha} B_{\alpha\sigma} + \Delta d^{(1)\sigma} \Big|_{\sigma} + \Delta d^{\sigma\alpha} B_{\alpha\sigma} + \Delta d^{(3)\sigma} \frac{\partial \Delta l^{\sigma\alpha}}{\partial \xi^{\sigma}} + \Delta F^{\sigma} \\
& + \Delta \left\{ \frac{\sigma}{\sigma\gamma} \right\} q^{\gamma} - \Delta B_{\alpha\sigma} l^{\sigma\alpha} + \Delta \left\{ \frac{\sigma}{\sigma\gamma} \right\} d^{(3)\gamma} + \Delta B_{\alpha\sigma} d^{\sigma\alpha} + \frac{\partial \Delta l^{\sigma\alpha}}{\partial \xi^{\sigma}} d^{\sigma\alpha} = 0 \quad (\text{III.153})
\end{aligned}$$

$$\Delta m^{\beta\alpha} \Big|_{\beta} - \Delta q^{\alpha} - \Delta d^{(1)\alpha} l^{\beta\alpha} + \Delta \left\{ \frac{\beta}{\gamma\sigma} \right\} m^{\sigma\alpha} + \Delta \left\{ \frac{\alpha}{\gamma\sigma} \right\} m^{\beta\sigma} - \Delta d^{\beta\alpha} d^{(3)\sigma} = 0 \quad (\text{III.154})$$

The increments in tensor quantities $d^{\sigma\alpha}$ and $d^{(1)\alpha}$ which are related to the stress in the shear chords need to be explicitly displayed. With Eq. (III.92) as the model we write

(III.154)

(III.155)

(III.156)

and hence

$$\Delta \theta^{\alpha\beta} = \sigma^* (\dot{u}_3^{\alpha\beta} + \dots) \quad (III.158)$$

H. FINITE DEFLECTION OF AN INITIALLY FLAT, INFLATED, UNIFORM SANDWICH PLATE

In this section the equations derived thus far will be applied to an initially flat inflated sandwich plate. We will assume the deflections are finite which means the rotations are of a magnitude such that the size of the angle of rotation can be replaced by the angle. Furthermore, only those rotations occurring about the base vectors \bar{x}_α are finite; rotations about the normal are infinitesimal in magnitude. The plate is rectangular in shape and will be described by coordinates y^α as shown in Fig. III.16.

Copy available to DTIC does not
 permit fully legible reproduction

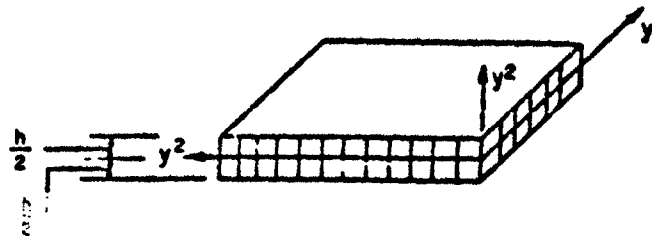


Figure III.13

We also will restrict our attention to a **rect** plate of uniform thickness with upper and lower surfaces of the same thickness ℓ .

The normal vectors of the inner and outer surfaces of the plate will be denoted by $\vec{\ell}_1$ and $\vec{\ell}_2$, i.e.,

$$\vec{n}_1 = \vec{\ell}_1$$

$$\vec{n}_2 = \vec{\ell}_2$$

(III.16)

We will list the pertinent formulas which are defined relative to the metric of the undeformed plate

$$\vec{v}_{(a)} = \vec{u} + \vec{s} \cdot \vec{\ell}_1$$

(III.17)

Copy available to DTIC does not
 permit fully legible reproduction

$$\vec{v}_0 = \vec{u} + \vec{s} + \frac{1}{2} \vec{t}_3 \quad (\text{III.162})$$

$$\vec{u} = u^\sigma \vec{t}_\sigma + w \vec{t}_3 \quad (\text{III.163})$$

$$\vec{s} = s^\alpha \vec{t}_\alpha + \vec{t}_3 \quad (\text{III.164})$$

$$\gamma_{\alpha\beta}^0 = \frac{1}{2} (u_{\alpha,\beta} + u_{\beta,\alpha} + w_{,\alpha} w_{,\beta}) \quad (\text{III.165})$$

$$k_{\alpha\beta}^0 = \frac{1}{2} (s_{\alpha,\beta} + s_{\beta,\alpha}) \quad (\text{III.166})$$

$$\gamma_{\alpha 3} = \frac{1}{2} (s_{\alpha} + w_{,\alpha}) \quad (\text{III.167})$$

The following comments are appropriate:

a. The S^3 component of \vec{S} (see Eq. (III.26)) has been set equal to unity in order to be consistent with the assumption of small rotations.

b. Only the nonlinear terms involving the finite rotations by $w_{,\alpha}$ are retained.

c. Since the components of the metric tensor of the deformed plate are of unit value, there is no distinction between covariant and contravariant components. The use of superscripts or subscripts is dictated by convention.

d. Covariant differentiation in a rectangular coordinate system is identical to partial differentiation. The comma notation, then, indicates a partial derivative.

The stress vectors on the upper membrane are expressed as

$$\vec{\sigma}_{(n)}^{\alpha} = \tau_{(n)}^{\alpha\sigma} \vec{H}_{\sigma}^{(n)} \quad (\text{III.168})$$

It can be shown that within the confines of the theory in this section,

$$\frac{\partial \vec{H}}{\partial y^{\sigma}} = -w_{,\sigma} \vec{t}^{\sigma} \quad (\text{III.169})$$

$$B_{\alpha\beta} = w_{,\alpha\beta} \quad (\text{III.170})$$

$$B_{\beta}^{\alpha} = B_{\alpha\beta} \quad (\text{III.171})$$

$$k^{\alpha} = k \quad (\text{III.172})$$

$$p_{\sigma}^{\alpha} = p_{\sigma} \quad (\text{III.173})$$

$$H_{(n)} = 1 \quad (\text{III.174})$$

$$\sigma^{\alpha} = p_{\sigma} \quad (\text{III.175})$$

Thus, the following simpler definitions prevail.

$$\vec{H}_{\sigma}^{(n)} = \vec{t}_{\sigma} + \frac{1}{2} \frac{\partial \vec{H}}{\partial y^{\sigma}} \quad (\text{III.176})$$

$$T^{\alpha\sigma} = t \left[\tau_{(u)}^{\alpha\sigma} + \tau_{(l)}^{\alpha\sigma} \right] \quad (\text{III.177})$$

$$V^{\alpha\sigma} = t \left[\tau_{(u)}^{\alpha\sigma} - \tau_{(l)}^{\alpha\sigma} \right] \quad (\text{III.178})$$

$$\vec{\ell}^{\alpha} = \ell^{\alpha\sigma} \hat{A}_{\sigma} = T^{\alpha\sigma} \hat{A}_{\sigma} \quad (\text{III.179})$$

$$\vec{m}^{\alpha} = \frac{i}{2} \left[V^{\alpha\sigma} - T^{\alpha\sigma} \right] \epsilon_{\sigma\tau} \vec{A}^{\tau} \quad (\text{III.180})$$

$$\vec{d}^{\alpha} = d^{\alpha\sigma} \hat{A}_{\sigma} + d^{(3)\alpha} \vec{N} \quad (\text{III.181})$$

$$\vec{p}^{\sigma} = p_{\alpha}^{\sigma} \vec{A}^{\alpha} \quad (\text{III.182})$$

$$d^{\beta\alpha} = p_{\alpha} s^{\beta} s^{\alpha} \quad (\text{III.183})$$

$$d^{(3)\beta} = p_{\alpha} s^{\beta} \quad (\text{III.184})$$

$$p_2^z = p_1^i = p_0^h \quad (\text{III.185})$$

$$\left\{ \begin{smallmatrix} \alpha \\ \beta\gamma \end{smallmatrix} \right\} \approx \left\{ \begin{smallmatrix} \alpha \\ \beta\gamma \end{smallmatrix} \right\}_0 \quad (\text{III.186})$$

The equilibrium equations assume the form (see Eqs. (III.108) - (III.110),

$$\ell^{\sigma\alpha} \Big|_{\sigma} + \kappa \left(d^{\sigma\alpha} \Big|_{\sigma} - d^{(0)\sigma} \right) + F^{\alpha} = 0 \quad (\text{III.187})$$

$$l^{\alpha\mu} B_{\alpha\mu} + \lambda (d^{(\alpha\mu)}|_r + d^{(\mu\alpha)} B_{\alpha\mu}) + F^{\lambda} = 0 \quad (\text{III.188})$$

$$m^{\beta\alpha}|_{\beta} - \lambda d^{(\beta\alpha)} = 0 \quad (\text{III.189})$$

We note that the vertical bar indicates covariant differentiation with respect to the metric of the ~~deformed~~ plate. However, our present theory is restricted to small rotations and since the Christoffel symbols of the deformed plate are approximated by those of the undeformed plate, the covariant differentiation can be accomplished relative to the metric of the undeformed plate, i.e., e.g.,

$$l^{\alpha\mu}|_{\alpha} = l^{\alpha\mu}_{,\alpha} \quad (\text{III.190})$$

Moreover the term multiplied by λ in Eq. (III.187) and the term $\lambda d^{(\mu\alpha)} B_{\alpha\mu}$ in Eq. (III.188) are at least one order of magnitude smaller than the other terms in their respective equations.

If we also substitute the approximation for the second fundamental tensor (Eq. (III.170)), the equilibrium equations simplify to

$$l^{\alpha\mu}_{,\alpha} + F^{\alpha} = 0 \quad (\text{III.191})$$

$$l^{\alpha\mu} w_{,\alpha\mu} + \lambda p_{\alpha} s^{\alpha} + F^{\lambda} = 0 \quad (\text{III.192})$$

$$m^{\beta\alpha}_{,\beta} - \lambda p_{\alpha} s^{\alpha} = 0 \quad (\text{III.193})$$

It will be convenient to split the tensor $L^{\sigma\mu}$ into the initial prestress plus an increment due to the loading F^a and F^b . We express this as

$$L^{\sigma\mu} = L_{(0)}^{\sigma\mu} + \Delta L^{\sigma\mu} \quad (\text{III.194})$$

where $L_{(0)}^{\sigma\mu}$ is the initial prestress due to the internal pressure P_0 . Note that since $L_{(0)}^{\sigma\mu}$ is a constant the force equilibrium equations become

$$\Delta L_{,\sigma}^{\sigma\mu} + F^a = 0 \quad (\text{III.195})$$

$$\Delta L_{(0)}^{\sigma\mu} w_{,\sigma\tau} + L_{(0)}^{\sigma\mu} w_{,\sigma\tau} + \frac{d}{dt} \frac{1}{h} \frac{\partial}{\partial \tau} + F^b = 0 \quad (\text{III.196})$$

The stress-strain relations for the membranes are now written in the form (see Eq. (III.112)),

$$\Delta \tau^{\sigma\mu} = E^{\sigma\mu\sigma\tau} \gamma_{\sigma\tau} \quad (\text{III.197})$$

where $E^{\sigma\mu\sigma\tau}$ is the elasticity tensor appropriate to the existing state of stress. For the flat configuration with the same thickness membrane treated in this section, the following simple relations can be used in place of Eq. (III.197).

$$L^{\sigma\mu} = 2t E^{\sigma\mu\sigma\tau} \gamma_{\sigma\tau}^0 \quad (\text{III.198})$$

$$w^{\sigma\mu} = \frac{t}{2} E^{\sigma\mu\sigma\tau} A_{,\sigma\tau}^0 \quad (\text{III.199})$$

FEL TDR 64-1A7

The quantities of interest are δ^{α} , δ_{α}^{β} , $\delta_{\alpha\beta}^{\gamma}$, $\delta_{\alpha\beta}^{\gamma\delta}$, $\delta_{\alpha\beta}^{\gamma\delta\epsilon}$, and $\delta_{\alpha\beta}^{\gamma\delta\epsilon\zeta}$ making a grand total of 18 unknowns. For the solution we have the seven strain-displacement relations given by Eqs. (III.145) - (III.147), the five equilibrium equations given by Eqs. (III.195), (III.196) and (III.193), and the six stress-strain relations given by Eqs. (III.198) - (III.199).

It should be observed that each of the equilibrium equations can be partitioned into three groups of terms. One group consists of changes in the force (or moment) resultants coupled together with the geometry of the shell in its deformed state, e.g., $\Delta F^{\alpha\beta}$, $\Delta M^{\alpha\beta}$. Another group consists of the force (or moment) resultants of the deformed state coupled together with the changes in the geometry, e.g., $\Delta \{ \delta^{\alpha\beta} \} \delta^{\gamma\delta}$, $\Delta \delta_{\alpha\beta}^{\gamma\delta} \delta^{\epsilon\zeta}$. The third group are the increments in the applied loads, ΔF^{α} and ΔF^{β} . Since the inflated sandwich shell can deflect more readily in the normal direction than in the tangential direction, our intuition leads us to expect that the terms involving changes in the second fundamental tensors are more important than those involving changes in the Christoffel symbols. Also it may be expected that many of the terms may be neglected as they are in the theory of thin shells. However, until an actual configuration is tackled, the relative orders of magnitude cannot be accurately determined.

LIST OF PRINCIPAL SYMBOLS FOR APPENDIX III

\vec{d}^a	Vectors representing effect of σ^a
$d^{ab}, d^{(2)ab}$	Tensor components of \vec{d}^a
ℓ^{ab}	Force resultant tensor
m^{ab}	Moment resultant tensor
\vec{p}^a	Pressure resultant
p^a_{σ}	Tensor components of \vec{p}^a
q^a	Transverse shear resultant tensor
s^a, s^b	Tensor components of \vec{s}
E	Young's modulus
E^{abcd}	Elasticity tensor
\vec{F}	Applied load vector
F^a, F^b	Components of \vec{F}
$\vec{H}_\sigma^{(u)}, \vec{H}_\sigma^{(l)}$	Base vectors on upper and lower membranes associated with \vec{N}
γ_{ab}	Strain tensor
γ_{ab}	Transverse shear strain
δ^a_b	Kronecker delta
$\epsilon_{ab}, \epsilon^{ab}$	Permutation tensor
μ	Shear modulus

SYMBOLS (Cont'd)

 ν

Poisson's ratio

 $\vec{\sigma}_{(u)}^\alpha, \vec{\sigma}_{(l)}^\alpha$

Stress vectors on upper and lower membranes

 σ^*

Effective stress of shear chords

 $\tau_{(u)}^{\alpha\sigma}, \tau_{(l)}^{\alpha\sigma}$

Stress tensor on upper and lower membranes

Associated with Undeformed Middle Surface

 \vec{a}_α

Covariant base vectors

 $a_{\alpha\beta}, a^{\alpha\beta}$

First fundamental tensor

 $b_{\alpha\beta}, b_\beta^\alpha$

Second fundamental tensor

 \vec{n}

Unit normal vector

 $\vec{r}_0(\xi^1, \xi^2)$

Position vector

 $\left\{ \begin{smallmatrix} \delta \\ \alpha\beta \end{smallmatrix} \right\}_0$

Christoffel symbol of second kind

Associated with Deformed Middle Surface

 \vec{A}_α

Covariant base vectors

 $A_{\alpha\beta}, A^{\alpha\beta}$

First fundamental tensor

 $B_{\alpha\beta}, B_\beta^\alpha$

Second fundamental tensor

 \vec{N}

Unit normal

 \vec{R}_0

Position vector

 $\left\{ \begin{smallmatrix} \delta \\ \alpha\beta \end{smallmatrix} \right\}$

Christoffel symbol of second kind

Assorted Marks

Repeated Greek indices to be summed from 1 to 2.

$(\quad)_{,\alpha}$ Signifies covariant differentiation with respect to metric of undeformed middle surface, e.g.,

$$l^{\sigma\alpha}_{,\sigma} \equiv \frac{\partial l^{\sigma\alpha}}{\partial x^{\sigma}} + \left\{ \begin{matrix} \sigma \\ \sigma\tau \end{matrix} \right\} l^{\alpha\tau} + \left\{ \begin{matrix} \alpha \\ \sigma\tau \end{matrix} \right\} l^{\sigma\tau}$$

$$g^{\sigma\alpha}_{,\sigma} \equiv \frac{\partial g^{\sigma\alpha}}{\partial x^{\sigma}} + \left\{ \begin{matrix} \sigma \\ \sigma\tau \end{matrix} \right\} g^{\alpha\tau}$$

$(\quad)|_{\alpha}$ Signifies covariant differentiation with respect to metric of deformed middle surface, e.g.,

$$l^{\sigma\alpha}|_{\sigma} = \frac{\partial l^{\sigma\alpha}}{\partial x^{\sigma}} + \left\{ \begin{matrix} \sigma \\ \sigma\tau \end{matrix} \right\} l^{\alpha\tau} + \left\{ \begin{matrix} \alpha \\ \sigma\tau \end{matrix} \right\} l^{\sigma\tau}$$

\times Vector product

\cdot Scalar product

Unclassified

Security Classification

REPORT CONTROL DATA - R1D <small>(Security classification of title, body of abstract and including classification must be entered when the report is classified)</small>		
1. ORIGINATOR'S ACTIVITY (Agency or other) Aeroelastic and Structures Research Laboratory Massachusetts Institute of Technology Cambridge 39, Massachusetts		2a. REPORT SECURITY CLASSIFICATION CONFIDENTIAL 2b. GROUP A
3. REPORT TITLE Aeroelastic Investigations of Inflatable Lifting Surfaces (U)		
4. DESCRIPTIVE NOTES (Type of report and inclusive dates)		
5. AUTHOR(S) (Last name, first name, initial) Martuccelli, John R., Zartarian, Garabed, McCallum, R. B.		
6. REPORT DATE February 1965	7a. TOTAL NO. OF PAGES 260	7b. NO. OF VOLS 13
8a. CONTRACT OR GRANT NO. AF33(657)-0568 a. PROJECT NO. 1370 c. Task No. 137003	8b. ORIGINATOR'S REPORT NUMBER(S) FDL TDR 64-147 8c. OTHER REPORT NUM(S) (Any other numbers that may be assigned to report) ASRL TR 114-1	
9. AVAILABILITY/LIMITATION NOTICES Qualified requesters may obtain copies of this report from DDC.		
11. SUPPLEMENTARY NOTES	12. SPONSORING MILITARY ACTIVITY AFTEL, FHB WPAFB, Ohio	
13. ABSTRACT <p>This report covers a program of research on analytical studies and experimental verification of the vibration and flutter characteristics of inflatable structures, as a first step toward establishing design criteria which will insure that lifting surfaces for future inflatable vehicles will be free from dynamic instabilities. The research effort was mainly confined to the AIRBAT - type structure, where the spacing of the surfaces is achieved by chords held in tension by internal pressure.</p> <p>A method is presented for constructing AIRBAT models which are suitable for use as wind tunnel flutter models. In addition to the standard vibration data, the vibration mode shapes of a delta wing, as determined by use of mirrors mounted on the model, are presented. Some experimental results on the properties of the model surface material are also included.</p> <p>Sixty-five flutter points were obtained for cantilevered, half-span delta-wing models over the Mach number range from 0.116 to 6.0. In addition to determining an experimental boundary for a basic delta W^{+1}, the effects of leading-edge sweep, angle of attack, and the pressure differential between the model and ambient air pressures were investigated at several supersonic Mach numbers.</p> <p>A theoretical investigation of membrane-type flutter of an inflatable panel and the development of the equations governing the structural behavior of an inflated AIRBAT section are presented in separate appendices.</p>		

DD FORM 1 JAN 64 1473

Security Classification

Copy available to DTIC does not permit fully legit's reproduction

UNCLASSIFIED